Characteristics of Saharan dust emission mechanisms in boreal summer: a satellite and modelling approach



Thomas Caton Harrison

Keble College

University of Oxford

A thesis submitted for the degree of

Doctor of Philosophy

Trinity 2021

Acknowledgements

This thesis and all the research it contains was funded by the Natural Environment Research Council as part of the Doctoral Training Partnership (DTP) in Environmental Research (NERC). I am grateful both to NERC and to the staff at the University of Oxford involved in the administration and teaching on the DTP. Thanks to them, I have been able to devote myself to independent research while also remaining part of a wider multidisciplinary community. I was also part-funded through a Met Office CASE studentship, allowing me to collaborate with the Hadley Centre and run model simulations. I would like to thank Richard Jones and Nick Savage for their part in this. I know that without Nick's depth of expertise and patience these simulations would have been impossible.

Richard Washington first suggested to me during my BA that I should consider Saharan dust emission mechanisms as a research topic. This led to an undergraduate dissertation, a Master's thesis and eventually this DPhil. Richard has been there at every step with guidance, wisdom and a stream of new ideas. The existence of this research as well as my own outlook as a scientist is thanks to him. My second supervisor Sebastian Engelstaedter introduced me to the world of coding and climate computation, something I never imagined I would find so absorbing. He has been an excellent mentor and his experience and wide perspective in the field of mineral dust has greatly enriched the DPhil. My thanks go also to Neil Hart and Ian Ashpole for the time they devoted to my Transfer and Confirmation of status, and to many other helpful discussions. Along with Ron Miller, Ian also examined this DPhil and I would like to thank both of them for a stimulating viva and for their thoughtful comments which substantially improved the thesis.

Even though a global pandemic cut my time in the Climate Lab and SoGE short, I am thankful for the company of the DPhils and Postdocs there that made it such a lively research environment, as well as those that worked with me to keep the Radcliffe Met Station going. Lastly, I want to thank my friends and family for all their support. I owe them a great deal.

Abstract

Mineral dust is one of the most abundant atmospheric aerosols and has a wide range of impacts on climate, meteorology, health and biogeochemistry. North African sources are responsible for about half of the total atmospheric burden, peaking as an emission source in the boreal summer months of June, July and August. In-situ data from the Fennec observation campaign of 2011 and 2012 indicates that cold pool outflows (CPOs) from convective downdrafts are the primary meteorological driver of these summertime emissions, followed by nocturnal low-level jet (LLJ) breakdown, both mesoscale phenomena which numerical models struggle to represent faithfully. Very few surface observations are available to characterise these emission mechanisms, however, and the extent to which Fennec observations are representative remains unclear. Satellite data from the Spinning Enhanced Visible and Infrared Imager (SEVIRI) offers both the volume of data and resolution to observe emission mechanisms on the long term.

In this thesis, two sets of automated algorithms are applied to 14 years of summertime SEVIRI data, the first of which categorises automatically identified and tracked dust by emission mechanism and the second of which tracks and characterises dust-laden cold pool outflows. CPOs account for 82% of the total observed dust and 88% at the point of emission in the central and western Sahara during boreal summer, which is the highest estimate yet of their contribution. Whereas CPO dust is widespread and the majority of dust source regions are primarily CPO-driven, LLJs dominate a small number of hotspots such as the Tidihelt Depression. CPOs are far-reaching, with 22.5% travelling over 300 km. They also follow a clear diurnal cycle which favours emissions in the late afternoon and evening. Unlike dust emission, CPO frequency peaks in August in southern Algeria.

In the final component of the thesis, satellite observations are used to support a Met Office Unified Model experiment diagnosing the role of orography in driving dust-emitting LLJs over central Algeria. Fluvial drainage from mountains is thought to contribute erodible sediment to western Saharan dust sources, but their effect upon emission mechanisms there is untested. Removing the Hoggar mountains reduces LLJ emission frequency by approximately 30% as an elevated heating anomaly helps sustain the strong pressure gradient driving low-level winds across the region in summer.

This thesis offers a meteorological perspective on satellite dust source maps, showing the contribution of erosivity to known summertime emission hotspots on climatic timescales. The fact that most central and western Saharan dust sources are predominantly activated by CPOs poses a challenge for numerical modelling of the dust cycle given the inadequate representation of downdrafts in models with convective parameterization.

Contents

List of Figures **xi**

List of Acronyms and Abbreviations **xv**

1 Introduction **1**
1.1 Preface . . . 1
1.2 Thesis structure . . . 3
1.3 Background . . . 4
1.3.1 Role of dust in the Earth system . . . 4
1.3.2 Dust emission processes at the microscale . . . 7
1.4 Dust emission modelling . . . 8
1.5 Observational approaches . . . 11
1.5.1 Reanalyses . . . 13
1.5.2 Campaign observations . . . 13
1.5.3 Satellite-based methods . . . 18
1.6 Summertime controls on erosivity in the central Sahara . . . 24
1.6.1 Synoptic variability . . . 24
1.6.2 Cold pool outflows . . . 27
1.6.3 Low-level jets . . . 31
1.6.4 Other emission mechanisms . . . 33
1.6.5 Role of orography . . . 35
1.7 Thesis aims and objectives . . . 38

2 Data and methods **41**
2.1 Background: image processing and feature tracking . . . 41
2.2 SEVIRI . . . 43
2.2.1 Pink dust composite imagery . . . 44
2.2.2 SEVIRI dust flags . . . 47
2.3 Met Office Unified Model . . . 49
2.4 In situ observations . . . 50
2.4.1 Fennec data . . . 50
2.4.2 MIDAS and IGRA data . . . 51

3 A 14-Year climatology of Saharan dust emission mechanisms inferred from automatically tracked plumes **53**
3.1 Abstract . . . 55
3.2 Introduction . . . 56
3.2.1 Low-level jets . . . 58
3.2.2 Cold pool outflows . . . 60
3.2.3 Aims . . . 61

3.3 Detecting and tracking emitted dust from satellite 62
3.4 Classifying observed dust plumes by emission mechanism 66
3.4.1 Manual classification 66
3.4.2 Automated classification 70
3.4.3 Timing of emission 70
3.4.4 Deep convection association 71
3.4.5 Geometry 73
3.4.6 Regression model 75
3.4.7 Other emission mechanisms 79
3.5 Comparison with manual detection methods and in situ observations 80
3.6 Climatology of emission mechanisms 82
3.7 Summary and conclusions 94
3.8 Acknowledgements 96

4 Satellite-derived characteristics of Saharan cold pool outflows during boreal summer 97
4.1 Abstract 99
4.2 Introduction 100
4.2.1 Background 101
4.3 Automated tracking of cold pool outflow boundaries 104
4.3.1 Algorithm phase 1: candidate CPO masking 106
4.3.2 Algorithm phase 2: discarding false positive tracked CPOs 109
4.3.3 Estimating propagation speed and direction 111
4.4 Validation 115
4.5 Results and discussion 118
4.5.1 Characteristics of tracked CPOs 118
4.5.2 Seasonality of CPOs and comparison with dust emission 122
4.6 Summary and conclusions 131
4.7 Acknowledgements 133

5 Influence of orography upon summertime low-level jet dust emission in the central and western Sahara 135
5.1 Abstract 137
5.2 Introduction 138
5.2.1 Background 138
5.2.2 Orographic effects on dust-emitting conditions in the Sahara 139
5.2.3 Aims 141
5.3 Data and model experiment setup 142
5.3.1 Model data 142
5.3.2 Observations 143

5.3.3 Model validation 144
5.3.4 Orography experiments 148
5.3.5 Composite method 149
5.4 Synoptic conditions 151
5.5 Model experiment results 154
5.5.1 Wind speed and vertical structure 154
5.5.2 Leeward circulation 156
5.5.3 Geostrophic wind analysis 162
5.5.4 Role in dust emission frequency 164
5.6 Summary and conclusions 170
5.7 Acknowledgements 172

6 Conclusions **173**
6.1 Introduction 173
6.2 Summary of thesis aim outcomes 175
6.3 Discussion 179
6.3.1 Geographical distribution of emission mechanisms 179
6.3.2 Importance and characteristics of cold pool outflows . . . 183
6.3.3 Orography as a control on erosivity 186
6.4 Research applications and future work 187
6.4.1 A meteorological perspective on dust source maps 187
6.4.2 Improving driving wind fields for dust models 188
6.4.3 Priorities for future research 190

Appendices

A Statement of Authorship **197**

References **199**

x

List of Figures

1.1 Seasonal variations in global Aerosol Optical Depth (AOD) from Multiangle Imaging Spectrometer (MISR) retrievals at 0.55 μm 5
1.2 Coverage of daily-reporting meteorological ground stations on the 9th February 2021 from the WIGOS Data Quality Monitoring System webtool 12
1.3 Overview of a number of field campaigns observing processes related to dust emission prior to and including Fennec 14
1.4 Relative contribution of different meteorological dust emission mechanisms to observations of dust loading measured by nephelometer scattering at Bordj-Badji Mokhtar for the June 2011 Fennec intensive observation period 16
1.5 Map of dust sources detected using the automated SEVIRI dust flag tracking method of Ashpole and Washington (2013a) 22
1.6 Diurnal cycle of instantaneous hourly uplift potential averaged over the 25th July to 3rd August 2006, simulated with the UK Met Office Unified Model at different grid-spacings 28
1.7 Prominent North African dust source regions identified in SEVIRI with the Schepanski et al. (2007) method (red hatched regions) overlain on a map of Saharan orography, with shading corresponding to elevation (metres) 36

2.1 Example of a SEVIRI RGB pink dust composite derived from SEVIRI brightness temperatures at 1400 UTC on the 23rd August 2006 45

3.1 Schematic diagrams of emission mechanisms 59
3.2 Example of SEVIRI dust flags applied to 1100 UTC SEVIRI retrievals on the 11th of June 2010 63
3.3 Examples of improvements to dust flagging introduced with an adjusted plume tracking system 66
3.4 Total counts of dust plume emission events in the Central and Western Sahara for June, July and August of 2004-2017 67
3.5 Plumes observed in SEVIRI 'pink dust' composites at 1200 UTC on June 17th 2011 68
3.6 Wind speed composites on days identified as having LLJ activity 72
3.7 Life cycle of a typical tracked plume (at 2 hourly intervals), shown as a delineated region of the RGB pink dust composite, with each timestep overlain (older detections plotted over newer ones) . . . 74
3.8 Mean change in the axis offset criterion since it was calculated in the previous timestep of a plume's evolution, plotted against the time since the emission of the plume 75

3.9 Distribution of values of predictors used for multiple logistic model of plume LLJ probability 78
3.10 Total yearly counts of pixels classified as belonging to cold pool outflow (blue) and low-level jet (red) driven dust events 83
3.11 Total counts of pixels classified as belonging to cold pool outflow events across the total lifetime of all plumes tracked from 2004-2017 84
3.12 Total counts of pixels classified as belonging to low-level jet events across the total lifetime of all plumes tracked from 2004-2017 . . 86
3.13 Percentage of emission pixels classified as being low-level jet driven for June, July and August 2004-2017 87
3.14 Controls upon observed CPO and LLJ-driven dust emission . . 91
3.15 Map of the Tidihelt region identified as both a major dust source and LLJ hotspot 92
3.16 Preferred propagation directions of plumes at selected dust sources 93

4.1 Steps of the CPO detection algorithm applied to a SEVIRI image from 0115 UTC 10th of July 2011 105
4.2 Flow chart showing steps involved in the CPO detection algorithm 106
4.3 Probability density functions of (a) brightness temperature difference gradient (K), (b) CPO duration (hours), (c) maximum pixel size reached by events during their lifetime and (d) distance from deep convection for true (white) and false (dark grey) events tracked manually through July 2010 109
4.4 Top-down (bird's eye view) 2D model of a CPO event observed by satellite 112
4.5 Results of algorithm used to calculate CPO propagation speeds, demonstrated for two CPOs lasting 8 hours and 30 minutes from 15:30 on 09/07/2010 (upper) and 6 hours and 30 minutes from 18:30 on 28/07/2004 (lower) 114
4.6 Examples from 2011 of automatically detected CPO outflow boundaries relative to other dust and deep convective cloud features in SEVIRI pink dust imagery 116
4.7 Examples of passages of automatically detected cold pool outflow boundaries compared with contemporaneous measurements of surface wind speed (solid black line) and relative humidity (dashed grey line) from the Fennec automatic weather station network . 117
4.8 Mean diurnal cycle of (a) CPO generation, taken as the first timestep of detection (blue bars), CPO propagation speed over the first two hours (box plots) 120

4.9 Distribution of CPO durations and mean propagation speeds (upper) and composites of all CPOs (lower) 121
4.10 Pixels classified as belonging to cold pool outflow events across the total lifetime of all features tracked from 2004-2017 123
4.11 Percentage of observations of weather codes associated with dust activity (orange) and thunderstorms (blue) at stations reporting to the Met Office Integrated Data Archive System (MIDAS) for June, July and August 127
4.12 Mean of Downdraft Convective Available Potential Energy (DCAPE) in J/kg measured from sonde ascents at Tamanrasset (blue), Agadez (pink) and Niamey (green) for June, July and August 2004-2017 128

5.1 Comparison between ERA5 (left) and 12 km horizontal resolution Unified Model remapped onto the ERA5 horizontal grid (right) 146
5.2 Mean 925 hPa control experiment wind speeds (ms^{-1}) outside of summer 147
5.3 Representation of orography as elevation above sea level in the 12 km UM simulations for the control experiment (left) and the FLATHOGGAR experiment (right) 148
5.4 Time versus height composite sonde measurements of temperature anomaly (shaded boxes) and wind speed/direction anomaly seen from a bird's eye view (arrows) taken at 1200 UTC at In Salah relative to the mean for June, July and August 1997-2007 152
5.5 Composite anomaly potential temperature and geopotential heights with wind vectors relative to the mean for June, July and August 1997-2007 153
5.6 Composite 925 hPa absolute wind speeds (left, filled contours and wind vectors) for the control (upper) and FLATHOGGAR (lower) experiments 155
5.7 Composite cross sections of wind speed (filled contours) calculated across the axes plotted as dashed lines on the horizontal wind field maps above each cross section 157
5.8 Control minus FLATHOGGAR experiment composite (a) 850 hPa geopotential height and (b) 850 hPa wind field (wind speed as filled contours) 158
5.9 Composite cross sections of u winds for the control (a-d) and FLATHOGGAR (e-h) experiments 159
5.10 Composite cross sections of v winds for the control (a-d) and FLATHOGGAR (e-h) experiments 160

5.11 Composite cross sections of air potential temperature for the control minus FLATHOGGAR experiments 161
5.12 Estimated 925-700 hPa geopotential thickness difference and geostrophic wind perturbation given the difference in the temperature profile between the control and FLATHOGGAR experiment, averaged across the June, July and August 2004-2007 period . . 163
5.13 Estimates of changes to dust emission frequency based on the difference in wind speed distributions between experiments . . . 166

6.1 Overview of mesoscale emission mechanisms overlaid on a SEVIRI dust source map of the central and western Sahara 180

List of Acronyms and Abbreviations

AERONET . . Aerosol Robotic Network

AEW . . . . . African Easterly Wave

AI . . . . . Aerosol Index

AMMA . . . . African Monsoon Multidisciplinary Analysis

AOD . . . . . Aerosol Optical Depth

AOT . . . . . Aerosol Optical Thickness

AVHRR . . . . Advanced Very-High-Resolution Radiometer

AWS . . . . . Automatic Weather Station

BBM . . . . . Bordj-Badji Mokhtar

BoDEx . . . . Bodele Dust Experiment

BT . . . . . Brightness Temperature

BTD . . . . . Brightness Temperature Difference

BTDG . . . . . Brightness Temperature Difference Gradient

CALIOP . . . Cloud-Aerosol Lidar with Orthogonal Polarization

CASE . . . . . Collaborative Awards in Science and Engineering

CBL . . . . . Convective Boundary Layer

CEDA . . . . . Centre for Environmental Data Analysis

CMIP . . . . . Coupled Model Intercomparison Project

CPO . . . . . Cold Pool Outflow

CWS . . . . . Central and Western Sahara

DABEX . . . . Dust and Biomass Experiment

DACCIWA . . Dynamics-Aerosol-Chemistry-Cloud Interactions in West Africa

DCAPE . . . . Downdraft Convective Available Potential Energy

DFID . . . . . Department for International Development

DJF . . . . . December January February

DODO . . . . Dust Outflow and Deposition to Ocean

ECMWF . . . European Centre for Medium-Range Weather Forecasting

FCFA . . . . . Future Climate for Africa

GERBILS . . Geostationary Earth Radiation Budget Intercomparison of Longwave and Shortwave Radiation

GISS . . . . . Goddard Institute for Space Studies

IASI . . . . . Infrared Atmospheric Sounding Interferometer

IGRA . . . . . Integrated Global Radiosonde Archive

IPCC . . . . . Intergovernmental Panel on Climate Change

IR . . . . . Infrared

ITCZ . . . . . Intertropical Convergence Zone

ITD . . . . . Intertropical Discontinuity

JJA . . . . . June July August

LAM . . . . . Limited Area Model

LLJ . . . . . Low-level Jet

MAM . . . . . March April May

MAPIR . . . . Mineral Aerosol Profiling from Infrared Radiences

MERRA . . . Modern-Era Retrospective Analysis for Research and Applications

MIDAS . . . . Met Office Integrated Data Archive System

MISR . . . . . Multiangle Imaging Spectrometer

MODIS . . . . Moderate Resolution Imaging Spectrometer

MSG . . . . . Meteosat Second Generation

NAFDI . . . . North African Dipole Index

NCEP-CFSR National Centers for Environmental Prediction Climate Forecast System Reanalysis

NERC . . . . . Natural Environment Research Council

OMI . . . . . Ozone Monitoring Instrument

RCM . . . . . Regional Climate Model

RGB . . . . . Red-Green-Blue

SABL . . . . . Saharan Atmospheric Boundary Layer

SAMUM1 . . Saharan Mineral Dust Experiment 1

SAMUM2 . . Saharan Mineral Dust Experiment 2

SDF . . . . . SEVIRI Dust Flag

SEVIRI . . . . Spinning Enhanced Visible and InfraRed Imager

SHADE . . . . Saharan Dust Experiment

SHL . . . . . Saharan Heat Low

SON . . . . . September October November

SYNOP . . . . Surface Synoptic Observations

TCWV . . . . Total Column Water Vapour

TID . . . . . Tidihelt Domain

TOMS . . . . . Total Ozone Mapping Spectrometer

TP . . . . . Triple Point of Mali-Niger-Algeria

TRMM . . . . Tropical Rainfall Measuring Mission

UKCP . . . . . UK Climate Projections

UM . . . . . Met Office Unified Model

UTC . . . . . Universal Time Coordinated

UV . . . . . Ultraviolet

WAM . . . . . West African Monsoon

WIGOS . . . . WMO Integrated Global Observing System

WMO . . . . . World Meteorological Organization

1 Introduction

Contents

1.1 Preface 1
1.2 Thesis structure 3
1.3 Background 4
1.3.1 Role of dust in the Earth system 4
1.3.2 Dust emission processes at the microscale 7
1.4 Dust emission modelling 8
1.5 Observational approaches 11
1.5.1 Reanalyses 13
1.5.2 Campaign observations 13
1.5.3 Satellite-based methods 18
1.6 Summertime controls on erosivity in the central Sahara 24
1.6.1 Synoptic variability 24
1.6.2 Cold pool outflows 27
1.6.3 Low-level jets 31
1.6.4 Other emission mechanisms 33
1.6.5 Role of orography 35
1.7 Thesis aims and objectives 38

1.1 Preface

This thesis has been written in the UK, far from the global 'dust belt' of high aerosol optical depth between 0 and 40°N (Muhs et al. 2014). Nonetheless, southerly conditions occasionally bring Saharan dust to western Europe, which perceptive observers might notice as a dim red hue in the sky or just a gloomy haze. In February 2021, a French NGO reported that it had measured high radioactivity associated with cesium-137 in samples of an ongoing Saharan dust episode. France had carried out nuclear weapons testing in the 1960s in southern

Algeria and, in an ironic turn, the residue had found its way to its original source[1]. A number of synoptic patterns can support this transport, but the Sahara is not a continuous source of mineral dust. The volume of suspended dust available for transport depends on the meteorology in the Sahara supporting emissions.

Simulated dust emission from North Africa differs greatly between models (Huneeus et al. 2011; Wu et al. 2020). In part this is due to ill-constrained surface characteristics and dust source geomorphology. Nevertheless, if the winds driving dust outbreaks from this region could be well approximated by characterising synoptic weather patterns, predicting changes to emissions in future might not be so difficult. In the Sahara's peak emission season of summer, however, short bursts of gusty wind are the major driver of dust source activation. in situ data from the Fennec Campaign of 2011 shows that convective downdrafts are the chief supplier of these gusts (Allen et al. 2013). Hence, even in the dry Sahara, moist convection has a profound effect on aeolian processes.

The research presented in this thesis is motivated by a need to characterise mesoscale winds responsible for Saharan dust emission on the long term, without recourse to ill-constrained reanalyses. It is argued that the small volume of in situ data available can be used to validate a satellite-based approach to inferring meteorological emission mechanisms. A long-term perspective is critical as Saharan emission varies considerably from year to year. The datasets resulting from this work are posed as constraints on model simulations, and in the final research chapter satellite observations are used to support an idealised model experiment.

Saharan dust is far more than a pollutant. The range of impacts described in Section 1.3.1 motivates a complete understanding of the dust cycle and a reasoned estimate of how it will evolve under anthropogenic climate change. An important

[1]One news article describing this is found at `https://www.euronews.com/2021/03/01/irony-as-saharan-dust-returns-radiation-from-french-nuclear-tests-in-the-1960s`

step in remedying model deficiencies is collecting observations of problematic processes and assessing controls on their variability and intensity. This thesis is a small part of this effort to improve numerical models by characterising physical processes responsible for dust emission.

1.2 Thesis structure

The research comprising this thesis is presented in the form of three submitted peer-reviewed journal articles, each addressing the meteorological mechanisms responsible for emission of dust from the central and western Sahara in boreal summer. The first two of these papers focus primarily on the development of novel satellite-based algorithms for identification and analysis of emission mechanisms, while the last paper applies part of this observational framework to support a model study of the role of orography in dust-emitting meteorological conditions.

This Chapter reviews the relevant literature encompassing the study of dust emission processes, including the importance and microphysics of dust (Section 1.3), modelling efforts and the need for observational benchmarks (Section 1.4), existing observational products and satellite approaches (Section 1.5). It follows with a review of the current understanding of processes controlling Saharan winds responsible for dust emission ranging from the synoptic (Section 1.6.1) to the mesoscale, with an emphasis on the two major processes described in this thesis, the cold pool outflow (Section 1.6.2) and low-level jet (Section 1.6.3). The role of orography is described in Section 1.6.5. Finally, the aims and objectives of the thesis are presented in Section 1.7.

The next Chapter (2) provides background on the primary data sources used in this thesis and critically evaluates their utility in the context of understanding dust emission. Each of the three research articles constituting the body of the thesis are then presented in Chapters 3-5. Conclusions for the thesis as a whole are made in Chapter 6.

1.3 Background

1.3.1 Role of dust in the Earth system

Emission of mineral dust is a phenomenon that connects the Earth's land surface with its atmosphere. Although global dust emissions are not monitored directly, global dust models with observational constraints on other aspects of the dust cycle indicate that North Africa, including the Sahara and Sahel, supplies approximately half of the annual atmospheric burden (Engelstaedter et al. 2006; Huneeus et al. 2011; Wu et al. 2020; Kok et al. 2021). Regions with high seasonally averaged aerosol optical depth can be seen in Figure 1.1, with Saharan dust an especially large contributor in summer, although the signal is also affected by biomass burning (e.g. along the Gulf of Guinea in winter and over southern China in summer) as well as sulfate and nitrate aerosols from industrial chemical precursors. Saharan dust has been observed in the Amazon basin (Swap et al. 1992), the Caribbean (Colarco et al. 2003), Scandinavia (Ansmann et al. 2003) and even the Arctic (Barkan and Alpert 2010) indicating it has a global reach. For those living in regions where dust outbreaks are common, the reduction in visibility and health impacts are a regular concern. Measured PM_{10} concentrations (particulate matter of 10 micrometres diameter or smaller) appear to spike concurrently with dust episodes in these regions (e.g., Querol et al. 2001) and are linked to respiratory conditions (De Longueville et al. 2010) and meningitis (Pérez Garcıa-Pando et al. 2014) in West Africa.

Beyond the direct impacts on human health, mineral dust affects the Earth's radiative budget and is therefore a contributor to the uncertain aerosol term in projections of the climate's response to greenhouse warming (Boucher et al. 2013). At a global scale, this radiative effect straddles the positive and negative depending on particle size, colour, height, chemical composition and shape (Nousiainen 2009), with coarse-mode particles thought to have a non-negligible contribution (Kok et al. 2017; Ryder et al. 2019). Direct effects on shortwave and longwave radiation are accompanied by indirect effects upon cloud formation

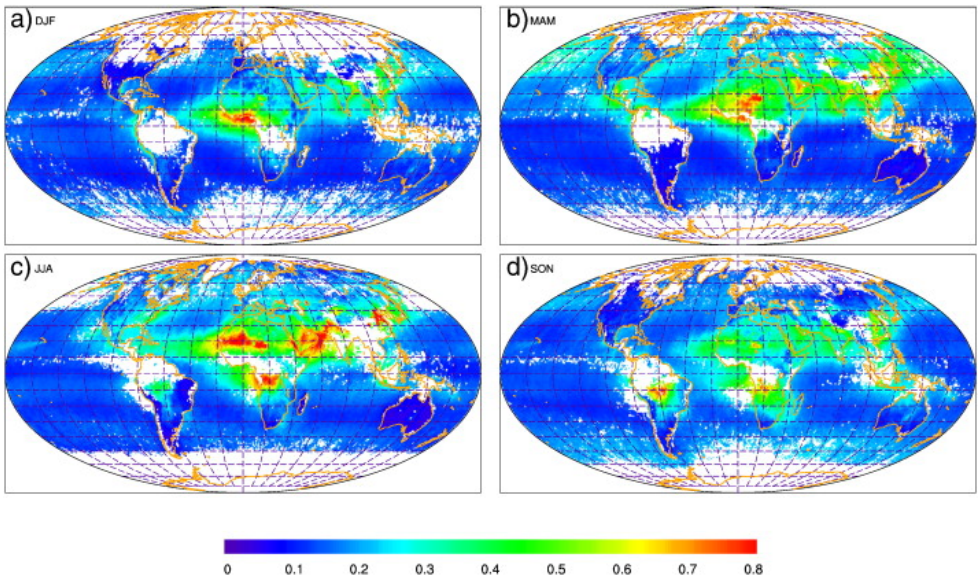


Figure 1.1: Seasonal variations in global Aerosol Optical Depth (AOD) from Multiangle Imaging Spectrometer (MISR) retrievals at 0.55 μm, including (a) DJF, (b) MAM, (c) JJA and (d) SON averaged over the period 2001-2011. Figure from Choobari et al. (2014). The authors identify that high AOD over Amazonia and southern Africa in JJA, along the Gulf of Guinea in DJF and MAM, over southern China in JJA and over Indonesia is primarily a result of biomass burning rather than emissions of mineral dust. Reproduced with permission from Elsevier.

and optical properties. There is evidence that mineral aerosols can act as cloud condensation nuclei depending on soluble coating (Kelly et al. 2007; Karydis et al. 2011; Kumar et al. 2011; Chen et al. 2019), and layers of Saharan dust have a particularly noticeable impact upon observed concentrations of ice condensation nuclei both near and far from source regions (DeMott et al. 2003; Klein et al. 2010; Price et al. 2018). Overall the annual mean top of the atmosphere radiative forcing from mineral aerosols is estimated to be -0.3 to 0.1 Wm^{-2} (Boucher et al. 2013), though an analysis accounting for missing coarse-mode indicates a range of -0.48 to 0.2 Wm^{-2}, suggesting more of a potential for a net warming effect as a result of this poorly understood category of dust particles (Kok et al. 2017).

Outbreaks of mineral dust can affect the development and variability of weather systems. The surface cooling and elevated diabatic heating associated with dust has been shown to inhibit convection in West Africa (Solmon et al. 2012), producing a stabilising effect to which the African easterly jet is sensitive

(Tompkins et al. 2005). Although an abundance of ice condensation nuclei can invigorate convective updrafts, lower cloud drop effective radii in aerosol-abundant environments appears to reduce cloud drop collision efficiency, inhibiting precipitation at the surface (Min et al. 2009; Gibbons et al. 2018). Tropical cyclone formation is thought to be modulated by the presence and coverage of the Saharan air layer given the inverse correlations between satellite dust observations and North Atlantic tropical cyclone frequency (Evan et al. 2011), but the significance and mechanism at work is a subject of considerable debate and uncertainty (Xian et al. 2020).

Dust has an effect upon biogeochemistry after deposition. Long distance transport to the Amazon is associated with nutrient supply such as phosphorus to rainforest soils lacking in soluble minerals (Swap et al. 1992; Koren et al. 2006; Yu et al. 2015) with a recent analysis suggesting the bulk of this material is most likely to originate in western Saharan sources (Yu et al. 2020) rather than the Bodele as proposed by Koren et al. (2006). Direct measurements of dust fluxes to the Amazon basin are scarce, however, and recent observations from French Guiana indicate deposition may be smaller than previously thought (Prospero et al. 2020). Deposition of Saharan dust also supports phytoplankton primary production as the dominant source of iron (Jickells et al. 2005; Mahowald et al. 2008). Regions such as the Southern Ocean are especially sensitive to variability in Saharan dust deposition as they contain high-nitrate low-chlorophyll zones which are iron-limited (Schulz et al. 2012). Variation in ocean primary productivity is in turn thought to affect drawdown of CO_2, with one hypothesis posing that it plays a major role in atmospheric CO_2 concentrations on glacial timescales (Martin 1990).

Given the climatological and biogeochemical significance of dust as well as its impacts on human health, research into dust emission, transport and deposition has formed a fast-growing body of work since the 1990s accompanying the development of Earth system science as a discipline (Engelstaedter et al. 2006;

Shao et al. 2011; Knippertz and Stuut 2014). Advances in the study of dust emission processes as presented in this thesis therefore have an impact downstream upon our understanding of the Earth system as a whole.

1.3.2 Dust emission processes at the microscale

Emission, transport and deposition of fine particles such as sand and dust falls within the class of aeolian processes, which are active on Earth and elsewhere in the solar system where surface material is sufficiently granular and winds are strong enough to mobilise it. The capacity for dust to be entrained from the surface into the atmosphere is therefore a function of erodibility and erosivity. Erodibility refers to the susceptibility of particles to being detached and emitted from the surface and is a characteristic of soils. Erosivity, the primary concern of this thesis, is the ability of an erosive agent such as the wind to fuel such emission (Lal et al. 1994).

The foundational work of Bagnold (1941) established the role of saltation as a dominant microscale process of dust emission under wind stress exceeding a threshold shear velocity. The strength of cohesive forces between particles is such that wind is not typically capable of lifting them directly. Instead, experimental evidence of particles eroding under varied wind speeds and in wind tunnels suggests that sandblasting during saltation is responsible for the majority of emission fluxes (Gillette et al. 1974; Shao et al. 1993). More recent research has highlighted the role that direct emission by wind (direct aerodynamic entrainment) can play under certain conditions, including convective turbulence (Klose and Shao 2013) and where wind speeds are very high over clay loams (Parajuli et al. 2016).

Once mobilised, dust is transported in varying regimes depending on wind speed and particle characteristics. The largest particles (over 70 μm) will either saltate or undergo reptation and creep. Relatively large particles of (20-70 μm) will typically undergo short-term suspension while smaller particles (under

approximately 20 μm) may remain in a state of long-term suspension lasting for days to weeks (Kok et al. 2012), producing the effects described in Section 1.3.1. The 20 μm upper bound on particle diameter typically used in dust models (Huneeus et al. 2011) may be unrealistic, however, as recent airborne observation campaigns close to remote dust sources show that coarse and giant dust particles (over 2.5 and 20 μm, respectively) are much more commonly found in high altitude suspension over the Sahara than previously thought possible under gravitational sedimentation alone (Ryder et al. 2019). Uncovering the physical processes responsible for long-distance suspension of coarse and giant mode mineral dust is an area of ongoing research (e.g. Ryder et al. 2013; Wang 2016; Van Der Does et al. 2018).

1.4 Dust emission modelling

The research presented in this thesis is motivated in part by a need to improve the fidelity of modelled Saharan dust emission and constrain uncertainties relating to the driving wind field. Estimates of the total atmospheric dust burden from year to year as well as the contribution from the Sahara depend heavily upon these models as in situ observations are sparse and typically only used to constrain model estimates (e.g. the 21 in situ observation sites used in the model developed by Tegen et al. (2002)) rather than make global estimates of emission fluxes. Current satellite-based approaches are discussed in Section 1.5.3. Originally confined to specific erodible regions, dust modelling is now global in its scope and underpins our knowledge of the Earth's dust cycle and its radiative effect (Shao et al. 2011). An early example is the global dust model of Tegen and Fung (1994) in which the GISS tracer transport model was used to simulate dust transport and European Centre for Medium range Weather Forecast (ECMWF) analysis data at 1.125° x 1.125° was used for driving winds.

Emission of dust, including its magnitude, patterns and variability through the year, is the largest source of uncertainty in models of the global dust cycle (Tegen 2003). The order of magnitude of yearly dust emissions from North Africa is itself uncertain (Uno et al. 2006), with global aerosol models producing annual emission totals ranging from 1,600 to 4,300 $Tgyr^{-1}$ and an estimated fractional contribution of around 50% to global dust loading (Kok et al. 2021). Estimating emission of dust depends on predicting or prescribing a range of factors. Model inputs include winds and surface conditions such as roughness, soil moisture, texture and snow cover. Exceedance of a threshold velocity is then required to trigger emission, though this threshold in turn depends on the size of erodible particles and the roughness of the surface (Marticorena and Bergametti 1995). Rough surfaces with rocks or vegetation have higher emission thresholds, as do soils with higher moisture content due to increased interparticle cohesive forces (Fécan et al. 1998) but detailed information on these surface characteristics on a global scale is also a critical source of uncertainty (Tegen 2003; Shao et al. 2011).

The wind field is an important part of dust modelling, but models and reanalyses used to drive dust models typically misrepresent the mesoscale winds responsible for a large proportion of dust emission (Tegen and Schulz 2014). One analysis of global models participating in the Coupled Model Intercomparison Project Phase 5 (CMIP5) shows that none were able to reproduce interannual variability in North African dust flux and that this deficiency is not due to misrepresentation of emission processes but rather erroneous surface wind fields (Evan 2018). A common result of comparative dust model studies is that model output is more sensitive to the driving wind field than the choice of emission scheme (Luo et al. 2003; Menut 2008; Fiedler et al. 2016).

A major difficulty with dust model wind fields is that dust emission depends to a large extent upon infrequent intense events and subgrid processes. For example, Cowie et al. (2015) examine synoptic surface observations of wind speed and dust weather codes from 70 sites across North Africa. They find that

25% of dust-generating winds occur only 0.1 to 1.4% of the time. Similarly, Marsham et al. (2013b) find that over a period of 21 days two individual events contributed over a quarter of the observed dust emission at a site in the central Sahara. The annual cycle of satellite-observed dust over North Africa is poorly correlated with mean surface wind speed, instead aligning more closely with changes to convergence and gustiness (Engelstaedter and Washington 2007) which is greatly influenced by moist convection. During boreal summer, short bursts of high winds associated with boundary layer low-level jets and cold pool outflows dominate the dust emission budget (Allen et al. 2013), both of which operate at the mesoscale and are inadequately represented in most coarse reanalysis and model products. Observations and simulations of these two mechanisms are discussed in greater detail in Sections 1.6.2 and 1.6.3.

With improvements to observing systems, most significantly remote sensing (see Section 1.5.3), model dust burdens have been tuned to match satellite retrievals of Aerosol Optical Thickness (AOT), producing comparable dust budgets in AeroCom models (Textor et al. 2006; Kok et al. 2020; Kok et al. 2021). However, tuning is liable to create compensating errors between emission and deposition totals (Knippertz and Todd 2012). Similarly, wind fields may produce appropriate dust emission totals but for the wrong reasons. One example is a study into the role of convection representation in regional simulations of the West African Monsoon by Marsham et al. (2013a). They find that a version of the model with parameterised convection produces erroneously high synoptic scale winds which compensate for missing cold pool outflows, a major dust emission mechanism in the summertime Sahara (see Section 1.6.2). Instead of tuning dust burdens or wind fields, there is a need for more realistic representation of dust emission processes, which will in turn improve simulated deposition (Knippertz and Todd 2012).

Another approach for tuning models for consistency with observations is to target emissions directly by constraining them to dust source regions. Known land-surface features such as topographic depressions (Ginoux et al. 2001a), ephemeral riverbeds (Feuerstein and Schepanski 2019) or exposed paleolakes (Tegen et al. 2002) have been imposed on dust models as preferential sources. A classification of dust source regions has also been defined by Bullard et al. (2011) based on a combination of satellite and in situ data. Although these approaches are important in the absence of better information on surface conditions and can improve the spatiotemporal distribution of dust emission (Miller et al. 2006; Cavazos et al. 2009; Heinold et al. 2016), the quality of meteorological information is still a limiting factor. For example, the dust model results of Feuerstein and Schepanski (2019) show significant uncertainties in realistically reproducing the seasonality of dust production close to monsoon-influenced dust sources in the southern Sahara, likely in part due to limitations of the ECMWF forecast model's representation of convection. Improving the realism of these physical processes in dust models requires a sound observational benchmark for validation purposes. A critical part of this is improving observations of dust-emitting winds close to source regions.

1.5 Observational approaches

The in situ observation network in the Sahara is one of the world's sparsest. In March 2020, the World Meteorological Organization (WMO) and ECMWF launched a web tool allowing users to monitor the quality and coverage of the world's reporting ground weather stations. A snapshot of stations reporting on the 9th February 2021 at 1800 UTC is shown in Figure 1.2, with a volume of reported data within the ensuing 6-hour period greater than or equal to 80% of that expected marked in green. The quality and quantity of observations varies through time but the broad patterns are representative. Although a network of sporadically reporting stations is present along the north coast of North Africa and in the Sahel, the central and western Sahara encompassing much of Niger,

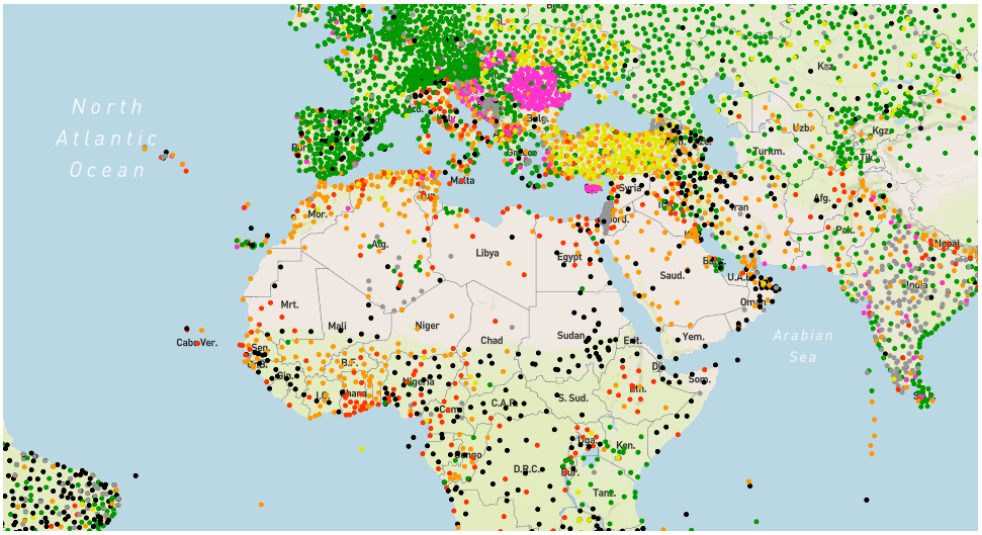


Figure 1.2: Coverage of daily-reporting meteorological ground stations on the 9th February 2021 from the WIGOS Data Quality Monitoring System webtool, developed by the World Meteorological Organization and hosted by the European Centre for Medium-Range Weather Forecasting. Dot colour indicates the volume of data received from the station during the 6-hour reporting period (in this case from 1800 UTC) relative to what was expected according to the station metadata. Pink dots have 100% reporting, green dots have at least 80%, orange dots have at least 30%, red dots have under 30%, black dots have no observations received on the daily period and grey dots have schedule issues. Further information is available at: https://wdqms.wmo.int/about.

southern Algeria, Mali and Mauritania has very poor coverage compared to the dense European network. Given this observational deficit, the challenge of understanding the Saharan climate system lies in making best use of short field campaigns and extracting the most information possible from satellite data.

Routine in situ dust observations on the long term are typically made using sun or sky photometers constituting the international Aerosol Robotic Network (AERONET) network (Holben et al. 1998) or manual dust storm observations from the SYNOP stations in Figure 1.2. AERONET stations are mostly located around the fringes of the Sahara, with the only long-term (10+ years) observations in the central Sahara available at Tamanrasset (Guirado et al. 2014). Despite their spatial heterogeneity, no global network of three dimensional observations exists for any aerosols, unlike the radiosonde network available for characterisation of weather (Miller et al. 2006).

1.5.1 Reanalyses

Reanalyses are a major tool in the meteorology and climate science, with papers describing them among the most cited in the field (Thorne and Vose 2010). A poor observational network in the Sahara, however, means reanalyses must be used with care. Correlations between Saharan observations and the ERA-Interim reanalysis (Dee et al. 2011) are low at sub-daily timescales compared to daily timescales, with ERA-Interim winds underestimating the amplitude of the observed diurnal cycle and the peak wind speeds associated with dust emission events, though synoptic and seasonal variability is well approximated in the central Sahara (Roberts et al. 2017). An absence of the strongest wind speeds and underestimated diurnal cycle is also a feature of the MERRA and NCEP-CFSR reanalyses (Largeron et al. 2015). In addition, ERA-Interim appears to underestimate the strength of nocturnal winds aloft in the boundary layer (Fiedler et al. 2013), possibly due to excessive vertical mixing under a stable stratification regime (Sandu et al. 2013). Monsoonal processes are a major source of uncertainty for reanalyses; disagreements between reanalysis low-level moisture fields peak during the boreal summer months, especially close to the intertropical discontinuity (ITD) where the value of inter-reanalysis difference in specific humidity can exceed half its typical magnitude, likely due to parameterisation of convection (Roberts et al. 2015). Improved observational benchmarks are critical to remedying these discrepancies.

1.5.2 Campaign observations

A growing research interest in mineral dust and in the climate of West Africa (particularly in the context of the monsoon) and a recognition of the observational paucity has given rise to a number of field campaigns, flight campaigns and efforts to improve the in situ network. Since 2000, these include JET2000, BoDEx, SHADE, DABEX, DODO, AMMA, SAMUM1, SAMUM2, GERBILS (see Ryder et al. (2015) Table 1 and references therein), as well as the Fennec Campaign (Washington et al. 2012) and DACCIWA (Flamant et al. 2018). Of these, the

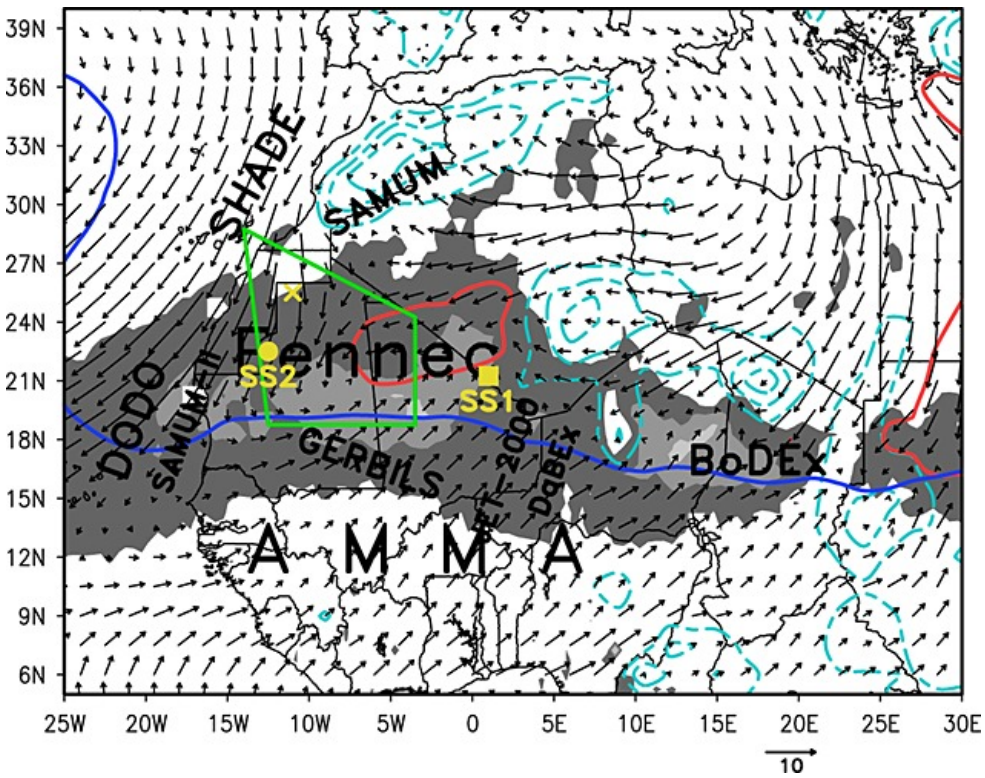


Figure 1.3: Overview of a number of field campaigns observing processes related to dust emission prior to and including Fennec. The two supersites marked as SS1 and SS2 correspond to Bordj-Badji Mokhtar (BBM) and Zouerate, respectively. The approximate Fennec aircraft flight zone is shown as a green polygon, as well an aerosol sampling station (yellow cross). Shaded contours are MISR aerosol optical depth at intervals of 0.4, 0.6 and 0.8. Mean 925 hPa winds (arrows) and the 1008 hPa sea level pressure contour (red) as well as the $10 gkg^{-1}$ specific humidity contour (blue) for June-September 1979-2012 from ERA-Interim are shown and represent the low-level circulation, Saharan heat low and intertropical disconinuity, respectively. Surface elevation at intervals of 1000, 1500 and 2000m are contoured in dashed cyan. Figure from Todd et al. (2013). Reproduced with permission from the American Geophysical Union.

Fennec Campaign, AMMA and GERBILS involved direct observations from the remote central and western Sahara. JET2000, AMMA and DACCIWA were oriented in particular towards observations of processes relevant to the West African Monsoon (WAM) such as African Easterly Waves (AEWs). An overview of the geographical scope of several field campaigns prior to and including Fennec is shown in Figure 1.3, taken from Todd et al. (2013).

Motivated by the apparent dominance of the Bodele Depression in northern Chad as a global dust source, instrumentation was deployed during the Bodele Dust Experiment (BoDEx) to measure wind-driven dust emission processes. The observers noted the intensity and regularity of high winds (Washington et al. 2006) and the substantial local radiative impact on days with high dust loading (Todd et al. 2007). An important result from this work is the demonstrable importance of a persistent nocturnal low-level jet. Enhancement of surface wind speeds above dust emission thresholds occurred on only a few of the sampled days (Washington et al. 2006). Supporting idealised regional modelling simulations show the relative roles of orography and synoptics as controls on the jet's intensity and variability (Todd et al. 2008b) (see Section 1.6.5 for further discussion of orography). Now that the major meteorological controls on emission in the Bodele are known, the sensitivity of the dust source to climatic variations and hence its potential to act as a climate tipping point are clearer (Washington et al. 2009).

In contrast to the Bodele, the central and western Sahara is home to many more widespead and disaggregated dust sources (Ashpole and Washington 2013a). As such, the task of diagnosing controls on dust emission is more complex. Several years after BoDEx, researchers involved in the Fennec Campaign of 2011 and 2012 carried out an unprecedented set of observations in the central Sahara close to the summertime dust maximum. Findings and data from the campaign underpin much of the satellite and model-based research undertaken for this thesis. The campaign included the establishment of two supersites, one near the west coast at Zouerate (Todd et al. 2013) and another at Bordj-Badji Mokhtar in southern Algeria near the climatological centre of the Saharan heat low (SHL) (Marsham et al. 2013b). As well as characterising the Saharan boundary layer and dust emission processes with flight observations (Ryder et al. 2015), an automatic weather station network was installed across western Algeria and northern Mauritania (Hobby et al. 2013), affording broad coverage of the heat low region.

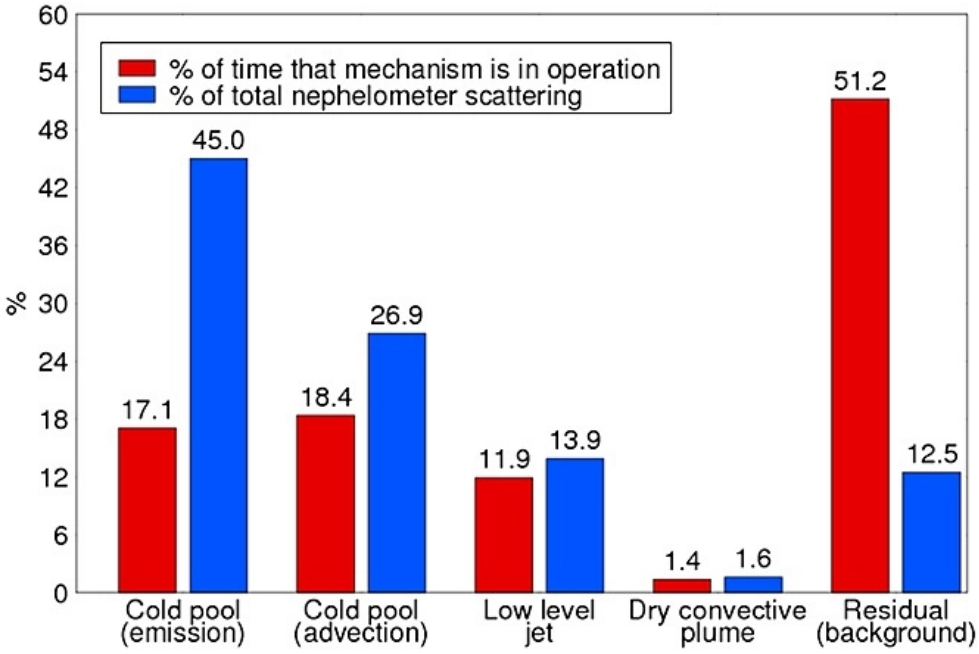


Figure 1.4: Relative contribution of different meteorological dust emission mechanisms to observations of dust loading measured by nephelometer scattering at Bordj-Badji Mokhtar for the June 2011 Fennec intensive observation period. Metrics include the percentage contribution to the total nephelometer scattering (blue) and the percentage of time each mechanism was in operation (red). Figure from Allen et al. (2013). Reproduced with permission from the American Geophysical Union.

A critical advancement made thanks to data from the Fennec Campaign has been the partitioning of meteorological dust emission mechanisms in the central Sahara. At Supersite 1 (Bordj-Badji Mokhtar) nephelometer data were collected in conjunction with a wide variety of meteorological observations such as Doppler lidar, supported by satellite observations and Met Office Unified Model forecasts. These lines of evidence are analysed in some detail for a first observing period in summer 2011 by Allen et al. (2013). Assigning instances of high nephelometer scattering to discrete 'dust events', they assess the most likely causal mechanisms behind dust emission through the observing period (Figure 1.4. For example, they use the occurrence of a raised nose in the lidar backscatter profile combined with a sudden wind speed spike and nearby deep convection to link events to cold pool outflow activity (see Section 1.6.2). Similarly, narrow 'spire' signals in the backscatter profile are linked to dry convective plumes where background winds are low. They also attempt to distinguish between local and

advected dust based on the timing of observed dust and correspondence between nephelometer scattering and exceedance of local wind speed thresholds. A key result from the analysis is the dominance of the cold pool outflow contribution to emitted and advected dust (72% of the total nephelometer scattering), with LLJs playing a secondary role (13.9%).

A parallel analysis of emission processes during the Supersite 1 intensive observation period is given by Marsham et al. (2013b), who show that a cold pool is present during approximately a third of the major moisture transport events towards the southern Algerian site. They also confirm the primary contribution of CPOs to dust emission, with around half of the observed 'uplift potential', a metric of the surface wind contribution to parameterized dust emission (Marsham et al. 2011), occurring at night when mature convective systems are active. Low-level jets (Section 1.6.3) are nonetheless shown to be a common phenomenon, embedded in both northeasterly Harmattan and southwesterly monsoon airmasses. Flights b600 and b601 on the 17th June 2011 recorded the highest observed low-level dust number and mass concentrations of the Fennec campaign; at this time nocturnal low-level jet breakdown had occurred over northern Mali injecting dust particles into the growing convective boundary layer of up to nearly 300 μm in size (Ryder et al. 2015). A second observing season in 2012 also showed cold pool activity generating the majority of dust emission, with a secondary role for low-level jets; Allen et al. (2015) find dust presence to be higher in this second observing season (likely due to a more vigorous monsoon) but record a similar partitioning of dust emission mechanisms to 2011.

In the context of erosivity, Fennec campaign observations demonstrate that the highest dust loadings are found in the remote central Sahara at a time of regular low-level monsoon inflow during boreal summer. Importantly, they also show dust emission at the peak season can be attributed mostly to two overarching mesoscale meteorological processes, cold pool outflows and high gusty surface winds due to nocturnal low-level jet breakdown. The observations are

representative of boreal summer to the extent that they sample a number of sites across two emission seasons. However, the western Sahara is vast and dust output from North Africa appears to be highly variable from year to year (Prospero and Lamb 2003; Mahowald et al. 2010; Tegen et al. 2013; Wagner et al. 2016). Furthermore, with the exception of the Bodele, there are few dominant dust sources in the Sahara; one manual analysis of satellite-observed dust emissions across a swathe of the northern Sahara found that 61% of plumes originated from sources for which they were the only emission event over a 2 year period (Lavi Bekin et al. 2020). in situ observations must therefore be supported by satellite data with greater spatiotemporal coverage.

1.5.3 Satellite-based methods

Satellite retrievals have a range of uses in the field of dust emission as well as differing uncertainties depending on the instrument in use. They are the method of choice for detection of remote dust sources, especially in the central Sahara where ground observations are extremely sparse. They also have an important role in model evaluation (e.g. Ginoux et al. 2001b; Miller et al. 2006; Basart et al. 2012; Tegen et al. 2013; Schwendike et al. 2016; Xu 2018; Chaibou et al. 2020). The application of thermal infrared (IR) data for dust detection was first demonstrated by Shenk and Curran (1974) who showed that the distinction between lower brightness temperatures atop dust plumes and land surfaces could be used to identify regions of dust over the Sahara then track them with visible imagery over the ocean. This brightness temperature difference derives in part from the atmospheric lapse rate; a more detailed discussion of dust detection in IR is given in Section 2.2.1 of Chapter 2. Thermal IR wavelengths are particularly well suited to dust detection thanks to the large particle size and warm surfaces from which dust is emitted (King et al. 1999). As well as IR, ultra-violet (UV) and near-UV have been successfully deployed to detect dust close to source regions, although visible wavelengths are typically insufficient for distinguishing dust over land (Schepanski et al. 2012).

Much early mineral aerosol detection by satellite was achieved using instruments not originally intended for that purpose. Two examples of this are the Advanced Very-high-resolution Radiometer (AVHRR) and the Total Ozone Mapping Spectrometer (TOMS), the former of which was intended for measurement of sea surface temperatures and vegetation and the latter for atmospheric ozone (King et al. 1999). A description of AVHRR aerosol retrieval is given by Stowe et al. (1997), with the equivalent documentation for TOMS aerosol retrieval in Herman et al. (1997). Datasets collected with each instrument have their own drawbacks; the backscatter UV aerosol index (AI) derived with TOMS is sensitive to aerosol layer height, whereas AVHRR is constrained to ocean measurements as AVHRR AOT is calculated from reflectance at 630 nm which can vary considerably over land (Husar et al. 1997). In a comparison of each instrument's mineral dust detection capability, Cakmur et al. (2001) show that the presence of cloud can limit the utility of AVHRR AOT for reliable monthly dust loading, whereas TOMS AI estimates are more consistently reliable due to better performance under cloudy conditions. This has been partly remedied, however, by a more sophisticated approach to distinguishing dust from cloud at higher AOTs (Evan et al. 2006). Engelstaedter and Washington (2007) apply TOMS AI to estimate controls on the seasonality of dust emission through the year, showing a clear peak in North African dust in June and July. Since September 2004, a similar aerosol index is derived from the Ozone Monitoring Instrument (OMI) aboard the NASA Aura spacecraft (Levelt and Noordhoek 2002). TOMS, AVHRR and OMI provide data once daily, with AVHRR having undergone some orbit drift that has caused variations in local overpass time (Giglio and Roy 2020).

The Moderate Resolution Imaging Spectrometer (MODIS) is another instrument commonly used for aerosol remote sensing, launched by NASA aboard the Terra and Aqua satellites. Multiple channels were used to develop the MODIS Deep Blue algorithm (MODIS DB), capable of detecting mineral dust via cloud screening, clear sky subtraction, inversion of a dust to smoke mixing ratio and

aggregation onto a 10 km grid (Hsu et al. 2004). As well as its global near-daily coverage, an important advantage of MODIS DB is the spectral information obtained from the use of multiple channels and hence the distinction of dust from other aerosols. This dataset has been used by Ginoux et al. (2012) to derive a global dust source map, inclusive of both natural and anthropogenic dust sources. MODIS DB is limited to bright surfaces, meaning it cannot readily identify dust sources over dark patches such as glacial outwash plains in Iceland (Prospero et al. 2012). Terra overpasses occur once daily at 0930 UTC over the Sahara while Aqua overpasses are at 1230 (Kocha et al. 2013).

Given the limits to temporal resolution afforded by instruments in polar or near-polar orbit and the difficulties using visible techniques nocturnally and over land, thermal imagery from the Spinning Enhanced Visible and Infrared Imager (SEVIRI) aboard Meteosat Second Generation (MSG) geostationary satellites has seen heavy use in the field of North African dust emission. As SEVIRI is the primary instrument used in this thesis, a more detailed description of its specifications and performance is given in Section 2.2. A key advantage is its 15 minute repeat cycle (Schmetz et al. 2002), providing unprecedented imaging of the diurnal variability of many critical dust sources. Differences between brightness temperatures at 10.8 and 8.7 μm as well as 12.0 and 10.8 μm are sensitive to lofted atmospheric dust (Ackerman 1997). Lensky and Rosenfeld (2008) define a SEVIRI Desert Dust RGB product based on these brightness temperature differences (BTDs). The result is that atmospheric dust takes on a distinctive pink colour in imagery composited with this method, which is useful for qualitative and quantitative tracking of dust storms.

With regular imaging of dust storms in remote desert regions and a long period of availability since 2002, SEVIRI imagery supports detection of active dust sources. Schepanski et al. (2007) validate the SEVIRI RGB dust imagery by showing high correlations between AOT values measured by AERONET (Holben et al. 1998) stations and 12.0-10.8 μm BTD. They then track plumes from the

RGB imagery by eye, aggregating the source of these plumes onto a 1 x 1° grid over the period March 2006 to February 2007. Their results show the activity of the Bodele Depression in Chad during winter and a range of western sources around southern Algeria, northern Mali and western Niger during summer, notably upstream (east) of OMI AI. They suggest that this discrepancy between SEVIRI and OMI is due to a mismatch between the sampling time of OMI (1345 UTC at the equator) and the timing of major emission mechanisms. In a follow-up paper (Schepanski et al. 2009), the authors argue that the timing of dust source activation in SEVIRI suggests a dominant role for low-level jet breakdown through the year, although the sampling period (March 2006 to February 2008) is short. MSG SEVIRI data appears therefore to offer both the capacity to track plumes and to infer useful information about meteorological processes. By contrast, for remote sensing studies with limited temporal resolution the timing of emission events is a key uncertainty and source of bias (Bryant 2013). For example, although AOT products and SEVIRI produce a summertime peak in dust emission, a recent demonstration of motion-based plume tracking using the Multiangle Imaging SpectroRadiometer (MISR) from Terra (Yu et al. 2018) does not reproduce this summertime peak at all, likely due to its morning overpass time and hence relative lack of convectively lifted dust which peaks later in the day.

SEVIRI dust tracking has been developed by Ashpole and Washington (2012) for application at higher spatial resolutions and to overcome issues associated with time-intensive and subjective manual tracking of dust plumes by eye over long periods. To achieve this, they define a set of four thresholds applied to BTD fields and a background subtraction method. The fulfilment of all threshold conditions at each pixel for a given SEVIRI scene constitutes a SEVIRI dust flag (SDF), used to identify the presence of dust automatically. With this method for delineating dust in SEVIRI imagery, Ashpole and Washington (2013a) develop an automated backtracking scheme to pinpoint dust sources, providing an unprecedented level of detail as shown in Figure 1.5. The granularity of these

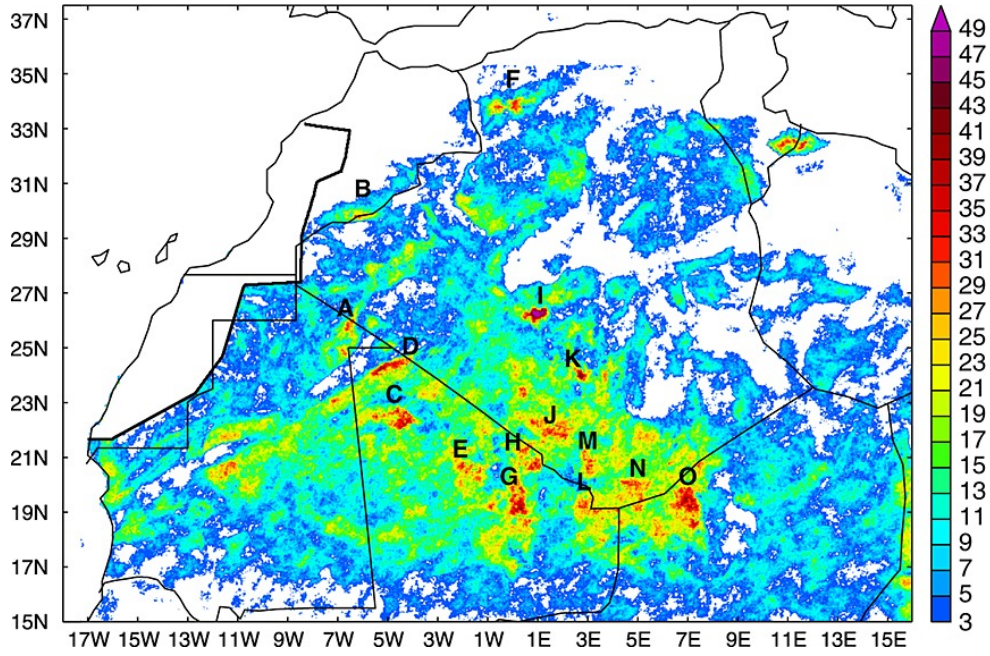


Figure 1.5: Map of dust sources detected using the automated SEVIRI dust flag tracking method of Ashpole and Washington (2013a). Colours represent the frequency of SEVIRI dust flagged pixels which belong to a plume in the first timestep of its lifecycle, with stronger reds and purple indicating the most prominent observable dust sources. Tracking is applied for June, July and August 2004-2010. Masking (white) is applied where the total counts are less than 5 or where the figure has been manually masked due to regular incursions of marine stratus which are falsely flagged (black contoured region). Letters correspond to notable dust source regions described in Table 1 of Ashpole and Washington (2013a). Figure from Ashpole and Washington (2013a). Reproduced with permission from the American Geophysical Union.

results allow individual sources near the Tidihelt Depression, Aïr Mountains, Hoggar Mountains, Taoudenni and Lake Iriki to be identified and linked to geomorphological features. Their dust detection and tracking approach is adopted and developed in Chapter 3 to create a climatology of emission mechanisms. Other uses of SEVIRI imagery for dust tracking include its application to southern African dust sources (Murray et al. 2016; Eckardt et al. 2020) and in a multiplatform approach to high resolution source characterisation (Bakker et al. 2019).

A difficulty facing most dust remote sensing platforms including SEVIRI is that information is only available in a column-integrated form. The vertical distribution of dust is important, however, as it can reveal transport processes

and help pinpoint source locations. Todd and Cavazos-Guerra (2016) apply the Cloud-Aerosol Lidar with Orthogonal Polarization (CALIOP) instrument (CALIOP) aboard the Cloud-Aerosol Lidar and Infrared Pathfinder Satellite Observation (CALIPSO) satellite to extract dust extinction profiles and constrain estimates of Saharan dust sources for the 2006-2013 period. Due to low sampling frequency they use a coarse grid, but find good consistency with the analyses of Schepanski et al. (2007) and Ashpole and Washington (2013a), lending credence to each of these independent analyses.

Recent studies of dust emission close to source regions have made use of hyperspectral imagery from the EUMETSAT Infrared Atmospheric Sounding Interferometer (IASI) on board Metop satellites. MODIS and OMI are limited to a single near-midday observation each day whereas IASI overpasses occur at 0930 and 2130 UTC at the equator, giving a snapshot of both morning and evening dust over North Africa. Chédin et al. (2020) and Vandenbussche et al. (2020) argue that the timing of these overpasses aligns well with that of the two major dust emission mechanisms operating in the Sahara, cold pool outflows and low-level jets, and hence is better suited to dust observations than once daily overpass data. In addition, Vandenbussche et al. (2020) apply the Mineral Aerosol Profiling from Infrared Radiances algorithm (MAPIR) (Callewaert et al. 2019) to the IASI data to estimate the vertical distribution of dust up to 6.5 km altitude. MAPIR derives its a priori vertical profile of dust concentration from CALIOP data. This allows the authors to distinguish between dust plumes at height and those found close to the surface, which they argue are more likely to be associated with the dust sources themselves. A discussion comparing the results of this thesis with IASI is given in Section 6.3.1.

The use of multiple platforms adds robustness to estimates of dust sources and emission processes (Flamant et al. 2009b; Todd and Cavazos-Guerra 2016; Yu et al. 2018). As a result, the development of independent sensors and indices or proxies for AOT reviewed in this section means that results can be

corroborated or challenged, especially where new methods fill gaps left by the old ones. With improvements to spatio-temporal resolution and postprocessing, a key advancement in remote sensing has been the shift from analysing seasonally or monthly averaged AOT towards observation and tracking of individual dust plumes through their entire life-cycle. One advantage of this approach is that it provides information about dust sources. Another demonstrable advantage is that useful insights into meteorological processes can be obtained, although such insights have typically only been inferred from the timing of emission (Schepanski et al. 2009; Tegen et al. 2013; Chédin et al. 2020; Vandenbussche et al. 2020).

Meteorological drivers of erosivity are just as important as the availability of erodible material and can make the difference between an inert dust source and one being actively deflated (Washington et al. 2009). Now that satellite-derived dust source maps are available, a critical next step is to interpret them in terms of erosivity controls. One aim of this thesis will therefore be to find novel methods for extracting meteorological information from satellite dust observations, taking advantage of SEVIRI's high rate of sampling. This process-oriented approach will allow dust model wind fields to be evaluated and improved, and will offer insights into the mesoscale meteorology of a critically underobserved component of Earth's climate. The following section reviews the current understanding of meteorological processes responsible for summertime dust emission from synoptic to mesoscales.

1.6 Summertime controls on erosivity in the central Sahara

1.6.1 Synoptic variability

Competing low-level flows bring variations to the Sahara's summertime dust loading. The most important influence upon these flows is the Saharan heat low (SHL), a quasi-stationary dome of elevated atmospheric thickness with a low pressure centre over the remote central Sahara during boreal summer (see the red contour in Figure 1.3). Typically defined by the depth of the 925-700

hPa layer, the SHL evolves from a climatological position south of the Darfur mountains (the 'West African heat low') in boreal winter towards the western lee of the Hoggar mountains in summer (Lavaysse et al. 2009). The heat low region of the Sahara is associated with high boundary layer potential temperature (θ) and dry convection, contrasting with the higher equivalent potential temperature (θ_e) and moist convection further south (Parker et al. 2005b). Easterly shear in the lower troposphere is driven by the meridional temperature gradient between these two regions. This gradient decreases with height as the dry adiabatic ascent profile of the Sahara meets the moist adiabatic ascent of the Sahel, predicting a maximum in easterly winds at 700 hPa (seen most clearly in idealised ascent profiles from Figure 2a of Thorncroft and Blackburn 1999). This is consistent with observations of the African easterly jet, a critical control on the development of monsoonal mesoscale convective systems and African easterly waves (Thorncroft and Blackburn 1999). The low-level thermally direct SHL circulation supports moist southwesterly monsoon flow into the dry Sahara along the eastern flank and dry 'Harmattan' northeasterlies along the western flank (Lavaysse et al. 2009).

As a result of intense solar heating and low static stability within the SHL region, the Saharan atmospheric boundary layer (SABL) is capable of reaching 6 km in depth, making it one of the deepest on the planet (Gamo 1996). The Sahara's convective boundary layer is overlain by a persistent residual layer from the previous day (Cuesta et al. 2008). The total depth of the SABL is thought to be highly variable, however, which poses problems given the poor sampling afforded by the Saharan radiosonde network (Garcia-Carreras et al. 2015). Vertical mixing associated with the SABL inhibits advection during the day (Parker et al. 2005a).

One variable component of the SHL flow and hence the depth of the SABL is the sea breeze circulation, a typical characteristic of heat lows over land with surrounding sea (Rácz and Smith 1999). In the western Sahara, the sea breeze takes the form of Atlantic inflow, a stationary front located near the

West African coast during the day which penetrates inland as SABL turbulence decays (Grams et al. 2010). Fennec Campaign observations show that eastward displacement of the SHL favours a maritime regime of cold air advection through the western Sahara with low atmospheric aerosol content while a westward shift in the SHL appears to produce a warmer, dustier SABL (Todd et al. 2013). The transition between the two phases is linked to deep propagating Rossby waves in the midlatitudes deforming the Azores high and enhancing or inhibiting Saharan ventilation by Atlantic inflow (Chauvin et al. 2010). This east-west variability has also been described in terms of a closely correlated North African Dipole Index (NAFDI), which itself is correlated with observations of dust concentration and coarse dust mode at the Izaña observatory on Tenerife (Rodrıguez et al. 2015). The authors of this index show a link between positive (dusty) NAFDI and low-level winds over the Sahara but do not link it explicitly to dust emission mechanisms.

Fiedler et al. (2015) show that synoptic postfrontal winds in the wake of cold air advection into North Africa (Harmattan surges) could be responsible for 30-50% of dust emission during their active season in winter and spring. By contrast, summertime dust outbreaks usually cannot be explained by synoptic winds alone (Knippertz and Todd 2012). Although synoptic conditions exert a control on the strength and timing of major emission events, mesoscale processes supply the gusty winds responsible for uplift (Allen et al. 2013). One example of this is an event on the 3-5th August 2006 in which an arc-shaped plume covered over 2,000 km of the Sahara through a 3-5 km boundary layer, exporting dust over the Atlantic towards the Caribbean. Bou Karam et al. (2014) show that this event was preceded by a deep SHL shifting northwestwards and displacement of the ITD north of its climatological position (a monsoon surge). However, the dust outbreak itself was triggered by a northward propagating mesoscale convective system and associated downdraft, comparable to other major summertime events

described in the literature (Cuesta et al. 2010; Knippertz and Todd 2010; Roberts and Knippertz 2014).

An interesting possible counterexample is the June 2020 Saharan dust outbreak, one of the largest ever observed, which Francis et al. (2020) argue is a rare case of a principally synoptic summertime event in which a circumglobal wavetrain intensified the high-low pressure pattern between an anomalous ridge near the Atlantic coast and the SHL in the southeast. They show that this pressure pattern produced record-breaking high surface winds over the Sahara. However, the complementary influence of mesoscale processes such as boundary layer jet breakdown is not explored, and observations from SEVIRI show major CPO events south of 20°N that likely contributed to the dust outbreak (Yu et al. 2021) and which are not accounted for by Francis et al. (2020).

In the sections that follow, the meteorological phenomena responsible for the majority of summertime dust emission are introduced in detail in the context of the approaches used to characterise them. A diagram of each emission mechanism is shown in Figure 3.1 in Chapter 3.

1.6.2 Cold pool outflows

Mesoscale convective systems and squall lines encompass broad regions of upwards and downwards motion. Convective cold pools are formed where hydrometeors evaporate, melt or sublimate, giving negative buoyancy to an airmass which can travel to the surface and spread laterally as a density current. Downwards motion may also be supported by drag from precipitation. Downdraft outflow scales can vary from 10-20 km microbursts up to 100-500 km mesoscale events (Houze 1977).

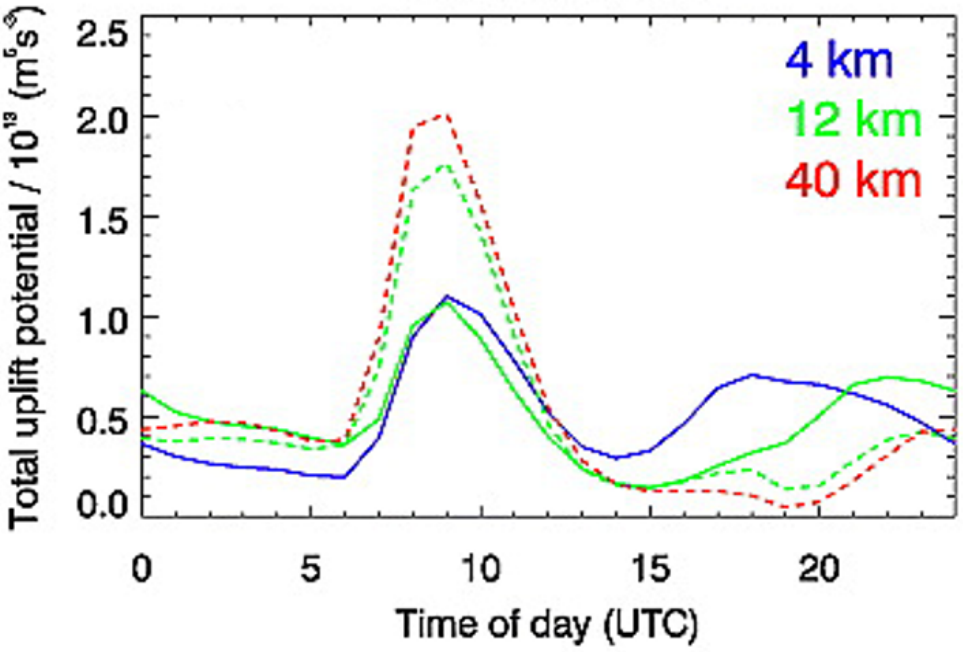


Figure 1.6: Diurnal cycle of instantaneous hourly uplift potential averaged over the 25th July to 3rd August 2006, simulated with the UK Met Office Unified Model at different grid-spacings including 40 km (red), 12 km (green) and 4 km (blue). Dashed lines correspond to runs with fully parameterized moist convection. Uplift potential is defined in Marsham et al. (2011) and refers to a quantity which measures the expected dust emission given the wind speed, a constant emission threshold of 7 ms^{-1} and the bare-soil fraction in a grid-box. Figure from Marsham et al. (2011). Reproduced with permission from the American Geophysical Union.

Good conditions for Saharan cold pool formation exist in summer as the dry midtroposphere supports evaporation of rainfall (Redelsperger and Lafore 1988) while the West African Monsoon sustains deep convection. A deep, dry-adiabatic unstable SABL also favours Saharan cold pools and makes them less sensitive to microphysics in model simulations than under more stable regimes (Knippertz et al. 2009). Emission of dust occurs in high turbulent winds at the leading edge of the density current's gust front (Knippertz et al. 2007) and dust storms raised in this way are referred to as haboobs. As well as driving dust emission, Saharan cold pool outflows are an important vehicle for moisture transport (Marsham et al. 2013a; Garcia-Carreras et al. 2013; Trzeciak et al. 2017) and effective at reinitiating convective cells (Dione et al. 2014).

Cold pool outflows are not currently well simulated in models which rely upon convective parameterization (Garcia-Carreras et al. 2013). For example, simulated dust aerosol depth in a global configuration of the Met Office Unified Model (UM) using parameterized convective downdrafts is evaluated by Pope et al. (2016). They show that the model underestimates dust emission during periods of gusty cold pool activity when mean winds are otherwise low. Similar results have been obtained with other models compared to convective-permitting runs (Chaboureau et al. 2016). When convection is parameterized, the UM appears to compensate for a dramatic decline in CPO dust emission with increasing uplift from LLJs and vice versa (Marsham et al. 2011; Roberts et al. 2018). Marsham et al. (2011) demonstrate this particularly clearly in Figure 1.6 with their diurnal cycle of uplift potential, which shows a much greater peak in the morning from LLJs when convection is parameterized compared to explicit runs as well as a missing afternoon peak in parameterized runs due to the lack of CPOs. They suggest that the compensating LLJ increase in parameterized runs could be due to a lack of ventilation (and hence cooling) of the SHL by CPOs. Using the same model, Heinold et al. (2013) show that choosing to parameterize convection has a larger effect upon the results than even the characterization of the land surface.

Explicit treatment of convection leads to improvements in simulating the structure of cold pools and their associated winds (Reinfried et al. 2009; Knippertz et al. 2009) but convective-permitting approaches are computationally expensive and are not applicable to coarse global models. To address this issue, Pantillon et al. (2015) develop a parameterization for radially expanding CPO gust fronts from the downdraft mass flux of the model convection scheme. The parameterization performs well against simulations with explicit convection (Pantillon et al. 2016). Another approach has been to apply a probability density function to subgrid wind variability, linked directly to the model convection scheme (Cakmur et al. 2004; Marcella and Eltahir 2010; Zhang et al. 2016; Foroutan and Pleim 2017), or to approximate gustiness due to moist convection empirically based on model

precipitation (Redelsperger et al. 2000; Lunt and Valdes 2002). However, a critical source of uncertainty in studies of both explicit and parameterized cold pools is the near-absence of remote Saharan observations with which to validate the results.

Like fronts, CPOs are travelling features. As a result, surface observations only capture the changes to meteorological conditions at the point of CPO passage. The most comprehensive observational analysis of CPOs from surface stations comes from the work of Engerer et al. (2008), who link cold pool passage to drops in temperature, changes in wind direction and increases in pressure and wind speeds across 110 surface stations in Oklahoma. Short-term observations from the Fennec Campaign indicate that CPOs do not have a unique signature in meteorological quantities measured from the ground (Allen et al. 2013; Hobby et al. 2013), although many events produce notable spikes in wind speed at the nose and relative humidity in their wake. Measurements taken at Niamey in Niger show that passing cold pools can bring gusts of 3-22 ms^{-1} (Provod et al. 2016).

In contrast to surface observations, satellite methods allow individual cold pools to be tracked and associated with deep convection. This approach has been used in a number of studies to support ground-based CPO observation, including for the Fennec Campaign (Allen et al. 2013; Allen et al. 2015) and for case studies of major emission events (Flamant et al. 2009a; Karam et al. 2014; Roberts and Knippertz 2014; Trzeciak et al. 2017; Yu et al. 2021), in each case taking advantage of the unique signature exhibited by CPOs in SEVIRI imagery, namely advancing arcs of lofted dust with a sharp leading edge. Similarly, Redl et al. (2015) develop a threshold-based approach for detecting CPOs in the Atlas mountains using supporting microwave satellite imagery to identify nearby deep convection, based on the manual density current detection scheme of Emmel et al. (2010).

Techniques which rely on surface meteorological observations are difficult to replicate for the summer dust maximum in the central Sahara where such data are lacking. Furthermore, the variety of surface signals induced by CPOs means

these approaches require manual intervention to confirm the presence of nearby deep convection. SEVIRI imagery, as described in Section 1.5.3, offers a high temporal resolution and nocturnal sampling and therefore the ability to observe emitted dust through its life-cycle. Given the consistent visual characteristics of dust-generating CPOs in satellite imagery, there is potential for new approaches to identifying CPOs automatically.

1.6.3 Low-level jets

'Low-level jet' (LLJ) is a term which has multiple uses in the fields of meteorology and climate science. LLJs in this thesis refer to boundary layer maxima in wind speed that are realised nocturnally prior to the transfer of momentum towards the surface in the morning. One of the most common mechanisms by which this occurs was first described by Blackadar (1957) and applies in many regions of the world. Large heat and momentum fluxes during the day are driven by the frictional effect of solar heating. After sunset, a stable nocturnal layer grows. Observations show that the wind vector atop this nocturnal layer oscillates around the geostrophic wind with a period depending on the coriolis parameter, which in turn depends on latitude. During the course of inertial oscillation, the winds may become supergeostrophic with a magnitude that varies according to the wind speed at sunset (Stull 2012); a typical modeled supergeostrophic enhancement of an LLJ is around 30% (Heinold et al. 2015). Synoptic variability and surface characteristics such as orography (Section 1.6.5) have an influence on the strength and location of these nocturnal maxima. The return of eddy-driven turbulence at sunrise carries momentum to the surface, resulting in a mid-morning peak in surface wind speeds capable of lofting dust. Jet development and its 'decoupling' from surface friction is also affected by sporadic shear-driven turbulence overnight and other factors such as cloud cover which can attenuate boundary layer stability (Knippertz and Todd 2012). Ambient or recently emitted dust may also reduce boundary layer mixing in the morning

by absorption of incoming shortwave radiation, driving a reduction of sensible heat flux from the surface (Miller et al. 2004; Pérez et al. 2006).

Compared with CPOs, there is evidence that Saharan LLJs can be well simulated by numerical models under certain circumstances without a convective-permitting configuration. Modelling of LLJs and their dust emission has been performed and validated in comparison with surface and pilot balloon data from BoDEx (Washington and Todd 2005; Bouet et al. 2007; Todd et al. 2008b; Haustein et al. 2012) as well as dropsonde data from Fennec flights (Schepanski et al. 2013). Fiedler et al. (2013) compare ERA-Interim with radiosonde launches from AMMA in the Sahel. ERA-Interim appears to significantly underestimate jet core wind speeds and place them too low, performing especially poorly for jet cores above 400 m and faster than 6 ms^{-1}. Fennec Campaign observations from southern Algeria analysed by Allen and Washington (2014) confirm this, showing ERA-Interim underestimation of both core speeds and morning surface speeds as well as inadequate jet structure for both monsoonal and Harmattan LLJs. In comparison, Allen and Washington (2014) show that northeasterly Harmattan LLJs are well represented by a regional configuration of the Met Office Unified Model (UM), with accurate core speeds in spite of poor performance under monsoonal conditions. The authors suggest that moist dynamics could pose a challenge for LLJ simulation. In general, models tend to represent synoptic variability and LLJ life cycles satisfactorily but disagree on core speeds and heights (Schepanski et al. 2015), which may be due to the parameterization of turbulence as well as inadequate representation of surface roughness and vertical resolution (Hourdin et al. 2015; Heinold et al. 2015).

LLJs have received considerable attention as a dust emission mechanism in the central Sahara. The margins of the SHL appear to favour LLJ development, as well as the west African coast and regions downwind of orographic channels (Fiedler et al. 2013). Heinold et al. (2015) show that regions with the surface roughness and latitude supporting the strongest LLJ core winds are found in a

band through the central Sahara from 20-25°N. There is some disagreement over their role in emissions, however. in situ observations in southern Algeria from June 2011 indicate a moderate contribution of 14% to the total nephelometer scattering (Allen et al. 2013), whereas an uplift potential analysis of the same period suggests a figure closer to 30% (Marsham et al. 2013b). An LLJ detection scheme applied to convective-permitting simulations indicates a 40% contribution in summer (Heinold et al. 2013). It has been argued in a number of papers using manual SEVIRI tracking that the timing of satellite-observed dust emissions points to LLJs as the dominant Saharan dust emission mechanism (Schepanski et al. 2009; Tegen et al. 2013; Heinold et al. 2016; Schepanski et al. 2017). In the latest of these papers (Schepanski et al. 2017), the authors suggest that as Saharan dust source activation occurs predominantly in the morning, LLJ breakdown is the primary driver of dust emission, with CPOs playing a larger role in the Sahel.

Understanding the relative contribution of emission mechanisms is important as it can help pinpoint the source of deficiencies in modeled dust emission. There is a need for a long-term observational analysis of Saharan LLJs which is capable of distinguishing them explicitly from CPOs, however, and which does not rely entirely on timing. This thesis will attempt to resolve discrepancies in the literature by taking a plume-by-plume approach to characterising emission mechanisms in SEVIRI.

1.6.4 Other emission mechanisms

A number of emission mechanisms are not included explicitly in the detection algorithms applied in this thesis as their contribution to dust emission observed at BBM during the Fennec Campaign was small (Allen et al. 2013). These include monsoon surges, dry convective plumes and dust devils.

Monsoon surges are incursions of the WAM low-level flow into the Sahara which can behave as density currents with elevated wind speeds at the leading edge. Aircraft observations show that this boundary region can itself loft mineral dust in regions of high gusts and turbulence (Bou Karam et al. 2008; Flamant et al. 2009b). In general, monsoon surges occur on 3-5 day timescales and are driven by intense pressure gradients from the Sahel into the core of the SHL, with a number of monsoon surges organised spatially by the northerly and southerly limbs of westward-propagating AEWs (Couvreux et al. 2010). Northward displacement of monsoonal moisture during surge conditions is capable of bringing rainfall as far as the Hoggar mountains (Cuesta et al. 2010). Critically, monsoon surges bring favourable conditions for cold pool formation in the dry Sahara (Marsham et al. 2008; Knippertz and Todd 2010). An in situ analysis by Allen et al. (2013) indicates that monsoon surges could have contributed 9.9% of the total nephelometer scattering from June 2011 at BBM, but the figure is uncertain as they cannot be unambiguously distinguished from CPO and LLJ events (Allen et al. 2013; Marsham et al. 2013b).

Dry convective plumes and dust devils are the smallest of the dust emission mechanisms, occurring in regions where solar heating generates intense turbulent updraft development. Whereas dry convective plumes refer to regions of ascent with a diameter of around 100 m, dust devils occur where this ascent develops rotational vortices within which wind speeds can exceed 10 ms^{-1} and induce sandblasting (Ansmann et al. 2009). The average diameter of dust devils is 7 m (Balme and Greeley 2006). These microscale mechanisms are not incorporated into dust models and are largely unobservable to satellite, hence their contribution as an emission mechanism has not been estimated at the scale of North Africa (Knippertz and Todd 2012), but Fennec campaign observations indicate that dry convective plumes contributed 1.6% of the total nephelometer scattering in June 2011 at BBM (Allen et al. 2013).

1.6.5 Role of orography

Chapter 5 addresses the role of central Saharan orography upon LLJs and their associated dust emission. Orography is a characteristic of the land surface that has an important impact upon emission and transport of dust plumes. At the simplest level, this is because the Sahara is not flat and uniform and hence the trajectory of dust travelling close to the surface is modified by terrain. For example, comparisons of model simulations at different horizontal resolutions show that decreased grid spacing produces dust concentrations which map onto observations more closely as a result of the varied and rugged terrain of typical emission regions (Schepanski et al. 2013).

More relevant to dust emission is the link between orography and erodibility. A seminal paper by Prospero et al. (2002) first characterised global mineral dust sources across the dust belt of the Northern Hemisphere using TOMS. They showed the critical role of alluvial deposits in topographic lows and suggested that runoff from highlands and mountains are significant sources of this fine erodible material, although many sources emit continuously without an apparent source of replenishment. A more recent analysis by Ginoux et al. (2012) corroborates these results for natural sources over North Africa. With the added spatial resolution of SEVIRI backtracking, Ashpole and Washington (2013a) show that the boundaries between emitting and non-emitting regions in the Sahara appear to map on closely to the edges of escarpments, for example bordering the Tademait Plateau of central Algeria, adding that the proximity of dust sources to high topography is evidence that erodible material probably drained from mountains in wetter periods of Earth's history. These findings suggest that orography is a major control on erodibility across natural dust sources.

As well as being a source of runoff, mountains may influence the erosive winds responsible for dust emission. In the Sahara this has been shown most clearly for the Bodele Depression, which sits downwind of a gap flow between the Tibesti

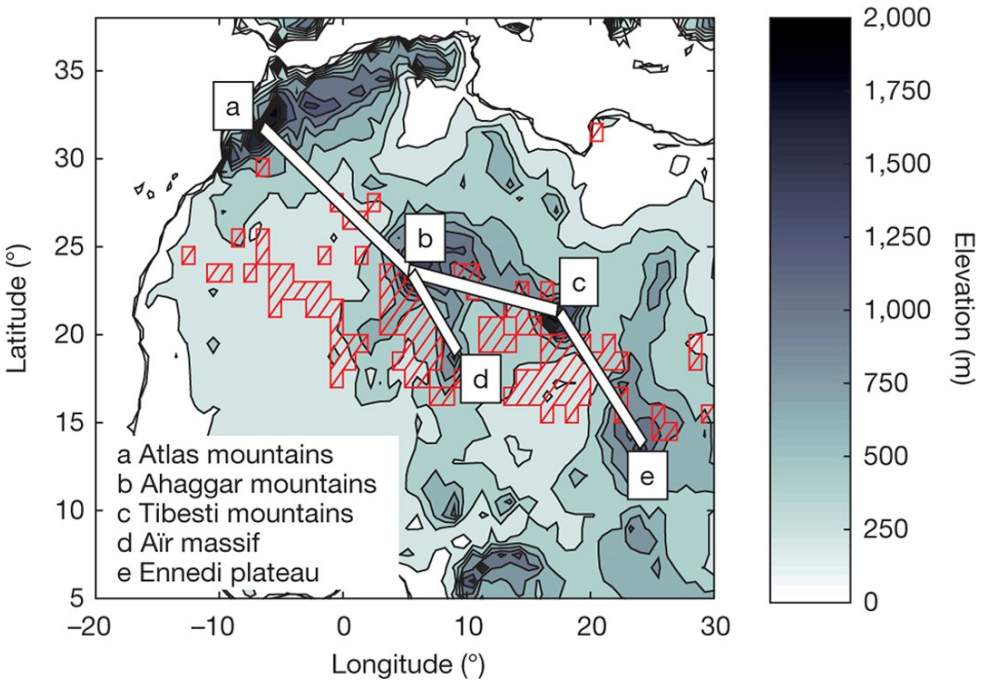


Figure 1.7: Prominent North African dust source regions identified in SEVIRI with the Schepanski et al. (2007) method (red hatched regions) overlain on a map of Saharan orography, with shading corresponding to elevation (metres). Dust source regions are obtained from manual SEVIRI backtracking for March 2006 to February 2010 in Evan et al. (2015), with 85% of emissions falling within the hatched areas. White transects are drawn to indicate corridors between the major orographic regions described in the legend. Figure from Evan et al. (2016). Reproduced with permission from Springer Nature.

and Ennedi massifs and is subject to accelerated LLJ winds during periods of enhanced synoptic forcing (Todd et al. 2008b). By comparison, orographic controls on mesoscale winds in the western Sahara are largely unquantified. Noting the geographical location of dust sources downstream of major orographic corridors (Figure 1.7), one reanalysis study goes as far as suggesting that the wind field responsible for dust emission is directly controlled by orographic flow acceleration across the Sahara from the Atlas mountains to the Ennedi plateau and that this orographic wind distribution can be projected onto climate models to predict the future of Saharan dust (Evan et al. 2016). Such results should be treated with caution given the coarseness and absence of convective dust emission from CPOs in their analysis, however. At smaller spatial scales, it has been suggested that the Aïr and Hoggar mountains intensify winds activating

southern Saharan dust sources (Ginoux et al. 2012) and that northeasterly flow into central Algeria may be accelerated by the presence of the Hoggar mountains (Birch et al. 2012; Hobby et al. 2013).

As the Hoggar mountains are proximate to key dust sources and appear likely to have an impact on the surface wind field, it is important to quantify their contribution to the erosivity component of North African dust source maps. Existing studies have emphasised the effect of the Hoggar mountains on the SHL and WAM development. Semazzi and Sun (1997) suppress North African orography in an idealised experiment with the NASA GEOS-1 general circulation model, finding a high-low pressure dipole over the central Sahara resulting from the high terrain. They show that an easterly flow over the Atlas and Hoggar mountain ranges is capable of producing this pattern. Sultan and Janicot (2003) suggest that this orographic enhancement could also explain the abrupt onset of the monsoon as the intertropical convergence zone (ITCZ) reaches Saharan mountains, combined with the deepening of the SHL via a leeward trough. A linear modelling approach is adopted by Drobinski et al. (2005) which also shows an intensifying anticylone over the Hoggar mountains driving enhanced easterly flow and the potential for a leeward trough close to the SHL. More recently, Birch et al. (2012) have shown in an idealised UM case study that the Hoggar mountains warm and deepen the SABL over and west of the main peaks and that they also act as a barrier to low-level flow.

Given the demonstrable effect of central Saharan orography upon the low-level wind field and potentially the SHL, linking the presence of the Hoggar mountains to dust-emitting winds is a natural next step. As described in Section 1.6.2 this is challenging for modelling of cold pool outflows which relies on convective-permitting simulations and is poorly validated. However, northeasterly LLJs can be effectively represented (Section 1.6.3) demonstrating that there is scope for an analysis of orographic effects on LLJ dust emission in regions where Harmattan flow dominates.

1.7 Thesis aims and objectives

This thesis is motivated by the need to understand the role, geographical distribution and functionality of mesoscale meteorological dust emission mechanisms in the central and western Sahara. Section 1 has contextualised the research and developed its rationale. In summary:

- Mineral dust is an important aerosol that affects human health, climate, meteorology and biogeochemistry, and is primarily driven at the microscale by sandblasting in aeolian environments;
- Emission is a major uncertainty for models of the dust cycle and is highly sensitive to model wind fields;
- Winds responsible for emission are commonly short-lived and driven by mesoscale processes;
- The Sahara is severely lacking in long-term surface observations, which helps explain underperformance of reanalyses for key dust-emitting winds;
- The Fennec Campaign collected in situ observations which show the dominant role of cold pool outflows and low-level jets as emission mechanisms in boreal summer, but only for a handful of point locations;
- Geostationary satellite data from SEVIRI can be used to track individual dust plumes, allowing information about meteorological processes to be inferred;
- Cold pool outflows are not well represented when convection is parameterised, and existing observations only capture events at the point of passage;
- Low-level jets can be represented in Unified Model simulations but have poor fidelity in monsoonal conditions;

- Orography affects the Saharan circulation but has not been linked explicitly to winds driving dust emission in the western Sahara.

The research papers presented in Chapters 3, 4 and 5 aim to use a combination of observational and modelling approaches to target key uncertainties relating to meteorological dust emission mechanisms in summer. These uncertainties can be described as follows:

- What is the relative significance of cold pool outflows and low-level jets as dust emission mechanisms in the summertime central and western Sahara on the long term?

- What is the geographical distribution of cold pool outflow and low-level jet dust emission and which of the two are most important for known dust source regions in the western Sahara?

- What role do cold pool outflows have in observed changes in net dust presence through summer?

- Does Saharan orography influence dust-emitting winds over dust sources and how?

The capacity of SEVIRI to observe dust emitting regions at high temporal resolution is exploited to derive datasets of low-level jet and cold pool outflow dust presence, critical for associating outbreaks across the Sahara with mesoscale meteorology. A novel algorithm is then developed and applied to the same satellite data to delineate and track advancing gust fronts from dust-emitting cold pool outflows. Finally, the link between orography and low-level jet dust emission in the Sahara is evaluated using numerical model simulations and post-processed satellite data from the first paper.

The aims of the thesis are as follows. The constituent papers address one or more of the aims:

1. Develop novel algorithms capable of characterising tracked dust plumes by dust emission mechanism and delineating outflow boundaries (papers 1 and 2);

2. Partition the relative roles of low-level jets and cold pool outflows as drivers of dust emission in the central Sahara (paper 1);

3. Map cold pool outflow occurrence in the Sahara and link it to the evolution of dust emission through the summer season (paper 2);

4. Diagnose the role of the central Saharan Hoggar mountains in the strength of northeasterly low-level jets and their associated dust emission frequency (paper 3).

2
Data and methods

Contents

2.1 Background: image processing and feature tracking 41
2.2 SEVIRI 43
2.2.1 Pink dust composite imagery 44
2.2.2 SEVIRI dust flags 47
2.3 Met Office Unified Model 49
2.4 In situ observations 50
2.4.1 Fennec data 50
2.4.2 MIDAS and IGRA data 51

2.1 Background: image processing and feature tracking

In this thesis, novel observational datasets are derived by applying image processing and feature tracking algorithms to geostationary satellite data. This Chapter does not describe the mechanics of the algorithms used, including the novel CPO detection approach of Chapter 4, as these are described in detail in Sections 3.4 and 4.3. Instead, an introduction and justification for datasets used through the thesis is given.

To extract useful information from satellite data, continuous patterns must be identified accurately, maximising a hit rate (signal) and minimising false positives (noise). In the case of this thesis, the useful information in question is a set of atmospheric processes relating to dust emission. The largest body of feature tracking literature in meteorology and climate science comes from observation of clouds, originating with the work of Ted Fujita, whose research team inferred cloud motion, morphology and height for numerical weather prediction and

analysis of atmospheric circulation (Menzel (2001) and references therein). This work includes the development of cloud motion vectors (CMVs), which are estimates of atmospheric winds from geostationary satellite often included in data assimilation procedures (Bormann et al. 2003). Satellite detection of winds has been particularly helpful for the southern hemisphere, where relatively few in situ observations are available (Schmetz et al. 1993). Important advances since this pioneering work in the 1960s and 70s include the development of water vapour motion vectors (Eigenwillig and Fischer 1982), increases in satellite coverage and improved automated tracer selection (Menzel 2001).

Tracers refer to regions within the imagery that can be most easily tracked through time and give the best information about the quantity being measured. For example, in the case of large-scale synoptic flow, a desirable tracer would be a cloud in motion driven by geostrophic or near-geostrophic winds. For this reason a number of assimilation systems reject CMVs in regions of significant mesoscale flow (Bedka and Mecikalski 2005). Inspired by these operational applications of satellite imagery, Chapters 3 and 4 make use of mineral dust as a tracer for mesoscale boundary layer emission mechanisms. One complexity of the research, therefore, is that dust is both the object of study and an intrinsic part of the observational technique.

An important consideration in image processing and feature tracking is whether or not features are 'rigid' and their interframe deformation. The bulk of early image processing literature analysed scenes containing objects that could be matched from one frame to the next with relative ease using template matching (Wu 1995). In contrast, clouds are typically non-rigid and can be displaced rapidly by upper level winds. A number of techniques to address this 'correspondence problem' are described by Evans (2006). Similar to cloud, dust plumes cannot generally be treated as rigid features as they are compressible and undergo considerable deformation during transport (Bachl et al. 2015). For this reason, velocity estimation can be difficult as features undergo motion resulting from

both deformation and background flow. However, a unique property of dust storms organised by CPOs is that they advance in the form of a wall with a sharply defined leading edge (Roberts and Knippertz 2012). This behaviour is exploited in Section 4.3.3 to estimate displacement vectors.

The work described in this thesis benefits from considerable overlap between observed dust plumes in subsequent scenes. By applying a minimum detection size to tracked features, plumes can be explicitly treated as continuous objects. Features in Chapters 3 and 4 are therefore masked as discrete entities rather than continuous fluids with a varying dust signal. This allows visual characteristics to be monitored through the entire life-cycle of a known plume, aiding interpretation of meteorological drivers.

2.2 SEVIRI

Observations from the Spinning Enhanced Visible and Infrared Imager (SEVIRI) are the primary dataset used in this thesis for tracking and characterising dust. SEVIRI is mounted aboard the Meteosat Second Generation series of satellites and is intended to provide continuous monitoring at a nominal position of 0° longitude over the equator. Described in detail in Schmetz et al. (2002), SEVIRI has 12 channels, a 15 minute repeat cycle and provides imaging at a sampling distance of 3 km at nadir for 11 channels and at 1 km for a high-resolution visible channel. 8 channels provide radiance measurements in the thermal infrared (IR). Channels of particular interest for dust detection include IR8.7 (referring to 8.7 μm), also applied for cloud characterisation, and the split window channels of IR10.8 and IR12.0 which have also found a use in detection of volcanic ash cloud (e.g. Dubuisson et al. 2014). Alongside monitoring of aerosols, thermal infrared imaging is valuable for flagging deep convection by identifying cold cloud tops, often with thresholds applied to the IR10.8 channel (see Table 1 in Bain et al. (2010a)).

The research in this thesis does not make use of the SEVIRI AOD product developed for North Africa and the Middle East by Banks and Brindley (2013), and hence does not attempt to quantify the exact dust loading associated with each emission mechanism. SEVIRI AOD requires a strong contrast between the background desert surface and lofted dust. This contrast is significantly reduced overnight, meaning that although dust can be tracked nocturnally SEVIRI AOD has only been used for 0600-1600 UTC, missing the main peak in CPO emissions (Banks and Brindley 2013) which is critical for this thesis. It should also be noted that there are disagreements between satellite AOD products over the Sahara; compared to IASI, MISR and MODIS, SEVIRI AOD appears to be biased high under low dust loading, performing better when AODs measured by AERONET exceed 1 (Banks et al. 2013).

High Rate SEVIRI Level 1.5 imagery for June, July and August (JJA) 2004-2017 has been downloaded from the EUMETSAT Data Centre at `https://navigator.eumetsat.int/product/EO:EUM:DAT:MSG:HRSEVIRI`.

2.2.1 Pink dust composite imagery

SEVIRI composite imagery (i.e. a combination of multiple channels into a single RGB image) is a powerful tool for studying dust plumes close to their sources in the Sahara and Sahel. Whereas the emissivity contrast between the ocean or vegetated surfaces and lofted dust plumes is typically small, over desert surfaces this contrast is greatly enhanced thanks to the fine particle size of atmospheric mineral dust compared to surface-bound material and high temperature of the surface compared to cooler dust plume tops (Wald et al. 1998). In 'pink dust' RGB composite imagery, IR12.0-10.8 corresponds to the red, IR10.8-8.7 corresponds to green and IR10.8 corresponds to blue. Coarse quartz particles have low emissivity at 8.7 μm, enhancing the green beam, which is heavily suppressed for finer dust particles (Lensky and Rosenfeld 2008).

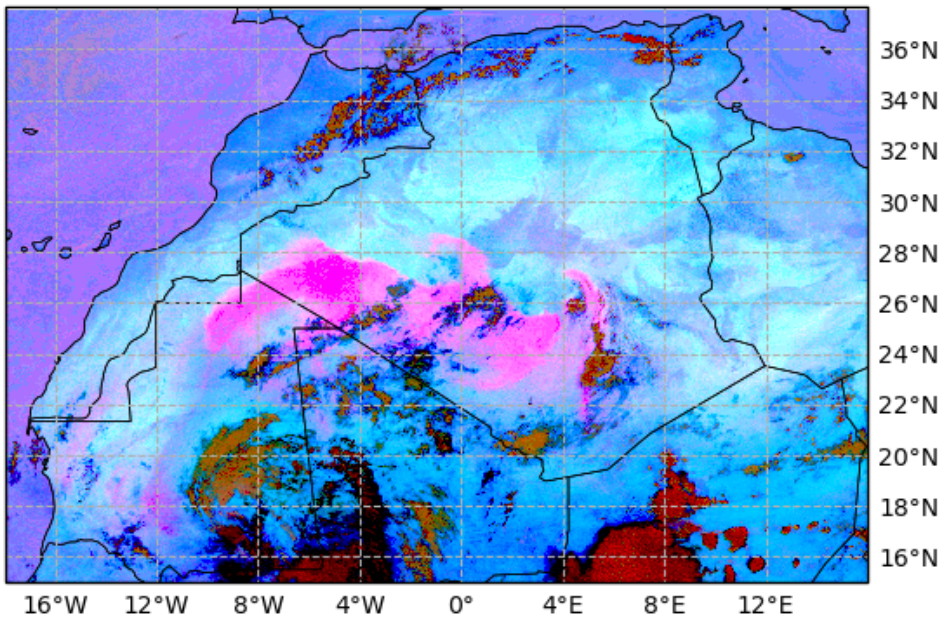


Figure 2.1: Example of a SEVIRI RGB pink dust composite derived from SEVIRI brightness temperatures at 1400 UTC on the 23rd August 2006. An interpretation is given in the text. Source: author.

Figure 2.1 gives an example of a SEVIRI scene at 1400 UTC on the 23rd August 2006, composited into an RGB pink dust image. At the time of the snapshot, the WAM has generated a number of cumulonimbus clouds, including mesoscale convective systems south of 20°N (dark red) and individual trailing cells. Dark red in the colour scheme corresponds to a strongly negative blue beam as a result of the cold cloud tops, along with slightly negative red and green beams. Black regions are thinner cirrus along the edges of the storm anvil. Brown patches (e.g. 20°N, 7°W) are thick water clouds with a slightly positive green beam. Quartz-rich sands appear as a bright blue where the blue beam has saturated (at its maximum temperature of 289 K or 15.85° C.) and both green and red are high. Rocky desert surface (e.g. the Tademait Plateau at 29°N, 3°E) takes on a slightly more purple appearance due to higher emissivity at 8.7 μm, suppressing the green beam. In sharp contrast, fine mineral particles have higher emissivity and hence a much smaller IR10.8-8.7, suppressing green and producing intense pink as seen around 27°N, 5°W, which corresponds to dust mixed up into the boundary layer following cold pool outflow activity the night before.

Interpretation of dust characteristics in SEVIRI is complicated by a number of uncertainties. The colour of dust in the RGB imagery is affected by total column water vapour (TCWV), dust altitude, lapse rate, composition and size distribution. Brindley et al. (2012) perform idealised radiative transfer simulations to assess the impact of these factors. They show that TCWV values exceeding 20-25 mm lead to masking of even high dust loadings. Second order controls include mineralogy and the height of dust plumes; at greater heights dust tops are colder and a stronger pink response is expected, depending on the lapse rate. Banks et al. (2018) couple a radiative transfer model with the COSMO-MUSCAT regional aerosol transport model and test the effect of size distribution, showing that coarse-mode particles as observed during the Fennec Campaign (Ryder et al. 2019) produce a weak response in pink dust imagery compared to finer material at an effective radius of 1.5 μm. In a follow-up paper, Banks et al. (2019) emphasise the significance of water vapour as a control on dust colour. Higher TCWV diminishes the red colour due to the higher absorption at 12.0 μm compared to 10.8 μm. The result of this is seen in Figure 2.1; dust south of the ITD in humid regions (e.g. 18°N, 12°W) takes on a more muted purple appearance. The authors also show that it is water vapour, not temperature, which tends to dominate the signal produced by dust altitude; high dust plume tops are found in a much drier atmosphere than dust in the bottom 1 km which is often masked. Lastly, the diurnal cycle plays a large role, with cooler desert surfaces often going below blue beam saturation as IR10.8 is relatively sensitive to skin temperature.

Pink dust imagery is extremely useful for monitoring dust source regions and offers information about both dust and convective processes. The relationship between these two phenomena is explored in detail in this thesis, making SEVIRI the ideal tool. Given the caveats outlined above, however, a number of provisions are made to ensure the results are robust, including adjustments to dust flagging to account for the diurnal cycle (Section 3.3), comparison with results weighted

for masking from water vapour and cloud (Section 3.6) and comparison with dust observations from ground stations (Section 4.5.2).

2.2.2 SEVIRI dust flags

Paper 1, presented in Chapter 3, makes direct use of SEVIRI dust flags (SDFs), while paper 2 (Chapter 4) adapts a similar tracking approach to characterise dusty outflow boundaries. SDFs are developed by Ashpole and Washington (2012) as a means of deriving a binary dust mask from thermal infrared channels. They achieve this by applying a threshold to the brightness temperatures (BTs) and brightness temperature differences (BTDs) comprising the RGB pink dust imagery. These thresholds include BT10.8 $\geq$ 285 K, BTD(12.0-10.8) $\geq$ 0 K and a BTD(10.8-8.7) $\leq$ 10 K. The last of these in particular (corresponding to the green beam) is critical for distinguishing fine material, but is strongly impacted by variable surface types; a rocky or vegetated surface can have a reduced BTD(10.8-8.7) even when no atmospheric dust is present (Brindley et al. 2012). To address this, Ashpole and Washington (2012) calculate a BTD(10.8-8.7) anomaly relative to a 15-day moving window centred on the time being observed and include a BTD(10.8-8.7) anomaly $\leq$ -2 K threshold as one of the flagging criteria. Tracking is performed by matching discrete plumes which overlap from one timestep to the next, easily achieved even for fast-moving plumes thanks to the high temporal resolution of SEVIRI. The authors evaluate SDFs against AERONET and OMI AI and find a good correspondence.

The SDF dataset is adopted and modified for the first paper in this thesis (Chapter 3). Two changes made to the SDF scheme include a less conservative restriction on plume size and an adjusted overnight detection scheme to reduce the effect of the diurnal cycle on plume visibility. These are applied to give a more precise dust source map and to allow the timing of emission to be analysed more accurately. Paper 2 (Chapter 4) develops a new dataset similar in principle to SDFs (e.g. making use of the 15-day moving window for background subtraction)

but targeted specifically at advancing cold pool leading edges. SDFs are also used as part of the paper 2 detection algorithm.

Although SDFs are useful and easily applied, a number of residual uncertainties remain and some of the research community has continued to use the manual tracking approach developed by Schepanski et al. (2007) in spite of its lower spatial resolution (Tegen et al. 2013; Evan et al. 2015; Wagner et al. 2016; Feuerstein and Schepanski 2019; Vandenbussche et al. 2020). No SEVIRI dust tracking technique is capable of tracking plumes under cloud or under existing lofted dust. Automated tracking is objective but the output it produces is also heavily modified by environmental conditions, especially patches of cloud which can obscure dust in convectively active regions. One advantage of entirely manual tracking is the ability of humans to integrate known regularities into perception of an object which is visually obscured (e.g. Chang and Jazayeri 2018), making it easier to track coherent features amidst atmospheric noise. Paper 2 addresses this deficiency for advancing cold pools by fitting them to an idealised arc-shape to estimate propagation speed (Section 4.3.3). It has also been suggested that manual approaches are comparatively less hindered by high TCWV and less likely to mistake mountainous regions for dust plumes (Fiedler et al. 2014; Wagner et al. 2016). Neither of these claims have been tested, however, and the moving window technique described in Ashpole and Washington (2012) is effective at subtracting stationary background features such as mountainous terrain.

Accuracy aside, objective algorithms which can be applied automatically are chosen over manual judgment for two key reasons in this thesis. First and foremost, they are reproducible. When comparing the results of two independent expert manual observers, Ashpole and Washington (2012) found 77% agreement during the day but only 52 % agreement at night. A much larger study of manual dust source mapping using MODIS found that analysts could pinpoint the same sources to within 17 km but that the vast majority of plumes were not tracked by all participants (Sinclair and LeGrand 2019), though the authors acknowledge

that missed plume timing due to polar orbit is an additional source of uncertainty and research into subjectivity of manual geostationary dust tracking is needed. Manual efforts can therefore produce varying results. Secondly, automated techniques are much more easily applied to large datasets. In this thesis many terabytes of data across 14 years are used, corresponding to 123,648 images. Analysis of a long satellite record has allowed for a climatological perspective on dust emission processes.

2.3 Met Office Unified Model

A regional configuration of the Met Office Unified Model (HadREM3-GA7.05) is used in paper 3 (Chapter 5), with a description of the model setup and sensitivity experiments given in Section 5.3.1. A 12 km configuration is used, with parameterized convection. The model was selected on the basis of practicality (the DPhil project is part-funded as a CASE collaboration with the UK Met Office) but also based on the widespread use of the UM for studies of West African atmospheric dynamics and dust emission. For instance, a 12 km configuration is similar to the setup used for the Fennec project Met Office Africa-LAM simulations (Allen and Washington 2014). The model is run in Chapter 5 with lateral boundary conditions provided by the ERA-Interim reanalysis in order to align the evolution of the model with real synoptic conditions and hence to allow SEVIRI dust observations to be used for compositing. ERA-Interim has shown a reasonable representation of wind variability at sub-seasonal timescales associated with synoptic patterns and hence is a useful constraint on the UM even though it cannot be relied upon to represent the peak winds on individual days (Roberts et al. 2017).

An analysis of a global configuration of the UM against reanalysis data is given by Fiedler et al. (2016). They show that the occurrence frequency of LLJs in the UM and ERA-Interim is close, but that they are up to 20% more frequent in central Algeria than in ERA-Interim and that core and surface winds tend to

be higher. A key difference between the model and reanalysis is the location of the SHL, with a south-shifted position in UM relative to ERA-Interim, indicated also by a dry bias over the Sahel (Diallo et al. 2014). It should be noted that the representation of the SHL in reanalyses is itself uncertain due to the scarcity of assimilated observations. For instance, the warming trend through the 1990s is captured in both the NCEP2 and ERA-Interim reanalyses but the spatial pattern is quite different (Lavaysse et al. 2016). A comparison between Fennec dropsonde observations of the SHL and Africa-LAM made by Engelstaedter et al. (2015) shows that the model has difficulty representing the afternoon position of the SHL (shifting it westward erroneously) and overestimates the growth of the CBL. SHL characteristics are better represented in the morning, including the location of the Harmattan low-level flow, critical for dry northeasterly LLJs. Afternoon discrepancies are particularly problematic for CPOs given the impact of a misrepresented SHL on moisture transport pathways. For these reasons as well as the poor fidelity of monsoon flow described in Section 1.6.3 and effects of convective parameterization on model error shown in 1.6, the object of study in Chapter 5 is the Harmattan LLJ (for which dry morning winds are most critical) and the domain is central Algeria which is relatively free of monsoon influence through summer. Further idealised model experiments closer to the monsoon rainband may first require improvements to the UM's SHL position, moisture transport and CPO parameterization.

2.4 In situ observations

2.4.1 Fennec data

The Fennec automatic weather station (AWS) network is used in Chapter 4 to demonstrate the correspondence between automatically tracked CPOs and measurable signals at the surface. A full description of the instrumentation and deployment is given by Hobby et al. (2013). In summary, eight stations were installed close to the climatological core of the SHL, intended to collect data continuously from May 2011 as part of the Fennec Campaign. Four of these

stations successfully transmitted data through 2011 and 2012, while another four only lasted a short time before failing due to solar panel outage under intense heating and insolation. These stations were subsequently reinitiated for the 2012 field season. Although the sampling period is relatively short, there are two advantages to using this AWS dataset. Firstly, as shown in Figure 1.2, a majority of surface weather stations are distributed around the fringes of the Sahara or in mountainous regions where cold pool activity is less common. In contrast, the Fennec AWS network samples CPOs close to the summer dust maximum. Secondly, Fennec AWS data are recorded every 3 minutes and 20 seconds, far better than hourly to 6-hourly SYNOP data from WMO-reporting manned and automatic weather stations which are likely to miss the spike in winds associated with cold pool passage entirely. Fennec datasets are available from the Centre for Environmental Data Analysis at `https://catalogue.ceda.ac.uk/uuid/819bdb021a644a9fb0b31704479523db`.

2.4.2 MIDAS and IGRA data

The Met Office Integrated Data Archive System stores land surface and marine observations from all over the world, including 3-hourly non-UK observations from many WMO-reporting stations shown in Figure 1.2. MIDAS records have been used to estimate dust emission thresholds across the Sahara as they provide observations of both wind speed and occurrence of visible dust storms as reported by manual observers (Cowie et al. 2014). SYNOP reports stored in MIDAS are used only in a limited capacity in this thesis to identify the frequency of dust storm observations through summer in Chapter 4. This serves as an additional line of evidence supporting the summertime trend in dust emission observed with satellite methods. Figure 4.11 in Chapter 4 shows each constituent station used and represents the relative data availability at each station as a circle. Data is extracted where available for the period JJA 1984 to 2016 from `https://catalogue.ceda.ac.uk/uuid/0ec59f09b3158829a059fe70b17de951`.

Radiosonde data is used in Chapter 4 to calculate Downdraft Convective Available Potential Energy (DCAPE) trends through summer as well as in Chapter 5 to describe the synoptic conditions associated with composited jet events in the UM control simulation. Data is sourced from the Integrated Global Radiosonde Archive (IGRA) (Durre et al. 2006) curated by the National Centers for Environmental Information (`https://www.ncdc.noaa.gov/data-access/weather-balloon/integrated-global-radiosonde-archive`. All available sonde ascents from the period JJA 2004-2017 are taken from the Tamanrasset, Agadez and Niamey stations for Chapter 4 whereas ascents for JJA 1997-2007 from In Salah are used in Chapter 5. Quality assurance procedures applied to IGRA data are described in Durre et al. (2006) and Durre et al. (2008). In brief, these procedures include elimination of duplicated data as well as flagging of physically implausible, excessively persistent or inconsistent values and climatological outliers.

3

A 14-Year climatology of Saharan dust emission mechanisms inferred from automatically tracked plumes

Thomas Caton Harrison[1], Richard Washington[1] and Sebastian Engelstaedter[1]

[1]Climate Research Laboratory, Oxford University Centre for the Environment, Oxford, UK

Published online 08/08/2019

J. Geophys. Res. Atmos., 124(16), 9665-9690, https://doi.org/10.1029/2019JD030291

Contents

3.1 Abstract 55
3.2 Introduction 56
3.2.1 Low-level jets 58
3.2.2 Cold pool outflows 60
3.2.3 Aims 61
3.3 Detecting and tracking emitted dust from satellite 62
3.4 Classifying observed dust plumes by emission mechanism 66
3.4.1 Manual classification 66
3.4.2 Automated classification 70
3.4.3 Timing of emission 70
3.4.4 Deep convection association 71
3.4.5 Geometry 73
3.4.6 Regression model 75
3.4.7 Other emission mechanisms 79
3.5 Comparison with manual detection methods and in situ observations 80
3.6 Climatology of emission mechanisms 82
3.7 Summary and conclusions 94
3.8 Acknowledgements 96

3.1 Abstract

The central and western Sahara (CWS) is the largest source of mineral aerosols during boreal summer, but observed ground-based data are extremely scarce and typically distant from key source regions. Knowledge of dust emission mechanisms has therefore been mostly limited to short-term observations from a point or model approximations. To address this deficiency, dust plumes from the CWS are classified according to emission mechanism for June, July and August of 2004-2017 using an automated inference method which accurately tracks the timing, convective association and geometry of plumes observed with the Spinning Enhanced Visible and Infrared Imager (SEVIRI) aboard Meteosat Second Generation satellites. From these characteristics, plumes are classified as either low-level jet or cold pool outflow events. The extensive data set is used to generate the largest available climatology of dust emission sources and Saharan emission mechanisms. Automated inference compares well with ground-based measurements from the Fennec Campaign (76% accuracy) as well as with an entirely manual approach (88% accuracy). Cold pool activity accounts for 82% of total observed dust and 88% at the point of emission. Dust from cold pools evolves seasonally from hotspots around the Mali-Niger-Algeria border triple point towards the central Sahara to the northwest, while dust from low-level jets is organised along the axis of the northeasterly Harmattan, and dominates emission within the Tidihelt Depression of central Algeria. The widespread importance of cold pool outflows in this research supports the findings of the Fennec Campaign, but low-level jets remain highly significant in certain isolated hotspots.

3.2 Introduction

Mineral dust is a highly abundant atmospheric aerosol (Zender et al. 2004; Choobari et al. 2014; Boucher et al. 2013), and its variable emission, transport and deposition affects the planet's radiative budget, human health, meteorological dynamics and biogeochemical cycles. 40-60% of the yearly global dust burden originates in the numerous sources of the Sahara (Engelstaedter et al. 2006), from which emissions peak during boreal summer (Prospero et al. 2002; Washington et al. 2003; Schepanski et al. 2007).

Information about local emission processes in the Sahara is desirable given the high values of dust loadings at low to mid atmospheric levels proximate to dust emission. However, active source regions within the central Sahara suffer from a severe lack of systematic long-term in situ observations with which to constrain emission characteristics (Marsham et al. 2013b; Allen et al. 2013; Garcia-Carreras et al. 2013). It is not surprising that dust emission in global climate models is highly divergent with emission totals varying by more than a factor of five (Huneeus et al. 2011). Furthermore, little evidence has been found that global climate models used in the Fifth Assessment Report of the IPCC faithfully reproduce any important components of North African emissions or transport (Evan et al. 2014).

Given the approximately cubic dependence of emissions upon wind speed, a crucial element to which dust models are sensitive is the wind field used to drive them (Menut 2008; Woodward 2011; Knippertz and Todd 2012; Fiedler et al. 2016). For emission of dust, winds capable of exceeding local emissions thresholds are needed (Bagnold 1941). These winds are embedded within a hierarchy of active processes. At the synoptic scale, these include wind regimes such as the Harmattan, Atlantic inflow and monsoon flow, as compared by Chaboureau et al. (2016). Describing these regimes helps to explain the underlying meteorological conditions associated with dusty conditions on a particular day. However, the

short-term processes generating the high winds directly responsible for uplift of dust usually operate below the synoptic scale (Tegen and Schulz 2014), meaning observation and model products which do not at least resolve the mesoscale are ill suited to study their behaviour. Reanalysis products typically used for this purpose have been found to underestimate the amplitude of the diurnal cycle of winds in the central Sahara (Allen and Washington 2014; Roberts et al. 2017).

The primary mesoscale meteorological drivers of dust source activation are nocturnal low-level jet (LLJ) breakdown and cold pool outflows (CPOs) from deep convection. The importance of these two key emission mechanisms has been shown with observations from the Fennec field campaign at Bordj-Badji Mokhtar during June 2011, where an analysis of locally emitted and advected dust found that only a tiny contribution (3%) was made by dry convective plumes, with CPOs and LLJs playing the dominant role (Allen et al. 2013). A better understanding of the relative role of these two emission mechanisms and where they operate with respect to major Saharan dust sources would help explain interannual and intraseasonal dust emission variability and allow a directly process-based improvement of dust models. Critical to this is information about emission mechanisms with the spatiotemporal resolution capable of linking wind processes directly to localised dust sources.

Existing estimates of the relative role of LLJs and CPOs from the Fennec campaign are based upon information collected at one point in space, during only one month of boreal summer (Allen et al. 2013; Marsham et al. 2013b). Partitioning of summertime emissions by LLJs and CPOs on a broader scale is also available from Marsham et al. (2011) (50% CPO) and Heinold et al. (2013) (40% CPO, 40% LLJ and 20% residual). However, these are derived from model simulations without observational evidence to support modelled CPO frequency, seasonality, distribution or strength in the central Sahara. We aim to address this observational gap.

3.2.1 Low-level jets

LLJs (Figure 3.1a) are thought to operate across the Sahara (Schepanski et al. 2009; Fiedler et al. 2013). Decoupling from surface momentum fluxes allows winds above the nocturnal boundary layer to become supergeostrophic as they oscillate around geostrophy (Blackadar 1957). Subsequent initiation of buoyancy-driven turbulence after sunrise by incoming solar radiation mixes this momentum to the surface, driving high winds which in the Sahara typically peak in the hours after sunrise and before noon (Parker et al. 2005a).

Methods to characterise LLJ activity depend upon the dataset used. in situ observations, while constrained to study locations, often afford a vertical component to which detection criteria can be applied. These make use of balloon, radiosonde and wind profiler data where available (Washington et al. 2006; Bain et al. 2010a; Allen and Washington 2014; Vanderwende et al. 2015) and are a valuable insight into jet frequency and strength for short time periods. As their spatial extent is small, however, few inferences can be made about LLJ activity across dust emission regions. Broader climatologies are obtained using model and reanalysis methods (Fiedler et al. 2013; Ranjha et al. 2013; Soares et al. 2014; Heinold et al. 2015; Ge et al. 2016), although in the context of dust emission these are limited by relatively poor reanalysis performance over remote desert regions (Koren and Kaufman 2004; Allen and Washington 2014; Roberts et al. 2017).

Aside from cloud motion vector and scatterometer methods to detect LLJs over oceans (Mahajan et al. 1989; Chelton et al. 2000; Garreaud and Muñoz 2005), satellite observations of LLJs are less common. Over land, one approach to identifying and quantifying LLJ winds has been to track plumes observed in high resolution satellite overpasses (Koren and Kaufman 2004; Todd et al. 2008b). Without an automated approach, this is a time-consuming and subjective method. To link LLJs to dust emission on a large scale, remotely sensed dust emission events have been classified according to their timing (Schepanski et al.

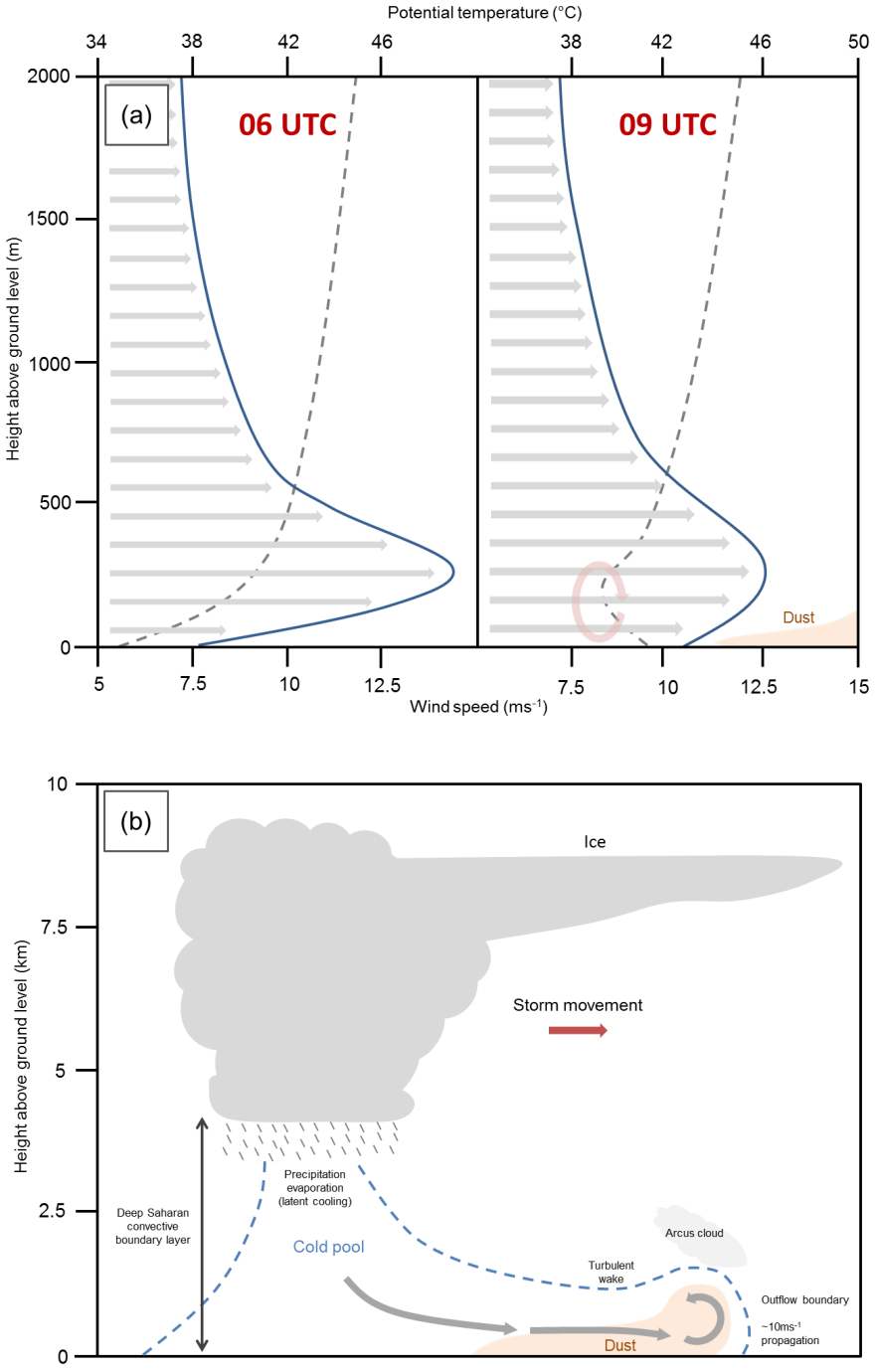


Figure 3.1: Schematic diagrams of emission mechanisms. (a) shows the nocturnal low-level jet (described in Section 3.2.1) as typical summertime central Saharan wind (solid blue) and potential temperature (dashed grey) profiles at 0600 UTC (left panel) and 0900 UTC (right panel). Convective turbulence in the morning mixes momentum from aloft to the surface, raising dust. (b) shows the mechanics of a cold pool outflow (described in Section 3.2.2) associated with a mature convective system, with the cold pool region delineated in dashed blue.

2009; Tegen et al. 2013). Events occurring during the morning are more likely to be driven by LLJ activity due to the consistent diurnal cycle of momentum mixdown. However, this approach is apt to overestimate the LLJ contribution where other mechanisms also operate (Allen et al. 2013). To date, it has also been limited to manual datasets of tracked satellite-observed plumes. A more advanced automated method for studying LLJ dust emission on a large spatiotemporal scale is therefore needed.

3.2.2 Cold pool outflows

CPOs (Figure 3.1b) in the vicinity of deep convection (termed 'haboobs' when they cause dust storms) are also a major supplier of dust-emitting winds (Bou Karam et al. 2008; Marsham et al. 2008). These occur as convective downdrafts reach the surface and fan out radially as density currents. Observations collected during the Fennec Campaign indicate that CPOs play the dominant role in emission of dust during the Saharan dust maximum in summer (Allen et al. 2013), and manual tracking of these events by satellite shows that they can encourage reinitiation of deep convection in the central Sahara where convective inhibition is high (Trzeciak et al. 2017). Although the bulk of outflow events are associated with the West African Monsoon (WAM), CPOs are also observed south of the Atlas mountain range where orography enhances convection (Emmel et al. 2010; Redl et al. 2015). Limited observations of these phenomena and their absence from models with parameterised convection leads to significant moisture transport and dust misrepresentation (Garcia-Carreras et al. 2013). Both CPO and LLJ activity is thought to be controlled in part by displacements of the Saharan heat low (Knippertz and Todd 2010; Cuevas et al. 2017), which during summer migrates along an east-west axis (Todd et al. 2013).

Building upon early observations of North African haboobs (e.g. Sutton 1925; Lawson 1971), studies supported by remote sensing have become the norm (Knippertz et al. 2007; Miller et al. 2008; Emmel et al. 2010; Allen

et al. 2013; Roberts and Knippertz 2014; Redl et al. 2015; Provod et al. 2016). Satellite observations aid in the identification of CPOs and in linking them to deep convective activity. However, each of these studies has focused upon small case study regions, meaning little information is available about cold pool activity across the Sahara as a whole and its relative importance in different dust emitting locations. Model experiments capable of resolving CPOs can fill this gap (Heinold et al. 2013), but lack systematic cold pool observations for validation and are typically short duration model runs owing to the computational demand of the high spatial resolution. A climatology of CPO dust with wide spatiotemporal coverage derived from identification of cold pool dust emission events is clearly desirable.

3.2.3 Aims

This study focuses upon the central and western Sahara (CWS), which supplies the bulk of Saharan dust output during boreal summer. To quantify the role of emission mechanisms in the Sahara directly, comprehensive observations of emission events close to source are needed. Ground-based observations are unable to fulfil this role and are unlikely to in the forthcoming decades. Methods to automate the identification and tracking of dust in Spinning Enhanced Visible and Infrared Imager (SEVIRI) imagery (Ashpole and Washington 2013a) do allow information on dust presence and emission drivers to be collected over long periods. Using quantifiable characteristics of automatically tracked plumes, the present study describes a more accurate method of inferring emission mechanisms for individual plumes. Being fully automated, we are able to apply the method to boreal summer over the period 2004-2017, providing observations of emission sources and processes of unprecedented length. This study aims to:

1. Accurately automate classification of SEVIRI-observed dust plumes in the CWS as either LLJ or CPO driven events;

2. Quantify the relative contribution of LLJs and CPOs to the total dust pixels observed using SEVIRI for June, July and August of 2004-2017;

3. Distinguish LLJ and CPO dominated source regions in the CWS.

Section 3.3 describes the approach used to delineate dust within SEVIRI, Section 3.4 demonstrates how automatically tracked plumes can be accurately classified and Section 3.5 validates the methodology. Finally, a climatology of low-level jet and cold pool outflow dust is presented in Section 3.6.

3.3 Detecting and tracking emitted dust from satellite

Brightness temperatures from the Spinning Enhanced Visible and Infrared Imager (SEVIRI) aboard Meteosat Second Generation (MSG) are used here for studying individual dust plumes as imagery is available at 3 km resolution (at nadir) with 15 minute temporal resolution. We adopt the 'SEVIRI dust flag' (SDF) approach of Ashpole and Washington (2012) and Ashpole and Washington (2013a) to identify regions of dust plume presence and track their evolution. The thresholding approach applied to the brightness temperatures is described therein, and follows the frequently exploited sensitivity of differences between the 12.0, 10.8 and and 8.7 μm channels to dust (Ackerman 1997; Schepanski et al. 2007; Lensky and Rosenfeld 2008; Ashpole and Washington 2012), yielding false colour images where dust presence is represented by pink colours (Figure 3.2a). Red regions represent cirrus clouds (e.g. over deep cumulonimbus convection), while lower clouds appear in orange and dark blue. During the day, the blue channel tends to saturate over the dry desert surface. Further discussion of the components of pink dust composites and the visibility of dust layers is found in Ashpole and Washington (2012).

Following Ashpole and Washington (2012), no information about dust quantity such as aerosol optical depth (AOD) is available from SDFs; only the presence or absence of dust (Figure 3.2b). Although the thresholds from which the dust flags were derived have been carefully tuned to AOD measurements from Aerosol

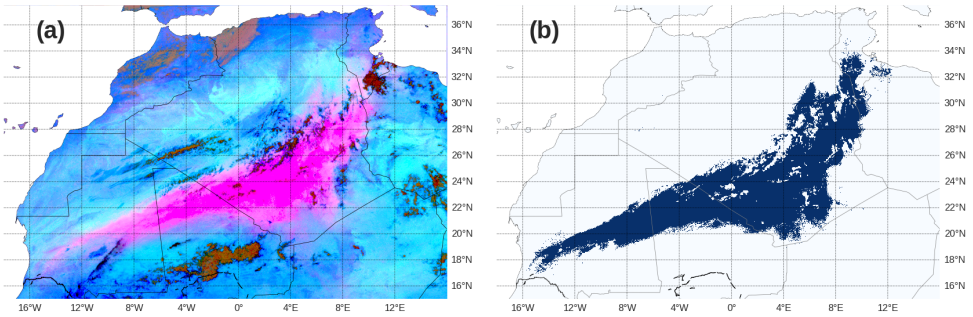


Figure 3.2: Example of SEVIRI dust flags applied to 1100 UTC SEVIRI retrievals on the 11th of June 2010, when a large plume stretched across the entire central and western Sahara. The 'pink dust' RGB composite produced from the 8.7, 10.8 and 12 μm channels is shown in (a), with flagged dust pixels (blue) only shown in (b). Pink regions in (a) are dust, with red and orange indicating cloud. The desert surface during the day appears in bright blue.

Robotic Network (AERONET) (Holben et al. 1998) stations, the magnitude of threshold exceedance is also affected by total column water vapour, lapse rate, dust top height, size distribution, particle shape and refractive index (Brindley et al. 2012; Banks et al. 2018).

The tracking of dust plumes used in this paper largely follows the approach described in Ashpole and Washington (2013a), whereby a discrete detected plume from one 15 minute timestep is traced into the next timestep if a spatial overlap is found. When multiple plumes merge, they become part of the largest contributor (in terms of pixel coverage). The capacity of this method to track plumes through time presents the opportunity to derive methods to establish the signatures of their driving emission mechanism, such as LLJs and CPOs.

Several adjustments have been made to the Ashpole and Washington (2013a) dust tracking scheme in order to better serve inference of plume emission mechanisms. First, the spatial resolution of plume detection is increased from 250 pixels to 50 pixels, meaning plumes are allowed to reach a minimum size of 50 pixels if they exceed 250 at some point in their lifetime. This allows plumes to be tracked slightly further back to source regions and maximises the detection of their entire life cycles. Furthermore, it addresses the small number

of plumes which flicker above and below the detection threshold (leading to false detections of emission). To test the usefulness of this change, 60 plumes in the existing dust tracking scheme were compared with imagery from SEVIRI. Of the total pixels across this period marked as being associated with dust emission (the first timestep of a plume's life cycle), 5.8% were found to be caused by a false detection from where an existing plume flickered below the 250 pixel size threshold. The new system with the adjustment described here was found to remedy 75% of these false emission cases.

An important caveat of the SDF method is the reduced capacity to observe nocturnal plumes, as it relies on an atmospheric lapse rate which renders dust plume tops thermally distinct from the desert surface. This often means that plumes which have aged overnight are falsely detected as new in the morning. Previous work using automatic tracking of SDFs (Ashpole and Washington 2012; Ashpole and Washington 2013a) has made little use of the timing of plume emission, focusing instead upon climatological and seasonal dust statistics. However, the observed timing of dust emission is a useful quantity with which to infer the driver of uplift (Section 3.4.3). In this paper, therefore, we attempt to partially address this issue by maximising nocturnal detection.

Visual inspection of SEVIRI 'pink dust' imagery reveals regions of dust observable by eye (Figure 3.3, leftmost panels). However, several of these emission events appear to go undetected by SDF in the early morning hours, as shown in the central column of panels in Figure 3.3. Missing events are all cold pool outflows, observed in central Mali in Figure 3.3a, around the Algeria-Niger border in Figure 3.3b, in southern Algeria in Figure 3.3c and along the Algeria-Mali border in Figure 3.3d. Thresholds used for SDF detection in Ashpole and Washington (2012) were empirically tuned to delineate dust presence while avoiding false detections from features such as cloud edges or maritime stratus (which can produce similar radiative signatures). Uniformly applying a more generous set of thresholds would therefore be inappropriate. However, analysis

of case studies shows that a BT 12.0-10.8 μm threshold of -1.5 K instead of 0 K reveals previously unobserved nocturnal dust when applied overnight. In our updated plume tracking scheme, we apply this modified threshold only to plumes detected overnight. To avoid additional spurious detection in this scheme, dust flagged using these relaxed threshold must fulfil two conditions not to be discarded. First, emission must take place between 2300 and 0800 UTC. Second, the plume must overlap at some point during its lifetime with the one detected using the original, stricter SDF scheme (i.e. the largest effect of this modification is to track morning plumes back further into the night). The new scheme is successful at backtracking aged plumes which would have been falsely detected as new, providing a more realistic emission time estimate (Figure 3.3, rightmost panels).

To test the effect of the new scheme upon plumes on an aggregate scale, we manually identified plumes from June 2011 which were falsely detected late (i.e. an aged plume detected as a new one). 51 cases were found, comprising 8% of the total events. This is likely an underestimate as some plumes will be entirely indistinguishable from the relatively cool nocturnal desert surface. The updated scheme fixes 32 (63%) of the erroneous cases, without introducing false alarms. Combined with reduced plume flickering as described above, this updated scheme significantly improves confidence in the timing of emission events.

Close correspondence between sources identified with updated SDFs and the plume source map developed in Ashpole and Washington (2013a) is found when the improved plume tracking method described above is applied to track dust plumes back to their source, with a clear Tidihelt region signal, as well as prominent sources around the Mali-Niger-Algeria triple point, at 19°N, 5°E (Figure 3.4). Smaller peak emission locations are due to the relaxation of the plume size constraint (from 250 to 50 pixels).

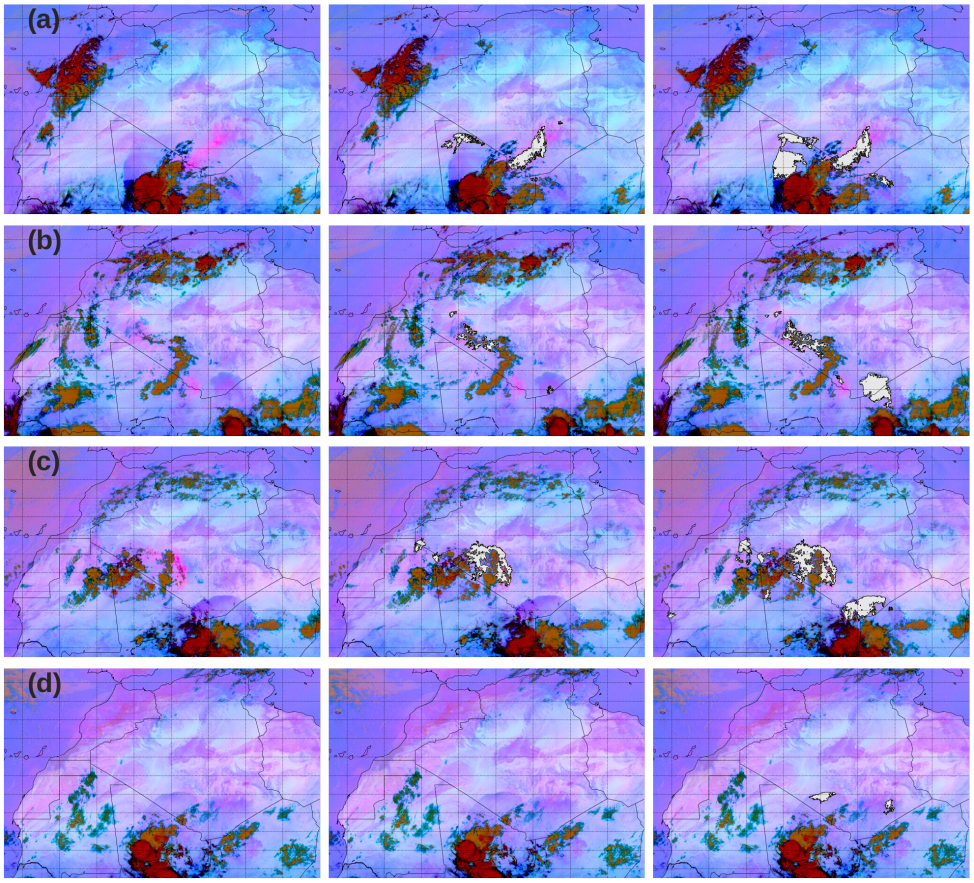


Figure 3.3: Examples of improvements to dust flagging introduced with an adjusted plume tracking system, showing the raw 'pink dust' composite (left), the original Ashpole and Washington (2013a) flagged image (centre) and the result of the improved method (right). Pixels flagged as dust are shown for both old and new algorithms with a white mask. Examples are shown for (a) 19/06/2011 at 0700 UTC, (b) 03/07/2012 at 0200 UTC, (c) 06/07/2012 at 0200 UTC, (d) 29/07/2012 at 0200 UTC.

In this paper, plumes are automatically tracked using the method described above for the period of June, July and August of 2004-2017. Next, each individual plume is analysed individually in order to infer the driving emission mechanism.

3.4 Classifying observed dust plumes by emission mechanism

3.4.1 Manual classification

In order to determine the emission mechanisms responsible for dust plumes, several physical principles are used by the observer. These principles may, in

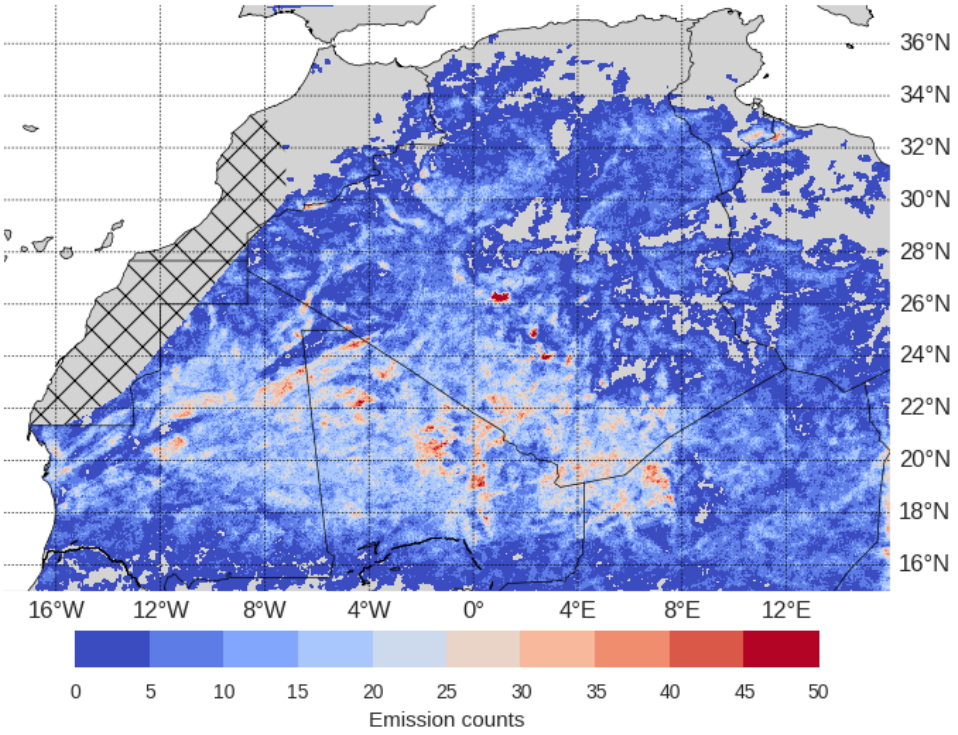


Figure 3.4: Total counts of dust plume emission events in the Central and Western Sahara for June, July and August of 2004-2017. A plume emission event is identified as the pixels covered by a plume during the first timestep of its lifetime. Map is constructed using the adjusted plume tracking approach described in Section 3.3. The western region of the CWS along the coast of the Atlantic is masked (hatched area) following Ashpole and Washington (2013a), as this region is prone to false detections due to incursions of marine stratocumulus.

turn, be used to train an automated method. Here, a case study from 2011 is used to demonstrate how emission mechanisms may be identified by eye.

As described with observations collected during the Fennec Campaign (Allen et al. 2013), on the 17th June 2011 the Saharan heat low was centred over the eastern CWS (northern Niger and southern Algeria) and was collocated with a deep dust layer mixed well into the atmospheric boundary layer up to 6 km (Ryder et al. 2015). Allen et al. (2013) identify the large southern dust feature delineated in Figure 3.5 around the Mali-Niger-Algeria triple point (19°N, 5°E) as a cold pool originating from a mesoscale convective complex, showing that its lofted dust was responsible for one of largest dust detection signals at Bordj-Badji Mokhtar. Inspection of the imagery reveals a sharp boundary in dust, propagating radially

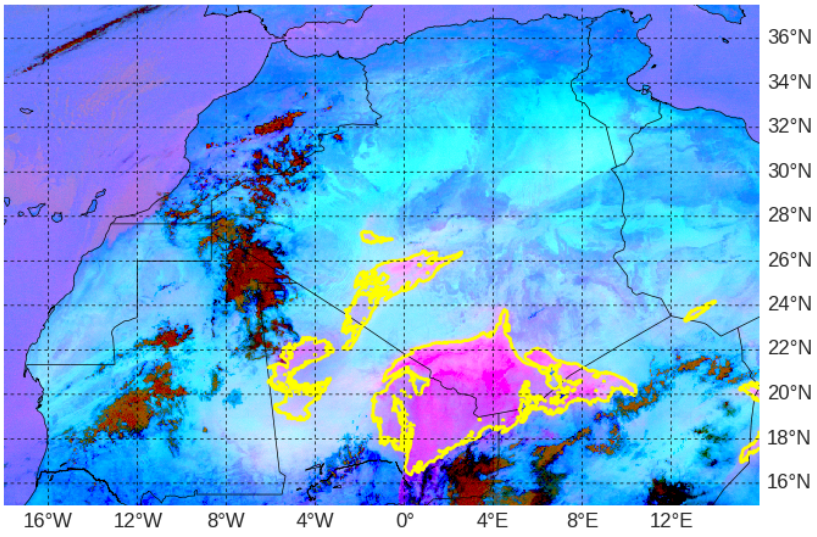


Figure 3.5: Plumes observed in SEVIRI 'pink dust' composites at 1200 UTC on June 17th 2011. Dust detected by the scheme used in Section 3.3 is delineated in yellow.

away from a deep convective system in the early hours of the morning. This spreading behaviour is typical of a density current, where a dense fluid undercuts another and is followed by turbulent conditions (Simpson 1969), here capable of lofting dust due to high gusty winds at the outflow boundary. The nocturnal timing of the events reflects the diurnal cycle of convection, with the strongest evaporative downdraft formation occurring in the evening (Garcia-Carreras et al. 2013). Surface fluxes during the day may also play a role in slowing the advance of daytime cold pools or hastening their erosion (Ross et al. 2004; Gentine et al. 2016; Huang et al. 2018). The presence of arcus clouds along some regions of the observed outflow boundary is indicative of cold pool advance and suggests relatively high moisture availability (Marsham et al. 2008). The spatial coherence of the feature is notable, and uplift of dust is organised perpendicular to the direction of the haboob's northwestwards travel, typical of the advancing 'wall' phenomenon they exhibit (Roberts and Knippertz 2012).

The LLJ example shown for June 17th 2011 is visible as the northernmost dust features delineated in Figure 3.5 in western Algeria. Ryder et al. (2015) identify a sharp downwards mixing of momentum in operational forecasts for the day over northern Mali, consistent with the nocturnal jet cycle, and suggest that the low-level winds are likely to have been deflected by the Hoggar mountains (22°N, 5°E). This down-mixing of momentum is a result of solar heating, as thermal eddies begin to mix the previously stable nocturnal boundary layer. A series of streak-like structures in lofted dust, visible by noon, is seen propagating southwestwards along the Harmattan channel. These include uplift over northern Mali and in the Tidihelt region of central Algeria. The timing, spatial structure and lack of nearby deep convection make this a clear LLJ case, therefore, even in the absence of model wind simulations. The typical streak-like appearance of LLJ dust could be due to a combination of orographic channelling and the highly localised nature of deposits of easily deflated material. Most highly active dust sources are likely to be associated with paleolakes and outwash plains (Ashpole and Washington 2013a) rather than large sand seas, meaning dust source activation is favoured at isolated hotspots. Cold pools appear to lift dust in much broader swathes, which may be due to highly effective vertical transport above the cold pool head (Huang et al. 2018). Greater dust altitude in turn makes it easier to observe using SEVIRI, which relies upon the thermal contrast between the dust plume top and the surface.

While some of the features above (such as the presence of arcus clouds) are not straightforward to identify automatically, quantifiable features, including emission timing, proximity to deep convection and geometry can act as indicators of a plume's consistency with either the LLJ or CPO visual archetype. This principle informs the method used to automate plume classification.

3.4.2 Automated classification

The longevity of the dust plume dataset available from the tracking scheme described in Section 3.3 can be used to assess the climatological and intraseasonal development of dust emission mechanisms. However, with over 41,000 tracked plumes (of which 18,141 were classified), manual identification of emission mechanisms becomes challenging and the reproducibility of the subjectively identified mechanisms questionable. While a 'deep learning' approach to automated detection is in principle possible, a large training dataset would be needed and the methodology would be opaque. Here, we base an automated approach upon the simple visual principles from Section 3.4.1. Three quantifiable characteristics of the observed dust plumes are used as predictors: the emission timing, the association with deep convection and the plume geometry.

3.4.3 Timing of emission

Emission mechanisms in the CWS tend to follow a diurnal cycle, as described in Section 3.4.1. The most consistent of these is the timing of LLJ emission, as this is controlled in large part by the timing of sunrise. As one of the three predictor variables, automatically detected plume emission timing can be compared with the expected peak time for LLJ momentum surface wind speed acceleration. To derive an estimate for the time at which dust activating LLJ winds are expected to peak, we analyse winds observed at 2 m by the Fennec automatic weather station (AWS) network (Hobby et al. 2013). Following Allen et al. (2015), we detect days on which an LLJ is clearly active by checking for a gradual increase and decrease of winds during the morning which follows a Gaussian shape.

The time between sunrise and peak LLJ winds is found to vary between 3.6 and 4.8 hours with a mean time of 4.55 hours (Figure 3.6). Each AWS exhibits a comparable increase towards peak LLJ winds in the morning followed by more variable winds in the afternoon. In each case, a small lag after sunrise of around an hour occurs on average before winds ramp up towards their peak. The station

with the largest delay of 4.8 hours after sunrise (133, Figure 3.6b) appears also to have the lowest average pre-sunrise winds and highest peak LLJ winds. This could indicate greater boundary layer stratification overnight, leading to a more momentum delivered to the surface at sunrise. On the whole however, variation between stations in this delay is small. We approximate a peak time for expected LLJ emissions at 4.5 hours after sunrise, with sunrise calculated separately for each emitted plume based on location and time of year. In practice, plumes may only be observable to the plume tracking system described in Section 3.3 a short while after emission, and some will precede the expected peak time. Hence, a time window of 0600 to 1600 UTC is specified in which LLJ emission is possible, although plumes very late or early in this period will score poorly in this timing criterion. Outside of these hours, emissions are assumed not to be associated with LLJ activity. Although sporadic turbulence overnight is possible due to wind shear, lidar profiles from the Fennec Campaign (Allen and Washington 2014) provide little evidence to suggest these drive overnight emission, as this process will actually tend to erode the LLJ too gradually for it to obtain erosive potential (Knippertz and Todd 2012).

3.4.4 Deep convection association

A second predictor of a plume's emission mechanism is its association with deep convection, as Saharan CPOs are a result of convective downdrafts.

Here, the distance of the centroid of a plume at the point of its emission to the nearest pixel with a BT10.8 μm value under 270 K is used as a proxy for its association with deep convection. Centroids throughout this paper are calculated from the mean of all latitude and longitude values associated with pixels comprising a feature. The choice of BT threshold follows the approach of Lavaysse et al. (2009) and Ashpole and Washington (2013a) for identifying deep convective cloud features. Although LLJ emission in close proximity to deep convection is a possibility, model estimates of dust emission under cloud suggest

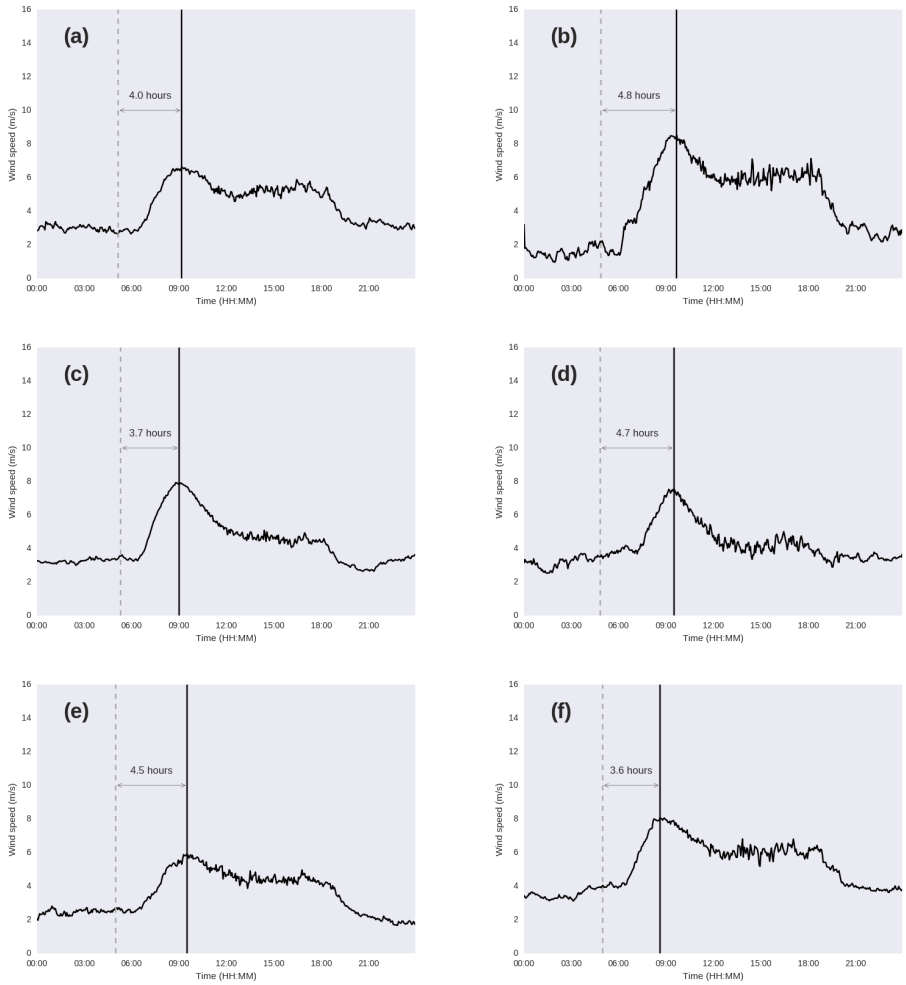


Figure 3.6: Wind speed composites on days identified as having LLJ activity, sampled from AWS (a) 131, (b) 133, (c) 134, (d) 135, (e) 138, (f) 140 (all measured at 2 metres above ground level). The black vertical line indicates the mean timing of peak LLJ momentum winds at the surface. The dashed grey line shows the mean time of sunrise. The interval between the two is marked with a horizontal arrow.

a small fraction of LLJ associated uplift occurs under cloud Heinold et al. (2013). Furthermore, dust emitted far (hundreds of kilometres) from deep convection is unlikely to be associated with cold pool outflows except for the most vigorous, far-ranging cases. Plumes with a high distance to deep convection are therefore more likely to be identified in this scheme as LLJ-related.

3.4.5 Geometry

In Section 3.4.1, it was shown that emission events associated with CPOs exhibit typical characteristics of an advancing wall, while LLJ-driven plumes behave more as streaks. The streak-like geometry of LLJ plumes is particularly clear when all pixels across their lifetime are considered (Figure 3.7b), and can be compared to the bow-like shape of a cold pool outflow event (Figure 3.7a).

To quantify this geometric distinction, two variables are required: the direction in which the plume is travelling and its orientation. Plume direction is calculated by taking the angle between the plume's centroid during its first and last timesteps. Orientation is calculated by taking the union of all pixels across the plume's lifetime (all activated pixels over all timesteps in Figure 3.7) and calculating the first eigenvector from a principal component analysis of these pixels (on a longitude-latitude axis). The difference between the plume direction and orientation may then vary from 0 to 90°. Lower values indicate a plume propagating along its orientation (more LLJ-like), while higher values suggest propagation perpendicular to orientation (more CPO-like). Here, this quantity is termed the 'axis offset' of a plume.

Unlike emission timing and association with deep convection, calculation of this quantity relies on obtaining a stable estimate of variables from a plume's total lifetime. For this reason, plumes with a very short duration are not reliable. Hence, in this paper a probability value is only calculated for plumes with a duration greater than or equal to two hours. Axis offset values tend to vary significantly within the first few timesteps of a plume's lifetime (Figure 3.8). After two hours, however, the change in axis offset from one timestep to the next does not exceed 10 degrees on average. Geometries calculated for plumes with this duration are considered to be representative of the plume's true emission mechanism.

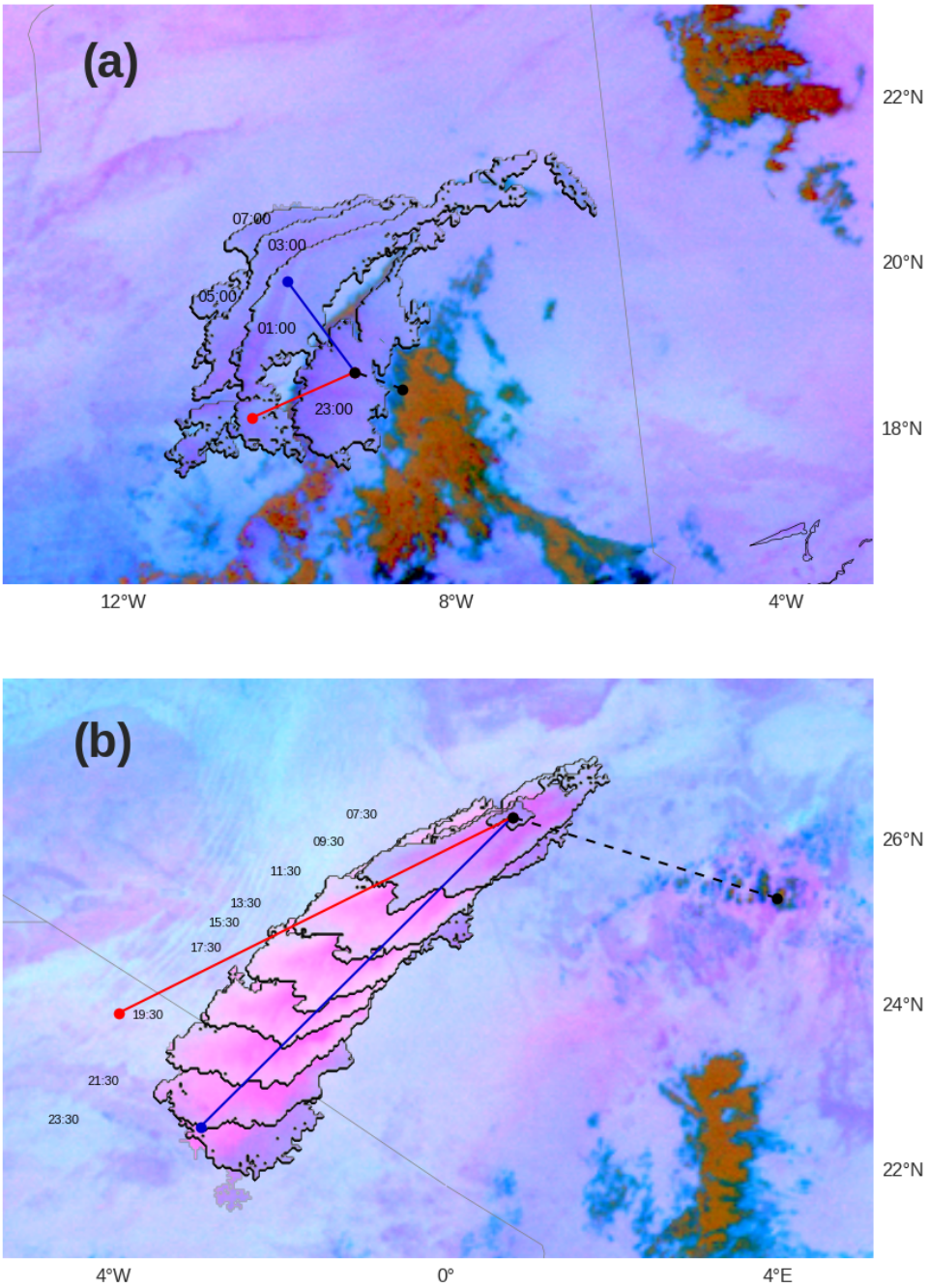


Figure 3.7: Life cycle of a typical tracked plume (at 2 hourly intervals), shown as a delineated region of the RGB pink dust composite, with each timestep overlain (older detections plotted over newer ones). The background shows the pink dust composite at the time of plume emission (i.e. 2300 in (a) and 0730 in (b)). Labels indicate the UTC time of each timestep (first predictor), the black dashed line indicates the distance to deep convection at the point of emission (second predictor) and the blue and red lines indicate the propagation direction and orientation, respectively (third predictor). A cold pool outflow case is shown in (a) with a low-level jet in (b).

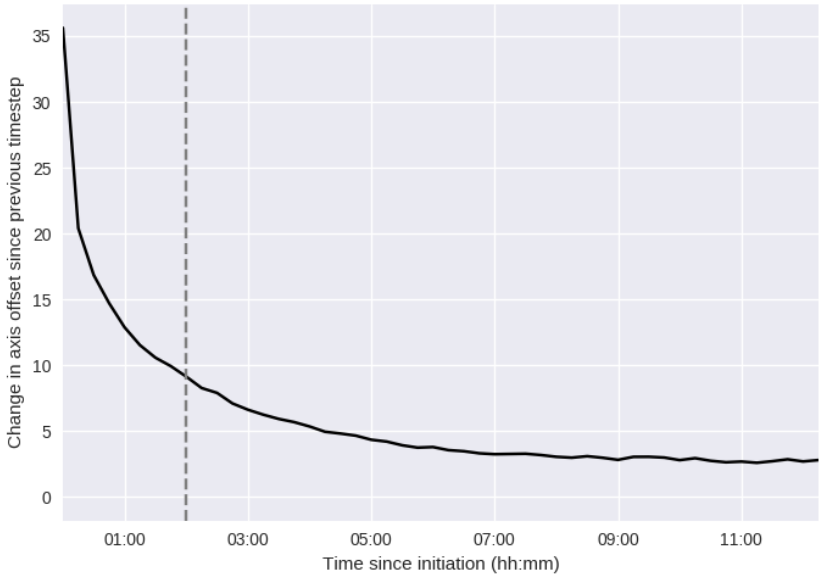


Figure 3.8: Mean change in the axis offset criterion since it was calculated in the previous timestep of a plume's evolution, plotted against the time since the emission of the plume. Calculated from the mean of all plumes from June, July and August of 2004-2017. The dashed grey vertical line indicates the 2 hour cutoff point before which plume probabilities are not calculated.

3.4.6 Regression model

A single probability is assigned to each plume, using a multiple logistic regression model to account for the three predictive characteristics. Logistic regression is used here as the dependent variable is a binary classification. It is assumed that a plume adopts one classification to the exclusion of the other, hence a plume cannot be both a highly probable LLJ and highly probable CPO. As a result, this probability varies from 0 (high confidence CPO) to 1 (high confidence LLJ) since the conditions bound up with the CPOs and LLJs are mutually exclusive. Each of the three predictive characteristics are therefore selected such that LLJs and CPOs produce opposite signals, as shown in sections 3.4.3 to 3.4.5.

The final assigned value should be interpreted as the probability that a manual observer would identify the plume as being LLJ-driven, assuming all events are driven by either LLJs or CPOs (see Section 3.4.7 for other mechanisms).

This value is calculated as:

$$P_L = \left(\frac{1}{1 + \exp(-\beta_0 - \beta_1 X_1 - \beta_2 X_2 - \beta_3 X_3)} \right) \tag{3.1}$$

where P_L is the probability of a given plume being an LLJ under the identification scheme, X_i is the value of predictors variables 1-3 (timing of emission, deep convective association and geometry), β_0 is the intercept value and β_i is the corresponding regression parameter for each predictor. As some events cannot be unambiguously categorised as LLJ or CPO driven, this system represents these with low probabilities (in this case values close to 0.5, indicating no strong preference either way).

Given a probability of being either LLJ or CPO-driven, a plume can be categorised based on a user-defined threshold. Here, we identify LLJ dust as being plumes with an LLJ probability of 0.5 or over, while CPO dust is identified where a plume's LLJ probability is under 0.5.

With values of X_i available from quantified plume characteristics, corresponding values for β_i are needed to obtain a final probability value for a given plume. These are obtained by fitting the model to a set of 'true' LLJ and CPO cases. As the goal of the probabilistic scheme is to replicate the manual observer automatically, this training dataset is generated by manually identifying a series of clear cases from the year 2010 only. 141 events are categorised in total; in order to maintain comparable sample sizes these are split almost evenly between LLJs (71) and CPOs (70). This is not, however, intended to represent the true partitioning of events.

For each predictor, a clear distinction between the distributions for manually identified LLJ and CPO events (Figure 3.9) demonstrates that the choice of criteria is appropriate. The majority of plumes manually identified as LLJs were found by the automated tracking system to have been emitted within 10,000 seconds (2.7 hours) of the peak expected time (3.9a). In the case of CPOs, a

flatter distribution is found, with little evidence for a preference for emission at any particular time. The distance of a plume from deep convection at the point of its emission is a clear identifier of CPO events. While LLJ plumes are somewhat clustered around 200-400 km away from deep convection, the vast majority of plumes manually identified as CPOs are emitted within 200 km of the nearest identifiable convective cell (3.9b). The metric of geometry, offset of the plume from its major axis (orientation), is similarly distributed to the timing metric (3.9c). Plumes identified as low-level jets align their propagation more closely with their orientation than do CPOs.

Solving the equation requires parameters (β_i) to be estimated from the training dataset. A Bayesian approach is taken to fitting the model defined in Equation 5.1. This means that rather than directly selecting the maximum likelihood estimate for the parameter values (β_i), a distribution ('posterior distribution') of model parameters is obtained. To approximate the posterior distribution given the observed data, the No-U-Turn Sampler (Hoffman and Gelman 2014) is used. This Bayesian approach in principle allows prior distributions to be specified and combined with the observed data to produce the posterior. In this paper, no prior distributions are specified (i.e. a uniform prior is used for each predictor), meaning there is little difference with the result that would be obtained using a maximum likelihood approach. With a posterior distribution of parameters, we obtain a corresponding distribution of probabilities from which the mean is calculated. Nonetheless, the adoption of a Bayesian approach means that priors could be incorporated into the methodology in future, for instance when better in situ observations of the morphology of LLJ and CPO dust plumes are available. One particularly applicable prior would be long-term surface measurements of the diurnal cycle of dust emission due to LLJs and the lag between such emissions and the dust top becoming visible in SEVIRI. By comparison, the current approach uses only information about wind speeds and the timing of sunrise. Specifying a

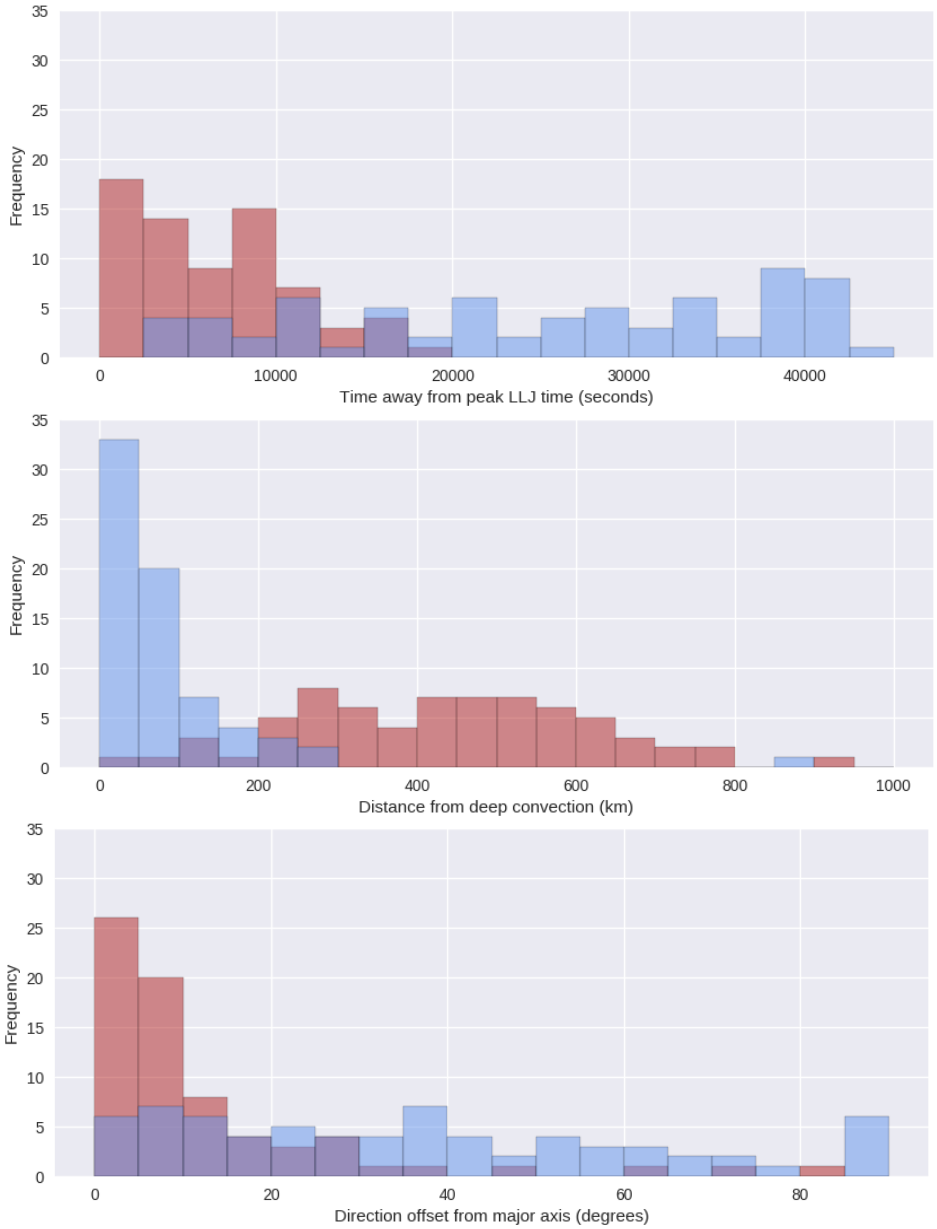


Figure 3.9: Distribution of values of predictors used for multiple logistic model of plume LLJ probability, as calculated for manually identified LLJs (red) and CPOs (blue) from 2010, including (a) the time in seconds away from peak expected LLJ emission time, (b) the distance to the nearest deep convection in km and (c) the offset angle (the maximum being perpendicular) of the plume's direction of propagation from its major axis (orientation).

prior distribution may then reduce the need for a fixed time window (of 0600 to 1600 UTC) in which LLJ emission is allowed.

3.4.7 Other emission mechanisms

Our method focuses upon dust emission visible in satellite imagery. Emission mechanisms operating on a significantly smaller scale, such as dust devils, are therefore unlikely to be observable.

Cold surges from maritime regions (Vizy and Cook 2009) have been observed to drive gusty winds with emission potential close to the Mediterranean (Knippertz 2008). No contribution to observed dust emission from such sources was found at Bordj-Badji Mokhtar during the Fennec Campaign (Allen et al. 2013) and, although these are uncommon and typically occur during winter (Wagner et al. 2016), events observed with this methodology are likely to be classified in this methodology as CPOs. To estimate the contribution of cold surges, imagery from June 2011 was analysed. Three large plumes of dust emitted radially from the Mediterranean region in the northeast of the CWS were identified during this period, each of which was also associated with some degree of deep convection. Assuming these were cold surges, however, they accounted for 4.4% of the total dust pixels flagged for the month using the method in Section 3.3, indicating a relatively minor contribution to total dust. Further work is required to distinguish cold pools generated by deep convection in the Atlas mountain regions and cold surges, driven for instance by lee cyclogenesis within the same region. As the bulk of dust emission during summer occurs further south in the Central Sahara than western Tunisia and northern Algeria near Mediterranean inflow regions, however (Ashpole and Washington 2013a), these events are likely to have only a small impact upon the net partitioning of emission drivers.

3.5 Comparison with manual detection methods and in situ observations

The availability of targeted observations from the Fennec Campaign in boreal summer allows the approaches used in this research to be validated in highly dust laden regions. We also validate the methodology against entirely manual identification based on SEVIRI imagery.

Table 3.1: Plume emission mechanisms identified at Bordj-Badji Mokhtar (June 2011) as identified by Allen et al. (2013)

Date (AM/PM)	Event type	Correct classification?
13/06/2011 AM	Cold pool advection	Yes
13/06/2011 PM	Cold pool emission	Yes
14/06/2011 AM	Cold pool advection	Yes
14/06/2011 AM	Low-level jet	No
14/06/2011 PM	Cold pool advection	Yes
15/06/2011 AM	Cold pool advection	No
16/06/2011 AM	Low-level jet	Yes
17/06/2011 AM	Cold pool advection	Yes
17/06/2011 PM	Cold pool emission	Yes
18/06/2011 AM	Cold pool emission	Yes
18/06/2011 AM	Low-level jet	No
19/06/2011 AM	Cold pool emission	Yes
19/06/2011 PM	Cold pool advection	Yes
21/06/2011 AM	Cold pool emission	Yes
21/06/2011 PM	Cold pool emission	Yes
22/06/2011 AM	Cold pool emission	Yes
22/06/2011 PM	Cold pool emission	Yes
23/06/2011 AM	Cold pool advection	Yes
24/06/2011 AM	Cold pool emission	Yes
24/06/2011 PM	Cold pool emission	Yes
25/06/2011 AM	Low-level jet	No
25/06/2011 PM	Cold pool emission	Yes
26/06/2011 AM	Low-level jet	Yes
27/06/2011 AM	Cold pool advection	No
29/06/2011 AM	Low-level jet	Yes
29/06/2011 PM	Low-level jet	Yes
30/06/2011 AM	Cold pool emission	Yes
30/06/2011 PM	Cold pool emission	Yes

Table 3.2: Plume emission mechanisms (LLJs and CPOs only) identified from Fennec flights as described by Ryder et al. (2015)

Date (AM/PM)	Event type	Correct classification?
17/06/2011 AM	Low-level jet	No
18/06/2011 AM	Low-level jet	Yes
21/06/2011 AM	Atlas cold pool	No
25/06/2011 AM	Low-level jet	Yes
27/06/2011 AM	Cold pool advection	No

The automated dust plume classification approach compares well with events identified using in situ Fennec data, but is limited by the sensitivity of SDFs to detect all emitted dust. Ryder et al. (2015) and Allen et al. (2013) catalogue several LLJ and CPO events distinguished using a variety of land-based and airborne instrumentation (Tables 3.1 and 3.2). In total, 25 of the 33 (76%) events were both identified as dust and correctly classified. Two cases of incorrect classification were found, in both instances with a probability value indicating high uncertainty. Each remaining missed event is either obscured by existing dust emission or undetected by the automated dust detection scheme due to insensitivity or the inability to observe dust under cloud. Many of the LLJ dust events observed at Bordj-Badji Mokhtar are undetectable in SEVIRI using either manual or automated methods, possibly due to the presence of a surface temperature inversion or LLJ-generated dust not getting injected high enough to be distinguished with SEVIRI (Allen et al. 2013). Very short-lived plumes are not within the scope of this paper, as probabilities are only calculated for plumes with a minimum duration of 2 hours. Analysis of SEVIRI here is therefore limited to large plumes which can be resolved and which have the vertical extent and/or duration to be distinguished from the desert surface. LLJs may, therefore, be a dominant driver of small-scale uplift which does not fulfil these conditions.

Automatically classified plumes are also compared with an entirely manual approach (as described in Section 3.4.1). Using imagery from 2011, 65 of the clearest events have been identified as being either cold pool or low-level jet driven. Of these, 57 were correctly identified using the automated method (87.7%). To

examine the added value of this, it has been compared with an approach based purely on the timing of events; the accuracy of this method can be maximised at 76.9% if plumes are always identified as LLJs when emitted between the hours of 0600 and 1500 UTC (a more conservative cutoff of 1600 UTC is used in this paper as late-emitted LLJ plumes are occasionally found). The difference between these two percentages is significant at 90% but not at 95%, however, demonstrating that most of the automated method's effectiveness comes from identifying plume timing, though it should be noted that the accuracy of the timing-only method comes also from the adjustments to SDFs described in Section 3.3.

3.6 Climatology of emission mechanisms

Having assigned probabilities to each plume of being associated with either an LLJ or CPO, in this section probabilities across the entire sampling period of June-August 2004-2017 are aggregated to build a climatology of dust-emitting LLJ and CPO events. This is achieved by identifying events with a probability of more than 0.5 as an LLJ and those with less than 0.5 as a CPO.

We analyse the contribution of each mechanism to the total SDF pixels across the sampling period to investigate their respective roles in Saharan emission although we recognise that this encapsulates both emission and transport processes (Ashpole and Washington 2012); no information on dust optical depth is provided by SDFs, so highly dispersed aged plumes appear the same as freshly emitted ones. Nevertheless, the dust tracking scheme used in this work allows new plumes to be distinguished from aged ones, meaning plume activity at the point of emission can be studied.

Dust is associated above all with CPOs, accounting for 81.6% of the total pixels (13,521 events compared to 4,620 LLJ events). The dominance of CPO dust is consistent in each year of the analysis (Figure 3.10), although the partitioning varies between 94% CPO in 2017 and 60% in 2012. Although the bulk of dust

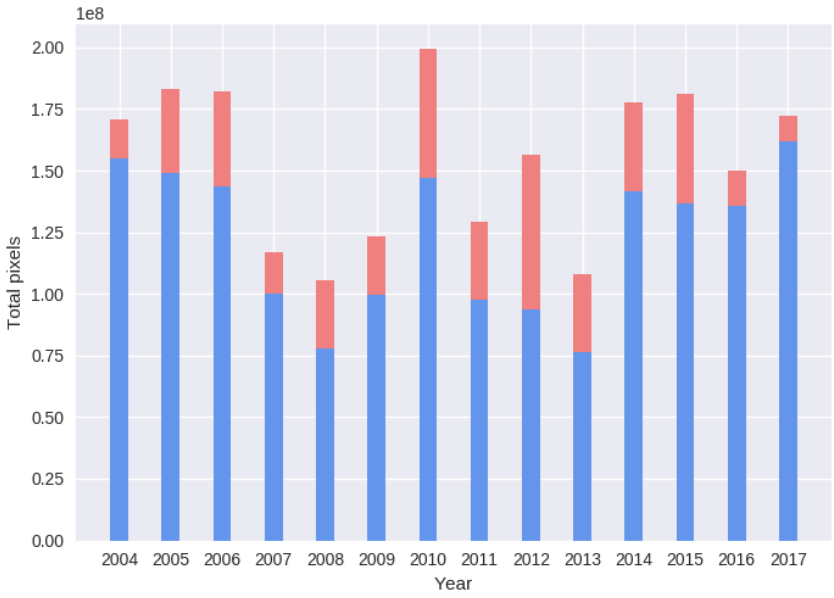


Figure 3.10: Total yearly counts of pixels classified as belonging to cold pool outflow (blue) and low-level jet (red) driven dust events.

present over the CWS during summer is invariably CPO-associated, the dustiest years are not necessarily those with the most CPO activity.

The largest concentrations of CPO-driven dust are found in a dipole pattern (Figure 3.11a) highly reminiscent of the distribution found by Ashpole and Washington (2012). One of these hotspots runs along the Mali-Algeria border, from 22 to 26°N. While monsoon surges far north of the peak WAM rain zone are a known phenomenon (Parker et al. 2005a; Lavaysse et al. 2011), the existence of this dust maximum suggests that northwards moisture transport around the southeastern flank of the Saharan heat low is directly linked to dust-emitting cold pool activity in remote Saharan dust sources, as suggested by Garcia-Carreras et al. (2013) and Engelstaedter et al. (2015). A second (but closely linked) contributor to these northern hotspots is likely to be recycled cold pools, which have been observed propagating as far north as the foothills of the Atlas mountains (north of 28°N) (Trzeciak et al. 2017). Although cold pool emission is significant around the northern and southern fringes of the Sahara (Marsham

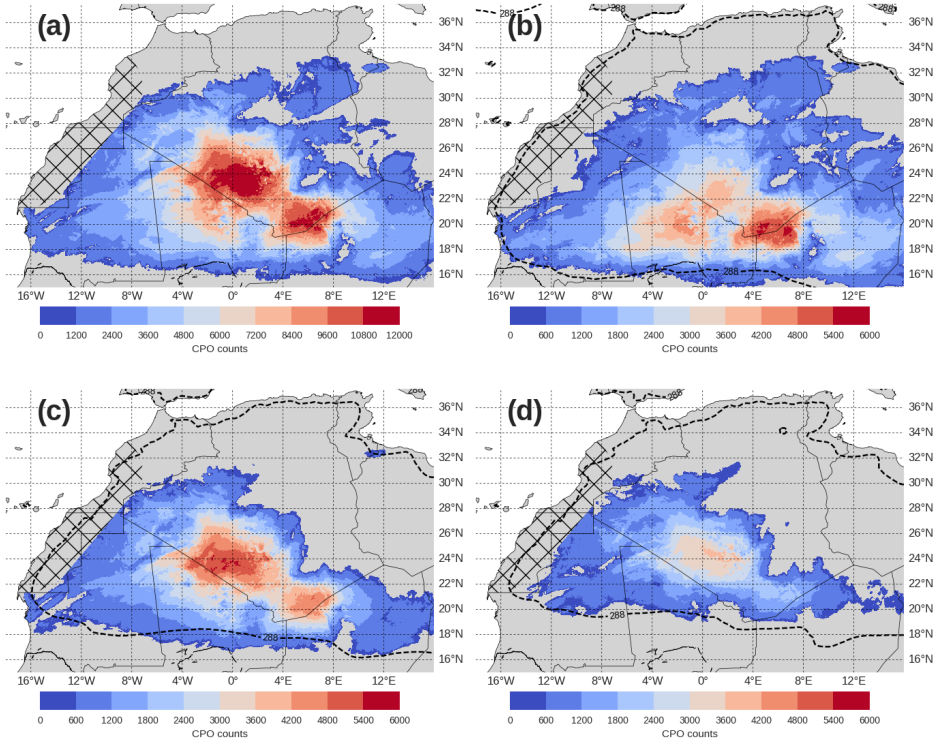


Figure 3.11: Total counts of pixels classified as belonging to cold pool outflow events across the total lifetime of all plumes tracked from 2004-2017. The total for JJA is shown in (a), along with June (b), July (c) and August (d). The western region of the CWS along the coast of the Atlantic is masked (hatched area) following Ashpole and Washington (2013a), as this region is prone to false detections due to incursions of marine stratocumulus. Dashed black contour indicates the mean position of the 288 K 10 metre dewpoint temperature line from ERA5 for each constituent month (same period).

et al. 2011), it also extends far into the central Sahara. The second region in the dipole, observed in the southeast around the Mali-Niger-Algeria triple point (19°N, 5°E), is coincident with a hotspot of orographic convection (Redl et al. 2015; Chaboureau et al. 2016) and significant dust availability from a large region of ephemeral fluvial systems draining the Aïr and Hoggar ranges (Bou Karam et al. 2008).

Seasonal displacement of the CPO signal is particularly pronounced around the triple point region (Figure 3.11b and 3.11d). Ashpole and Washington (2013b) found that the early season dust maximum around the Mali-Niger-Algeria triple

point migrates northwestward along the Mali-Algerian border as the summer progresses. Figures 3.11b and 3.11c indicate that this signal is dominated by the CPO dust response, lending credence to the importance of monsoon dynamics in this transition. A particularly significant component of these dynamics is the June onset of the WAM, during which accumulated convective inhibition, maintained in part by the dry northeasterly Harmattan, is broken and the rain band shifts north (Sultan and Janicot 2003). While preonset monsoon surges advect considerable moisture into the central Sahara on weekly timescales (Couvreux et al. 2010), this onset coincides with the northward jump of cold pool emitted dust. Deep convective cloud cover increases considerably over these dust-emitting regions in July, reaching its maximum in August (Figure 3.14a-c). The extension of deep convection north towards the border of Mali and Algeria during July (Figure 3.14b) coincides with the development of the CPO hotspot along this border region observed in Figure 3.11c. The evolution of this northwards extension in monsoonal convection over Mali is likely, therefore, to be a major driver behind CPO-driven dust emissions in the remote Sahara north of 22°N.

LLJ-related dust (Figure 3.12) is lower in quantity (note the difference in the scale between Figures 3.11 and 3.12) and more geographically confined. A particular streak of high LLJ-driven dust emission is observed downstream (southwest) of the highly active Tidihelt Depression in central Algeria (26-27°N, 1°E), pointing to the existence of a distinct alley of LLJ activity between the Hoggar (22°N, 5°E) and Atlas (30°N, -4°E) mountains, in which CWS jet-driven dust peaks in boreal summer. As shown from the Fennec Campaign in 2011, dust emitting LLJs are also active close to the dust source maximum further south along the southwestern Algerian border (Allen and Washington 2014).

Similar to CPOs, a south-north propagation is evident in the intraseasonal development of LLJ dust (Figures 3.12b, 3.12c and 3.12d). Dust in June is observed in the southeast of the domain around 17°N, 13°E in Niger south of the Ténéré Desert and west of Lake Chad, but this activity is absent in July and

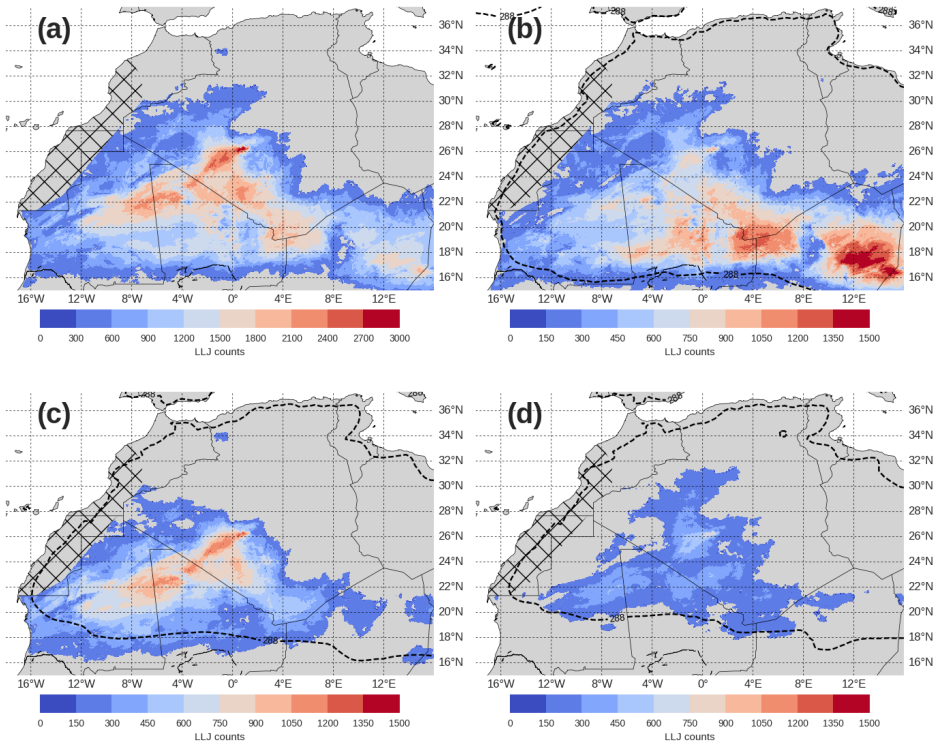


Figure 3.12: Total counts of pixels classified as belonging to low-level jet events across the total lifetime of all plumes tracked from 2004-2017. The total for JJA is shown in (a), along with June (b), July (c) and August (d). The western region of the CWS along the coast of the Atlantic is masked (hatched area) following Ashpole and Washington (2013a), as this region is prone to false detections due to incursions of marine stratocumulus. Dashed black contour indicates the mean position of the 288 K 10 metre dewpoint temperature line from ERA5 for each constituent month (same period).

August. LLJ dust is also observed further north in June than in later months, with a band of emission aligned through the Grand Erg Occidental north of 27°N. The highest counts of activations within the Tidihelt Depression region occur during July, with LLJ activity dropping off considerably in August. A likely contributor to the development of this July maximum is the summertime evolution of the Saharan heat low (Figure 3.14d-f). Whereas in June the low is centred over southern Algeria (Figure 3.14d), it extends northwestwards during July setting up a major pressure gradient region over central Algeria. This is evident in low-level wind fields (Figure 3.14g-i), where a hotspot of surface wind speed develops around 27°N, 4°E in July, having been absent during June,

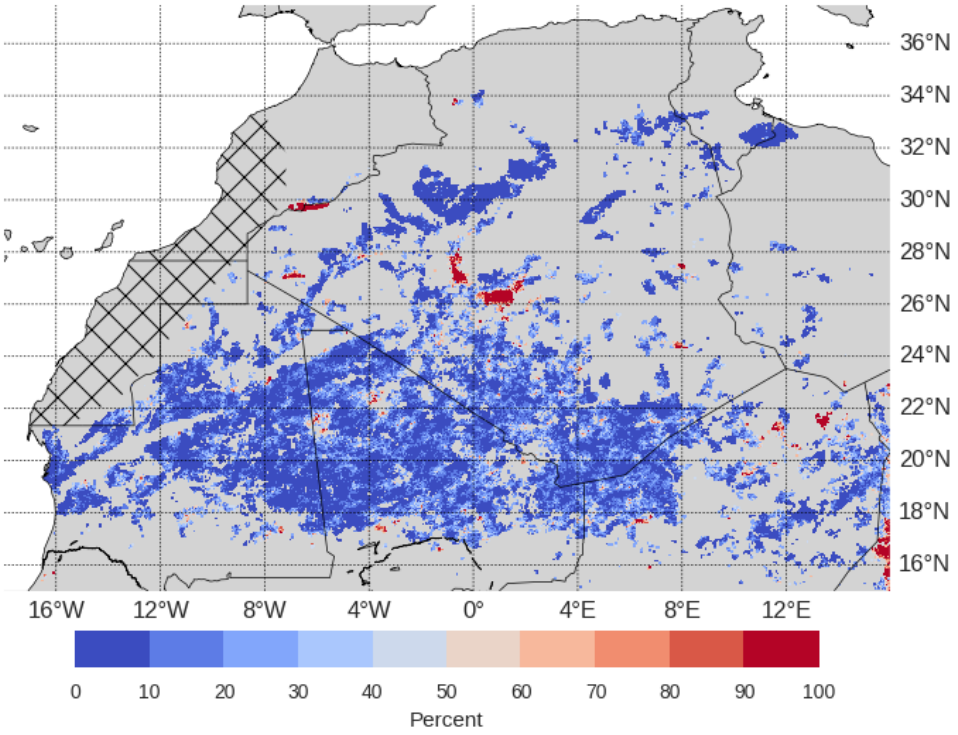


Figure 3.13: Percentage of emission pixels classified as being low-level jet driven for June, July and August 2004-2017, with the remaining proportion classified as being cold pool outflow driven. Each pixel of a plume during the first four timesteps of its life cycle is identified as an emission pixel. Regions with fewer than 10 emission pixels identified across the sampling period are masked out. The western region of the CWS along the coast of the Atlantic is masked (hatched area) following Ashpole and Washington (2013a), as this region is prone to false detections due to incursions of marine stratocumulus.

reducing in August. Coincident with the Tidihelt region, this is the most likely driver behind the mid-summer peak in the LLJ alley observed in 3.12c. A weakening in the SHL in August may be responsible for the decline in dustiness for this month. Although Figure 3.14i suggests the effect upon surface winds is minor, the threshold-driven nature of dust emissions may be highly sensitive to the reduction in LLJ strength as a result of the gentler pressure gradient.

An interesting feature of the results is that although deep convective cloud reaches its maximum during August (Figure 3.14a-c) as measured by the total hours in SEVIRI with pixel BT at 10.8 μm under 230 K, this is the month when both CPO and LLJ dust totals actually drop off significantly. Enhanced cloud

cover and water vapour over southern regions may explain some of this reduction in LLJ and CPO activity over monsoon regions in August. For instance, a comparison of SEVIRI dust source mapping with CALIOP observations suggests the southern Sahara and Sahelian sectors may be underobserved due to water vapour presence (Todd and Cavazos-Guerra 2016). Multiple lines of evidence support a decline in overall dustiness during August, however. AERONET 500 nm aerosol optical depth observations from Tamanrasset for 2007, 2008 and 2011-2016 show a decline from a mean value of 0.52 in June to 0.43 in July and 0.36 in August. It is also suggested by a significant drop in August Aerosol Index over the CWS measured with the Total Ozone Mapping Spectrometer (TOMS AI) calculated from 1980-1992 (Engelstaedter et al. 2006) as well as MODIS DeepBlue aerosol optical thickness measured from 2006-2009 (Schepanski et al. 2012).

Although other datasets support this seasonal decline in observed dust, bias in SEVIRI may be contributing to the seasonality of the results presented here. As discussed in Ashpole and Washington (2012), dust cannot be observed under cloud, and is obscured where high column water vapour is present (Brindley et al. 2012; Banks et al. 2018). Assuming seasonal variation in dust optical properties are negligible, water vapour and cloud is likely to be the main source of any bias when comparing early and late summer dust observations. To test this, we estimate a mask representing the percentage of timesteps masked (i.e. invisible for detection of dust) across the domain for each of the three months (Figure 3.14j-l). This is calculated by flagging a pixel as masked if it is either cloud-covered (BT10.8 μm value under 270 K) or located south of the Intertropical Discontinuity (ITD), using the ERA5 288 K dewpoint temperature contour. The ITD represents the confluence of the monsoonal and harmattan airmasses in the central Sahara (Engelstaedter and Washington 2007; Bou Karam et al. 2008) and is a region with a sharp increase of low-level atmospheric moisture content, with surface dewpoint temperature values between 287 and 289 K used previously as a proxy for the position of the ITD (Eldridge 1957; Buckle 1996; Marsham et al.

2008). In general, dust is obscured south of the climatological location of this boundary; this is demonstrated in Figures 3.11 and 3.12 by marking the mean seasonal position of the ITD. The analysis is applied to hourly data to match with the resolution of the ERA5 reanalysis. Maps of CPO and LLJ dust adjusted for masking effects (not shown) do not differ significantly from the results presented in Figures 3.11 and 3.12. Our unadjusted results show a 59% (75%) drop in CPO (LLJ) dust pixels between June and August, whereas adjusted results show a 53% (69%) drop. Hence, while biases in SEVIRI do play a small role in reducing visibility of dust during the peak of the monsoon, they are unlikely to be the driving factor behind the seasonality of the results presented here.

As the decline in dustiness during August is therefore likely to be genuine, questions remain as to why dust would decrease even as deep convective activity grows. One possible explanation is a decline in dust transport, for instance due to a weaker SHL (3.14f), but results from Ashpole and Washington (2013a) indicate that emissions also drop in this month. Assuming erodibility is constant, enhanced convective activity may not necessarily correspond to increased generation of outflows. This will be tested in a subsequent paper which focuses more directly upon the occurrence of these outflow boundaries.

Next we analyse the percentage of emission events driven by each mechanism in order to link CPO and LLJ activity to individual source regions. A pixel associated with a plume in the first timestep of its life cycle is designated as an emission pixel. No information about plume transport is obtained from this metric, but it affords a more faithful description of the geographical distribution of the emission processes themselves.

Overall, 87.5% of emission pixels are associated with CPOs. The preference for CPO emission events is widely distributed across the peak CWS emission regions (blue regions in Figure 3.13). Of the dust sources shown in Figure 3.4,

the majority are dominated by CPO emissions, including around the Mali-Niger-Algeria triple point. In this region, marked as (f) in Figure 3.16, plumes tend to propagate in a westward or northwestward direction, bounded by the Aïr Mountains to the west. The area labelled under (d) as the Tamanrasset region in Figure 3.16 has a more even distribution of plume directions, indicating the hotspot of cold pool generated dust present in July in Figure 3.11c is associated with locally generated cold pools as well as those propagating from the ITD zone in the south. Almost all emissions in Mali are associated with CPOs, with a small contribution from LLJs near the Taoudenni basin (22°N, 4°W), long identified as a dust source of global significance (Washington et al. 2003). Probabilities for regions with high CPO activity are typically dominated by values of zero, with 80% of CPO pixels having been assigned this value. This signifies that in most instances, plumes identified as CPOs were given that classification simply because they occurred at a time of day when only CPOs are considered possible under the automated system (Section 3.4.3).

Unlike the widespread emissions from CPOs, frequencies of LLJ emission are dominated by activity within the low lying Tidihelt region of central Algeria (Figure 3.13, and shown in Figure 3.15). This indicates that although CPOs are a dominant emission mechanism across the CWS during boreal summer, the single most frequently activated source at this time of year is almost entirely driven by LLJs. Within the broad Harmattan channel between the Atlas and Hoggar ranges, the Tidihelt region is approximately 200 km southeast of the windiest observed region in Algeria, Adrar (28°N, 0°E) (Chellali et al. 2011). The numerous endorheic basins (in particular Sebkha Mekerrhane and Sebkha Azzel-Matti) with large saline deposits and erodible material lie in the lowland plain near In Salah at the opening between the Tademaït Plateau and Mouydir Mountains, which drain into the Tidihelt below (Hughes 1992). Along with the Tohat Oases to the northwest, these are the last major emission hotspots before the desert opens out into Erg Chech to the west. The idealised map of regions of

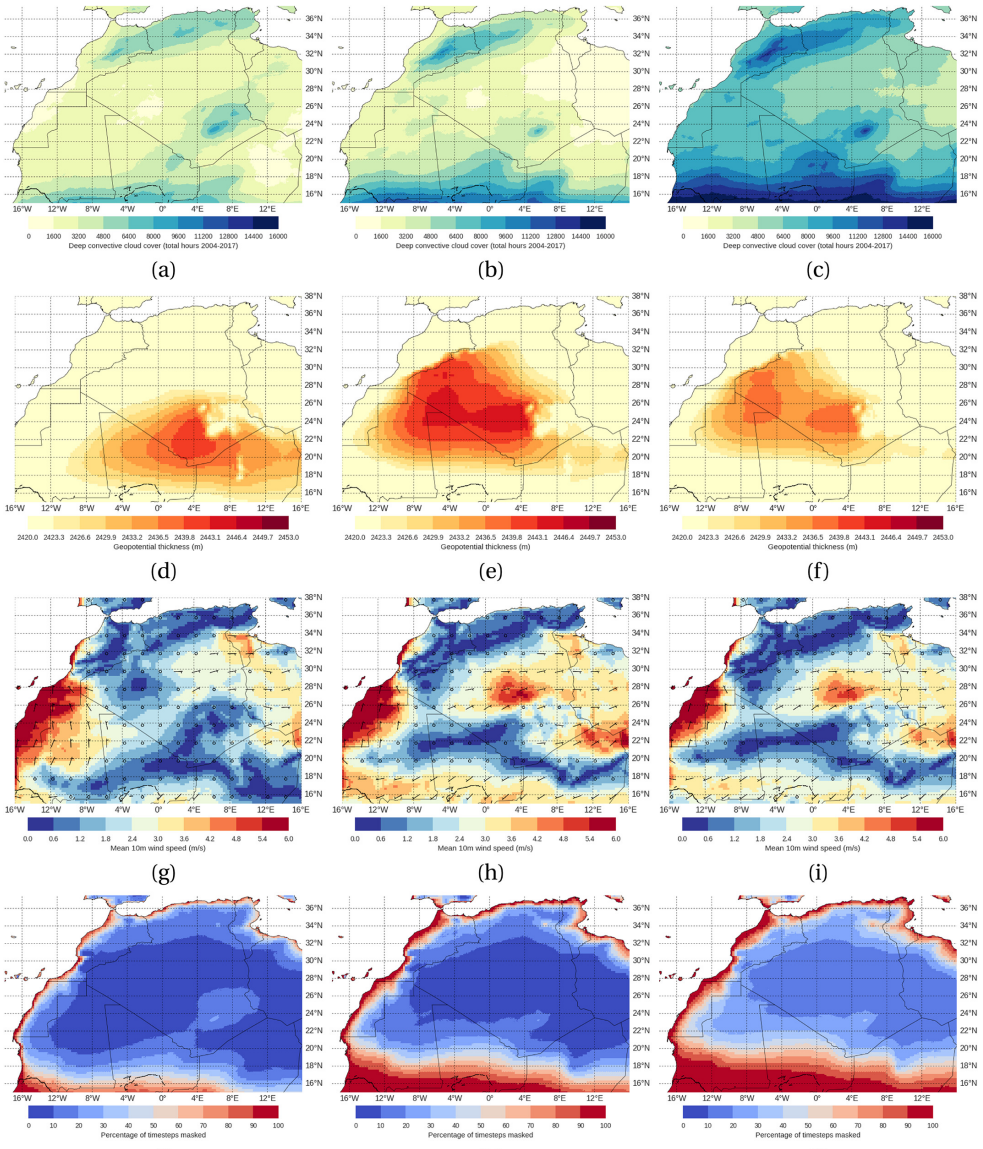


Figure 3.14: Controls upon observed CPO and LLJ-driven dust emission. Top row: total hours of deep convective cloud pixels in SEVIRI, defined where BT10.8 μm is under 230 K, for (a) June, (b) July and (c) August. Second row: position of the Saharan heat low calculated as the mean 925-700hPa geopotential thickness (metres) (following Lavaysse et al. (2009)) from ERA5 for (d) June, (e), July and (f) August. Third row: mean ERA5 10m wind speed for (g) June, (h) July and (i) August. Fourth row: the percentage of timesteps from 2004-2017 classified as masked (i.e. not visible for dust tracking) for (j) June, (k), July, (l) August.

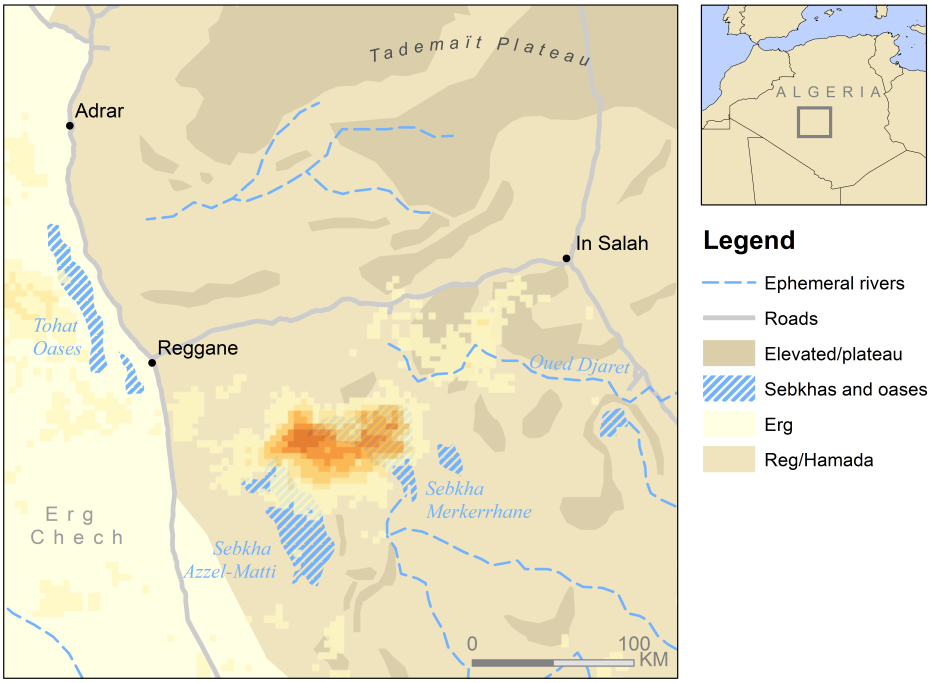


Figure 3.15: Map of the Tidihelt region identified as both a major dust source and LLJ hotspot. Dust source activation totals from Figure 3.4 are overlain in shades of orange. Features of interest are symbolised as shown in the key. Region location within Algeria is shown in the top right.

likely LLJ enhancement derived by Heinold et al. (2015) suggests that the surface roughness in this region may be particularly conducive to ageostrophic winds and hence high amplitude inertial oscillation. Although plumes identified as CPOs are active, dust source activation in the Tidihelt is almost entirely associated with LLJs propagating southwestwards in the dry Harmattan (Figure 3.16). The lack of further LLJ hotspots to the southwest also suggests that the LLJ signal many hundreds of kilometres downstream of the Tidihelt observed in Figure 3.12a is largely a result of transported events rather than fresh emission. Tidihelt LLJs are therefore highly effective at contributing to long-range transport by the Harmattan, which is important for the production of a Saharan air layer over the Atlantic (Bou Karam et al. 2008; Schwendike et al. 2016). A further study will explore drivers of LLJ activity within the Tidihelt region in more detail.

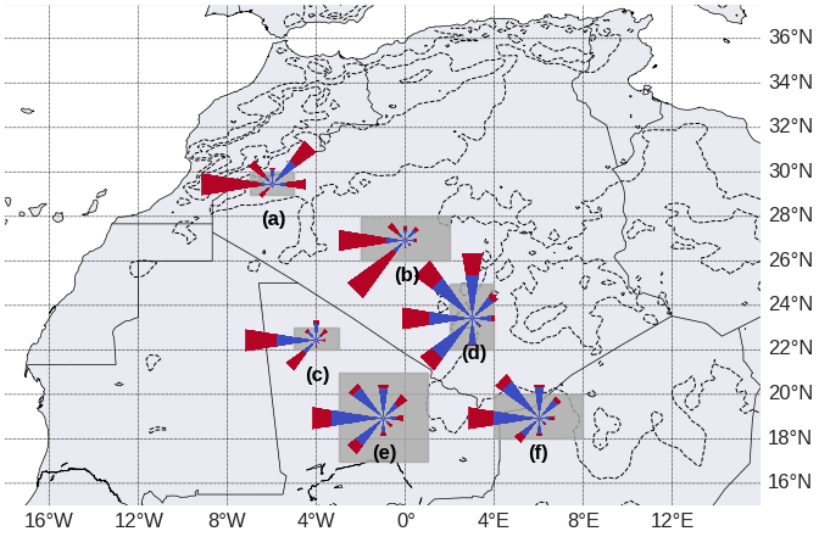


Figure 3.16: Preferred propagation directions of plumes at selected dust sources. Wind rose segments indicate the percentage frequency of a direction in which plumes are travelling (i.e. a segment pointing west indicates plumes travelling west). The red component of the segment indicates the proportion of events associated with LLJs, while the blue represents CPO events. Propagation direction is calculated from the difference between the centroid of the plume in its first timestep and its last. Grey boxes represent the region from which plumes were sampled for each wind rose. Sample regions include (a) Lake Iriki, (b) Tidihelt Depression, (c) Taoudenni region, (d) Tamanrasset region, (e) Adrar des Ifoghas region and (f) Vallée de l'Azaouagh. Dashed black contours indicate orography at 500m intervals

An additional LLJ hotspot is found along the border of Mali and Morocco, in the dust source identified by Ashpole and Washington (2013a) as Lake Iriki (30°N, 6°W). This is a much less active dust source than the Tidihelt (Figure 3.4), but the preferred direction for plumes here is westward (Figure 3.16), indicating a possible local constraint on plume propagation. Other sources with greater CPO activity (e.g source (d) in Figure 3.16) have a more even distribution of preferred plume directions, except that plumes seldom travel southeastwards. Although LLJ hotspots have preferred directions, LLJs on the whole are not unique to one particular wind regime; as found in Allen et al. (2013), they may be embedded in both dry northeasterly and moister southerly or southwesterly flow.

The results shown in this section demonstrate that while CPO-emitted dust is widespread across the central Saharan dust sources, LLJs dominate in a small selection of hotspots. Most of the observed pattern of summertime dust as observed using SEVIRI is not, therefore, attributable to LLJ activity. Nevertheless, as suggested in Section 3.5, LLJs may be important for short-lived plumes which go undetected by the SDF scheme, and they play a very large role in one of the desert's single most frequently activated source regions. Accurate representation of LLJ emission of dust therefore relies upon an understanding of local surface and orographic conditions and how they influence inertial oscillation. Although LLJs are typically represented in most wind fields used to drive offline dust models, a more meticulous analysis of the erosive conditions in a small set of highly concentrated LLJ-dominated source regions is needed. By contrast, CPOs are not explicitly simulated in most models and represented typically via convective parameterization schemes, and therefore contribute to moisture transport errors (Garcia-Carreras et al. 2013). The overwhelming significance of CPO dust found in this analysis is in agreement with in situ observations (Allen et al. 2013) and confirms the strong link between WAM dynamics and uplift of dust during the boreal summer emission maximum.

3.7 Summary and conclusions

Automatically tracked dust plumes emitted during boreal summer for the period 2004-2017 have been probabilistically categorised as either LLJ or CPO emissions. To support this approach, an improved method to track dust with SEVIRI dust flags has been developed. The new dust tracking scheme is better at accurately detecting dust emission time and fewer aged plumes are incorrectly classified as freshly emitted due to flickering or weak nocturnal detection. Three quantifiable characteristics were identified which can be used to classify plumes: the timing of emission, the distance from deep convection at the point of emission and the orientation relative to the direction of propagation. Combining each of these into a multiple regression model yields an accurate method of partitioning

satellite-observed dust by mechanism. This classification scheme improves upon approaches based entirely upon the timing of plumes. Short-lived plumes from LLJs are likely to be underestimated, however, as the thresholding approach relies upon plumes being lofted high enough to be thermally distinct from the surface.

CPO activity is found to dominate the dust signal overall, accounting for 81.6% of the dust-flagged pixels. This may be a slight overestimate, however, as a manual analysis of a sample of the data revealed that 4.4% of dust pixels were associated with possible cold surge events, and these are likely to have been classified as CPOs by the automated system. Dust from cold pools is organised into a dipole pattern which evolves from a preference for the triple point of Mali-Niger-Algeria in June towards higher activity further north along the Algerian border with Mali later in the season. A similar northward shift is observed for LLJs. However, diminished activity along the fringe of the Sahel later during the monsoon season is likely also a result of bias introduced by advancing cloud from the onset of the WAM. LLJ dust is organised along a northeasterly channel originating between the Hoggar and Atlas ranges. Partitioning of mechanisms at the point of emission reveals that while the bulk of emission from sources along the foothills of the Hoggar range, around Adrar des Ifoghas and within northern Niger are due to cold pool activity, LLJs are extremely important in the Tidihelt Depression of central Algeria. This indicates that while cold pools have the widest reach in activation of the CWS, LLJs are responsible for one of the single most frequently activated source regions.

The dataset derived in this study for the central Sahara is a useful means of linking variability in Saharan dust back to atmospheric controls of the emission processes at source. Furthermore, its application to a very large sample of satellite imagery offers a robust climatological perspective, which confirms the central role of deep convective processes for emissions in the world's largest boreal summer dust source. These findings underscore the need for dust models to be driven with meteorological datasets capable of resolving both deep convection

and cold pools. Most current generation reanalysis products fall short of this, however. It follows that an improved understanding of the controls on cold pool outflow and low-level jet variability through summer will be essential as the next generation of driving datasets are developed and validated.

3.8 Acknowledgements

MSG SEVIRI data are available online from the EUMETSAT Data Centre (`https://navigator.eumetsat.int/product/EO:EUM:DAT:MSG:HRSEVIRI`). AWS data were obtained during the Natural Environment Research Council (NERC) Fennec field campaign (Grant NE/G017166/1), with thanks to those who installed and maintained the instrumentation, including the Algerian and Mauritanian Meteorological Offices. Fennec data are available from the Centre for Environmental Data Analysis (`http://archive.ceda.ac.uk/`). ERA5 data is maintained by the European Centre for Medium-Range Weather Forecasts and is available from the Copernicus Climate Change Service (`https://climate.copernicus.eu/climate-reanalysis`). TCH is funded through the NERC doctoral training partnership (NE/L002612/1). RW was partly supported by the NERC-Department for International Development (DFID)-funded Improving Model Processes for African Climate (IMPALA) project (Grant NE/M017206/1), as part of the Future Climate for Africa (FCFA) program (`http://futureclimateafrica.org/project/impala/`). We would like to thank Ian Ashpole for his assistance with the use of SEVIRI dust flags, as well as three anonymous reviewers for their insightful comments.

4

Satellite-derived characteristics of Saharan cold pool outflows during boreal summer

Thomas Caton Harrison[1], Richard Washington[1] and Sebastian Engelstaedter[1]

[1]Climate Research Laboratory, Oxford University Centre for the Environment, Oxford, UK

Published online 29/12/2020

J. Geophys. Res. Atmos., 126(3), https://doi.org/10.1029/2020JD033387

Contents

4.1 Abstract 99
4.2 Introduction 100
4.2.1 Background 101
4.3 Automated tracking of cold pool outflow boundaries 104
4.3.1 Algorithm phase 1: candidate CPO masking 106
4.3.2 Algorithm phase 2: discarding false positive tracked CPOs 109
4.3.3 Estimating propagation speed and direction 111
4.4 Validation 115
4.5 Results and discussion 118
4.5.1 Characteristics of tracked CPOs 118
4.5.2 Seasonality of CPOs and comparison with dust emission 122
4.6 Summary and conclusions 131
4.7 Acknowledgements 133

4.1 Abstract

Cold pool outflows (CPOs) are thought to be the most significant meteorological mechanism of mineral dust emission from the world's largest source in the central and western Sahara in boreal summer. An absence of CPOs from numerical models and reanalyses used to simulate Saharan dust emission leads to considerable error in modelling of dust fluxes from the Sahara. As such, the role of CPOs in the observed variability of dust through the monsoon season remains unclear. To remedy these issues, an improved observational benchmark is needed. In this research, an automated approach to identify and track CPOs in dust imagery from the Spinning Enhanced Visible and Infrared Imager (SEVIRI) is derived. The approach is found to flag 74.2% of events identified manually (26/35). 1,559 events are tracked for June, July and August of 2004-2017. CPOs follow a clear diurnal cycle, peaking at 1700-1900 UTC. Propagation speeds decay exponentially through their lifetime, but on average speeds are 1.5 m/s higher at night. 22.5% of the observed events exceed a total travelled distance of 300 km, with an overwhelming preference for northwestwards propagation. Common across the southern central and western Sahara, CPO activity shifts north through summer in line with observed dust emission. The exception to this is the development of an intense hotspot of CPO activity in southern Algeria in August, which does not parallel any known late season outbreaks of dust. The results underline the importance of the southernmost Saharan dust sources, activated by frequent CPO occurrence in early summer.

4.2 Introduction

The central and western Sahara (CWS) is the world's most active dust-emitting region during boreal summer (Washington et al. 2003). Mineral aerosols play an important role in the Earth's radiation budget on climatic and meteorological timescales, as a source of nutrients and as a pollutant (Boucher et al. 2013). Surface observations and satellite retrievals from the CWS indicate that cold pool outflows (CPOs) from deep convection are the dominant summertime meteorological dust emission mechanism (Allen et al. 2013; Allen et al. 2015; Caton Harrison et al. 2019); Lidar observations from the core of the central Sahara in June 2011 show that two-thirds of emission events detected can be traced to this process (Allen et al. 2013). CPOs responsible for dust emission are often referred to as 'haboobs' (Sutton 1925).

CPOs are the result of mesoscale density currents formed from the latent heat exchange of evaporating precipitation in deep convective downdrafts. Hence, although they are hypothesised to be the dominant dust emission process in the world's largest source region, representation of this process is not surprisingly missing or poor in operational forecasting analyses (Sodemann et al. 2015; Redl et al. 2016; Pope et al. 2016; Trzeciak et al. 2017). They are also mostly unrepresented in coarse resolution global model simulations used for the Coupled Model Intercomparison Project (CMIP) which rely upon convective parameterization (Marsham et al. 2011; Knippertz and Todd 2012; Roberts et al. 2018), although some attempts have been made to parameterize the role of convective downdrafts (Lunt and Valdes 2002; Cakmur et al. 2004). Similarly, the resolution of all available reanalysis products, including ERA5 at around 30 km grid spacing (Hersbach and Dee 2016), is too coarse for inclusion of CPOs. The consequences are stark for dust simulation whether it is embedded in the global models we rely on for climate prediction or derived from offline emission models driven by reanalyses. Exclusion of this key process means that models either emit too little dust or else do so for the wrong reasons (Marsham et al.

2013a). Missing CPOs also lead to biases in moisture flux (Garcia-Carreras et al. 2013) which in turn have a large impact upon the simulated top of the atmosphere energy balance in the central Sahara (Marsham et al. 2016).

In the meantime bespoke numerical model simulations run at convection-permitting scales are able to simulate CPOs (Heinold et al. 2013) with efforts to parameterise the missing processes in mass-flux dependent coarser resolution models (Pantillon et al. 2015). To test these approaches and remedy model deficiencies, an improved observational benchmark is needed. However, direct observations of CPOs are only currently available from extremely sparsely distributed meteorological station data at point locations within the Sahara and Sahel. The characterisation of the frequency, diurnal cycle, intensity and distribution of CPOs across the CWS is critical to evaluating numerical model simulation of dust emission from the world's largest source regions.

4.2.1 Background

CPOs from mesoscale convective systems (MCSs) propagate often in the summer from the Sahel (Bou Karam et al. 2008; Marsham et al. 2008; Flamant et al. 2009a; Allen et al. 2013) and less frequently from the Atlas mountains (Knippertz et al. 2007) into the Sahara, especially during the peak of the West African Monsoon (WAM). CPOs are known also to play a part in sustaining convection as they travel north across the desert, lifting low-level airmasses above the considerable summertime convective inhibition (Roberts and Knippertz 2014; Trzeciak et al. 2017). CPOs appear to be the dominant meteorological mechanism of dust emission, but more attention has been devoted at the intraseasonal timescale to variability in synoptic drivers, including African Easterly Waves (Cuesta et al. 2009; Knippertz and Todd 2010; Grogan and Thorncroft 2019), the Saharan heat low (SHL) (Todd et al. 2013; Ryder et al. 2015), cold surges (Vizy and Cook 2009) and upper-level dynamics (Knippertz and Fink 2006; Roberts and Knippertz 2014). Although these processes are not usually directly

responsible for summertime emission, they are sufficiently large to be resolved in the datasets typically used to study them.

Drivers of CPO variability through summer are a subject of debate, as dust emissions appear to peak in June even though this marks only the beginning of the northward migration of the Intertropical Discontinuity (ITD) low-level convergence band (Engelstaedter and Washington 2007), with lower dust loadings during the parallel southward retreat in September (Marsham et al. 2008). It has been suggested that dry midtropospheric conditions during the early monsoon season could favour CPO development (Marsham et al. 2008), with a small number of observed cases supporting this (Provod et al. 2016). Other possible drivers of this summertime seasonality include suppression of Sahelian dust by rainfall (Engelstaedter and Washington 2007; Bergametti et al. 2016; Bergametti et al. 2017), masking of dust in satellite imagery (Williams 2008; Heinold et al. 2013) and the role of other emission mechanisms such as the nocturnal low-level jet (Fiedler et al. 2013; Allen and Washington 2014). Recent model-based research shows that the seasonality of dust uplift due to CPOs may differ between the Sahel and Sahara (Pantillon et al. 2016). Observations of cold pool occurrence through summer represent an important missing piece of evidence in this debate.

Observational research into Saharan cold pools makes considerable use of satellite imagery to support detection from in situ observations. This is in part because CPOs do not have a unique signature at the surface (Allen et al. 2013; Hobby et al. 2013), but they do exhibit consistent spatial characteristics in remotely sensed imagery due to an evolving dust arc originating from nearby convective cloud. For instance, Redl et al. (2015) develop an objective scheme for CPO identification by combining in situ surface observations with microwave satellite data. More common is the use of data from the Spinning Enhanced Visible and Infrared Imager (SEVIRI) above the Meteosat Second Generation (MSG) series of satellites. Allen et al. (2013) and Allen et al. (2015) identify CPO passage at Bordj-Badji Mokhtar in southern Algeria (within a region of key dust

sources) based upon sharp step-changes observed in 10m wind speeds when they exceed local emission thresholds in conjunction with nearby convective cloud detected in SEVIRI data. Imagery from this satellite has also been deployed by Provod et al. (2016) to detect deep convective cloud over Niger, confirm the presence of CPOs and distinguish individual storm clouds from mesoscale convective systems (MCSs). Manual tracking of individual CPO events in SEVIRI has been used to explain the largest dust emission events (Schepanski et al. 2007; Karam et al. 2014) and moisture transport through the Sahara (Flamant et al. 2009a; Trzeciak et al. 2017). The 15-minute temporal resolution of SEVIRI data makes it well suited for the study of mesoscale dust-emitting processes which operate on a timescale of hours.

In this study, an automated method is derived for the first time to delineate and calculate the propagation speed of outflow boundaries associated with cold pools observable in SEVIRI imagery by virtue of lofted dust at their leading edge. This is used to generate the first dataset of cold pool occurrence across dust-emitting regions of the CWS. As dust emission from the Sahara is highly variable from year to year (Prospero and Lamb 2003; Mahowald et al. 2010; Tegen et al. 2013; Wagner et al. 2016), we use a large SEVIRI dataset covering June, July and August of 2004-2017. A previous study (Caton Harrison et al. 2019) made use of the same satellite dataset to infer whether observed dust plumes could be linked to CPO activity. Whereas Caton Harrison et al. (2019) aimed to account for all SEVIRI-observed dust, the focus of this paper is a subset of these plumes which can be found at the leading edge of CPO density currents and which therefore render the CPO density current itself visible to satellite. By contrast, a majority of plumes in Caton Harrison et al. (2019) had either no clear outflow boundary or persisted in the atmosphere long after this sharp boundary had dissipated. In summary, this paper aims to:

1. Derive an automated method for identifying and tracking Saharan CPOs in SEVIRI imagery;

2. Characterise the diurnal cycle, propagation speed, direction of travel and distribution of CPOs;

3. Relate patterns of CPO activity through boreal summer to the seasonality of Saharan dust.

Section 4.3 is devoted to the data and methodology used to detect and track CPOs, with the approach validated in Section 4.4. A dataset of events is presented and linked to dust emission in 4.5.

4.3 Automated tracking of cold pool outflow boundaries

The first step in automated CPO tracking is to identify accurately an advancing haboob from satellite. CPOs achieve their distinctive appearance in SEVIRI false colour pink dust composites owing to sharp boundaries induced at their leading edges, with a gradient towards more purple colours in the wake of the outflow boundary as a result of the difference in moisture and dust content between the two airmasses (Flamant et al. 2007; Flamant et al. 2009a). An example of this is shown in Figure 4.1a. Brightness temperature difference (BTD) fields have been used in the past to pinpoint dust in this type of imagery (Ashpole and Washington 2012; Bachl et al. 2012; Liu et al. 2012; Murray et al. 2016). One such field is the difference between the 10.8 and 8.7 μm channels; both regions of dust and rocky desert surfaces exhibit higher emissivity at 8.7 μm (Banks et al. 2018), but the latter may be subtracted by calculating a BTD anomaly field relative to a 15-day moving window (Figure 4.1b) as in Ashpole and Washington (2012). It follows that the regions of the image undergoing the most rapid changes in BTD are the most likely to be situated in regions of sharp environmental change such as the abrupt gradients at the leading edge of passing density currents. It is important to note that the methodology in this paper is not geared towards observing and tracking all dust plumes as in Ashpole and Washington (2013a) or Caton Harrison et al. (2019). Instead, we focus specifically upon the leading edge

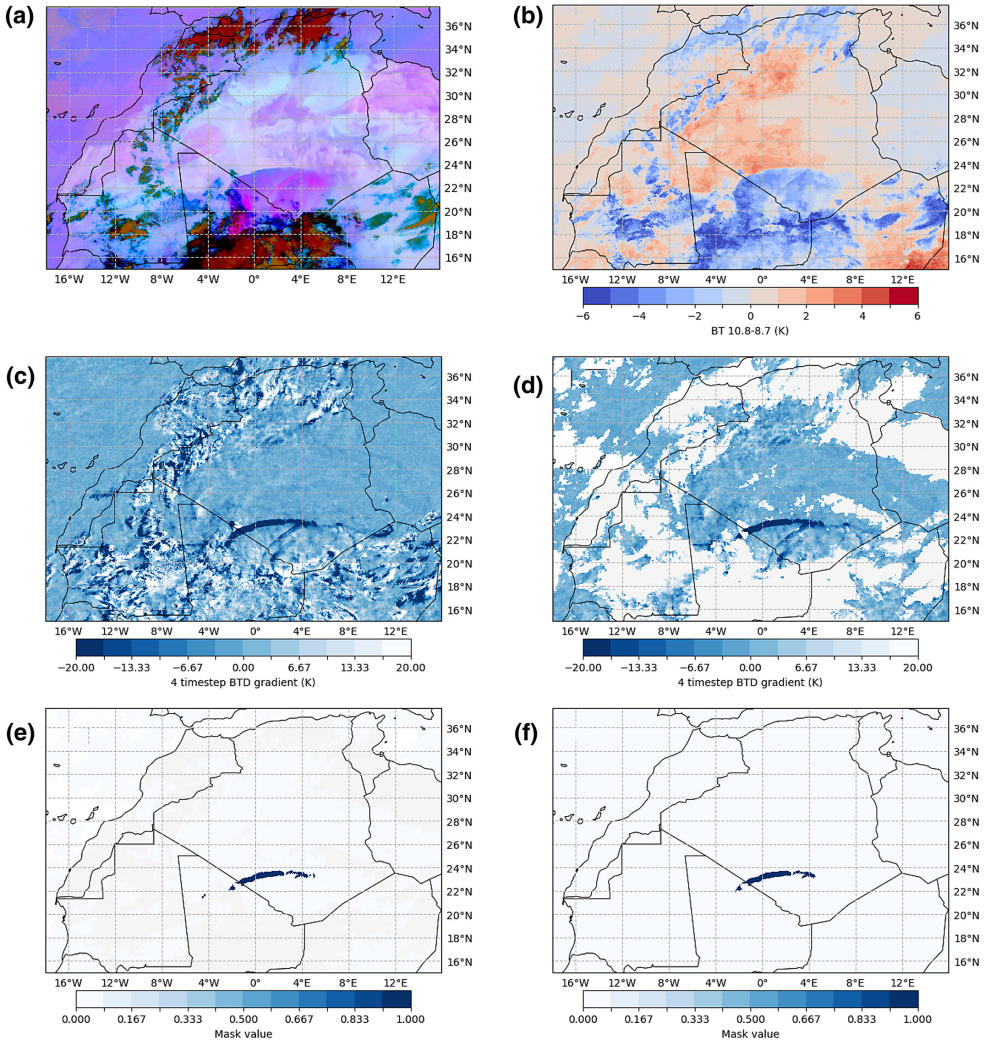


Figure 4.1: (a) Original SEVIRI pink dust composite from 0115 UTC 10th of July 2011. (b) Difference (K) in the 10.8 and 8.7 μm brightness temperature channels, taken as an anomaly relative to a 15-day moving window. (c) The sum of the differences between the BTD field shown in (b) and that of each of the previous three timesteps, described in Figure 4.2 third blue panel from the top. (d) Cloud masking applied. (e) Only regions where the values of (c) are under -20 K and contain at least one pixel with a value under -30 K (with a total pixel cluster size over 20). (f) Final tracked CPO after events not meeting the tracking conditions (red boxes in Figure 4.2 are discarded.

of CPOs which are uniquely observable in the CWS thanks to an abundance of erodible material. Hence, our aim is to extract information about the density currents marked by dust rather than all dust plumes identifiable in SEVIRI.

Figure 4.2 provides an overview of the detection scheme adopted in this paper. The algorithm operates in two overarching phases. In the first phase, imagery is

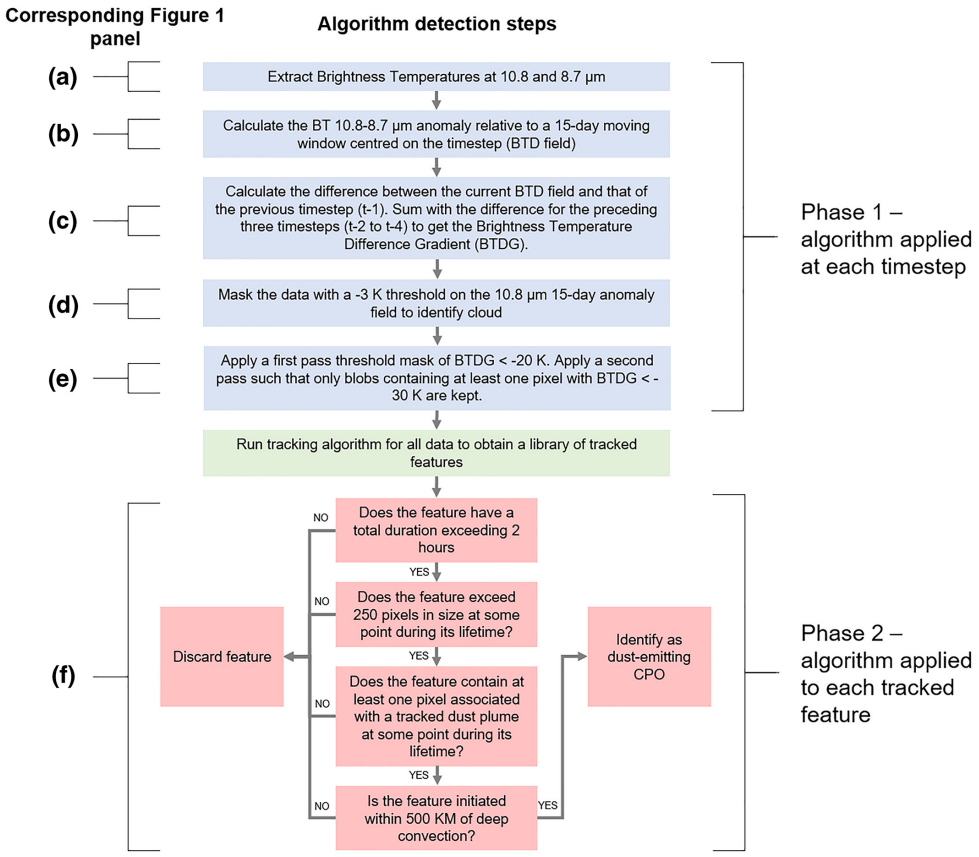


Figure 4.2: Flow chart showing steps involved in the CPO detection algorithm. Boxes shaded in blue represent the initial detection phase applied to each timestep of raw SEVIRI data, corresponding to panels in Figure 4.1. The output from this is run through the tracking algorithm (green box) and conditions are applied to the tracked features to determine which events are retained or discarded (red boxes).

processed to extract the 10.8-8.7 μm anomaly field, a persistence-based temporal gradient is applied and a mask is used to delineate candidate CPO features. In the second phase, these features are tracked as objects; those with a low duration and peak size are discarded, as well as events with no association with deep convection or to any dust pixels.

4.3.1 Algorithm phase 1: candidate CPO masking

A first step is to identify regions with rapidly changing BTD. To achieve this, the sum of the differences between the BTD anomaly of the image being analysed and each of the previous four images (i.e. one hour) is taken. The use of a sum over four images identifies pixels at which a brightness temperature gradient is

not only induced but also maintained, hence an image with a brief appearance of cloud may produce a large difference in BTD relative to each of the previous three images, but in the following image cancellation of this difference will occur if the cloud is not sustained. By contrast, an outflow boundary will produce the same response as a cloud, but in the following image a signal will also be present in its trail, albeit weakened, due to the sustained change in environmental conditions. The gradient of BTD calculated over four 15-minute intervals (one hour) is referred to henceforth as the BTD Gradient (BTDG). The CPO boundary is clearly defined at this point (Figure 4.1c), but also a myriad of other features at the edges of prominent clouds.

Clouds are identified and subtracted in this paper as in Ashpole and Washington (2012), using the BT 10.8 μm channel. In order to bypass the effect of varied cloud-top radiance through the day upon masking, the anomaly of the 10.8 μm channel relative to a 15-day moving window average for the given time of day is taken, as for BTDs. Pixels with a BT 10.8 μm anomaly of less than -3 K are masked as cloud (Figure 4.1d). The EUMETSAT cloud mask product was also tested, but not used as it falsely identifies lofted dust as cloud, masking a large number of CPO events.

To identify and delineate unique objects, a threshold-based mask is applied to the BTDG field which categorises each pixel within the scene for a given timestep as 'CPO' or 'No CPO'. Unlike in a model-based approach (Heinold et al. 2013; Pantillon et al. 2016), there is no physical basis for selecting a particular value of BTDG as the threshold, so an empirical approach is adopted to applying the correct mask.

To test for an optimal threshold to apply to the imagery, a training period is used. A very generous starting threshold of BTDG $\leq$ -10 K was applied to all data from July 2010, and the resultant features were tracked. Each of the

2,976 images for the month was analysed manually to identify genuine CPO features according to the following conditions:

1. The feature is not an artefact from the presence of cloud;

2. Deep convective cloud is present upstream of the feature (within approximately 500 kilometres);

3. A sharp frontal boundary in lofted dust and low-level moisture is present;

4. The feature was recently generated (i.e. not an aged dust plume with a sharp edge).

The corresponding automatically tracked features from the training dataset were then identified. All events generated for the training dataset which did not fulfil the conditions described above were classified as false alarms. BTDG values for both true and false events were then compared to determine an appropriate threshold to distinguish the two.

A distinction between genuine and false alarm CPOs becomes clear below a BTDG around -30 K (Figure 4.3a). This value is selected as the basic threshold for CPO detection. Two issues remain, however: firstly, a large number of true CPOs have BTDG values above -30 K. Secondly, false alarms are still common even below -30 K. To address the first issue, a 'second pass' threshold of BTDG $\leq$ -20 K is applied, which allows all pixels passing this threshold to be accepted as long as they are connected to an existing feature of BTDG $\leq$ -30 K values. With these two masks applied, the clear CPO in Figure 4.1e is successfully delineated. To address the second issue, however, an additional set of identification criteria is needed.

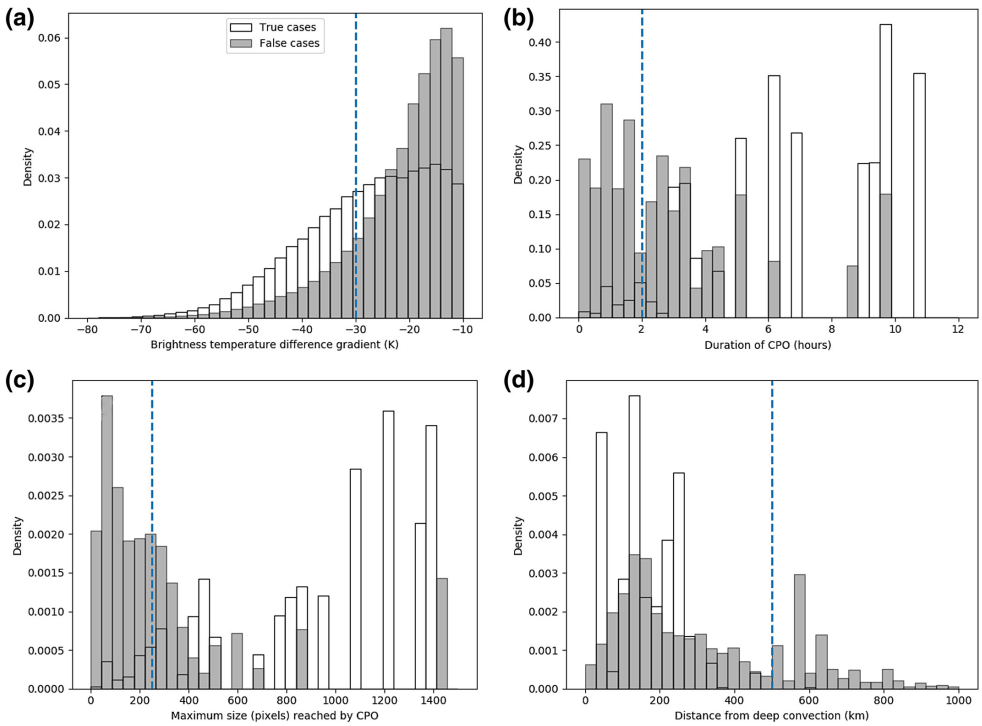


Figure 4.3: Probability density functions of (a) brightness temperature difference gradient (K), (b) CPO duration (hours), (c) maximum pixel size reached by events during their lifetime and (d) distance from deep convection for true (white) and false (dark grey) events tracked manually through July 2010. Each pixel of an event (true or false) counts as one sample in the distribution. Blue dashed vertical lines indicate the thresholds chosen for the CPO detection algorithm.

4.3.2 Algorithm phase 2: discarding false positive tracked CPOs

In order to further reduce false alarms (for example seen in Figure 4.1e near 22°N, 4°W), events are discarded according to characteristics calculated across their entire lifetime. Genuine events are commonly found to exhibit much longer durations (Figure 4.3b), whereas false events cluster under the 2 hour mark and none exceed 10 hours. We therefore apply a minimum duration of 2 hours to the detection scheme. 3.6% of true pixels and 42.5% of false pixels are below this threshold. A second factor is the maximum size individual events reach during their lifetime, as measured by the number of pixels belonging to a feature. Most true CPOs exceed 250 pixels at some point during their lifetime (Figure 4.3c), so this is also used as a cutoff. 6.6% of true pixels and 60.7% of false pixels are below this threshold. Third, CPOs whose centroids were more than 500 km

from deep convection (identified here where BT 10.8 μm has a value less than 250 K) at the point of generation are excluded (Figure 4.3d). For this criterion, only 0.4% of true pixels are above the 500 km threshold, whereas 30.2% of false pixels are. Finally, CPOs may only be detected if they are also associated with a dust-flagged (following Ashpole and Washington (2012)) pixel at some point in their lifetime. This final condition reduces the hit rate from 82% to 80% but crucially decreases the false alarm rate from 13.8% to 5.2%. The result of these conditions in the case of Figure 4.1f is an isolated CPO feature.

A value of 250 K is on the warm end of thresholds for detection of convective cloud, especially when looking for mature systems for which 215-225 K may be used (Bedka et al. 2010; Bedka and Khlopenkov 2016). Table 1 in Bain et al. (2010b) gives a range of IR thresholds used for detection of convective cloud. Warmer thresholds have been used to detect deep convection over West Africa, including 270 K in Lavaysse et al. (2009) and Ashpole and Washington (2012). 270 K was tested but found to be too generous, flagging regions of thin cirrus and thick mid-level clouds. On the other hand, stricter thresholds such as 230 K were too stringent, flagging only the deepest systems and missing warmer cloud tops near developing CPOs.

Several caveats limit the usage of this algorithm. First, at a fundamental level, the method relies upon the appearance of clear boundaries in low-level dust indicating the presence of a cold pool outflow boundary. Hence, as with all dust detection (Brindley et al. 2012), an atmosphere with high column water vapour already is likely to obscure outflow boundaries. Second, as with many other forms of remote sensing, cloud cover is also a factor which hinders observation. For the purposes of this paper, this means that only the strongest CPOs which become spatially separate from their generative convection are observed. The algorithm as a whole is constrained by the need to minimise false alarms, hence it is not suited for detection of small, brief ($<$ 2 hours) events and misses weaker events which could be detected manually. The accuracy of the algorithm is quantified further

in Section 4.4. Nevertheless, the major strength of this automated approach is its capacity to cover a long period of data with an entirely reproducible approach.

4.3.3 Estimating propagation speed and direction

One of the defining features of an outflow boundary observed from space is its organisation along a semi-ellipse-like axis elongated perpendicular to its direction of propagation (Caton Harrison et al. 2019). Detected outflow boundaries are expected to adhere to a certain shape throughout their lifetime, consisting of radial expansion away from convective cloud with a clearly defined leading edge. Radial spreading of downdraft mass has been used as a conceptual framework for parameterized CPOs in the Met Office Unified Model (Pantillon et al. 2015). Seen from the top down without vertical information, an even simpler approach can be used to track the speed of satellite-observed CPOs.

Speed-tracking is achieved here by fitting CPOs identified with the technique in Sections 4.3.1 and 4.3.2 to a simple 2D top-down model of an idealised propagating outflow boundary (Figure 4.4). In this model, the direction of the CPO is perpendicular to its orientation and the speed is calculated by taking the distance between the leading edge of detected features at consecutive 15-minute timesteps. CPO propagation direction here refers to the direction of the flow induced by its radial expansion, and not the bulk translation of the entire system by background winds (i.e. advection), which is assumed not to play a major role. As a simple test of this assumption, each event from the July 2011 validation dataset (Section 4.4) was checked manually. Two cases (on the 10th and 15th July) were found where the propagating outflow boundary was so long-lived that it veered slightly towards the north/northeast, likely due to low-level monsoon southwesterlies, but this small shift was within the 30 degree tolerance described below. All of the other 33 events exhibited little to no change in direction during the period for which they were tracked.

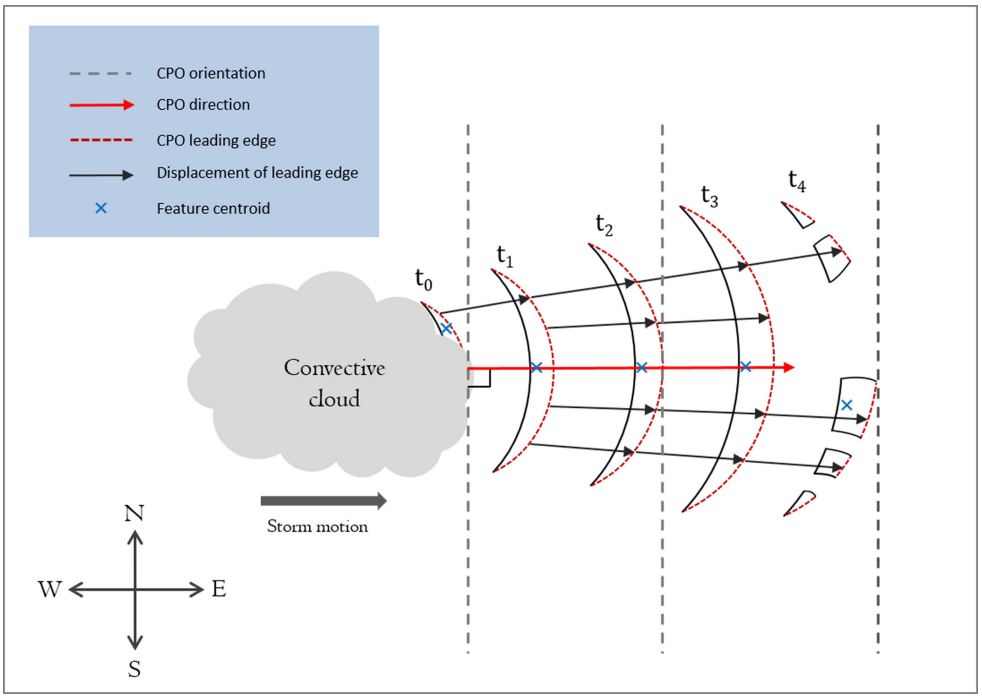


Figure 4.4: Top-down (bird's eye view) 2D model of a CPO event observed by satellite. Arcs propagating eastwards from a convective cloud represent the progress through time of the outflow boundary. The orientation of the CPO (dashed grey vertical lines) is fixed, and its direction (red horizontal arrow) is perpendicular to its orientation. Red dotted lines represent the leading edge of the advancing outflow boundary while black solid lines represent the trailing edge. Black arrows represent the displacement of this leading edge from t_{n-1} to t_n. The event is first observable at t_0, (although obscured by cloud) and last observable at t_4 (although the feature has disintegrated into separate entities). Blue crosses indicate the feature centroid.

This approach is simplistic and assumes background winds do not significantly modify the direction of CPO travel. However, its main advantage is that it overcomes the issue of variable signal strength when detecting features from satellite. At the beginning of an event's lifetime (shown as t_0 in Figure 4.4), only a small proportion of the event's true size is visible to a satellite. This is in part because the BTDG gradient has not reached its peak yet when measured across several timesteps, but also because cloud obscures the signal as the CPO emerges from below. Furthermore, towards the end of the CPO's lifetime (shown as t_4 in Figure 4.4), the feature's total area tends to diminish as the signal weakens. Hence, if the more flexible approach of tracking feature centroids (marked as blue crosses in Figure 4.4) had been used in isolation, the position

of the CPO through time would have been observed to evolve erratically as parts of the CPO became obscured.

Two key ingredients are needed to calculate propagation speed from this model. First, a direction of propagation is needed in order to identify the leading edge of the CPO. Second, displacement vectors are needed between consecutive leading edges. As this model assumes that CPOs propagate in a direction perpendicular to their orientation, the direction of travel can be obtained from the orientation of a CPO. This orientation is in turn calculated from the timestep with the largest number of detected pixels, comprising the most complete view of the CPO (highlighted in white in Figure 4.5).

The pixels which are furthest along the axis of the approximated direction of travel are assigned as the leading edge of the CPO, shown as red dots in Figures 4.4 and 4.5. Finally, leading edge pixels are matched between consecutive timesteps to obtain displacement vectors (shown as black arrows in Figures 4.4 and 4.5); pixels are matched if they are nearest neighbours and if the angle between them does not differ from the CPO propagation direction by more than 30°. A displacement vector is only calculated when a pixel has a match. The final speed value for a given timestep is calculated from the mean of all displacement vectors for that timestep. CPOs which appear to regularly switch direction are discarded as unreliable, here defined as events for which under 90% of timesteps have a centroid direction within 30° of the CPO propagation direction calculated from its orientation.

This rigid 2D model fitting approach is effective for estimating propagation speeds as many samples are collected for each CPO event; CPOs may be travelling at a slightly different speed in different regions along its leading edge (for instance due to surface roughness), but as samples are taken across its entire width the final mean value is representative. Furthermore, it is robust to periods in the CPO lifetime when detection is poor as it assumes a fixed direction and orientation.

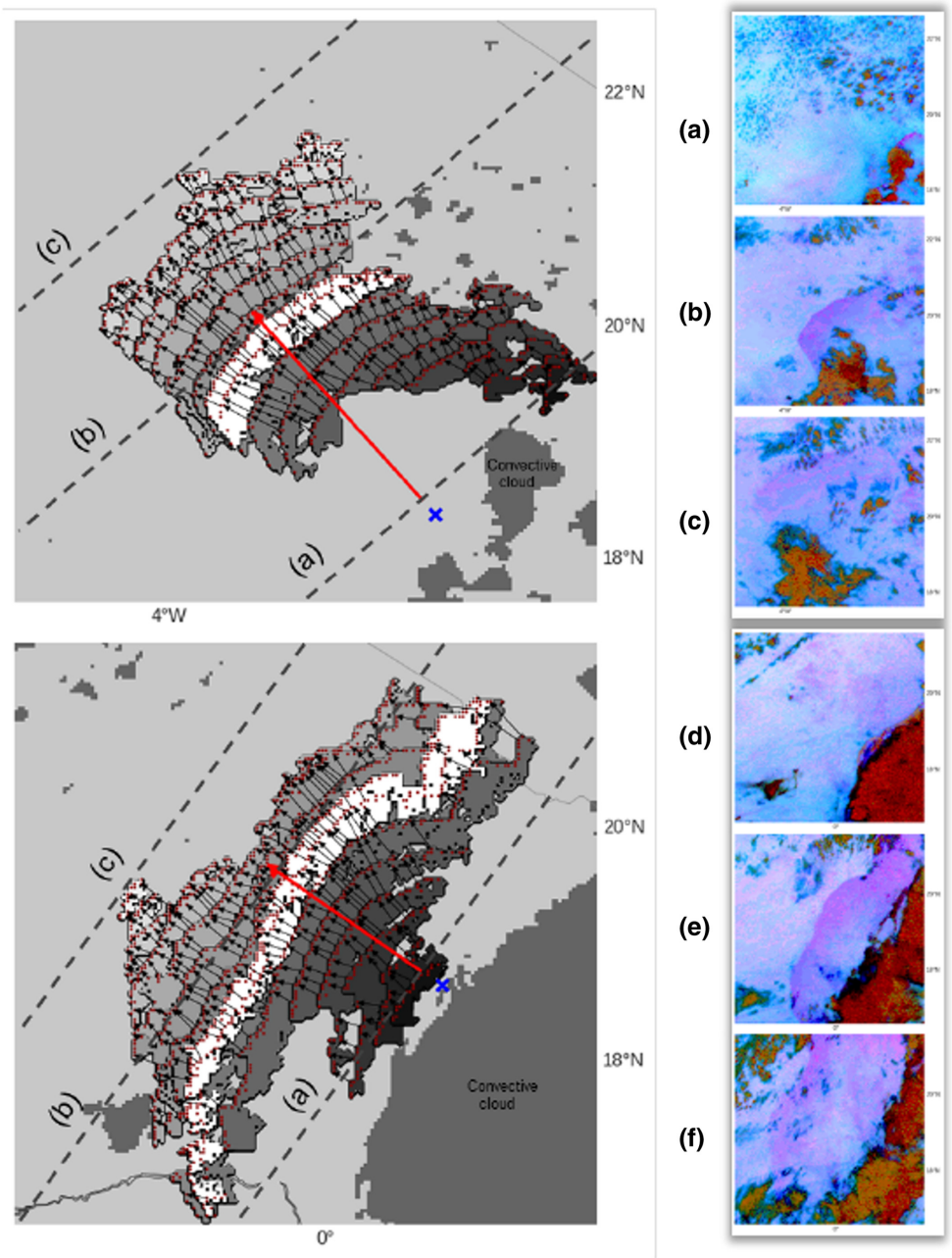


Figure 4.5: Results of algorithm used to calculate CPO propagation speeds, demonstrated for two CPOs lasting 8 hours and 30 minutes from 15:30 on 09/07/2010 (upper) and 6 hours and 30 minutes from 18:30 on 28/07/2004 (lower), with pink dust imagery shown for (a) the first timestep, (b) the timestep with the most pixels and (c) the final timestep. Every second timestep of the CPO's lifetime is overlain, from the earliest (darkest greys) to the latest (lightest greys). The timestep corresponding to (b) is shaded in white. Dashed grey lines show the orientation of this timestep, from which the CPO direction (red arrow) was calculated. Also shown is the leading edge of each timestep (red pixels) used to obtain propagation speeds (vectors marked as black arrows). A blue cross is marked as an estimate of the origin of the CPO, used for CPO composites in Figure 4.9.

4.4 Validation

Cold pool outflow boundaries detected automatically by the algorithm developed in Section 4.3 are intended to map onto those identified by the manual observer. We adopt two validation criteria:

1. Consistency with manual observations from SEVIRI;

2. A clear signal in surface observations.

As the parameters of the detection algorithm were tuned to data obtained from July 2010, a separate period (July 2011) is used to validate the method and determine its accuracy for criterion 1.

Examples of the algorithm masking pink dust imagery (Figure 4.6) show that outflow boundaries are successfully detected in proximity to deep convection in the Sahel and Sahara, typically with dust trailing behind. Some curvature of the feature is evident in each case. In some instances (Figure 4.6c and 4.6e), parts of the outflow boundary are either masked by arcus cloud or the gradient at the leading edge is too low. The algorithm appears to be capable of distinguishing between genuine outflow boundaries and the edges of cloud features, aged dust or nocturnal low-level jet dust.

35 events in total were identified manually from July 2011, with 26 identified by the automated scheme, indicating a 74.2% hit rate. Only 6.8% of the total pixels flagged by the automated CPO tracking scheme could not be assigned to a genuine event visible to the manual observer. Hence, although certain events are missed the false alarm rate is low.

To address criterion 2, a comparison between Fennec automatic weather stations (AWS) (Hobby et al. 2013) and automatically identified CPOs is made and provides strong evidence that events identified with this method correspond to phenomena observable at ground level. Here, days within the AWS dataset

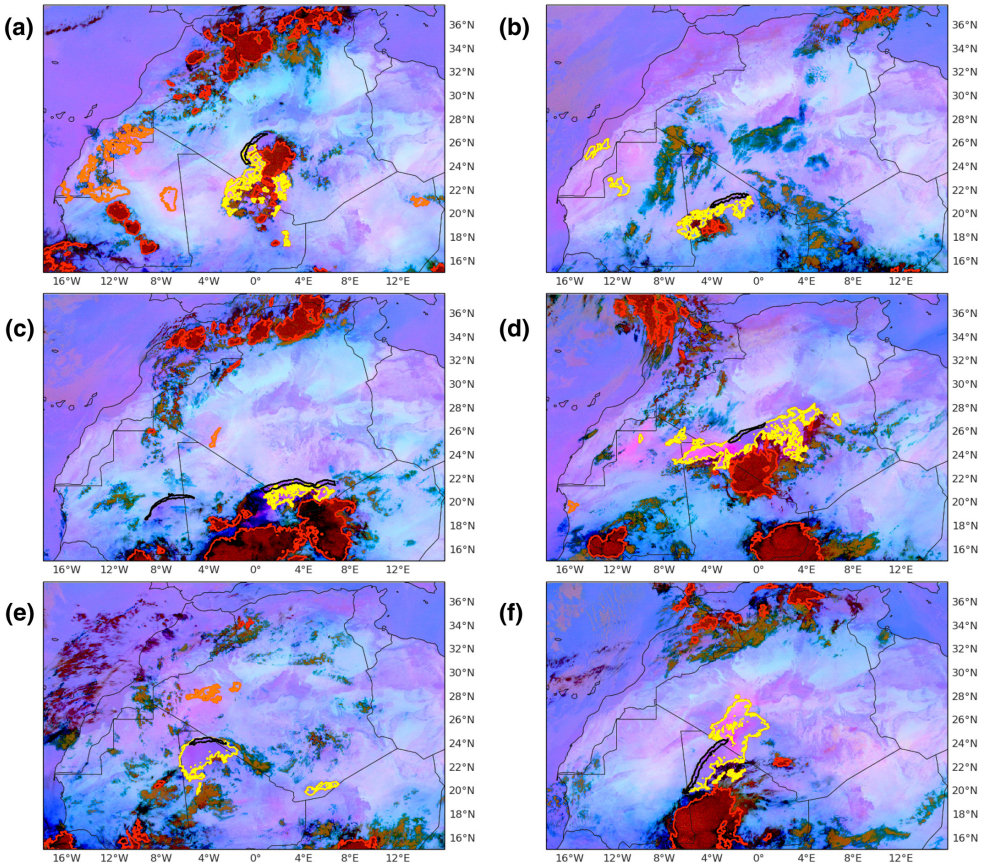


Figure 4.6: Examples from 2011 of automatically detected CPO outflow boundaries relative to other dust and deep convective cloud features in SEVIRI pink dust imagery. Contoured features include outflow boundaries (black), deep convective cloud (red), dust emitted due to CPO activity (yellow) and dust emitted due to nocturnal low-level jet activity (orange), distinguished with the method described in Caton Harrison et al. (2019). Times shown include (a) 20:00 UTC on 21/06/2011, (b) 01:00 UTC on 05/07/2011, (c) 20:45 UTC on 09/07/2011, (d) 04:45 UTC on 01/08/2011, (e) 04:00 UTC on 09/08/2011 and (f) 05:15 UTC on 29/08/2011.

for 2011 and 2012 are flagged where an automatically identified CPO boundary passes within 1 decimal degree of latitude or longitude (about 111 km) of the station. Each individual case is then reviewed with manual analysis of SEVIRI imagery to check that the outflow boundary did indeed pass over the station.

Meteorological variables used to detect the passage of a CPO from AWS data include sharp changes in wind direction, pressure, gustiness and temperature (Engerer et al. 2008; Emmel et al. 2010; Provod et al. 2016) as well as dewpoint temperature and mean wind speed (Allen et al. 2013; Redl et al. 2015). However,

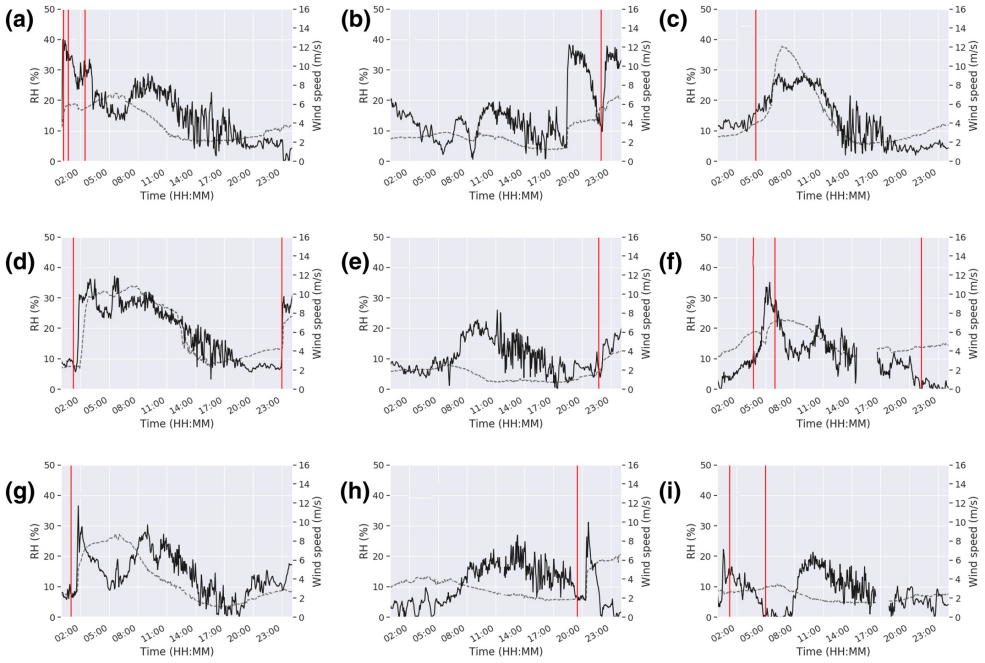


Figure 4.7: Examples of passages of automatically detected cold pool outflow boundaries compared with contemporaneous measurements of surface wind speed (solid black line) and relative humidity (dashed grey line) from the Fennec automatic weather station network. The closest passage of the detected cold pool outflow is marked with a vertical red line. Events shown are those observed at AWS 134 and 138 as these had the most complete set of measurements, including (a) 21/06/2011 (138), (b) 21/06/2011 (134), (c) 05/07/2011 (134), (d) 10/07/2011 (134), (e) 14/07/2011 (134), (f) 23/06/2012 (138), (g) 27/06/2012 (134), (h) 05/07/2012 (138) and (i) 26/07/2012 (138).

observations from the CWS show that passing CPOs do not always induce temperature, moisture or pressure changes but that wind speed jumps of at least 3/ms are a robust criterion (Allen et al. 2015). By this metric, of the 23 SEVIRI-detected CPO events occurring near the AWS network, 17 exhibit a signal within the AWS data. A selection of examples is shown in Figure 4.7. Although a response in both wind speed and humidity is present in almost every case, the magnitude and rapidity of the change induced varies considerably, with some events (e.g. Figures 4.7a and 4.7b) exhibiting small jumps in humidity in spite of large changes in wind speed, while others (e.g. Figures 4.7d and 4.7g) exhibit large jumps in both variables.

Although this algorithm is effective at identifying the leading edges of dust-laden CPOs in SEVIRI, it is important to emphasise that it relies upon the presence of erodible material for a visual signature and cannot account for CPOs entirely hidden under cloud. The dataset presented here is therefore a sample of the total population of CPOs and is more suitable for observing long-lived events associated with multi-cellular convection rather than those caused by microbursts which may only be brief (Roberts and Knippertz 2012). A complete climatology of CPOs would require a dense surface observation network capable of tracking CPO passage from ground-level where cloud cover is present. Nevertheless, CPOs are regularly visible to satellite and this algorithm detects the majority of them (74.2%). The resulting dataset is large enough to calculate long-term statistics and has only a small contribution (6.8% of pixels) from false positives.

4.5 Results and discussion

4.5.1 Characteristics of tracked CPOs

1,559 events are tracked for the period June, July and August 2004-2017, comprising an average of 111.4 ± 27.0 (one standard deviation) events detected per summer season in the CWS.

A clear diurnal cycle of CPO occurrence is observed (Figure 4.8a), with peak time for generation of CPOs between 1700-1900 UTC. This peak likely lags the true outflow production time as the algorithm developed in Section 4.3 depends upon the leading edge of the CPO emerging from beneath convective cloud as it begins to spread horizontally. The diurnal cycle presented here confirms that the significance of nocturnal dust emission (Marsham et al. 2013a; Allen et al. 2013; Todd and Cavazos-Guerra 2016) is a result of the sharp peak in cold pool generation in the evening as convective systems mature, corresponding also to the peak in convective cloud (Figure 4.8b) and approximate peak rainfall time observed in TRMM data (Hirose et al. 2008). The results also suggest that this peak in nocturnal dust emission is likely to occur before midnight,

though significant emission may occur after midnight if turbulent gusts persist at the leading edge of the outflow.

With no ambient flow and a constant mass flux feeding the expanding outflow, the outflow boundary propagation speed U is expected to decay through its lifetime with the form

$$U \propto (t - t_0)^{-\frac{1}{4}} \tag{4.1}$$

following Parker (1996), where t_0 represents the time at which the cold pool was generated. Neither assumption inherent in this model is entirely appropriate for the features observed here; ambient flow is present and mass flux depends upon the lifetime of the convection from which the cold pool originates. In this paper CPOs are tracked for up to 10 hours, comparable to the lifetime of convective storms in the satellite-based CMORPH dataset over the Sahel, for which 99% appear to be under 10 hours in duration (Crook et al. 2019, Figure 2c). Furthermore t_0 cannot be accurately quantified as cold pools are not visible to satellite at the point of inception. Nevertheless, we note that mean propagation speed evolution in Figure 4.9a conforms well to exponential decay, with event speed greatest closest to the initiation point of the CPO (Figure 4.9d). The decline in speeds is greatest during the first two hours of a CPO's lifetime, in which speeds drop by 2-2.5 m/s, falling by a further 2.5 m/s over the next 6-7 hours.

When composited, an extremely dominant signal of north-northwestwards propagation is found, with a small signal from events propagating towards the southwest (Figure 4.9b). The events with the greatest duration and reach (over 9 hours and 500 km, respectively) are northwestwards. The detection algorithm adopted here depends upon lofting of dust at the outflow boundary, which is expected to contribute to a preference for apparent northwards propagation into the relatively drier and dustier Sahara due to the visibility of the material. Dust emission is, in turn, nonlinearly related to horizontal wind speeds (Bagnold 1941). However, simulated cold pool outflows exhibit asymmetrical horizontal

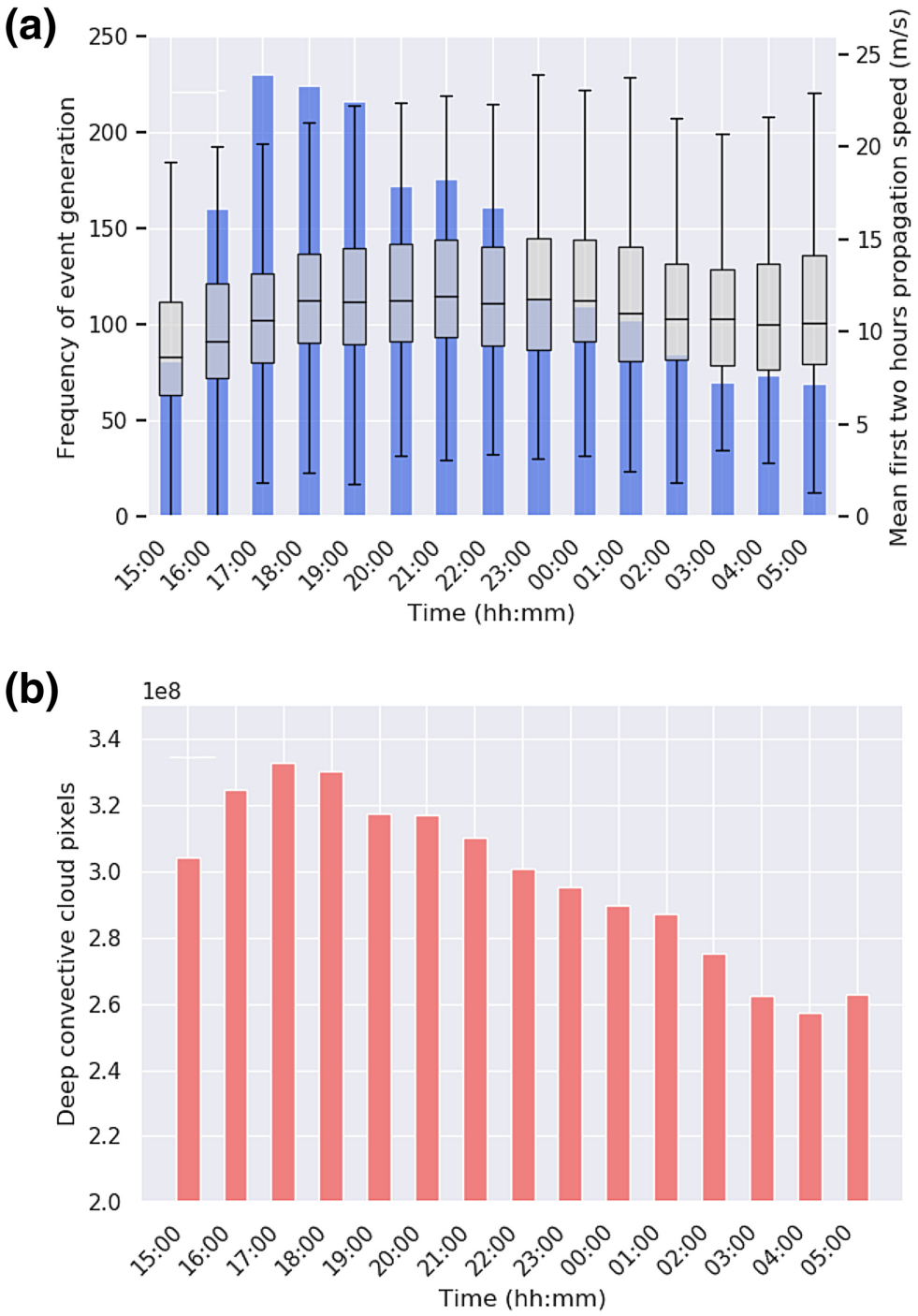


Figure 4.8: Mean diurnal cycle of (a) CPO generation, taken as the first timestep of detection (blue bars), CPO propagation speed over the first two hours (box plots). Shown in (b) is the diurnal cycle of deep convective pixels (where BT 10.8 μm < 250 K). All diurnal cycles are calculated for the period June, July and August 2004-2017.

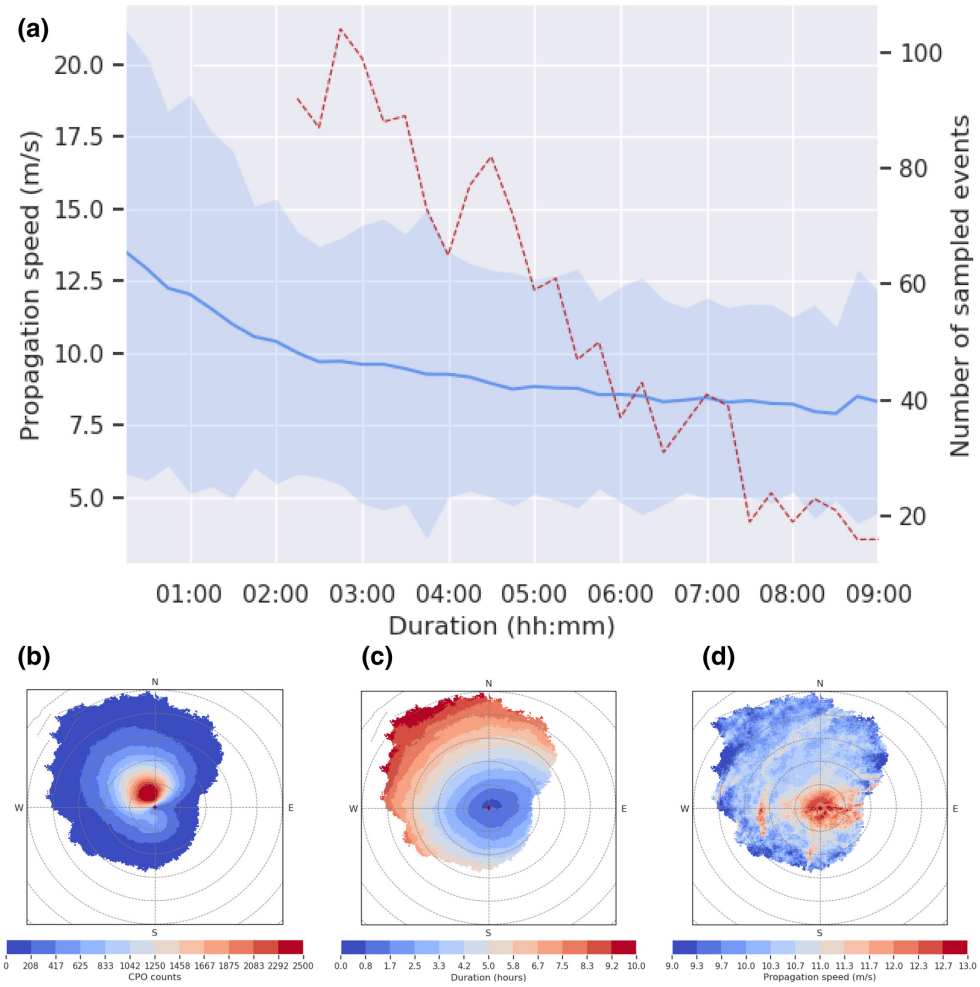


Figure 4.9: (a) Distribution of CPO durations (red dashed line) with mean propagation speed at that point in the CPO's lifetime (solid blue line, with one standard deviation shaded in light blue). Composites of all CPOs across all timesteps are shown below (b-d). Grey dashed concentric circles are spaced at distances of 100 km, with each detected event overlain and centred using its source point, shown as a blue cross in Figure 4.5, such that the source point is located at the small red cross at the centre of b-d. Composites include (b) frequency, (c) mean duration and (d) mean propagation speed.

wind speeds across their radius; wind speeds realised at the point of cold pool passage are a function of both the radial velocity of the outflow and the 'steering' wind aloft from which momentum is transported during the downdraft process (Parker 1996; Holmes and Oliver 2000; Pantillon et al. 2015). Hence, upper-level flow opposing the propagation direction of the outflow will slow its progress and reduce the low-level wind speeds responsible for dust emission. These observations support this model of cold pool development; a combination of high

dust availability to the north and an easterly steering jet aloft during summer (Thorncroft and Blackburn 1999) results in a dominant northwestward outflow propagation direction. Cold pools are less prone to propagate along the axis of the dominant summertime southwesterly low-level flow (Parker et al. 2005a). 22.5% of CPOs (351 events) exceed 300 km in reach in the dataset (Figure 4.9b), demonstrating that over the 14 year period (1,288 days), far-reaching events are relatively common.

Propagation speed also exhibits a slight diurnal cycle (Figure 4.8a). To remove the effects of the speed decay upon this diurnal cycle (considerably more events are initiated at 1900 UTC than 0800 UTC so average speeds would naturally be higher as per Figure 4.9a), a mean value has been calculated from the first two hours of speeds (i.e. 8 samples). CPO speeds reach a peak at 2100 UTC, several hours after the 1900 UTC maximum in CPO occurrence. Speeds for most daytime hours are not shown, as a manual check of the small sample size of these rare daytime CPOs indicates that more than half are false positives (not shown). Speeds for the hours of 1500-1700 UTC average at 10.7 m/s, compared with 12.3 m/s for all other shown hours. Lower propagation speeds during the daytime demonstrate the effect of boundary layer mixing; eddy-driven turbulence in the daytime convective boundary layer inhibits horizontal transport (Parker et al. 2005a).

4.5.2 Seasonality of CPOs and comparison with dust emission

CPO activity is non-uniform across the CWS (Figure 4.10). The vast majority of detections are found south of 28°N and propagate northwestwards, indicating the major CPO generation mechanism is deep convective activity associated with the WAM. The peak in CPO activity occurs close to the Mali-Niger-Algeria triple point (TP) at 4°E, 20°N. This CPO maximum is proximate to a hotspot of orographic deep convection (Redl et al. 2015), known to be a likely driver of enhanced cold pool activity (Kocha et al. 2013). Other hotspots of activity are

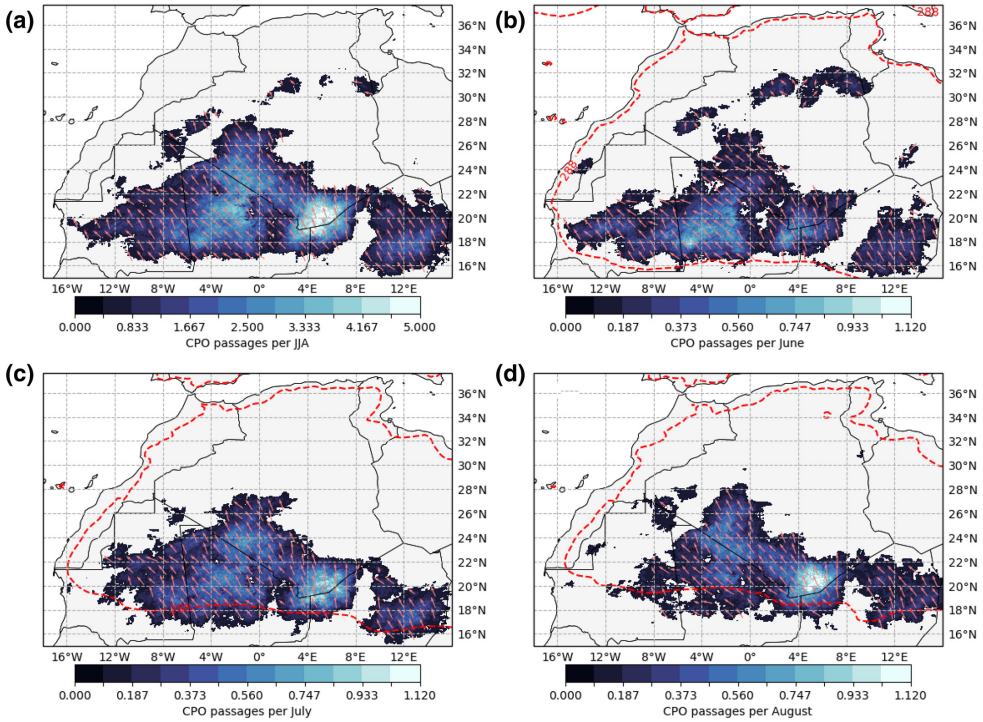


Figure 4.10: Pixels classified as belonging to cold pool outflow events across the total lifetime of all features tracked from 2004-2017. Counts per JJA are shown in (a), along with (b) June, (c) July and (d) August. The 270 K 10 m dewpoint temperature line is plotted in red (dashed), of which the southern boundary is a proxy for the ITD position. Pink arrows represent the mean propagation direction of detected events.

found along the western flank of the Adrar des Ifoghas mountains (4 to 0°W, 20°N) and to the north along the Mali-Algeria border. CPOs are demonstrably far-reaching in the CWS, with a climatological signal hundreds of kilometres north of the peak WAM rainband. The high occurrence of CPOs in the hyperarid Sahara confirms that moisture transport pathways exist capable of ventilating the remote SHL region (Engelstaedter et al. 2015) and that CPO recycling may play an important role in sustaining this (Trzeciak et al. 2017) although further work is needed to pinpoint the dominant mechanism by which CPOs are generated this far north of the climatological ITD.

The spatial distribution of CPO hotspots evolves through the summer season. One notable component of this is a northward shift in the band of peak CPO activity, tracing the displacement of the ITD. In June, the maximum in CPO occurrence is found around 18°N in western Mali (with pixels averaging more

than one passage per June) and is mirrored by comparably frequent passages east of the Adrar des Ifoghas mountains at 3°E in the region south of the triple point (Figure 4.10b). During July these pixels lose their prominence and a broader distribution of occurrence is observed, including passages north of the Algeria border (24°N) and the development of a CPO hotspot directly north of the triple point (Figure 4.10c). In August, the southernmost hotspots of occurrence are entirely inactive and the maximum north of the triple point develops to its highest frequency (Figure 4.10d). Whereas the early monsoon season is associated with a high production of CPOs at Sahelian latitudes, the late season is dominated by activity in the central Sahara. These findings broadly align with modelled dust uplift potential from cold pool outflows calculated for the 'Sahara West' domain in Pantillon et al. (2016), where a peak is reached in August (in contrast to an earlier monsoon peak in the Sahel). The patterns are also consistent with maps of CPO-associated dust presence in Caton Harrison et al. (2019) in which a noticeable shift occurs from dust presence in the southern Sahara (including central Mali) towards hotspots further north in southern Algeria in August. However, one important inconsistency between the two datasets is that an intense peak in CPOs in August over the TP in Figure 4.10d does not appear to map on to the drop in late season dust presence seen in Caton Harrison et al. (2019). Only a broad comparison of patterns between the two approaches is made here as the exact quantity of CPO pixels through time is influenced by their visibility in cloudy conditions, and the CPO pixels in Caton Harrison et al. (2019) account for a much wider set of dust outbreaks, i.e. virtually all visible nocturnal dust which could be tracked for at least 2 hours.

A decline in atmospheric dust loading from the early to late monsoon season is a well-documented feature of the annual cycle of the CWS. It has been noted in SEVIRI dust flags (Ashpole and Washington 2013a; Ashpole and Washington 2013b; Caton Harrison et al. 2019), MODIS/MISR aerosol optical depth (Schepanski et al. 2012; Ridley et al. 2012) and TOMS AI (Engelstaedter

Table 4.1: Possible mechanisms for the late summer decline in Saharan dust emission

	Mechanism	**Possible drivers**
1	Declines in late summer dust emission are an artefact of satellite observing methods	Dust emission obscured by cirrus anvils (Williams 2008; Heinold et al. 2013; Redl et al. 2015) Masking by increased late-season column water vapour (Brindley et al. 2012)
2	Decreasing frequency or strength of CPOs drives declines in dust emission during late summer	Lower DCAPE in the late summer season due to decreasing midtropospheric dryness (Marsham et al. 2008; Provod et al. 2016)
3	Decreasing frequency or strength of nocturnal low-level jets drives declines in dust emission during late summer	Decreased nocturnal boundary layer stability due to the northward advance of the ITD
4	Key dust sources cease to be collocated with the main meteorological drivers of dust emission during late summer	Less available erodible material in northern/Saharan dust sources as the ITD advances northward
5	Dust emission remains constant through summer but material is more rapidly deposited or less widely circulated as the season progresses	Increased scavenging of dust due to a late monsoon peak in Saharan rainfall (Engelstaedter and Washington 2007)
6	Increased rainfall late in the summer season inhibits dust emission	Limits to wind erosion due to capillary forces within the soil induced by increased moisture content Fécan et al. 1998; Bergametti et al. 2016; Bergametti et al. 2017) or crusting (Rajot et al. 2003)

and Washington 2007). Given the importance of CPOs for dust emission, here we compare our CPO dataset with observed dust presence through boreal summer.

The relationship between dust emission mechanisms such as CPOs and total dust emission is not straightforward. Table 4.1 summarises a number of possible mechanisms responsible for declining late summer Saharan dust emission.

Mechanisms 3, 5 and 6 in Table 4.1 are not tested directly in this paper, which focuses instead upon CPOs. Peak nocturnal low-level jet occurrence (mechanism 3) is thought to shift northwards through summer (Fiedler et al. 2013) like CPOs. This emission mechanism is secondary to CPOs (Caton Harrison et al. 2019), but may play a complementary role in the overall decline. Differences in dust transport (mechanism 5) are an additional possible factor, but the analysis of Ashpole and Washington (2013a) (Figure 8 therein) clearly flags fewer 'dust emission' pixels on average in August compared to June and July. Rainfall (mechanism 6) may also act to inhibit uplift of dust (i.e. decreasing erodibility) in the late monsoon season. This has been explored in some detail for the Sahel by Bergametti et al. (2016) and Bergametti et al. (2017) who find that precipitation inhibits around 25% of dust uplift potential, suggesting only a small role in the late season dust decline. For comparison, rainfall totals (not shown) at Tamanrasset (22.8°N, just north of the apparent August CPO hotspot) reach around 20 mm in August on average, compared to over 140 mm at Tahoua (14.9°N) which is still further north than the field sites used by Bergametti et al. (2017) (e.g. Banizoumbou at 13.5°N). The scarcity of rainfall in the region of the August CPO hotspot therefore casts doubt on the importance of this process, but in situ observations to test for rainfall inhibition over central Saharan dust sources would be extremely valuable.

To test whether the observed dust decline is merely an artefact of satellite observations (mechanism 1), we compare our results to weather observations (in the form of weather codes) from stations reporting data to the Met Office Integrated Data Archive System (MIDAS) within the broader triple point (TP) region of the CWS. To achieve this, the TP region is split into two domains (Figure 4.11a): TP-South and TP-North. TP-South represents the region south of the Algerian border for which large declines in dust emission are observed in Ashpole and Washington (2013a) as the dust band shifts north, while TP-North represents the region to the north where dust is observed to be more stable

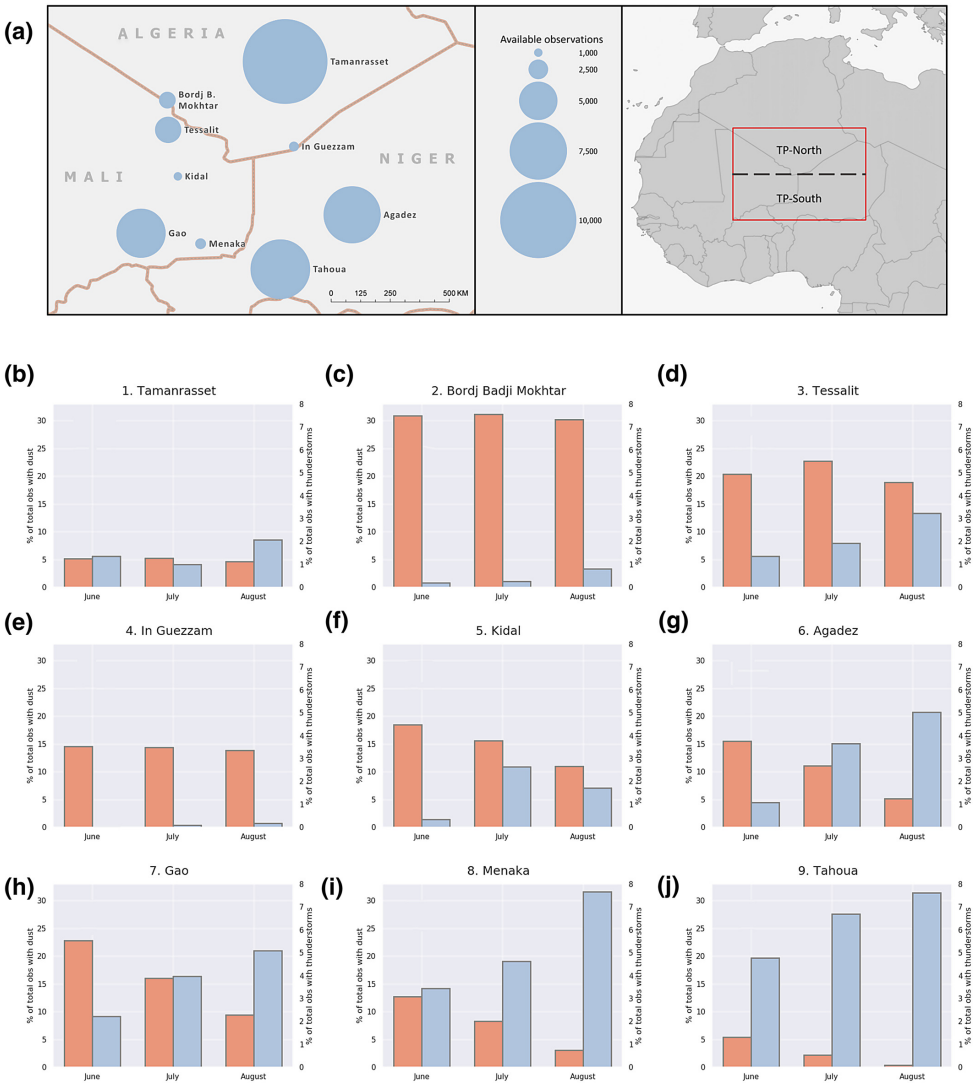


Figure 4.11: Percentage of observations of weather codes associated with dust activity (orange) and thunderstorms (blue) at stations reporting to the Met Office Integrated Data Archive System (MIDAS) for June, July and August. Sampling domain and location of stations is shown in (a) along with the size of circles representing the available samples at each station. The location of the domain as well as the division between TP-North and TP-South are shown in the rightmost panel. Observations are taken from (b) Tamanrasset, (c) Bordj Badji Mokhtar, (d) Tessalit, (e) In Guezzam, (f) Kidal, (g) Agadez, (h) Gao, (i) Menaka and (j) Tahoua.

through the summer season but where a CPO hotspot is observed to develop late in the season (Figure 4.10d).

The majority of stations within the sampled domain report a decline in the relative frequency of dust-related weather codes in August (Figure 4.11). In parallel, most stations also report that August is subject to the highest levels of

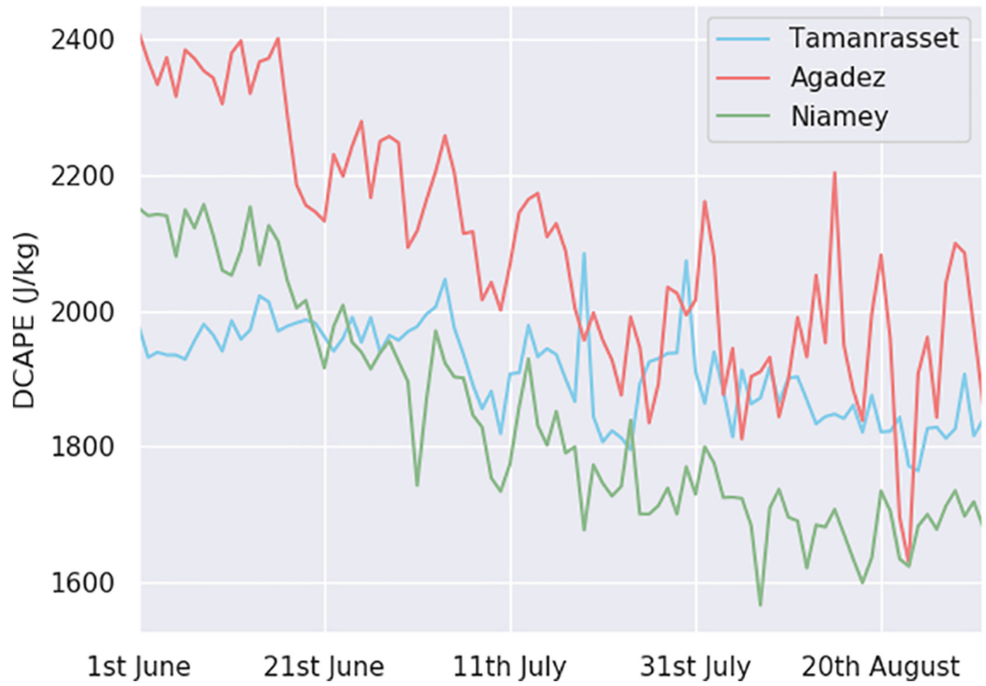


Figure 4.12: Mean of Downdraft Convective Available Potential Energy (DCAPE) in J/kg measured from sonde ascents at Tamanrasset (blue), Agadez (pink) and Niamey (green) for June, July and August 2004-2017. Daily sonde ascents at 00 and 12 UTC are included in the average. DCAPE is calculated from the level with the lowest wet bulb potential temperature, corresponding to the greatest possible evaporative cooling, following Gilmore and Wicker (1998).

thunderstorm activity, lending credence to the late season CPO hotspot observed in Figure 4.10d. Dust declines are much larger in TP-South; across the entire sampling period, Tahoua reports only 25 dust observations for the month of August, compared with over 400 in June (Figure 4.11j). By contrast, counts in Tamanrasset (Figure 4.11b) and Bordj Badji Mokhtar (Figure 4.11c) in TP-North are relatively consistent through the summer months, with only a slight decline in August compared to June. A sharper drop in dust activity further south is consistent with Ashpole and Washington (2013a), in which the dust band is observed to shift northward, and implies that this is not merely a result of enhanced cloud cover at these latitudes. These results do not therefore support a hypothesis that dust decreases in August can be explained as a satellite artefact (mechanism 1). There is, however, evidence that the drop in dust is dominated by the seasonality of the southernmost dust sources (mechanism 4).

Mechanism 2 from Table 4.1 poses that dust emission totals through summer are directly controlled by the frequency of CPOs across the Sahara. Patterns of CPO activity through summer (Figures 4.10b to 4.10d) suggest that this hypothesis can explain the sharp declines observed in the southernmost dust sources. Both observed dust (e.g. Figure 11 in Caton Harrison et al. (2019)) and CPOs exhibit a clear northward shift in the southern boundary of their occurrence, suggesting that reduced CPO activity south of 20°N is responsible for the drop-off in dust at those latitudes. A possible explanation for this observed decline in the southernmost CPOs is reduced Downdraft Convective Available Potential Energy (DCAPE), as described by Marsham et al. (2008) and Provod et al. (2016). At the peak of the monsoon season, tropical to extratropical moisture transport inhibits dry midtropospheric conditions conducive to diabatic cooling and downdraft formation. It should be noted that although it is an important ingredient for cold pool activity, DCAPE alone is generally limited as a predictor of the occurrence and strength of negatively buoyant downdrafts. For example, a parameterization of CPOs based primarily upon DCAPE was found to misplace the peak in CPO activity over the central Sahara at the expense of southern events (Pantillon et al. 2016). DCAPE is shown in Figure 4.12 for Agadez and Niamey (located in and just south of TP-South, respectively). All available sonde ascents at each of the two stations (red and green lines) are averaged across the period 2004-2017, exhibiting declines of around 500 J/kg through summer. Decreased DCAPE would explain reduced efficiency of CPO production at these latitudes even as thunderstorm activity increases (Figure 4.11).

Mechanism 2 alone is too simplistic, however, and assumes dust sources are as abundant in TP-North as they are in TP-South. Although declines in CPOs over southern regions are observed in the late summer, a large intense hotspot of CPO occurrence also develops further north during August (Figure 4.10d). The development of this TP-North hotspot is not paralleled by any major increases in late-season dust observations anywhere in either TP-North or TP-South (Figure

4.11). Although Tamanrasset in TP-North does undergo a slight but statistically significant (at the 0.01 level) decrease in DCAPE (Figure 4.12, blue line), TP-North is located northwest of a major late-season hotspot of deep convective cloud development in the lee of the Aïr Mountains (not shown). This region of preferred convective triggering in August is particularly clearly shown with the microwave satellite imaging method of Redl et al. (2015). Hence, in spite of a general trend of declining DCAPE, large increases in Saharan deep convection around the TP drive a late monsoonal hotspot of southern Algerian CPOs.

Given that CPOs increase in frequency over TP-North during the late summer season, one plausible explanation for reduced dust presence during August is that the CPO hotspot is not collocated with any major dust sources (mechanism 4), and hence that a northward shift in peak CPO activity leads to an overall decline in emission. Although the CPO-tracking algorithm relies on the presence of erodible material to make CPOs visible, it is possible that many of the arcs observed in August are linked to dust in shorter supply or coarser material which is immediately redeposited. This suggests that the location of meteorological dust emission mechanisms is just as important as their frequency; as Figure 4.10 shows, CPO frequency is highly heterogeneous across the Sahara, but for large atmospheric dust loading to occur, they must also be collocated with suitable sources of fine erodible material.

Overall, three important points come out of this analysis. Firstly, several independent datasets show that atmospheric dust loading over the Sahel and Sahara declines in late summer as the ITD moves north and DCAPE declines over the Sahel. Secondly, manual observations of dust storms decline more rapidly through summer in the TP-South domain than TP-North. Lastly, convective activity and CPOs appear to actually increase over TP-North and the central Sahara during late summer despite no corresponding increase in dust production at these latitudes. Together, these results suggest that the southernmost dust sources play a major role in the summertime dust budget. However, as shown by

Todd and Cavazos-Guerra (2016), dust sources south of 17°N are likely to be under-represented in the most widely cited Saharan dust source maps (Schepanski et al. (2007) and Ashpole and Washington (2013a)). Further in situ observations may also be needed to understand why sharply increasing late-monsoon convective and CPO activity over TP-North has such a minor role in dust production.

4.6 Summary and conclusions

Motivated by an absence of observations and reliable model simulations, a 14-year dataset of cold pool outflow boundary passage has been derived from high temporal resolution satellite data. To the authors' knowledge, it is the first method for tracking individual dust-laden CPOs through time, and comprises the largest set of Saharan CPO observations in general. It is used here to identify typical CPO characteristics and to analyse the drivers of seasonal trends in Saharan dust activity.

The 10.8-8.7 μ Brightness Temperature Difference field from Meteosat SEVIRI data is found to be sensitive to regions where outflow boundaries emit dust and raise local humidity. In order to flag only pixels associated with genuine outflow passages, a multi-step algorithm is applied to the data. Regions with a high Brightness Temperature Difference Gradient (BTDG) in time are highlighted as possible CPO occurrence regions. Thresholds are then applied to the value of the BTDG field, the duration, maximum size reached by individual events and their proximity to deep convection in order to flag genuine CPO pixels. Propagation speed is also estimated for each tracked CPO by fitting events to an idealised 2D model of outflow boundary displacement.

When validated against manually identified CPOs from satellite data for July of 2011, the automated system flags 74.2% of the total events, with only 6.8% of flagged pixels corresponding to false alarms. Of the automatically tracked

events which are observable from surface weather station data for 2011 and 2012, a majority leave a clear signal in high resolution wind speed data.

With 1,559 events tracked for June, July and August of 2004-2017, the following findings are made:

- CPO occurrence follows a clear diurnal cycle, peaking at 1700-1900 UTC, consistent with a nocturnal peak in dust emission;
- Outflow boundary propagation speeds decay exponentially from the point of CPO generation, peaking overnight (around 1.5 m/s higher) as vertical mixing is reduced;
- Events are overwhelmingly northwestwards propagating, with 351 observed events (22.5%) exceeding 300 km in distance travelled;
- CPOs are active across northern Mali, eastern Mauritania, along the western Algerian border and at the triple point of Mali, Niger and Algeria;
- The spatial pattern of CPO activity through boreal summer maps onto changes in dust presence, with a northward and eastward shift in CPO occurrence as the monsoon season progresses;
- The development of the largest CPO hotspot over the northern triple point region during August does not appear to counteract declines in dust further south, indicating that the southernmost dust sources play a large role in the summertime budget.

Saharan CPOs are widespread, diurnally varying, northwestward propagating phenomena which occur further north as the summer season progresses and which peak in frequency to the north of the Mali-Niger-Algeria triple point during August. The results of a comparative analysis of CPO and dust activity suggest that the decline in Saharan dust through summertime is subject to a complex interplay between cold pool outflow activity and the geography of dust

availability, with the southernmost sources activated almost exclusively during the early monsoon season. The development of a late-season hotspot of cold pool outflows over southern Algeria does not compensate for this southern decline, indicating that emission within the Sahel is more responsive to varying cold pool activity and may play a pivotal role in the dust budget for the summer season.

4.7 Acknowledgements

MSG SEVIRI data can be accessed online from the EUMETSAT Data Centre at `https://navigator.eumetsat.int/product/EO:EUM:DAT:MSG:HRSEVIRI`. AWS data were collected during the Natural Environment Research Council (NERC) Fennec field campaign (Grant NE/G017166/1). We would like to thank those who installed and maintained the instrumentation, including the Algerian and Mauritanian Meteorological Offices. Fennec data can be accessed from the Centre for Environmental Data Analysis (`http://archive.ceda.ac.uk/`). MIDAS data is available from CEDA at `http://catalogue.ceda.ac.uk/uuid/220a65615218d5c9cc9e4785a3234bd0`. TCH is funded through the NERC doctoral training partnership (NE/L002612/1). RW was partly supported by the NERC-Department for International Development (DFID)-funded Improving Model Processes for African Climate (IMPALA) project (Grant NE/M017206/1), as part of the Future Climate for Africa (FCFA) program, described `http://futureclimateafrica.org/project/impala/`. We are grateful to Ian Ashpole, Neil Hart and three reviewers for insightful discussions and comments which helped improve the manuscript.

5

Influence of orography upon summertime low-level jet dust emission in the central and western Sahara

Thomas Caton Harrison[1], Richard Washington[1], Sebastian Engelstaedter[1], Richard Jones[1, 2] and Nick Savage[2]

[1]Climate Research Laboratory, Oxford University Centre for the Environment, Oxford, UK

[2]Met Office, FitzRoy Road, Exeter, UK

Submitted 07/04/2021 to J. Geophys. Res. Atmos.,

Contents

5.1 Abstract 137
5.2 Introduction 138
5.2.1 Background 138
5.2.2 Orographic effects on dust-emitting conditions in the Sahara 139
5.2.3 Aims 141
5.3 Data and model experiment setup 142
5.3.1 Model data 142
5.3.2 Observations 143
5.3.3 Model validation 144
5.3.4 Orography experiments 148
5.3.5 Composite method 149
5.4 Synoptic conditions 151
5.5 Model experiment results 154
5.5.1 Wind speed and vertical structure 154
5.5.2 Leeward circulation 156
5.5.3 Geostrophic wind analysis 162
5.5.4 Role in dust emission frequency 164
5.6 Summary and conclusions 170
5.7 Acknowledgements 172

5.1 Abstract

Low-level jets (LLJs) drive frequent emission of mineral dust in the central and western Sahara in boreal summer. A major hotspot for this process is central Algeria and northern Mali and Mauritania, through which blow the dry near-surface northeasterly trade (or Harmattan) winds, with a peak in dust emission around the low-lying Tidihelt region. Orography is thought to contribute to the strength of the LLJ over the Bodele dust source in Chad and influence the West African Monsoon onset, but its influence on erosivity over summertime source regions remains unquantified. In this paper, the role of central Saharan orography in controlling the strength of Harmattan LLJs is tested and the effect upon LLJ dust emission frequency is estimated. An idealised simulation without the Hoggar mountains is compared with a control using the Met Office Unified Model at 12 km horizontal resolution. In the absence of the Hoggar mountains, dust emission frequency estimated using an empirical relationship with surface wind speeds is found to decline across the entire northeasterly 'LLJ alley', including by 31% in the Tidihelt where composited jet surface winds drop from 9.0 to 7.3 ms^{-1} under a more easterly regime. The mountains are linked to a low-level leeward geopotential height perturbation, with a northern limb reinforcing northeasterlies through the Tidihelt. A dome-shaped elevated heating anomaly situated over the Hoggar mountains explains the difference between the simulated wind fields in the two experiments. These findings suggest that central Saharan orography plays an important role in sustaining erosive dusty conditions during boreal summer.

5.2 Introduction

5.2.1 Background

Mineral dust is an abundant and important naturally emitted aerosol. The largest proportion of atmospheric loading of mineral dust originates in the Sahara (Engelstaedter et al. 2006), with peak emissions in boreal summer. Saharan dust has a varied radiative effect (Boucher et al. 2013), as well as impacts on ice nucleation (Hoose et al. 2008), tropical cyclone development (Evan et al. 2011), rainforest fertilisation (Mahowald et al. 2010) and human health (De Longueville et al. 2010). Activation of Saharan dust sources is sporadic and sensitive to relatively infrequent intense winds linked to mesoscale atmospheric processes (Cowie et al. 2015; Marsham et al. 2013b; Allen et al. 2013; Caton Harrison et al. 2019).

Dust models diverge considerably in their estimates of net North African yearly dust fluxes (Huneeus et al. 2011; Wu et al. 2020). Although part of this is due to the formulation of the model itself, a large proportion of the uncertainty stems from differences between driving wind fields (Luo et al. 2003; Fiedler et al. 2016). Several modelling and observation studies aim to characterise the mesoscale processes responsible for dust emission (e.g. Washington and Todd (2005), Washington et al. (2006), Knippertz et al. (2007), Schepanski et al. (2009), Heinold et al. (2013), Allen et al. (2013), Caton Harrison et al. (2019), and Caton Harrison et al. (2020)) and to evaluate their representation in wind speed products commonly used to drive offline dust models (Roberts et al. 2017; Allen and Washington 2014; Schepanski et al. 2015; Garcia-Carreras et al. 2013).

A major meteorological emission mechanism at work in the Sahara during boreal summer is the morning breakdown of the nocturnal low-level jet (LLJ). Winds atop the nocturnal boundary layer accelerate under a stable regime due to decoupling from surface friction and inertial oscillation (Blackadar 1957). Mixing of jet momentum to the surface as a result of eddy-driven turbulence in the

morning raises surface wind speeds, leading to dust emission in the strongest cases (Miller et al. 2004; Allen and Washington 2014). An analysis of the ERA-Interim reanalysis indicates that favourable locations for LLJs are found along the margins of the Saharan heat low (SHL) in regions of Atlantic, Mediterranean and monsoon inflow, as well as downwind of of orographic channels (Fiedler et al. 2013). LLJs embedded in both northeasterly and monsoon flows were regularly observed during the June 2011 intensive observation period of the Fennec campaign, contributing 14% of the observed dust loading (Allen et al. 2013; Allen and Washington 2014). Automated tracking of over 100,000 summertime dust plumes observed in SEVIRI from 2004-2017 indicates that LLJs are responsible for 18% of flagged dust pixels, and as much as 40% in 2012 (Caton Harrison et al. 2019).

A robust feature of both model and satellite analyses of Saharan dust is a prominent hotspot of activity and dust emission around central Algeria (Schepanski et al. 2007; Ashpole and Washington 2013a; Heinold et al. 2013; Evan et al. 2015; Todd and Cavazos-Guerra 2016; Wu et al. 2020), as well as more generally within the broad northeasterly Harmattan 'alley' of the northern Sahara. The central Algerian surface wind speed maximum, referred to as the Tidihelt jet in this paper, is evident in reanalysis (see e.g. Figure 13g-i in Caton Harrison et al. 2019) and surface observations (Chellali et al. 2011; Messaoudi et al. 2019). The Tidihelt region is unique in that unlike almost all other dust sources, it is predominantly activated by LLJs (Caton Harrison et al. 2019). A map of the Tidihelt dust source showing potential erodible salt flats is given in Figure 15 of Caton Harrison et al. 2019. The LLJ alley containing the Tidihelt jet is bounded by the Atlas mountains to the north and the Hoggar mountains to the south.

5.2.2 Orographic effects on dust-emitting conditions in the Sahara

Although the proximity of many Saharan dust sources to orographic channels has been noted (Schepanski et al. 2007; Fiedler et al. 2013; Evan et al. 2015), few studies have drawn an explicit link between Saharan orography and the

frequency or strength of dust emission, especially for western sources such as the Tidihelt. The Bodele in northern Chad is frequently activated when a ridging Libyan high pressure system drives statically stable northeasterlies through a gap between the Tibesti and Ennedi massifs, splitting the flow upstream and accelerating winds in the exit region by up to 40% (Washington et al. 2006; Todd et al. 2008b). A secondary effect from elevated heating and cooling over the mountains is also apparent. The Bodele is much larger and more active than western Saharan dust sources, but serves nonetheless as a useful analogue.

Elevated terrain stretching from the Atlas mountains in the north to the Aïr mountains in the south has been linked to a variety of atmospheric effects relevant to dust emission. Kelvin waves regularly propagate along the barrier of the Atlas mountains, organising downslope winds and jet adjustment processes responsible for severe dust storms in the Harmattan channel (Pokharel and Kaplan 2019). A relationship may exist between the Atlas range and the remote Saharan boundary layer, with ascent over the mountains and compensating descent over the central Sahara (Flamant et al. 2007). There is also a plausible but untested connection between orography and triggering of convection in the southern Sahara during the late monsoon season, which in turn produces convective downdrafts responsible for dust emission (Caton Harrison et al. 2020).

The Hoggar mountains south of the Tidihelt have a peak of 2,918m, span 800 km and consist of rock pinnacles and volcanogenic formations, with widespread dust sources in their western lee and southern flank formed from outwash fluvial and paleo-lacustrine deposits (Prospero et al. 2002; Ashpole and Washington 2013a). These mountains are thought to have some role in the onset of the West African Monsoon due to their interaction with the SHL via lee cyclogenesis. It has been shown that background easterlies and northeasterlies around the mountains could be capable of initiating a leeward trough or depression as the subtropical anticylone is amplified over the elevated terrain, in turn deepening the SHL (Semazzi and Sun 1997; Drobinski et al. 2005). The mechanics of such a process

have not been demonstrated in detail, however, and have not been associated explicitly with dust emission. A previous set of idealised model experiments flattened the Hoggar mountains in the Met Office Unified Model, showing how the orography heats and deepens the convective boundary layer over the Sahara several hundred kilometres west of the main peaks, as well as redirecting cooler maritime easterlies upstream (Birch et al. 2012). These thermodynamic effects could offer an additional or alternative explanation for the interaction between the Hoggar mountains and summertime dust emission, but the effect of orography upon dust emission frequency from nearby dust sources has not been explored.

5.2.3 Aims

In this paper, we aim to test the effect of the Hoggar mountains upon a prominent climatological peak in summertime wind speeds over central Algeria associated with a frequent LLJ, identified here as the Tidihelt jet. Boreal summer is selected for analysis as dust emission from the central and western Sahara, including central Algeria, is high at this time of year (Engelstaedter et al. 2006; Ridley et al. 2012; Schepanski et al. 2012; Kok et al. 2021) and because automated satellite detection of LLJ dust has been developed for the summer months (Caton Harrison et al. 2019). The study also estimates the impact of these winds on dust emission frequency. To achieve this, we identify the synoptic conditions favouring the Tidihelt jet, test for elevated heating and lee cyclogenesis associated with the elevated terrain and estimate the wider impacts of the orography upon dust emission frequency in the northern Saharan LLJ alley. In summary, the research aims to:

1. Quantify the effect of the Hoggar mountains upon dust-emitting winds in central Algeria;

2. Identify a mechanism linking the Hoggar mountains and high surface wind speeds;

3. Estimate the effect of the Hoggar mountains upon dust emission frequency within the LLJ alley of the northern Sahara.

Model and observation data used are described in Section 5.3, as well as a composite method. The synoptic conditions associated with dust emission in central Algeria are described in Section 5.4, with the results of the model experiment presented in Section 5.5.

5.3 Data and model experiment setup

5.3.1 Model data

This study uses a regional climate model (HadREM3-GA7.05) in a limited area configuration of the GA7.05 Unified Model (UM) (Walters et al. 2019), closely based on the 12 km model configuration used in UKCP18 climate projections (Murphy et al. 2018). It is set up in atmosphere-only mode with a limited area domain centred over North Africa on a 12 km horizontal grid with 57 vertical levels. The UM dynamical core solves deep atmosphere non-hydrostatic equations with a semi-implicit, semi-Lagrangian formulation discretised onto a regular latitude-longitude grid with terrain-following hybrid height coordinates (Walters et al. 2019). In this configuration, convection is parameterized and sea surface temperatures and sea ice extents are prescribed using the analyses of Reynolds et al. (2002), in addition to aerosol properties and cloud droplet number concentration derived from the MACv2-SP dataset for the historical (Stevens et al. 2017) scenario. The method used to implement these aerosol effects is identical to that used in the 12 km RCM in UKCP (Murphy et al. 2018), although with a difference source dataset. As dust emissions is not explicitly simulated, the effects of winds upon dust emission are derived empirically based on satellite-observed dust source LLJ activity, described in Section 5.3.2.

Of particular relevance to the simulation of LLJs is the boundary layer scheme. While inertial oscillation is handled by the dynamical core, the UM boundary layer scheme (Lock et al. 2000; Brown et al. 2008) is responsible for all vertical mixing by turbulent motions and is therefore critical for LLJ decoupling and decay. In an unstable boundary layer, diffusion coefficients (K profiles) are defined for sources of turbulence from both the surface and cloud top, whereas in a stable regime a local Richardson number scheme (Smith 1990) applies. Shallow and deep sub-grid cumulus convection is handled by the UM mass-flux convection scheme, with an extension to include parameterization of downdrafts (Gregory and Rowntree 1990; Walters et al. 2017).

Lateral boundary conditions are supplied to the limited area model from the ERA-Interim reanalysis (Dee et al. 2011) via one-way nesting. ERA-Interim has a horizontal resolution of approximately 80 km, and helps align the model with the quasi-observed state of the atmosphere represented in the reanalysis as it steps forwards in time, although the region of interest is far away from the domain boundaries at 20.1°W to 23.8°E and 7.9°N to 37.6°N meaning the UM plays a dominant role in the simulation of LLJ processes therein. Simulations are run for June, July and August 2004-2007. Although ERA-Interim underestimates surface winds associated with Saharan LLJs (Allen and Washington 2014), it is capable of realistically reproducing wind variability associated with synoptic and seasonal variations (Roberts et al. 2017) which is important for lateral boundary conditions.

5.3.2 Observations

A key characteristic of the summertime Sahara is that the majority of dust sources, including many in the Harmattan channel, are regularly influenced by cold pool outflows (CPOs) (Caton Harrison et al. 2019). In this paper, data from the Spinning Enhanced Visible and Infrared Imager (SEVIRI) are used to identify days with dust present and to compare simulated wind speeds with dust emission frequency. Dust is identified in SEVIRI from Brightness Temperatures at 15

minute intervals and 3 km nadir resolution using the SEVIRI dust flags approach of Ashpole and Washington 2012 and subsequently filtered to identify plumes associated with low-level jet activity following the method in Caton Harrison et al. 2019. Critically, this allows dust associated with LLJs to be distinguished from CPO dust. Although SEVIRI is commonly used for dust detection (Ackerman 1997; Lensky and Rosenfeld 2008; Schepanski et al. 2007), split-window techniques using wavelengths from 8-12 μm such as SEVIRI dust flags are also sensitive to column water vapour and cloud (Brindley et al. 2012). By this measure, central Algeria is uniquely easy to observe as it is exceptionally dry and has a high percentage of cloud-free days (e.g. see Figure 13 in Caton Harrison et al. 2019).

Radiosonde data used in this paper to identify synoptic conditions linked to dust emission are obtained for In Salah (27.19°N, 2.47°E), approximately 150 km upwind (northeast) of the Tidihelt dust sources. Daily soundings at 1200 UTC are sourced from the Integrated Global Radiosonde Archive (Durre et al. 2006) maintained by the National Centers for Environmental Information.

5.3.3 Model validation

The UM is selected as the modelling system for this project as it has demonstrable fidelity in simulating both the large-scale synoptics and the jet core wind speeds within the boundary layer. A 12 km horizontal grid-spacing configuration of the UM has been deployed (as 'Africa-LAM') to support the Fennec Campaign of in-situ observations in 2011 and 2012 (Washington et al. 2012). Comparisons between Africa-LAM and observations from supersite 1 located at Bordj-Badji Mokhtar in southern Algeria (approximately 500 km south of the TID region) reveal 'excellent agreement' between model wind speed profiles at 0600 UTC and Lidar measurements for Harmattan LLJs (Allen and Washington 2014), equivalent to the northeasterly jets considered in this paper. Allen et al. 2015 also find a hit rate of 85% in simulating morning LLJ winds at the surface compared to Fennec automatic weather station data, but they note that the frequency of the highest

(> 10 ms^{-1}) winds is underestimated. Dropsonde measurements from Fennec flights show that forecasts accurately represent large-scale wind fields around the SHL but underestimate morning wind speeds (Engelstaedter et al. 2015).

Figure 5.1 compares the 12 km configuration of the UM used in this paper with the approximately 31 km horizontal resolution ERA5 reanalysis. With a severe paucity of in-situ observations in the central Sahara, there is little for reanalyses to assimilate. As a result, significant disagreements exist between reanalyses over North Africa. This has led to uncertainty in their ability to faithfully represent the Saharan heat low (Marsham et al. 2011), mesoscale convective systems (Roberts and Knippertz 2014) and the intertropical discontinuity (Roberts et al. 2015). Comparison against ground stations from other parts of the world indicates ERA5 outperforms other reanalyses in representing diurnal variability of surface winds (Ramon et al. 2019), but an extensive evaluation of ERA5 winds against ground stations and other reanalyses has not yet been carried out over the Sahara. We adopt it here only for a broad comparison of synoptic features, given that it likely inherits underestimation of peak Saharan surface winds shown in ERA-Interim (Allen and Washington 2014; Roberts et al. 2017). ERA5 is not used for lateral boundary conditions in this research as the UM infrastructure does not currently support it.

A close match between the large-scale wind field is evident in comparing the UM and ERA5 (Figures 5.1a and b). Northeasterlies enter the region of the SHL via a gap between the Atlas and Hoggar mountain ranges, as well as Atlantic inflow from the northwest. A minimum in wind speeds occurs at 22°N within the climatological ITD. The highest winds are found along the Atlantic coast where a persistent coastal low-level jet linked to the Azores High and SHL overlies the Canary Current (Soares et al. 2019). Crucially for the purposes of this project, the UM accurately reproduces a wind speed maximum in central Algeria, evident in both the reanalysis and surface observations (Chellali et al. 2011). Wind speeds in the core of this maximum are 1-1.5 ms^{-1} higher in the UM compared

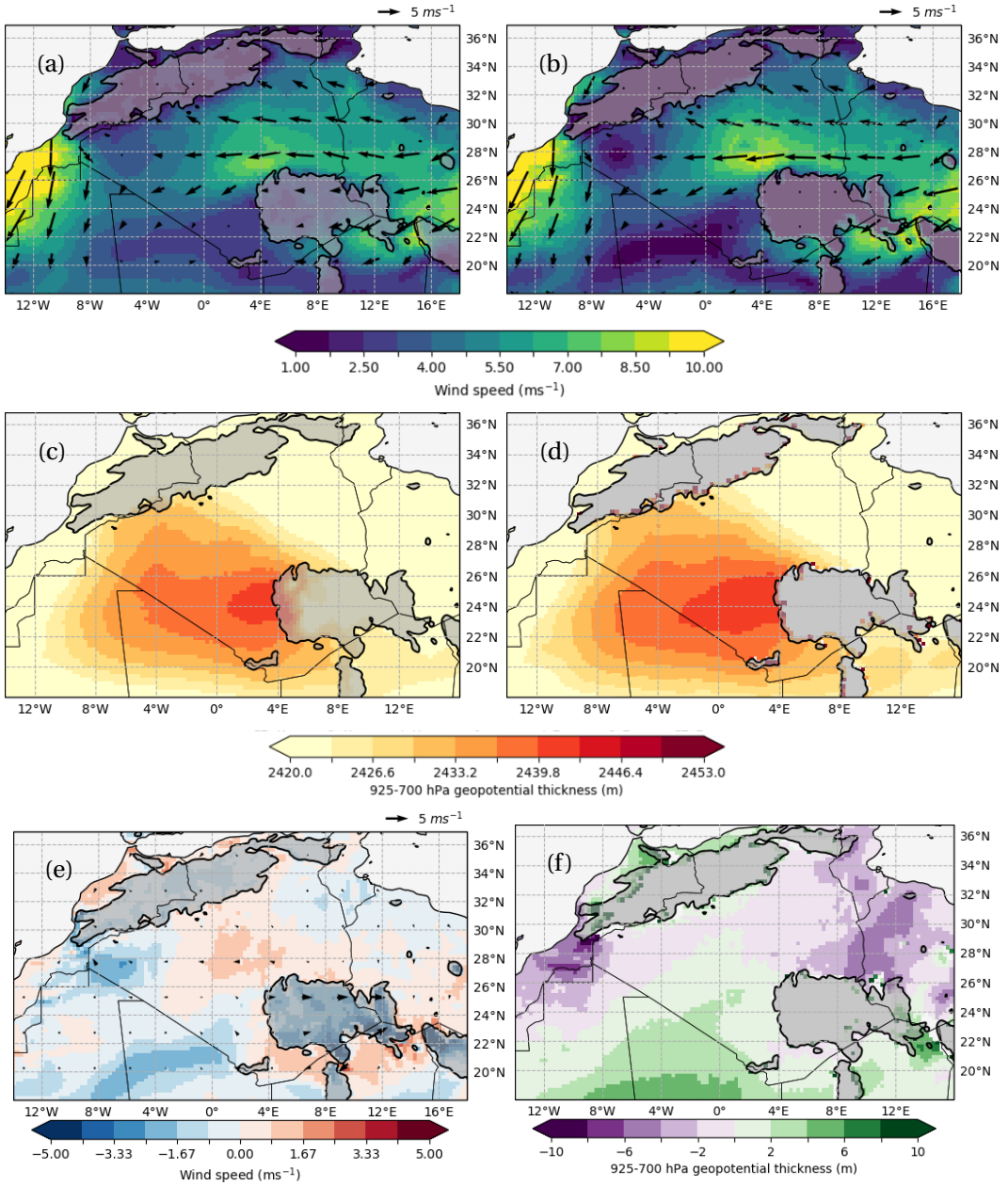


Figure 5.1: Comparison between ERA5 (left) and 12 km horizontal resolution Unified Model remapped onto the ERA5 horizontal grid (right). Filled contours in (a) and (b) represent 925 hPa wind speeds (ms^{-1}). Filled contours in (c) and (d) are the thickness of the 925-700 hPa geopotential height layer (m). (e) and (f) show the difference between the two fields (UM minus ERA5) for the 925 hPa wind field and geopotential thickness, respectively. Both quantities are averaged over June, July and August of 1997-2007. Regions above 700m elevation are contoured and shaded in grey.

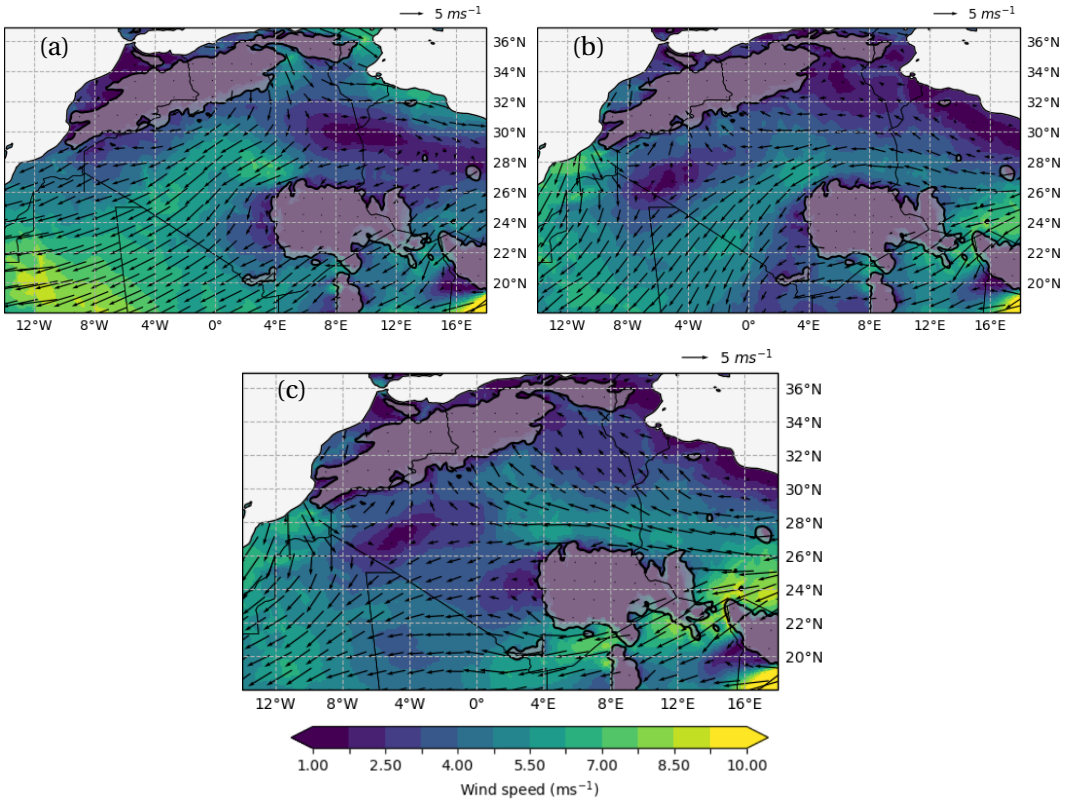


Figure 5.2: Mean 925 hPa control experiment wind speeds (ms^{-1}) outside of summer, including (a) DJF, (b) MAM and (c) SON for the period 1997-2007. Regions above 700m elevation are contoured and shaded in grey.

to ERA5, which may be due to a deeper SHL (Figures 5.1c and d), driving a sharper pressure gradient through central Algeria as well as due to the higher spatial resolution of the UM (12km compared to 30km in ERA5).

An interesting feature of the Tidihelt jet is that it appears as a small local wind maximum year-round (Figure 5.2), including when the SHL is situated much further south than its central Saharan position in JJA (Lavaysse et al. 2009). This shows that a local control is important for the position of these high winds, rather than simply being the result of synoptic pressure patterns. Nonetheless, the jet is at its strongest in JJA (Figure 5.1b).

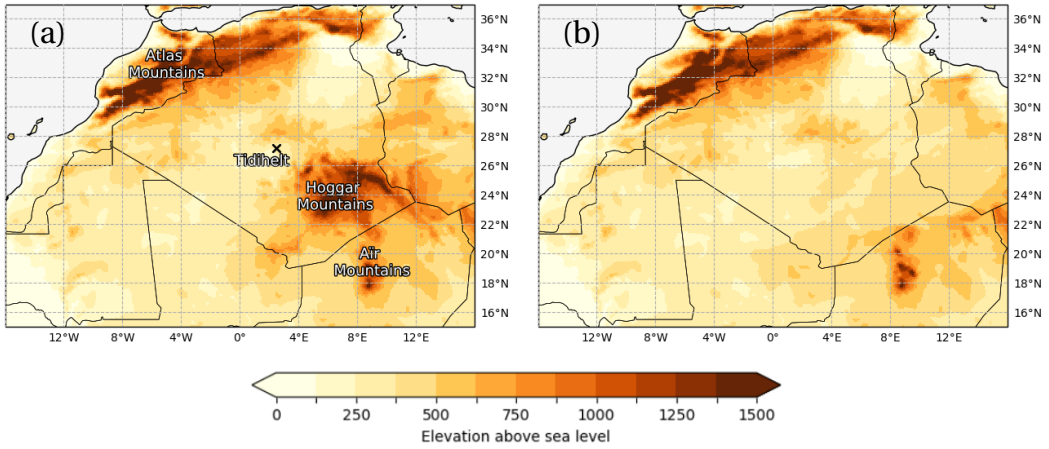


Figure 5.3: Representation of orography as elevation above sea level in the 12 km UM simulations for the control experiment (left) and the FLATHOGGAR experiment (right). Relevant geographical features are labeled in (a), as well as a black cross indicating the location of In Salah where sonde ascents were obtained.

5.3.4 Orography experiments

Two simulations are run. In the first (CONTROL, Figure 5.3a), the UM is run with full orography over the limited area domain. In the second run (FLATHOGGAR, Figure 5.3b), the region encompassing the Hoggar mountains is smoothed to a uniform level. Unlike Birch et al. 2012, we do not remove the Aïr mountains at 19°N, 9°E as our goal was to isolate the role that mountains adjacent to the Tidihelt region have upon winds there; furthermore, the Aïr Mountains are an important site of late summer convective triggering (see Redl et al. 2015, Figure 6 therein) which could have an impact upon the low-level monsoon circulation. The same lateral boundary conditions are supplied by ERA-Interim in both experiments, meaning that although the removal of the Hoggar mountains may influence the large-scale flow beyond the limited area domain, this effect is not accounted for in this paper.

One approach tested for flattening the Hoggar region was to apply a mask and level all terrain therein to a maximum of 350 m above sea level. This introduced sharp horizontal discontinuities, especially towards the east of the domain around 12-14°E which produced local wind acceleration in the simulations.

In addition, this approach introduces a region of totally flat land, meaning subgrid parameterizations including flow blocking, form drag and gravity wave drag would be set to zero, which would be difficult to disentangle from the effect of the mean orography. The solution adopted here is to smooth the mountains by cloning terrain from the lowlands in the central Saharan Erg Chech and El Djouf (4°W-0°E) over the Hoggar plateau, introducing a more gradual incline towards the higher elevation of eastern Algeria and Libya. Terrain from the western Sahara is selected for cloning as it is homogeneous in elevation over spatial scales of hundreds of kilometres and therefore best approximates a flat sand sheet with no orography.

Edits are applied to a 1 km resolution topography dataset prior to using this dataset to generate the UM ancillary files describing the properties of the orography thus ensuring representations of sub-grid orography, including the effects of flow blocking, orographic form drag and orographic gravity wave drag are calculated consistently following the method described in Walters et al. 2017 (see Section 2.6 and 3.5 therein). In summary, effects at the smallest scales (at which buoyancy effects are negligible) are represented by an effective roughness length (i.e. indirectly) while sub-grid orographic effects at larger scales up to the model resolution are represented with a drag scheme originally developed by Lott and Miller (1997) with slight modifications described in Section 3.5 of Walters et al. (2017). No changes are made to albedo, which is tested in more detail in Birch et al. 2012 and shown to exert a smaller influence on the boundary layer than the orography itself. Surface roughness is also not edited in these experiments beyond the effective roughness length described above.

5.3.5 Composite method

The composite method in this paper selects high northeasterly surface wind days with visible dust emission. Compositing is used in this analysis rather than a simple comparison between quantities averaged over the whole of the simulations

for two reasons. Firstly, although northeasterlies are the most common wind regime in the Tidihelt region, other wind regimes are active through summer due to occasional incursions from monsoon winds and Atlantic inflow. Secondly, high wind days are disproportionately important for dust emission. The bulk of the results presented in this paper are obtained from a comparison of composited days between the two experiments. An analysis of the overall effect on the potential for dust emission across all days is presented in Section 5.5.4, however. Dates to select for compositing are derived from the control experiment data and applied to both experiments.

A sub-domain within the limited area of the model simulations is delineated and corresponds to the Tidihelt Depression in central Algeria, described in more detail in Caton Harrison et al. 2019. The boundaries are 25 to 28°N, 1.5°W to 3°E. Henceforth, this is referred to as the TID region.

Mornings with high surface winds and visible local LLJ-linked dust emission in the control experiment TID region are selected for compositing. It is important to emphasise that dust emission is not computed in the model simulations, hence information about emission must be obtained from the contemporaneous satellite record. The period of June, July and August (JJA) 2004-2007 is used as this contains an overlap between the period for which UM data is available (1997-2007) and the period for which SEVIRI dust tracking has been performed (2004-2017). Each selected day must fulfil the following conditions for the day to count as a dust day:

1. At least 500 total dust pixels visible between 0500 and 1300 UTC in SEVIRI in the TID region which the algorithm from Caton Harrison et al. 2019 identifies as LLJ dust;

2. Any dust observed is freshly emitted (within the same morning).

3. Mean 10 metre wind speed within the TID region exceeds 7 ms^{-1};

4. Mean 10 metre wind direction within the TID region for the day is between 0 and 90°;

A wind direction constraint is included in order to limit the analysis to a northeasterly wind regime associated with the dry Harmattan. As identified in Section 5.3.3, the existing analysis of UM performance in Allen and Washington 2014 indicates that fidelity is excellent for northeasterly jets. On the other hand, it is relatively poor for southwesterly jets embedded within the monsoon. Northeasterlies are by far more common than southwesterlies in the TID region.

The 30 days with the highest mean wind speed and which also fulfil the conditions above are selected for inclusion within the composites. Composites are averaged over 0500-1200 UTC to target a period in which both the core strength of the jet peaks and the mixing of momentum to the surface occurs. Note that an extra hour is included on the end of the SEVIRI dust observation window as occasionally dust plumes emitted in the mid-morning do not become visible until around midday.

The 7 ms^{-1} wind speed threshold chosen here is conservative compared to estimated dust emission thresholds at surface stations in central and southern Algeria (Cowie et al. 2014), but provides a good sample of days to choose from given the limited time analysis time period of 4 years; 46 days fulfilling each composite condition are found, of which the top 30 are selected. For a clearer picture of the likely dust emission threshold for the TID region, an analysis of the relationship between simulated winds on these composite days and observed dust is given in Section 5.5.4.

5.4 Synoptic conditions

Lag-lead composites of 1200 UTC soundings from In Salah (Figure 5.4) reveal that a cold northeasterly boundary layer anomaly accompanies strong winds and

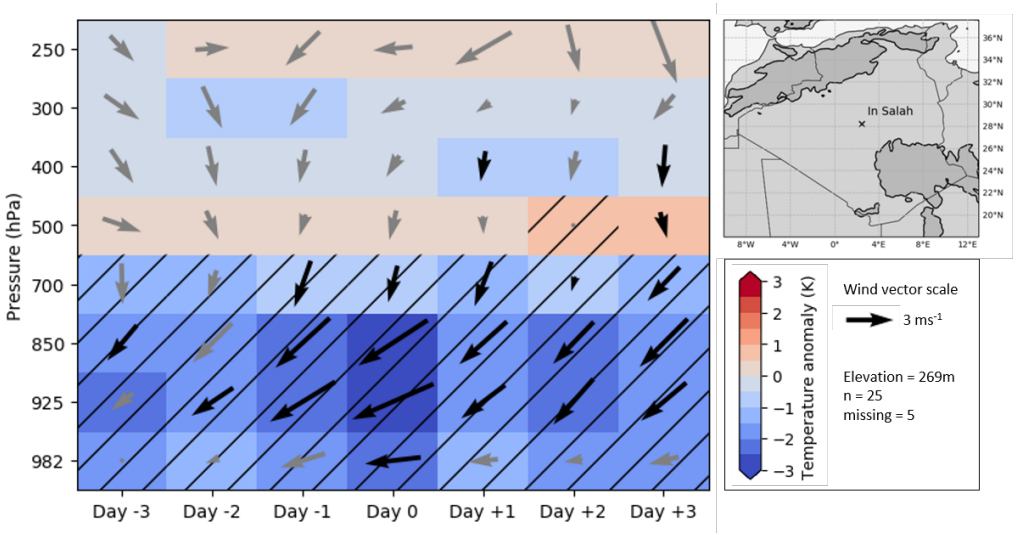


Figure 5.4: Time versus height composite sonde measurements of temperature anomaly (shaded boxes) and wind speed/direction anomaly seen from a bird's eye view (arrows) taken at 1200 UTC at In Salah relative to the mean for June, July and August 1997-2007. Each column represents a lag relative to the composite event at Day 0. Temperature anomalies significant at the 95% level are hatched. Wind speed anomalies significant at the 95% level are represented in bold. An inset map identifying the location of the sonde launches is shown in the top right.

dust emission over the Tidihelt region. Cold anomalies of -0.5 to -3 K, significant at the 95% level, are observed up to 700 hPa through from Day -3 to Day +3. By Day -1 there is a significant northeasterly anomaly of 4.8 ms^{-1} at 925 hPa, backing to northerly at 700 hPa. The coldest layer is found at 925-850 hPa on Day 0 along with a wind anomaly of 5.6 ms^{-1} at 925 hPa and a 3.6 ms^{-1} anomaly observed at the surface level of 982 hPa. Days +1 to +3 see a continued cold anomaly with winds backing more northerly.

Patterns in the fields from the UM control experiment map on well to observations from Figure 5.4 and reveal the synoptic processes driving the wind anomalies (Figure 5.5a-d). A cold anomaly extends from the Mediterranean to central Algeria, advected by northeasterlies which reach their westernmost extent on Days 0 and +1. This strengthens winds through the Harmattan LLJ alley into the core of the SHL and also drives an intense warm anomaly on the Atlantic coast by blocking cooler maritime inflow.

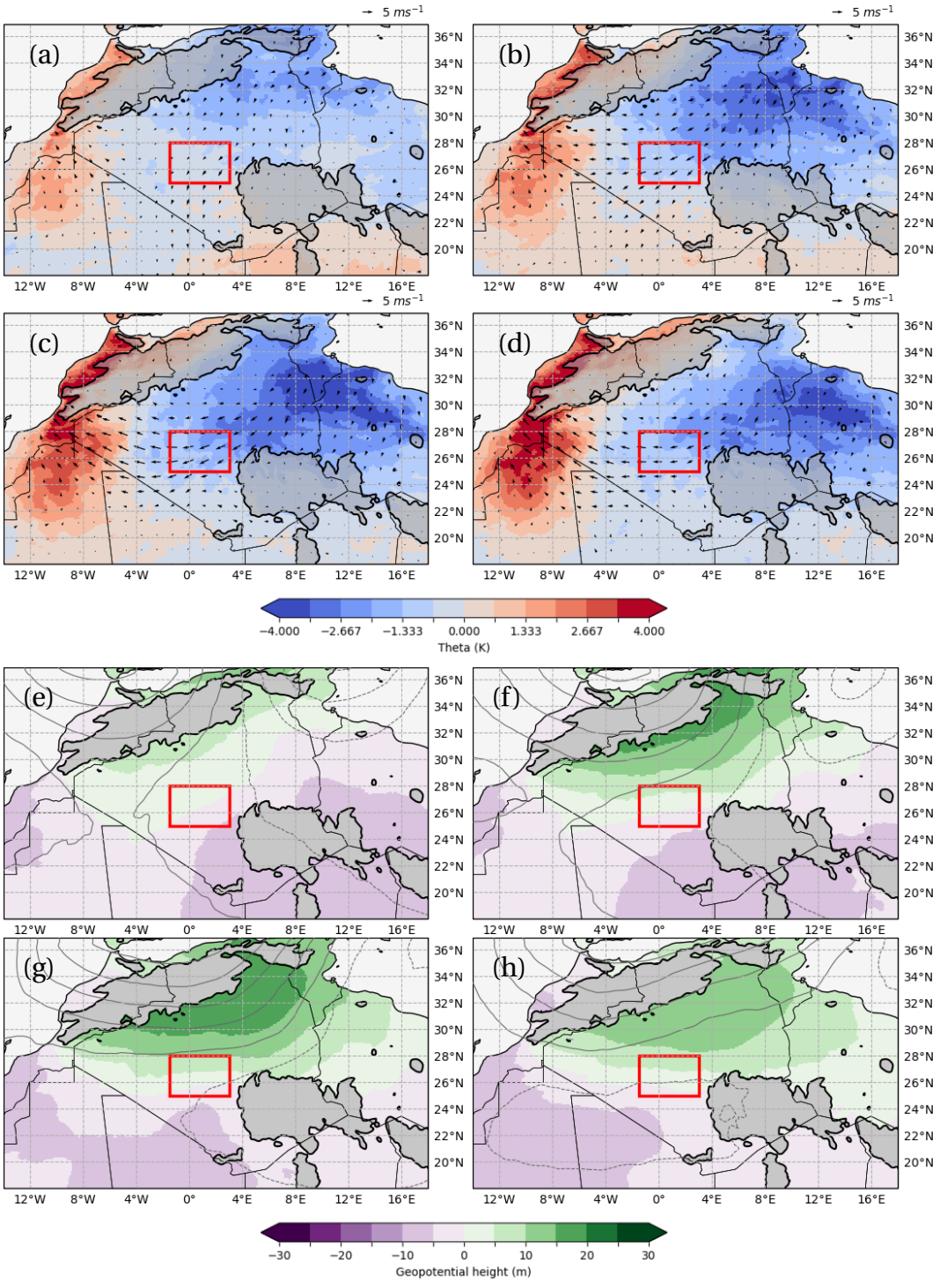


Figure 5.5: Upper plots (a-d) show control experiment composite anomaly potential temperature at 130m height (filled contours) with wind vectors relative to the mean for June, July and August 1997-2007, going from day -2 (a) to day +1 (d). Lower plots (e-h) show control experiment 925 hPa composite anomaly geopotential height (filled contours) and 200 hPa geopotential height (contours, negative where dashed) relative to June, July and August 1997-2007, going from day -2 (e) to day +1 (h). The red box identifies the region from which high wind/dust days are selected for the composite. Regions above 700m elevation are contoured and shaded in grey.

Intensification of subtropical low-level high pressure over the eastern Sahara associated with intrusion of a midlatitude trough and cold inflow from the Mediterranean has long been linked with strengthened Harmattan winds (Kalu (1979), Figures 5.4 and 5.5). Synoptic conditions shown in Figure 5.5 resemble a typical Mediterranean cold surge event which can persist over North Africa for up to 10 days and which are linked to an enhanced upper tropospheric ridge-trough pattern (Vizy and Cook 2009). Upper level ridging over the Atlas mountains in the UM simulation is accompanied by a trough over the Mediterranean (Figure 5.5e-h) which propagates eastward through the composites. At low levels, a low-pressure anomaly is seen to travel westwards, with low pressure in the lee of the Hoggar mountains at Day 0, accompanied by a deepened SHL and intense anticyclogenesis over the Atlas mountains, producing conditions associated with a high North African Dipole Index (NAFDI) (Rodrıguez et al. 2015).

In the remainder of the paper, we study the low-level circulation patterns for the lag 0 composite days in both the control and FLATHOGGAR simulations.

5.5 Model experiment results

5.5.1 Wind speed and vertical structure

925 hPa composite winds in the control experiment (Figure 5.6a) exhibit a maximum northwest of the Hoggar mountains, extending from 6°E to the Algerian border with Mali and Mauritania. Northeasterlies between 56° and 79° account for over 40% of composite winds averaged across the TID domain. TID is also situated at a confluence with southeasterlies along the western flank of the Hoggar mountains. The northern limb of the SHL circulation is found around northern Mali at 24°N, with northerlies across Mauritania.

A substantial reduction in wind speeds occurs over the Tidihelt region in the absence of the Hoggar mountains (Figure 5.6c), with mean composite winds within TID dropping from 9.0 to 7.3 ms^{-1}. A slight local maximum nonetheless

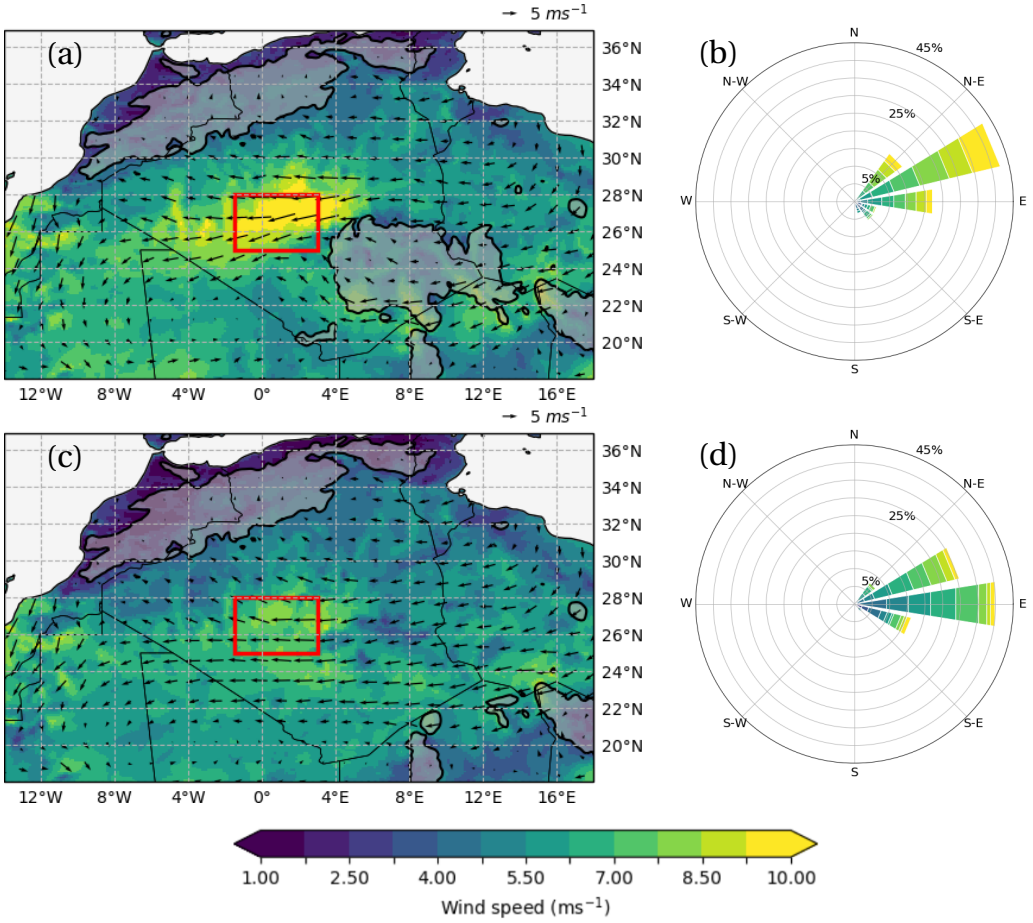


Figure 5.6: Composite 925 hPa absolute wind speeds (left, filled contours and wind vectors) for the control (upper) and FLATHOGGAR (lower) experiments. Wind roses are shown on the right, calculated from the average of the 925 hPa winds within the composite region (red boxes). Regions above 700m elevation are contoured and shaded in grey.

persists over central Algeria. A shift in the wind regime can be seen over the TID region (Figure 5.6b), with winds in the 56 to 79° range reduced (Figure 5.6d) in favour of easterlies (79 to 101° on the wind rose), which also prevail over the region previously occupied by the Hoggar mountains. Southeasterlies are no longer evident in southern Algeria and the SHL circulation appears to be shifted southward, with a northern limb extending down to 22°N and reduced northerlies in eastern Mauritania.

It should be noted that a potential drawback of a compositing approach here is that data in the control experiment is selected for high wind speeds, whereas data

in the counterfactual FLATHOGGAR experiment is not; removal of orography could affect the timing of high wind events and the wind regime in which they occur and hence cause winds to peak on different days. When the same analysis as in Figure 5.6 is carried out for the entire dataset instead of composite days, a similar result emerges in a subtler form; the dominant shift is still a reduction of wind speeds proximate to the Tidihelt (by 10.1% instead of the 18.9% obtained with compositing) and a slight preference for easterlies over northeasterlies (not shown). The effect of orography upon modeled winds is therefore greater than usual on days with synoptic forcing driving an intense northeasterly jet. There is no indication, however, that the strongest winds seen on composited control days occur at other times in the FLATHOGGAR results. Further evidence of this may be found in Section 5.5.4 (Figure 5.13a) in which non-composited wind speed distributions are compared for the two experiments.

A composite cross section across the TID region in the control experiment reveals that the Tidihelt jet is a low-level nocturnal feature, extending to approximately 1800 m above sea level at 00 UTC (Figure 5.7a). The jet core is close to the surface at 1000 m above sea level or approximately 100 m above the surface. During the day, winds within the boundary layer are well-mixed with a much slower core below 10 ms^{-1} extending up to above 2000 m above sea level (5.7b). Although the nocturnal jet extends from 1 to 6°E, the highest winds are found south of the Tademaït Plateau in the low-lying Tidihelt Depression, corresponding to the TID region (25 to 28°N, 1.5°W to 3°E). In the FLATHOGGAR experiment (Figure 5.7c-d), the jet core is significantly eroded and less clearly defined, although the winds are still accelerated nocturnally (Figure 5.7c).

5.5.2 Leeward circulation

The difference between the two experiments at 850 hPa reveals a circulation pattern centred over the TID (Figure 5.8). The circulation has a northern

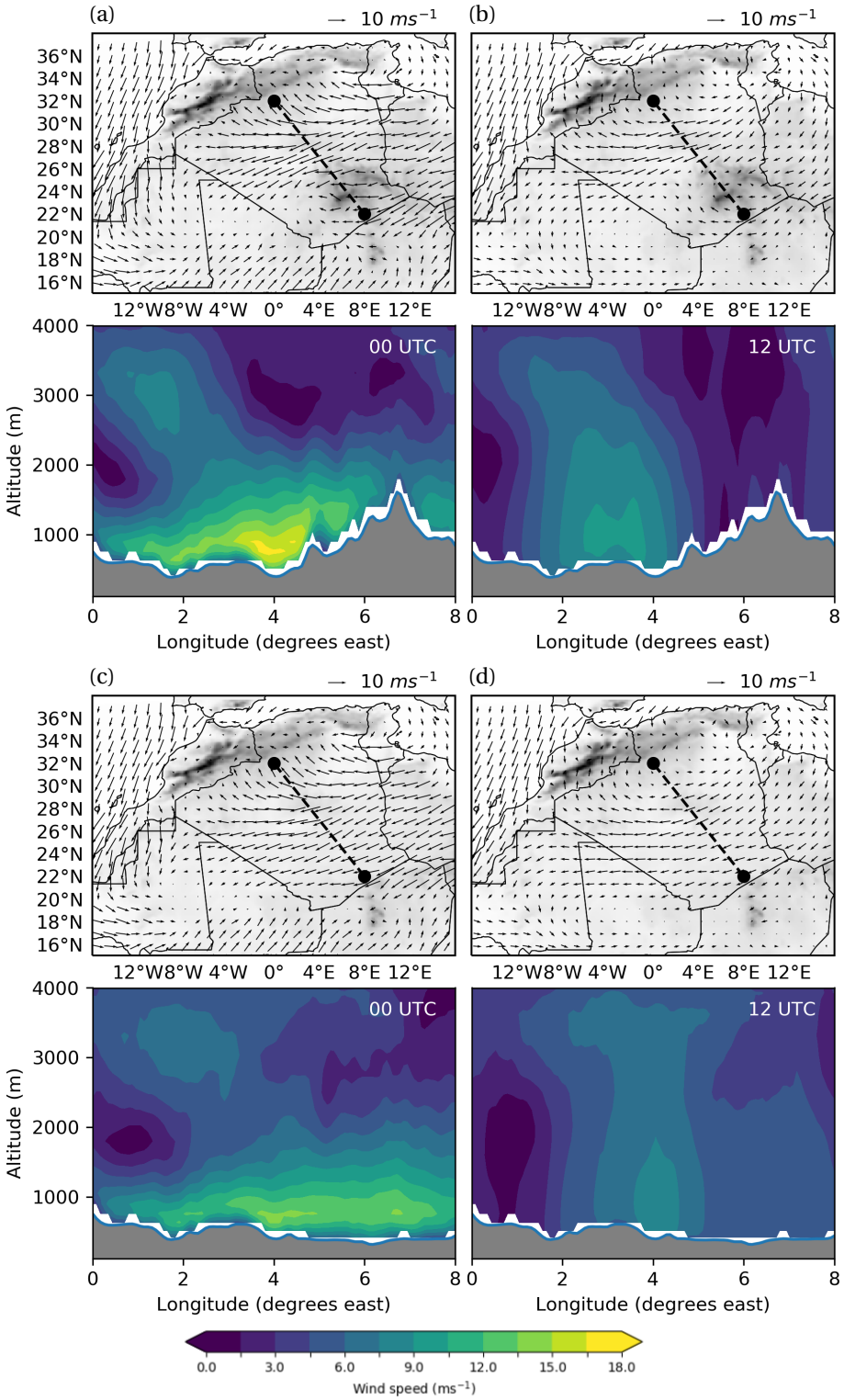


Figure 5.7: Composite cross sections of wind speed (filled contours) calculated across the axes plotted as dashed lines on the horizontal wind field maps above each cross section, in which composite wind barbs at 925 hPa are also plotted and orography shaded in the background. Composite times of 00 and 12 UTC are shown for the control experiment (a and b) and the FLATHOGGAR experiment (c and d). Model orography for both experiments is shaded in dark grey over the composite cross sections.

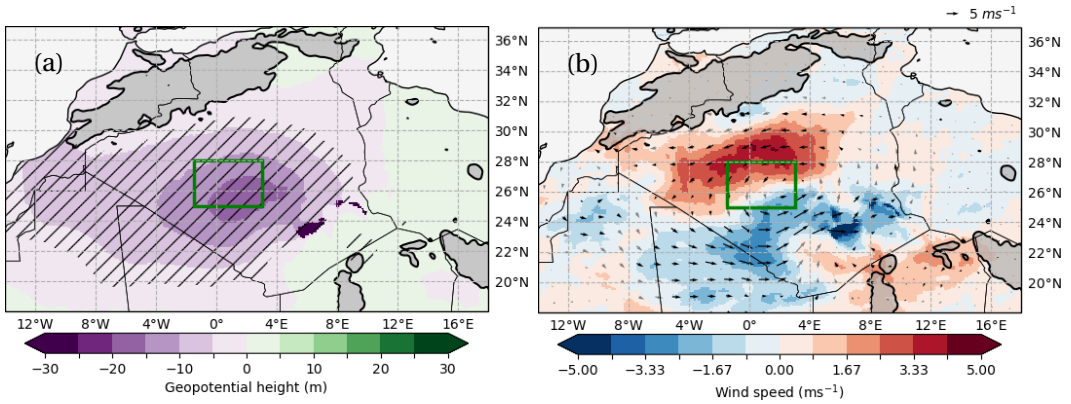


Figure 5.8: Control minus FLATHOGGAR experiment composite (a) 850 hPa geopotential height and (b) 850 hPa wind field (wind speed as filled contours). Significant geopotential height differences at the 95% level are hatched. Significant wind speed differences at the 95% level are shown as bold black wind vectors. The green box identifies the region from which high wind/dust days are selected for the composite.

limb of northeasterly anomalies through central Algeria and a southern limb of southeasterlies and easterlies in the lee and over the Hoggar mountains (Figure 5.8b). This is associated with a geopotential height perturbation of -15 to -20 m over the TID region at 850 hPa (Figure 5.8a), with significant differences of 5-10 m as far west as the Atlantic coast.

East-west cross sections through the Hoggar mountains indicate a diurnal variation in the circulation pattern. In both the control (Figure 5.9a-d) and FLATHOGGAR (Figure 5.9e-h) experiments, easterlies persist nocturnally, albeit weakened on the western slopes in the control. During the day, however, (Figures 5.9c and d) easterlies drop to zero in the control, whereas in FLATHOGGAR they are maintained at 3-5 ms^{-1} (Figures 5.9g and h). This suggests an upslope wind anomaly in the control experiment driven by enhanced sensible heat fluxes over the elevated terrain driving a thermally direct circulation (Wolyn and Mckee 1994; Zängl and Chico 2006). In this instance, however, no actual upslope winds develop as the background flow is too strong. Differences between the meridional circulation are more stark; whereas in FLATHOGGAR a mild southerly component is present at 0600 UTC (Figure 5.10f) and eroded entirely

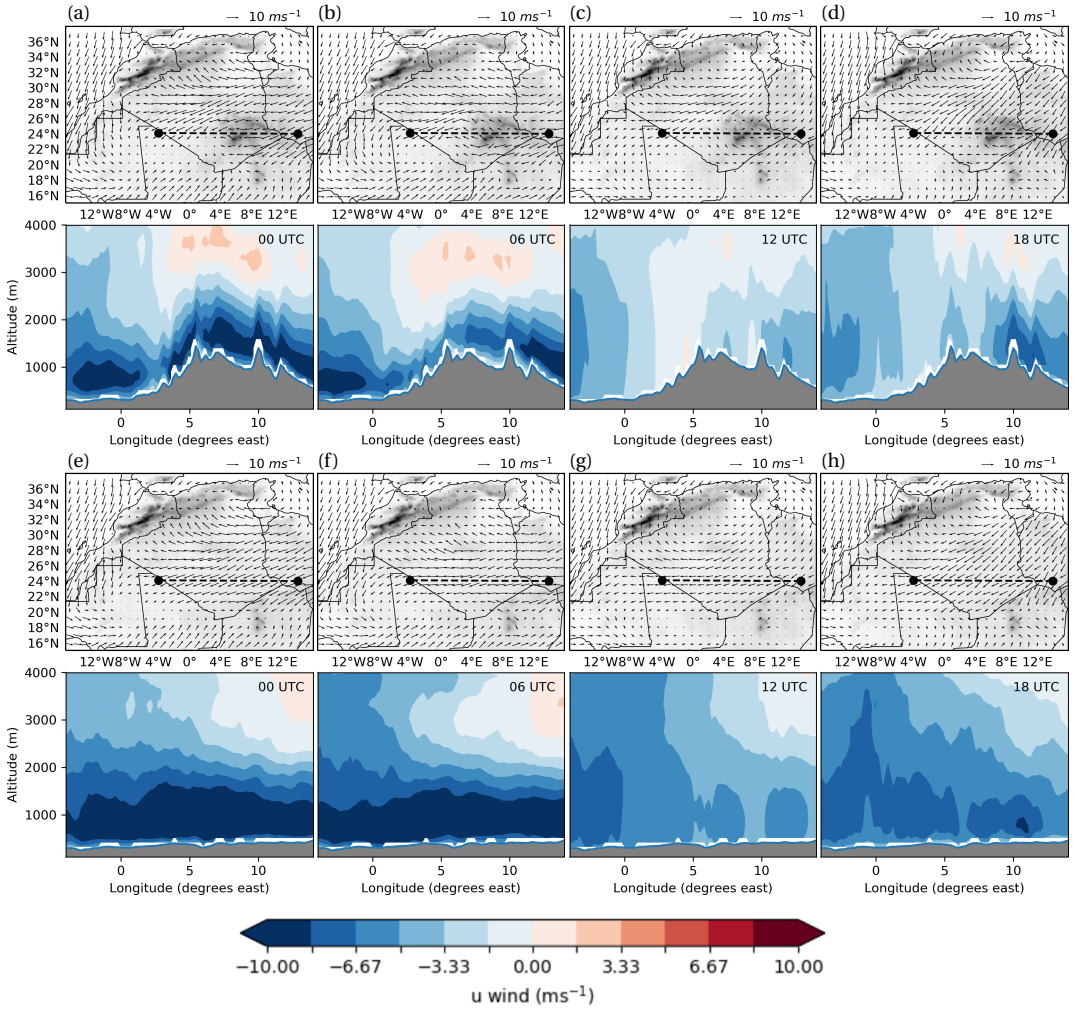


Figure 5.9: Composite cross sections of u winds for the control (a-d) and FLATHOG-GAR (e-h) experiments. Cross sections are calculated across the axes plotted as dashed lines on the horizontal wind field maps above each cross section, in which composite wind barbs at 925 hPa are also plotted an orography shaded in the background. Composite times of 00 (a,e), 06 (b, f), 12 (c, g) and 18 UTC (d, h) are shown. Model orography for both experiments is shaded in dark grey over the composite cross sections.

during the day (Figure 5.10g), in the control experiment a southerly flow develops overnight over the peak of the Hoggar and reaches a maximum of up to 5 ms^{-1} at 0600 UTC (Figure 5.10b) at which point it is located over the western mountain lee slopes. The result is a net southeasterly into the Tidihelt Depression. During the day this flow weakens and shifts further westward (Figure 5.10c).

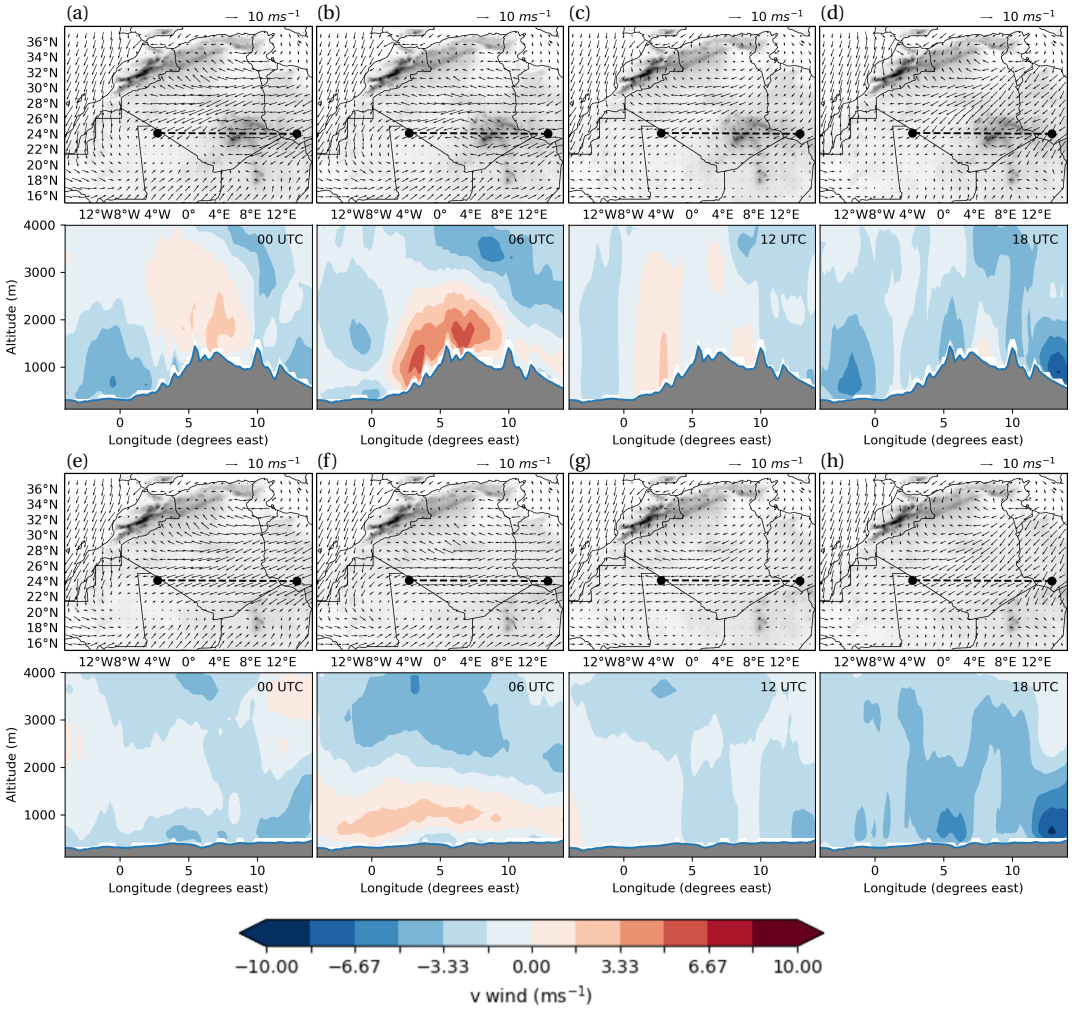


Figure 5.10: Composite cross sections of v winds for the control (a-d) and FLATHOGGAR (e-h) experiments. Cross sections are calculated across the axes plotted as dashed lines on the horizontal wind field maps above each cross section, in which composite wind barbs at 925 hPa are also plotted an orography shaded in the background. Composite times of 00 (a,e), 06 (b, f), 12 (c, g) and 18 UTC (d, h) are shown. Model orography for both experiments is shaded in dark grey over the composite cross sections.

The Hoggar mountains are subject to intense heating during the day. The difference between potential temperature fields of the two experiments becomes greatest at 1200 UTC (Figure 5.11c), with a peak over the summit extending up to 3,000 m in a dome shape. During the night, this heating anomaly shifts westward (Figures, 5.9d, a and b) and is situated within a residual layer above the surface over 0-5°E. This elevated heating due to the presence of the Hoggar mountains induces a horizontal temperature gradient over the plateau (about

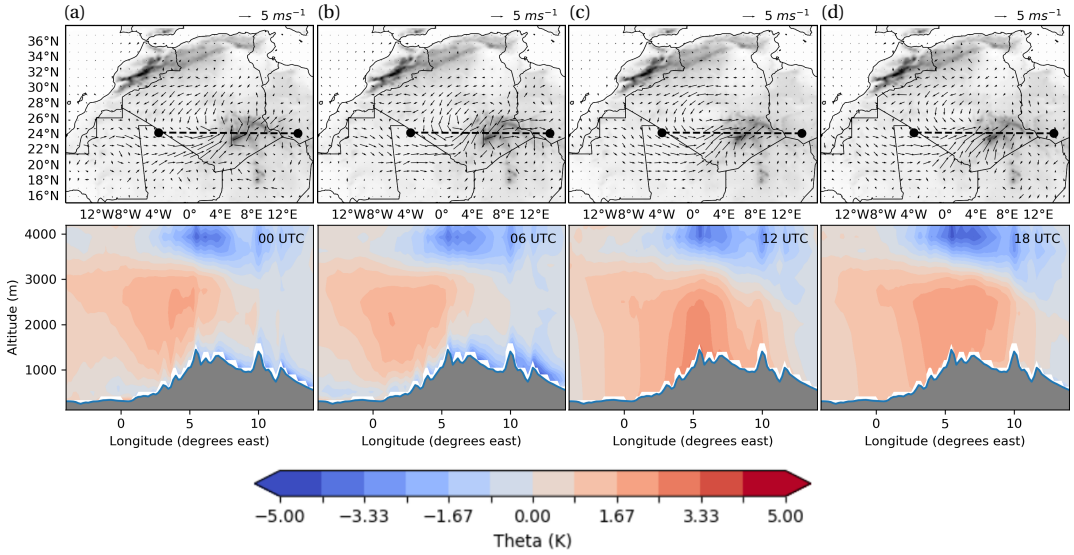


Figure 5.11: Composite cross sections of air potential temperature for the control minus FLATHOGGAR experiments. Cross sections are calculated across the axes plotted as dashed lines on the horizontal wind field maps above each cross section, in which control minus FLATHOGGAR composite wind barbs at 925 hPa are also plotted and orography shaded in the background. Composite times of (a) 00, (b) 06, (c) 12 and (d) 18 UTC are shown. Model orography from the control experiment is shaded in dark grey over the composite cross sections.

1500 m elevation) relative to the low lying Sahara to the west (about 300 m elevation). A gradient between the cooler maritime west and the SHL exists in the absence of the mountains (not shown) but is greatly intensified when elevated terrain is present. The existence of elevated heating and baroclinicity suggests that the Hoggar mountains may be capable of setting up a thermal low or trough within the much broader SHL, deepening and extending it.

The Tidihelt jet is a nocturnal phenomenon; 925 hPa composite winds in the Tidihelt region reach their maximum at midnight UTC and minimum at 1300 UTC, whereas the minimum mean 925 hPa geopotential height in the lee of the Hoggar mountains occurs at 1700 UTC (not shown). This temporally shifted relationship aligns with the theoretical behaviour of heat lows which develop to their lowest central pressure in the afternoon and evening. Being out of quasi-geostrophic balance, however, the peak winds and relative vorticity occur several hours after the pressure minimum (Rácz and Smith 1999; Spengler and

Smith 2008). The exact timing of the peak in low-level winds can also depend on the coriolis parameter and its effect on inertial oscillation (Rácz and Smith 1999) ; this is tested by Heinold et al. (2015) who show that a later timing of maximum supergeostrophy (i.e. closer to sunrise) is favoured at 20°N compared to 30°N, with the Tidihelt at a latitude of about 26°N. A daytime minimum in low-level winds is driven by intense mixing of the convective boundary layer, which inhibits horizontal flows (Parker et al. 2005a). Furthermore, it is plausible that the background easterlies act to shift the centre of the heat low westward to its mean position seen in Figure 5.8a, similar to the effect of background easterlies on the Australian heat trough (Spengler et al. 2005).

5.5.3 Geostrophic wind analysis

To test the role that elevated heating could have upon winds in the Tidihelt notwithstanding any additional dynamic effects, we estimate the geostrophic winds induced by a heating anomaly equivalent to the difference between the control and FLATHOGGAR experiment. It should be noted that as the diabatic heating and cyclonic circulation are out of phase the real Tidihelt jet is not in geostrophic balance; furthermore its peak core wind speeds are subject to supergeostrophy due to inertial oscillation. These estimates instead serve to identify the expected spatial pattern of winds induced by thermal forcing for comparison with Figure 5.8.

Atmospheric thickness is estimated for the 925-700 hPa layer from the temperature profile of the control and FLATHOGGAR experiments to account for the heating effect of the Hoggar mountains. Assuming hydrostatic balance, the atmospheric thickness in a given layer corresponding to a temperature profile is given by the hypsometric equation:

$$z_2 - z_1 = \frac{R_d}{g} \int_{p_1}^{p_2} T_v \mathrm{d} \ln p \tag{5.1}$$

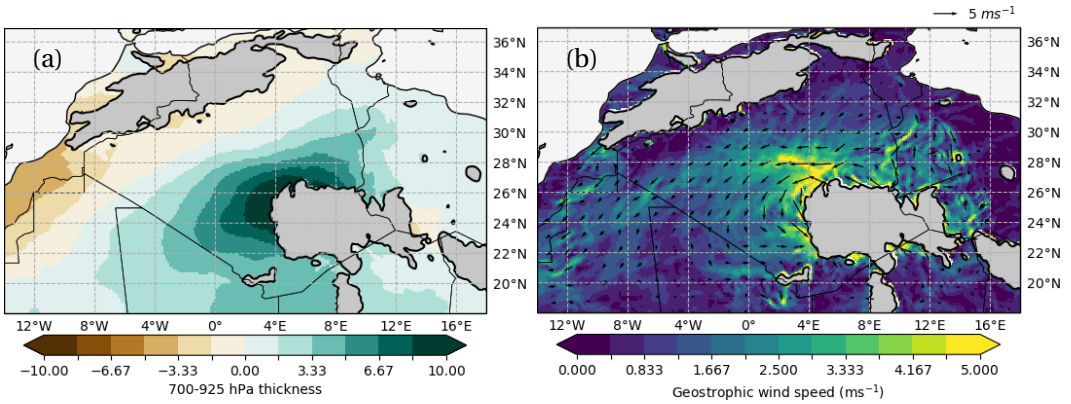


Figure 5.12: (a) Estimated 925-700 hPa geopotential thickness difference given the difference in the temperature profile between the control and FLATHOGGAR experiment, averaged across the June, July and August 2004-2007 period, calculated with Equation 5.1. (b) Geostrophic wind speed increase from the FLATHOGGAR to the control experiment which would be induced by a lowering of geopotential height contours by the amount shown in (a).

in which z_1 and z_2 are the lower and upper heights of the layer between pressure levels p_1 and p_2 (925 and 700 hPa in this instance), R_d is the gas constant for dry air, g is gravity and T_v is the virtual temperature.

The difference between the estimated atmospheric thickness of the two experiments (Figure 5.12a) shows a thickness anomaly of over 10 m centred over the lee of the Hoggar mountains, in close resemblance to the 850 hPa anomaly (Figure 5.8a). Negative differences (warmer temperatures in the control) extend through central Algeria and into Mali, with evidence of positive differences (cooler temperatures in the control) along the west coast. This pattern is comparable to the SHL itself (Figure 5.1d) but its core is situated slightly further east over the Hoggar mountains themselves. Nonetheless, these results suggest the presence of the mountains is capable of introducing elevated heating which could deepen or extend the SHL.

To understand the effect such heating could have upon the winds, we compute the geostrophic wind anomaly induced if geopotential heights at an arbitrary level (within 925 to 700 hPa) were lowered by the thickness differences shown

in Figure 5.12a. The results show a circulation pattern centred around the thermal low (Figure 5.12b), with peak geostrophic winds in excess of 5 ms^{-1} within and upstream of the TID domain where the pressure gradient peaks. This circulation closely resembles the spatial structure of the wind difference between the control and FLATHOGGAR experiments at 850 hPa (Figure 5.8b). Such a similarity suggests that heating alone is capable of explaining the pressure pattern and that a local maximum in winds over the Tidihelt is the result of a thermodynamically forced nocturnal low-level jet.

Our explanation for lee cyclogenesis over and west of the Hoggar mountains does not rely on the generation of an upstream anticyclone at low levels to enhance northeasterly winds as shown in the comparable idealised model experiment of Semazzi and Sun 1997. In contrast with their analysis, our composite appears to show only minor differences in anticylonic circulation on the windward side of the Hoggar mountains (Figure 5.8a) although an enhanced anticyclonic return flow is observed atop the leeward circulation, especially above 500 hPa. Instead, the results suggest that the enhanced elevated heating of the boundary layer is the primary control upon the deepening of the eastern SHL and enhancement of the winds through the Tidihelt.

A low level lee circulation over central and southern Algeria appears in each climatological season (not shown), suggesting it is a stationary feature which helps maintain the elevated winds in the Tidihelt through the year (Figure 5.2), with peak strength when the lee circulation is collocated with the SHL in summer.

5.5.4 Role in dust emission frequency

The Tidihelt depression is an important and frequently activated dust source (Schepanski et al. 2007; Ashpole and Washington 2013a; Caton Harrison et al. 2019). Our results show that the Hoggar mountains play an important role in accelerating low level winds over the region. We hypothesise that the mountains could therefore be partly responsible for the prominence of this dust source,

meaning they are important for erosivity on their leeward flank. To test this hypothesis, an estimate of the relationship between wind speeds and dust emission is needed. To achieve this, we compare simulated wind speeds with satellite observations of LLJ dust plumes. Unlike previous results, no compositing is applied in this analysis as the aim is to estimate the net effect of orography upon dust emission conditions. Results are instead calculated from all model output from JJA 2004-2007 between the hours of 0500 and 1300 UTC (i.e. when freshly emitted LLJ dust is visible to satellite).

The method for distinguishing LLJ dust from CPO dust in SEVIRI imagery is described in Caton Harrison et al. 2019. In brief, the timing of emission, plume geometry and distance from deep convection is combined in a multiple regression model to assign a value from 0 to 1 to each discrete dust plume masked in SEVIRI data, with higher values indicating a higher probability of being LLJ-associated (other plumes are assumed to originate from convective cold pool outflow activity).

Here, we count dust emission events over the Tidihelt region and assign them to a wind speed bin corresponding to the mean 10m wind speed simulated over the TID domain for the timestep at which the dust is observed. Dust counts are obtained as hourly totals and compared to hourly UM values. Only LLJ dust emitted the same day and within the TID domain is included. In addition, if the sum of cloud pixels (identified where BT 10.8 μm $<$ 270 K, following Caton Harrison et al. 2019) in the domain for the hours of 0200 and 1800 UTC exceeds 500, the day is considered cloud masked and skipped. 0200 and 1800 UTC are chosen to approximately sample the diurnal cycle of cloud cover. This condition results in 21% of hourly timesteps being skipped. The results of this analysis (Figure 5.13b, dark grey bars, with dust frequency as red crosses) give an approximation of the relationship between simulated wind speed and observed LLJ dust emission across JJA 2004-2007. The most commonly occurring wind speeds are in the 3-5 ms^{-1} range, but the winds associated with

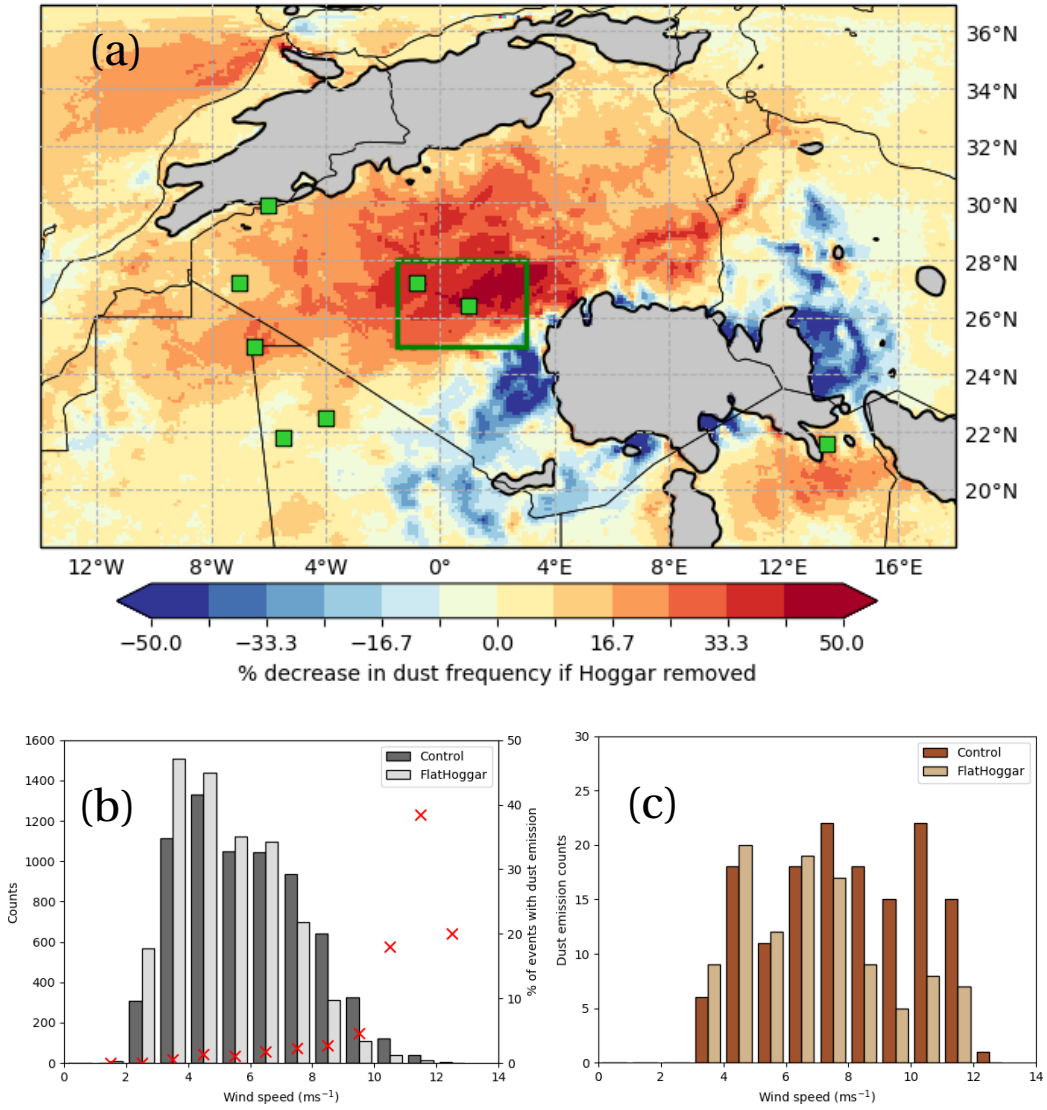


Figure 5.13: (a) Map of estimated percentage decrease in the frequency of dust emission events if the influence of the Hoggar mountains on the low-level wind field were removed, with green squares showing the approximate locations of important LLJ dust sources and a green box identifying the TID domain. In (b), the distribution of hourly composite mean wind speeds in the TID region in the control (dark grey) and FLATHOGGAR (light grey) experiments is shown. The percentage of events which are accompanied by an LLJ Tidihelt dust emission event in SEVIRI is plotted as a red cross for each wind speed bin. (c) shows counts of such emission events in SEVIRI in the TID domain for the control experiment (dark brown) and an estimate of what those counts would be in the FLATHOGGAR experiment given the change in frequency for that wind speed bin (light brown). Model and satellite data is obtained from 0500 to 1300 UTC on all 2004-2007 JJA days.

the highest frequency of dust emission events are found in the 10-12 ms^{-1} range. This exponential increase in dust emission frequency at higher wind speeds is consistent with the theoretical cubic dependence of dust emission on surface wind speed (Marticorena and Bergametti 1995). As lower wind speeds are much more common, the counts of dust events in each bin is relatively even (Figure 5.13c, dark brown). Note that the very highest wind speed bin with any data (12-13 ms^{-1}) has only 16 samples in the control experiment, which may explain why the dust emission frequency drops off again here.

The FLATHOGGAR experiment is observed to shift the 10m wind speed distribution within the TID domain in favour of lower wind speeds (Figure 5.13b, light grey bars), with the largest differences found in the high tail; for example, wind speeds in the 8-9 ms^{-1} range decrease by over 50%. To estimate the effect of this upon dust emission in the Tidihelt, we assume the relationship between wind speed and dust emission holds as a constant between experiments and adjust the frequency of dust emission in each wind speed bin accordingly. For example, 2.8% of wind speed events falling into the 8-9 ms^{-1} wind speed bin have an LLJ emission event observable in SEVIRI at the same time (18 of 643 counts), so for FLATHOGGAR the estimated dust counts would be 2.8 % of 311 counts, or 8.7 counts. This approach results in a 'simulated' distribution of dust emission counts for the FLATHOGGAR experiment (Figure 5.13c, light brown bars). Figure 5.13c is derived for the TID region and hence shows the change in estimated emission frequency for this subdomain. As high wind speeds are so important for dust emission, the effect of changes in the tails of the wind speed distribution is substantial; overall the TID region sees an average reduction in dust emission frequency of 31%. To estimate the wider effect of this shift on the entire model domain, the relationship between wind speed and dust emission is assumed to hold across the entire domain, and an estimated FLATHOGGAR dust emission frequency distribution is calculated at each gridbox based on the shift in the wind speed distribution at that gridbox.

As Figure 5.8b shows, the effect of the Hoggar mountains on the wind field is not unique to the Tidihelt region. Instead, wind speed changes are observed through the entire LLJ alley. To estimate the wider effect of this shift on the entire model domain, the relationship between wind speed and dust emission identified for the TID region in Figure5.13b is assumed to hold across the entire domain, and an estimated FLATHOGGAR dust emission frequency distribution is calculated at each gridbox based on the shift in the wind speed distribution at that gridbox in both the control and FLATHOGGAR experiments. Hence, to achieve this, an estimate of counts of dust emission is derived at each gridbox (whereas above this method was applied to the mean wind distribution averaged across the TID region). The difference between the two experiments' estimated dust emission frequency (Figure 5.13a) indicates how emission frequency in the central and western Sahara might be different in the absence of the Hoggar mountains.

Removing the Hoggar mountains is estimated to have the greatest impact upon dust emission frequency in the Tidihelt region, with percentage decreases over 50% in the 0 to 4°E region most strongly impacted by a combination of background northeasterlies and the leeward circulation observed in Figure 5.8b. Effects are also observed further north close to the southern foothills of the Atlas mountains as well as over northern Mauritania. To give an estimate of the relationship of this wind speed reduction with prominent dust sources, locations with active LLJ-related dust sources are marked in Figure 5.13. These are locations where a cluster of at least four SEVIRI pixels are each flagged with 10 or more LLJ dust emission events from June, July and August of 2004-2017 following the method described in Caton Harrison et al. 2019. As well as sources within central Algeria, reduced wind speeds are observed to affect dust emission frequency at sources in northern Mali, Mauritania and western Algeria. By contrast, the mountains are responsible for increased estimated emission frequencies in the immediate lee as well as upstream in western Libya (12-16°E) as a result of flow blocking and an

upslope wind anomaly induced by the elevated heating discussed in Section 5.5.2, though these regions do not contain clear satellite-observed LLJ dust sources.

Realistically, this counterfactual set of results comes with caveats. First and foremost, discussing the impact of the mountains in terms of an alternative situation in which those mountains didn't exist implies that other conditions would be held constant in such a scenario. Orography is not only responsible for increased erosivity due to accelerated surface winds, however; a large proportion of active dust sources appear to be located close to Saharan mountains around alluvial fans, chotts and sebkhas in the foothills (Middleton and Goudie 2001; Schepanski et al. 2007), suggesting mountains drainage is also a factor in local erodibility. A second caveat is that dust emission thresholds are not constant across North Africa, and a shift in emission frequencies applicable to the Tidihelt does not necessarily hold elsewhere; for example, emission thresholds are thought to be higher in northern Algeria (Cowie et al. 2014). In addition, the lateral boundary conditions are held constant in this experiment but removal of the mountains may be expected to feed back upon the wider circulation. Lastly, as aerosols are prescribed, the modification to the atmosphere in the FLATHOGGAR experiment does not include dust radiative feedbacks, which may directly alter the local circulation via redistribution of heating within the atmospheric column (Miller and Tegen 1998) including boundary layer stability and LLJ formation (Miller et al. 2004; Pérez et al. 2006), or indirectly, for example by introduction of ice condensation nuclei (DeMott et al. 2003; Klein et al. 2010; Price et al. 2018). The advantage of the present setup is its relative simplicity, isolating the local impact of the orography directly upon the winds as an empirically associated proxy for dust emission frequency, and the results show that even a moderate shift in the wind speed distribution can have large impacts on dust emission, but a more sophisticated setup is needed to consider the mediating effects of varied land surface conditions, feedbacks on the wider circulation and feedbacks from dust.

5.6 Summary and conclusions

The role of the Hoggar mountains in dust-emitting wind conditions within the northeasterly LLJ alley through the central Algerian Sahara has been tested with parallel Met Office Unified Model (HadREM3-GA7.05) experiments. Lateral boundary conditions are supplied by the ERA-Interim reanalysis and a composite method is derived using dust plume observations from SEVIRI to identify days with evidence of both high northeasterly winds and visible LLJ-related dust emission within the Tidihelt region of central Algeria, chosen as a representative dust source. Reanalysis, in-situ observations and model simulations suggest a local maximum in wind speeds exists here, identified in this research as the Tidihelt jet.

High wind and dust conditions within the Tidihelt during boreal summer are associated with a long-lived northeasterly cold anomaly within the boundary layer. This is in turn linked to Mediterranean inflow from an intensified subtropical anticyclone and the passage of an enhanced upper level ridge-trough pattern, typical of cold surge conditions.

To test the role of the Hoggar mountains in the existence and strength of the Tidihelt jet, a control experiment is compared with a counterfactual experiment in which the Hoggar mountains are smoothed to be continuous with the Saharan sand sheet over the region of the SHL. The two experiments are run in parallel for the period 2004-2007 to overlap with available SEVIRI data and the 30 composite high wind, high dust days are compared. The following results are found when the Hoggar mountains are removed in the composites:

1. Mean composite wind speeds within the Tidihelt region decline from 9.0 to 7.3 ms^{-1}, although a slight local maximum persists over central Algeria;

2. The wind regime shifts from favouring northeasterlies to a more easterly prevailing wind;

3. The Hoggar mountains are responsible for a geopotential height perturbation at 850 hPa of -15 to -20 m over the TID region, but with significant differences extending as far west as the Atlantic coast;

4. The northern limb of this cyclonic circulation anomaly is collocated with the Tidihelt jet;

5. A dome-shaped daytime elevated heating anomaly situated over the Hoggar mountains can explain the simulated wind field difference between the experiments, indicating an orographic thermal low is responsible for peak Tidihelt winds;

6. Based on an empirical relationship between surface wind speeds and LLJ dust observed in SEVIRI imagery, an absence of Hoggar mountains is estimated to reduce dust emission frequency over the Tidihelt region by an average of 31%.

The results of this orography experiment show that the Hoggar mountains play a direct role in the surface wind field of the northern Sahara, including the dusty northeasterly low-level jet alley through central Algeria. Elevated diabatic heating is shown to be an effective explanation for accelerated low-level flow around a shallow heat low disturbance centred around the lee of the Hoggar mountains. This, in turn, is estimated to have a substantial role in dust emission frequency in LLJ-dominated regions.

This work contributes to a body of literature demonstrating the role that orography plays in both the erosivity and erodibility of key western Saharan dust sources. However, it is limited in scope to LLJs, which are thought to play a secondary role in summertime dust emission. The availability of convective-permitting simulations (e.g. Knippertz et al. (2009), Marsham et al. (2011), and Heinold et al. (2013)) and cold pool outflow parameterizations (e.g. Grandpeix and Lafore (2010) and Pantillon et al. (2015)) mean more attention could be

devoted to orographic impacts upon convective triggering and cold pool formation around southern Saharan and Sahelian dust sources. The dust budget from year to year in the Sahara is a function of both the availability of erodible material and the frequency and strength of mesoscale meteorological emission mechanisms. Efforts to understand the controls on these emission mechanisms will allow model estimates of dust emission to be constrained via improvements to driving wind fields.

5.7 Acknowledgements

MSG SEVIRI data are available online from the EUMETSAT Data Centre (`https://navigator.eumetsat.int/product/EO:EUM:DAT:MSG:HRSEVIRI`). ERA5 data is maintained by the European Centre for Medium-Range Weather Forecasts and is available from the Copernicus Climate Change Service (`https://climate.copernicus.eu/climate-reanalysis`). IGRA data can be accessed from the National Centers for Environmental Information at `https://www.ncdc.noaa.gov/data-access/weather-balloon/integrated-global-radiosonde-archive`. TCH is funded through the NERC doctoral training partnership (NE/L002612/1). RW was partly supported by the NERC-Department for International Development (DFID)-funded Improving Model Processes for African Climate (IMPALA) project (Grant NE/M017206/1), as part of the Future Climate for Africa (FCFA) program (`http://futureclimateafrica.org/project/impala/`). We are grateful to Callum Munday, Ian Ashpole and Ron Miller for useful discussions about experimental design and interpretation of the results.

6 Conclusions

Contents

6.1 Introduction 173
6.2 Summary of thesis aim outcomes 175
6.3 Discussion 179
6.3.1 Geographical distribution of emission mechanisms . . 179
6.3.2 Importance and characteristics of cold pool outflows . 183
6.3.3 Orography as a control on erosivity 186
6.4 Research applications and future work 187
6.4.1 A meteorological perspective on dust source maps . . 187
6.4.2 Improving driving wind fields for dust models 188
6.4.3 Priorities for future research 190

6.1 Introduction

The research presented in this thesis fits within a small body of literature which offers a perspective of Saharan meteorological dust emission processes directly constrained by observations. A tenet of the research has been that the few in situ observations which do now exist can be used to support a satellite-based approach offering a climatological, domain-wide perspective. The reliance on modelling and reanalyses in the research community is not ill-founded; until recently observation campaigns have offered little sampling of atmospheric processes close to remote natural dust sources, which appear to contribute the bulk of North African emissions (Ginoux et al. 2012). Models and reanalyses are not just poorly constrained, however. At coarse resolutions they fail to represent the sporadic mesoscale winds responsible for the bulk of emissions in summer, the dustiest time of year for the world's largest emission region.

Section 1.5.2 showed that Fennec Campaign observations indicate a dominant role for convective cold pool outflows (CPOs) as drivers of summertime dust emission (Allen et al. 2013) and there is now the observational support and motivation to estimate a partitioning across the wider central and western Sahara. Section 1.5.3 described advancements in remote sensing of dust emission and demonstrated that the resolution of infrared geostationary satellite data and existence of automated dust tracking methods allows meteorological properties to be inferred from plumes observed through their lifetime, comparable to deriving properties of atmospheric circulation from cloud motion (Section 2.1). New observational approaches are especially critical for convective CPOs, with no existing measurements capable of tracking them through their lifetime. By comparison, it was shown that nocturnal low-level jets (LLJs) can be justifiably modelled when embedded in dry northeasterlies, but much more work is required to improve their representation when monsoonal conditions prevail.

On the back of these research imperatives, the thesis set out to derive novel objective algorithms for observing meteorological dust emission processes in the central Sahara, partition the role of the two leading drivers of uplift in boreal summer on the long term, map out and characterise Saharan cold pool outflow occurrence and diagnose the relationship between Saharan orography and dry northeasterly LLJs. A satellite-based methodology is developed for the observational component of the project, alongside idealised modelling to test the role of orography. The research has been structured in the form of three submitted journal articles.

This Chapter summarises outcomes of the research in terms of the aims set out in Chapter 1, discusses the evidence supporting each key finding and evaluates the significance of the thesis for the dust emission research community and beyond. A final Section (6.4.3) suggests future research avenues which draw on the research outcomes. The aims of the thesis were to:

1. Develop novel algorithms capable of characterising tracked dust plumes by dust emission mechanism and delineating outflow boundaries (papers 1 and 2);

2. Partition the relative roles of low-level jets and cold pool outflows as drivers of dust emission in the central Sahara (paper 1);

3. Map cold pool outflow occurrence in the Sahara and link it to the evolution of dust emission through the summer season (paper 2);

4. Diagnose the role of the central Saharan Hoggar mountains in the strength of northeasterly low-level jets and their associated dust emission frequency (paper 3).

6.2 Summary of thesis aim outcomes

The outcomes of each research aim can summarised as follows:

Develop novel algorithms capable of characterising tracked dust plumes by dust emission mechanism and delineating outflow boundaries

Two algorithms have been developed and validated, both applied to brightness temperature data from the Spinning Enhanced Visible and Infrared Imager (SEVIRI) instrument aboard Meteosat Second Generation (MSG) satellites. The principle of these algorithms is to use visual information about features tracked across multiple satellite scenes to identify them against a noisy background and extract useful information about meteorological processes responsible for their emission. These algorithms are then upscaled and applied to large volumes of data from June, July and August 2004-2017.

The first algorithm tracks automatically flagged dust plumes and attempts to assign them to either the low-level jet or cold pool outflow category. 47,878 plumes are tracked and categorised. The underlying dust flagging procedure is adapted from Ashpole and Washington (2012). As timing is a key characteristic of emitted

plumes, a more generous BT(12.0-10.8) threshold is applied overnight to prevent tracked dust from erroneously disappearing due to the lack of contrast against the lower skin temperature of the night-time desert surface (Banks et al. 2019). A second modification is a more generous minimum plume size. Three visual characteristics are used to categorise plumes: their timing of emission, association with deep convection and geometry. A probability of being LLJ-driven is then assigned to each plume, with low probabilities indicating a higher probability of being CPO-driven. The methodology compares well against a manual approach (88% accuracy) and when compared with ground-based measurements from the Fennec Campaign (76% accuracy). The latter hit rate is mostly reduced by plumes observed from the ground which were missed by the tracking algorithm, with only two incorrect classifications (out of 27), both with probabilities close to 50% indicating high uncertainty.

The second algorithm identifies, delineates and tracks the leading edges of cold pool outflow boundaries which emerge from under cloud and loft fine material from the desert surface. Unlike the first algorithm, no attempt is made to track all dust in the imagery. Instead, the technique identifies regions in the satellite imagery where a sharp gradient in the BT(10.8-8.7) occurs and is sustained for an hour or more. Cold pool outflow boundaries are successfully distinguished from cloud edges and other unrelated features by applying a cloud mask, a two-pass threshold and minimum requirements for characteristics tracked across the CPO's lifetime such as duration and proximity to deep convection. A simple 2D model of a forward-propagating arc is imposed on observed CPOs in order to derive a stable propagation speed estimate amidst considerable noise. The algorithm successfully flags 74.2 % of events identified manually, with only 6.8% of all flagged pixels classified as false alarms. The approach is limited to dust-laden CPOs and cannot capture small microburst events or outflows which are completely obscured by cloud.

Partition the relative roles of low-level jets and cold pool outflows as drivers of dust emission in the central Sahara

The algorithm derived in Chapter 3 is used to estimate the relative contribution of nocturnal low-level jets and cold pool outflows to observable summertime dust emission and dust presence in the central and western Sahara. A very large contribution from CPOs is found, corresponding to 81.6% of total flagged dust pixels and 87.5% of emission pixels. Although CPOs are consistently responsible for the majority of observable dust, there is notable interannual variability with a 60% contribution in 2012 compared to a 94% contribution in 2017.

CPO dust presence is organised in a dipole pattern along the Mali-Algeria border, with a preference for the southern Sahara in the early monsoon season and a northward shift in July. A similar northward shift occurs with LLJ dust, which is common close to the ITD in June as well as downwind of the Bodele Depression before moving north into the northeasterly dry Harmattan axis in July. Both emission mechanisms undergo a considerable decline in activity in August.

Dust sources in southern Algeria and around the triple point (TP) of the Mali, Niger and Algeria borders are dominated by CPO-driven emission which tends to travel in all directions except southeastwards. These include the western flank of the Hoggar mountains, the Adrar des Ifoghas region and the Valle de l'Azaouagh. In contrast, sources in central and northwestern Algeria and around the Taoudenni basin of northern Mali have a larger LLJ component and tend to exhibit a preference for southwestward propagation. The Tidihelt Depression downwind of In Salah is noted as the most significant LLJ dust hotspot as well as one of the most frequently activated sources.

Map cold pool outflow occurrence in the Sahara and link it to the seasonality of dust emission

The CPO-tracking algorithm from Chapter 4 is applied to June, July and August 2004-2017 and tracks a total of 1,559 events. A clear diurnal cycle of

CPO occurrence is found, which maps onto the diurnal cycle of deep convective cloud. CPO propagation speeds decay through their lifetime and exhibit a slight diurnal cycle.

CPOs are predominantly associated with the WAM and propagate overwhelmingly in a northwestward direction. Many are far-reaching, with 22.5% of CPOs exceeding 300 km in reach. Occurrence of CPO activity is nonuniform across the domain; almost all observations are south of 28°N, especially around the TP, along the Mali-Algeria border and the western flank of the Adrar des Ifoghas mountains. A notable northward shift in the band of peak CPO activity occurs through summer in line with the displacement of the ITD, with the most intense hotspot of occurrence found at the southern tip of Algeria in August in association with a burst of deep convective initiation likely to be of orographic origin.

Dust emission and presence is thought to generally decline in August. This phenomenon is corroborated by multiple satellite datasets. In Section 4.5.2 an August decline is also shown in manual dust storm observation frequency from surface stations. Assuming CPOs have a major role in summertime emission frequency and atmospheric dust loading, the northward shift of CPO activity from the Sahel to the central Sahara appears to be a contributor to this decline. A surprising result is that the major August hotspot of CPO occurrence north of the TP in southern Algeria is not collocated with any obvious climatological late season dust outbreaks. Section 4.5.2 argues that the most likely reasons for the mismatch are a combination of higher sensitivity of the southernmost dust sources to CPO emission and relatively low availability of fine suspendable dust directly north of the TP.

Diagnose the role of the central Saharan Hoggar mountains in the strength of northeasterly low-level jets and their associated dust emission frequency

The impact of the Hoggar mountains on LLJ winds and LLJ dust emission within the northeasterly Harmattan axis found in Chapter 3 is explored in

Chapter 5 in an idealised model experiment with HadREM3-GA7.05, a regional configuration of the Met Office Unified Model driven at the boundaries by ERA-Interim. As well as a control, a counterfactual simulation is run for the period 1997-2007 with the Hoggar mountains smoothed manually to be continuous with the western Saharan sand sheet. The effects of this change are tested for LLJ days composited over the Tidihelt region, a major dust source with some of the highest mean wind speeds in Algeria and an overwhelming preference for LLJ dust emission. Days with high control wind speeds and LLJ dust identifiable using the technique applied in Chapter 3 are composited. Peak winds are associated with maritime cold surge conditions driven by an upper tropospheric ridge-trough pattern over the Atlas mountains and Mediterranean sea.

Removing the Hoggar mountains reduces composited mean surface wind speeds from 9.0 to 7.3 m/s and shifts them towards an easterly regime. This is due to a dome-shaped heating perturbation driving a negative geopotential height anomaly downwind of the Tidihelt, enhancing the pressure gradient across the dust source region. Critically, an absence of orography reduces dust emission frequency from the Tidihelt by an estimated 30.5% and has similar impacts across the entire northeasterly LLJ alley south of the Atlas mountain range. This is mostly due to a reduction in the highest wind speed events which have a disproportionate role in dust emission.

6.3 Discussion

6.3.1 Geographical distribution of emission mechanisms

A number of dust sources and dust-emitting regions can be linked to a dominant emission mechanism. This is an important finding as it means errors in the geographical distributions of modelled emission fluxes can be partially traced to misrepresentation of meteorological processes. Figure 6.1 maps out known Saharan summertime dust sources from Figure 3.4 averaged across the summer season and overlays data from this thesis which help interpret erosive controls.

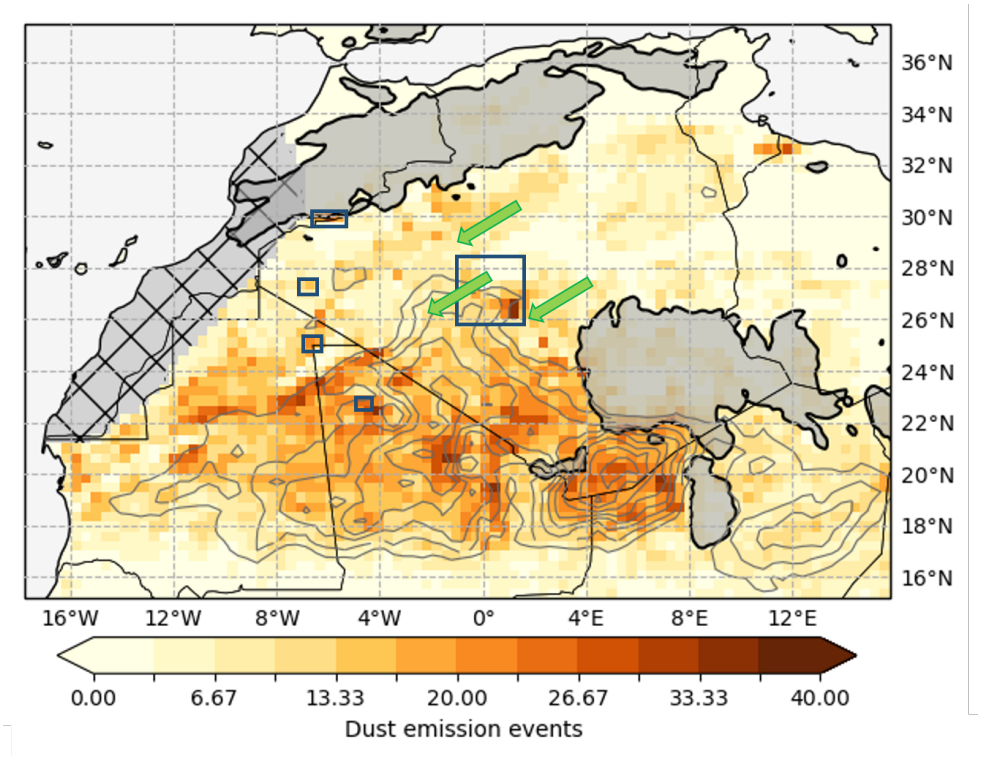


Figure 6.1: Dust source map for JJA 2004-2017 from Figure 3.4 remapped to 8% of its original resolution. Grey contours are the cold pool outflow occurrence from Figure 4.10a for the same period, with the outermost contour corresponding to 16 passages over the JJA 2004-2017 period and the innermost contour corresponding to 64. Blue boxes indicate hotspots of dust emission to which LLJs are a major contributor and the green arrows indicate the region in which the most low-level wind acceleration due to the Hoggar mountains is found. Regions above 700m elevation are contoured and shaded in grey. The western region of the central and western Sahara along the coast of the Atlantic is masked (hatched area) following Ashpole and Washington (2013a), as this region is prone to false dust detection due to incursions of marine stratocumulus.

Dust emission in the CWS is not strongly constrained to individual hotspots; sources registering at least 10 emission events in the 14-year sampling period are found across a vast swathe of desert stretching from the Hoggar mountains to the western border of Mauritania. A preference for emission activity encircling the TP may partly be due to elevated CPO frequency in this region. Conversely, a relative lack of emissions north of 25°N may relate to the infrequency of cold pools at these latitudes. Very few dust sources are primarily activated by dry processes. The leading exception is the Tidihelt, which is a major LLJ dust source and is supported by orographic enhancement of low-level winds.

The results of Chapter 3 disagree with the assessment by Schepanski et al. (2017) that West African summertime emissions can be divided into a dominant LLJ component for the Sahara and a smaller downdraft component for the Sahel. Schepanski et al. (2017) derive their estimate from an assumption that dust source activation observable in SEVIRI in the morning (0000 to 1200 UTC) is predominantly LLJ-driven. However, 54% of satellite-observed CPO dust plumes inferred in Chapter 3 are first observable in the morning half of the day (as well as 84% of LLJ plumes) indicating that such an assumption is likely to be misleading. Similarly, Tegen et al. (2013) and Heinold et al. (2016) show an overwhelming preference for summertime emissions between 06 and 12 UTC using the manual tracking approach of Schepanski et al. (2007), suggesting LLJs are the main drivers of dust emission. Heinold et al. (2016) acknowledge that the tracking method applied may exhibit a bias towards morning observations, however. Results presented in this thesis do indicate that LLJ dust emission is more common in the central Sahara than the Sahel but also that CPO dust emission is widespread and frequent in many of the same areas. Without a detection algorithm to reproduce, it is difficult to compare and reconcile manual approaches with the method presented in Chapter 3.

SEVIRI and IASI analyses also exhibit differences which may relate to sampling bias. The parallel analyses of Chédin et al. (2020) and Vandenbussche et al. (2020) show a geographical distribution of JJA dust emission in IASI centred around the TP with intense activity over northern Mali and southern Algeria, similar to Figure 3.4. Both sets of results show more frequent dust source activation in the morning (0930 UTC) compared to the evening (2130 UTC) and hence appear to corroborate Schepanski et al. (2017). Frequent early morning emissions by CPOs could be a major contributor to ambient dust observed at 0930, however, even when attempts are made to exclude plumes at high altitudes. Furthermore, the average time at which LLJ-driven plumes are first spotted by automated SEVIRI tracking is 0953 UTC, suggesting many LLJ events will be difficult to

observe at 0930 and hence that such a preference for dust at this time may be a result of CPO activity rather than LLJs. The 'night-time minus daytime' index of Todd and Cavazos-Guerra (2016) using CALIOP (derived from 01:30 and 13:30 UTC respectively) corresponds more closely to the results of Chapter 3, showing the most intense dust concentrations nocturnally around the TP. It appears that assessments of meteorological emission drivers based purely on the timing of emissions should be treated with caution.

It is perhaps not surprising that dust sources close to the Sahel are CPO-dominated, especially given the frequency of CPO passage south of 20°N shown in Chapter 4. Sources near the TP south of the Hoggar mountains and west of the Aïr Mountains have been known since the pioneering dust source study of Schepanski et al. (2007). Airborne lidar and dropsonde observations by Bou Karam et al. (2008) linked monsoonal dust emission in this region to convective density currents. CPO dust sources further north in the central Sahara are consistent with frequent in situ CPO observations at Bordj-Badji Mokhtar (BBM) (Allen et al. 2013; Marsham et al. 2013b) and evidence of dust emission close to high rainfall and lightning events across the western Sahara (Pope et al. 2016).

As well as northeasterly Harmattan LLJs in the north, LLJs are important emitters of dust in the southern Sahara, especially during June (Figure 3.12b). Allen and Washington (2014) observe frequent monsoon-embedded southwesterly LLJs during June 2011 at BBM. Fennec Campaign LLJ observations taken only in June may not be representative of the full summer season, however; Harmattan LLJ emissions become more common in July as LLJs in the Sahel drop off in frequency.

An interesting outcome from the dust source map of Ashpole and Washington (2013a) was the prominence of the Tidihelt Depression in central Algeria, which features as the single most frequently activated summertime source in their analysis and in Figure 3.4, although it is also uniquely visible to satellite due to

low cloud cover. Chapter 3 shows that this source is almost exclusively driven by LLJs, a result which informs the model experiment designed in Chapter 5. A corridor of summertime dust emission appears in central Algeria in a number of model estimates as well as the multimodel mean from CMIP5 (Evan et al. 2015; Todd and Cavazos-Guerra 2016). So far, however, no observation campaigns have targeted this dust source region nor have attempts been made to monitor its long-term variability. Dust emitted from within the Harmattan corridor may be an important contributor to the summertime Saharan Air Layer over the Atlantic (Rodrıguez et al. 2015; Lamancusa and Wagstrom 2019) as well as to the Iberian peninsula (Escudero et al. 2006).

As identified in Section 3.6 and in Section 4.5.2, some Sahelian dust emission could not be observed in this project due to column water vapour and cloud biases in SEVIRI, and there is some evidence from CALIOP spaceborne Lidar data that the summer dust hotspot near the TP may extend as far south as 16°N (Todd and Cavazos-Guerra 2016). Without a directly comparable dataset unaffected by these biases, however, it is only possible to speculate on how these southernmost emissions could affect the results here. Adjustment factors calculated in Section 3.6 based on cloud cover and ITD position suggest only a small impact from this bias on the magnitude of the decline in dust pixels through summer, and surface observations shown in Figure 4.11 corroborate the summer trend observed in SEVIRI. Given the dominance of CPOs as an emission mechanism in the southern Sahara, it is plausible that they also drive the unobserved emissions south of the ITD, in line with in situ observations of regular CPO activity there (Bou Karam et al. 2008; Provod et al. 2016; Bergametti et al. 2017).

6.3.2 Importance and characteristics of cold pool outflows

A growing body of modelling and observational studies have shown that CPOs play either a major or a dominant role in summertime Saharan dust emission (Marsham et al. 2011; Allen et al. 2013; Marsham et al. 2013b; Kocha et al. 2013;

Heinold et al. 2013; Ashpole and Washington 2013b; Allen et al. 2015). The estimate of the relative role of CPOs given in Chapter 3 is the highest yet. It has been shown by Allen (2015) that although LLJs are common across the CWS only a minority (12-36%) drive any dust emission and CPOs appear to be more 'efficient', producing higher ground-observed nephelometer scattering for the time they are in operation. Figure 4.10a indicates that even in the single most intense hotspot of CPO activity at the southern tip of Algeria a single pixel is only passed by a satellite-detectable CPO about 5 times on average per summer season. In part this is due to masking of CPOs by convective cloud (Heinold et al. 2013) but it also suggests that the mechanism primarily responsible for summertime dust uplift is relatively infrequent.

Considering dust pixel totals for individual years (Figure 3.10), the results of Chapter 3 are in agreement with the findings of the Fennec campaign, showing a 75.3% contribution from CPOs in 2011 and a 59.7% contribution in 2012 with a 23.3% increase in dust pixels from 2011 to 2012, consistent with the conclusions of Allen et al. (2015) that although 2012 was dustier than 2011 the primary emission mechanism was CPOs in both years. The analysis of this thesis shows that these two intensive observation periods were representative of conditions on the more climatological timescale of 14 years.

The CPO contribution derived in Chapter 3 is high despite the influence of cloud. Heinold et al. (2013) estimate that 60% of LLJ-associated morning emissions occur under clear skies. For afternoon and nocturnal emission this figure is only 10%, suggesting the CPO contribution derived from SEVIRI may even be an underestimate. However, it is important to note that the plume classification method described in Section 3.4.2 does not account for other possible emission mechanisms, including monsoon surges, Mediterranean cold surges and smaller scale phenomena such as dust devils and dry convective plumes. Any monsoon surges that were observable in SEVIRI were classified as CPOs in this analysis as they typically behave as density currents and are difficult to

distinguish from convective downdrafts without in situ data (Bou Karam et al. 2008; Marsham et al. 2013b; Allen et al. 2015). Frontal cold surges are treated the same way and account for 4.4% of CPO dust pixels in a manual survey of one month of data. As shown in Chapter 5, even though cold surges are infrequently directly responsible for emission, they are often synoptic precursors to major LLJ emission events. SEVIRI may struggle with observation of LLJ dust when a low-level temperature inversion is present (Brindley et al. 2012). Nevertheless, as shown in Section 3.5, a majority of events described during the Fennec intensive observation period at BBM were both visible to SEVIRI and correctly classified.

The timing of CPOs (Figure 4.8a) appears to map on to estimates of dust emission timing derived from high resolution modelling. The UM analysis of Marsham et al. (2011) includes a 1.5 km resolution simulation of a convectively active period, showing a peak in dust uplift potential at 1700 UTC. Simulations with an NWP model over Adrar for June 2006 show a peak in gustiness at 1800 UTC followed by a peak in AOT at 2200 UTC (Kocha et al. 2013). Although the CPO diurnal cycle derived in this thesis is consistent with these model simulations, a gap of several hours between peak CPO occurrence and peak atmospheric dust loading is plausible. The timing of CPOs is likely also to explain why UM simulations of CBL growth appear to be error-prone in the afternoon (Engelstaedter et al. 2015), given the contribution of CPOs to the Saharan moisture budget (Garcia-Carreras et al. 2013) and in turn the radiation budget (Marsham et al. 2016).

The dominant northwestward propagation of CPOs may also be significant for the geographical location of the summertime satellite-observed dust maximum visible in MODIS and MISR (Ridley et al. 2012) as well as TOMS AI (Engelstaedter and Washington 2007). These satellite products show high concentrations of JJA dust over northern Mali and eastern Mauritania, west of the apparent peak emission regions shown in Figure 3.4. Section 4.5.1 suggests that an easterly steering wind aloft combined with high dust availability north of WAM

convective hotspots may generate this northwestwards signal, but further analysis of individual convective outbreaks is needed to test this.

6.3.3 Orography as a control on erosivity

The Hoggar mountains are thought to deepen the Saharan heat low (Sultan and Janicot 2003; Drobinski et al. 2005) and influence boundary layer development (Birch et al. 2012). The analysis in Chapter 5 is the first to quantify their potential role in summertime dust emission processes. The conceptual model proposed in this thesis does not rely on orographic channelling to explain LLJ enhancement in the northeasterly corridor between the Atlas and Hoggar ranges, nor is the role of surface roughness and inertial oscillation tested as in Heinold et al. (2015). Instead, the results underscore the effect of elevated heating upon the low-level circulation in the lee of the mountains. This thermodynamic explanation for an enhanced LLJ through central Algeria therefore differs from the Bodele LLJ, for which Todd et al. (2008a) suggest elevated heating is only a secondary control.

It is possible that channelling or gap flow is a contributor to erosivity in the CWS. As shown in Section 1.6.5, Evan et al. (2016) project emissions derived from the manual SEVIRI-tracking approach of Schepanski et al. (2007) onto a map of Saharan orography (Figure 1.7). They point out that a majority of the most frequent emission regions are located downwind of gap regions between North African orography including the Atlas, Hoggar, Tibesti, Aïr and Ennedi mountains, although the use of reanalysis here misses the effects of CPOs. Idealised simulations of airstreams undergoing gap flow show that the highest velocities should be found in the exit region of a channel where mountain wave-breaking generates a region of intense flow acceleration, depending on mountain height (Gaberšek and Durran 2004). This behaviour aligns with observations, contrary to 2D models of channelling which would situate the peak flow acceleration in the centre of the gap (Jackson et al. 2013). The Tidihelt jet as well as the region of maximum orographic enhancement shown in Figure

5.13a is situated approximately in the centre of the gap between the Atlas and Hoggar mountains. This contrasts with the Bodele low-level jet which is found at the exit of the Tibesti-Ennedi gap (Washington and Todd 2005) and is more indicative of channelled flow. Other gaps between the Hoggar, Tibesti and Aïr mountains remain untested, although they do not encapsulate the range of LLJ dust sources that the Atlas-Hoggar gap does (Figure 6.1).

A second orographic effect implied by the results of this thesis is the role of the Aïr mountains in deep convective triggering CPO generation. This is shown in Chapter 4 where a maximum in summertime CPO observations is found to occur downstream (assuming a northwesterly outflow direction) of an August hotspot of deep convective cloud situated over the massif, visible from microwave satellite imaging (Redl et al. 2015). An analysis of orographic effects on convective triggering could help explain the distribution of CPO-dominated dust sources in the lee of Saharan mountains. No attempts have yet been made to test the impact of orography on dust-emitting CPOs in idealised modelling, but effects such as leeward wind convergence and albedo could contribute to convective outbreaks and downdraft production during the monsoon season. The observations in this thesis could be used to support such an analysis.

6.4 Research applications and future work

6.4.1 A meteorological perspective on dust source maps

As described in Section 1.4, satellite-derived dust source maps have been applied as constraints on dust model emissions. These maps are some of the most useful tools for improving our understanding of Saharan dust emissions as they can be used to discover new dust sources, evaluate simulated emission fields, pinpoint priority locations for field campaigns and identify erodible geomorphological features. However, dust emission hotspots seen in these maps are the combined result of surface features and meteorology. This is most clearly seen in the significant changes that occur in these dust source maps through summer (Ashpole

and Washington 2013a) as well as the collocation of major dust sources with hotspots of downdraft activity and LLJ enhancement (Figure 6.1). As such, dust sources imposed on models based on satellite dust tracking may incur a stationarity problem under anthropogenic climate change; even if natural dust sources remain fixed, the geographical distribution of meterological emission mechanisms may evolve and favour new source regions which are currently inert and hence invisible to satellite methods. This motivates a process-based approach to evaluating simulated emissions. Critically, it also motivates an interpretation of current dust source maps which takes meteorological drivers into account. The results of this thesis offer insights that can help achieve that, as described in Section 6.3.1.

6.4.2 Improving driving wind fields for dust models

Findings from this thesis can be used as an observational constraint for both dust models and their driving (or interactively generated) wind fields. Dust source maps and satellite AOD have been previously used to evaluate model emission estimates. For example, COSMO-MUSCAT at 28 km resolution (a meteorological model coupled with an aerosol transport and emission component) and ECHAM6-HAM2 at approximately 208 km resolution (an aerosol-climate model) are compared with SEVIRI-derived dust sources in Figures 2 and 3 of Tegen et al. (2013) and Heinold et al. (2016), respectively. Compared to results from Chapter 3 with its added meteorological perspective, COSMO-MUSCAT appears to simulate the summertime distribution of LLJ dust sources reasonably well, but misses key CPO hotspots around the triple point (TP) of Mali, Algeria and Niger. A similar interpretation of ECHAM-HAM2 can be made; sources in central Algeria and northern Mali which favour LLJ-driven emission are apparent but peak emissions are located west of the observed peak CPO zone that develops in June and July in Figures 4.10b and c. Perhaps unsurprisingly, these results suggest a deficiency in the geographical distribution of simulated dust sources results from an absence of gusty downdraft winds, not represented explicitly at

either grid resolution. Without these downdrafts, emissions are very likely to be underestimated as mean wind speeds close to the TP are low (Kocha et al. 2013). Future model evaluation studies would benefit from an observational benchmark which takes into account both source strength and meteorological drivers as this approach can help pinpoint model shortcomings.

A second contribution of this thesis that could support model improvement is an observational dataset of CPO occurrence and characteristics. As described in Chapter 4, the dustiness of the Sahara makes gust fronts associated with convective downdrafts uniquely observable. CPO observations which exploit this phenomenon provide information about both the mesoscale meteorology of downdraft processes and dust emission. One example of a CPO parameterization is the circular wake model of Grandpeix and Lafore (2010), in which cold pool propagation depends on a diabatic term from a coupled convection scheme, advection, entrainment, detrainment and damping from gravity waves. CPO observations could help tune this parameterization to constrain the propagation speed, decay, geographical distribution and frequency of CPOs which result, improving the fidelity of both simulated convective triggering and dust emitting winds. Similarly, CPO observations may help improve the CPO parameterization developed by Pantillon et al. (2015), who identify the absence of observations as a key source of uncertainty in verifying their results.

Evaluation of simulations with explicit convection (e.g. Marsham et al. 2011; Heinold et al. 2013; Birch et al. 2014; Chaboureau et al. 2016) is another avenue of research, although it could be argued that the computational expense of explicit modelling makes realistic parameterizations a more pressing priority for global climate models with a dust component. Convective-permitting models appear to produce an improved diurnal cycle in surface winds with some evidence from short timescales that they can improve the representation of the mean AOD field (Chaboureau et al. 2016). However, as modelling approaches become more complex, it is critical to ensure that models are producing realistic results

for the right reasons, and improved observational constraints on CPOs are only part of this. Roberts et al. (2018) express this particularly well: to simulate realistic emissions, dust models must capture large-scale variations in the surface heating balance, the distribution of moist convection and its incursions into the dry desert, the spatiotemporal variability of soil properties and the long tail of high winds associated with mesoscale emission mechanisms operate at subgrid scales. As numerical models complexify, a host of new observations are needed to evaluate them.

6.4.3 Priorities for future research

Until the meteorological processes responsible for mineral dust emission are realistically incorporated into numerical models, predicting changes to North Africa's dust output under climate change remains an unachievable task. This is particularly challenging for the Sahara in boreal summer because at this time of year moisture-driven processes appear to dominate the dust budget as shown on short timescales by the Fennec Campaign and on longer timescales in this thesis. Convective processes in the Sahara are difficult to characterise climatologically as both global and regional models represent them inadequately (Knippertz and Todd 2012). As shown in Chapter 5, there is more to learn about dry emission processes too, though summertime dust sources in the Sahara which are primarily activated by dry processes are scarce. An improved process-based understanding of controls on dust emission mechanisms at all timescales is needed. The satellite component of this thesis is one observational line of evidence that can be used to support this enquiry, and one of the few that offers a long-term perspective.

A number of extensions could be made to the observational analysis of Chapters 3 and 4. Firstly, relatively little attention has been given in this thesis to drivers of sub-seasonal variability in satellite-observed mesoscale emission mechanisms, other than the late summer dust decline in Chapter 4. To address this, it would be possible to analyse LLJ and CPO dust emission patterns with respect to the

displacement and strength of the SHL, timing of WAM onset and variability of AEWs. A preference for high dust states during monsoon surges has been shown by Ashpole and Washington (2013b), with lower dust states corresponding to a retracted monsoon flow and extended northeasterly low-level harmattan winds. Enhanced southerly flow associated with African Easterly Wave development appears to be a key mechanism driving this, which Knippertz and Todd (2010) link to cold pool activity within the southerly sector of the AEW followed by enhanced LLJs in the ensuing northerly sector. This hypothesis has not been tested with satellite observations of LLJ and CPO events, however. AEW activity controlling outbreaks of CPO occurrence are likely in turn to be linked to the 'heat low' phase of the SHL's east-west displacement (Todd et al. 2013; Ryder et al. 2015). AEW activity may also increase under anthropogenic climate change due to enhanced heating of the Saharan interior (Skinner and Diffenbaugh 2014). An observational analysis of CPO variability associated with AEWs could therefore provide a plausible mechanism linking greenhouse gas forcing to Saharan dust emission in summer.

A second extension of this thesis would be to characterise the formation and evolution of convective outbreaks associated with observed CPOs on the long term. Analyses of individual mesoscale convective systems and associated cold pool emission provide valuable insights into the atmospheric dynamics responsible for some of the largest observed dust plumes (e.g. Cuesta et al. 2010; Knippertz and Todd 2010; Roberts and Knippertz 2014) but automated satellite observations could allow for a more climatological perspective on the relationship between convection and dust. This could be achieved by attempting to relate satellite-observed outflows described in Chapter 4 to the convective cells responsible for their generation. Triggering of new convection as a result of downdrafts is a significant component of the convective lifecycle. Trzeciak et al. (2017) argue that this mechanism is particularly important in the remote Sahara as cold pools are typically moister than the environment; they show in a

case study that recycling of CPOs in this way allows them to traverse the entire meridional extent of the desert. There is a need to test the relative contribution of recycling to CPO occurrence far north of the climatological ITD as it may constitute a key process needed for both realistic moisture transport and dust emission in models. Automatically tracked CPOs derived in this thesis are one piece of evidence that could be used to formulate such an analysis.

Third, this thesis focuses only on the JJA monsoon and hence makes no attempt to quantify the relative significance of CPOs or LLJs outside the peak dust season. CPO detections south of the Atlas mountains are made by Emmel et al. (2010) and Redl et al. (2015) in all months of the year apart from December and January. Given that Fennec observations are restricted to summer, no attempts have been made to observe the role of CPOs in remote Saharan dust emission through the entire year, although model simulations with explicit convection and with parameterized CPOs suggest the CPO contribution to dust emission may begin earlier and extend beyond the peak in JJA (Pantillon et al. (2016), Figure 12). Both the analyses in Chapters 3 and 4 could be extended in this way, but would also depend on an evaluation of SDFs outside of summer and consideration for classifying other important emission mechanisms such as Harmattan surges (Fiedler et al. 2015) and Mediterranean cold surges and fronts (Vizy and Cook 2009; Knippertz and Fink 2006). Availability of LLJ identification from SDFs in non-summer months could also support an extended analysis of the effect of the Hoggar mountains on the Harmattan LLJ corridor when the SHL is shifted south closer to the equator and diabatic heating over the Sahara is reduced (Lavaysse et al. 2009).

Lastly, given the volume and variety of Saharan dust sources located close to mountains, it is likely that orography exerts many more influences upon local erosivity than have been explored in Chapter 5, which emphasises the large-scale impact of the Hoggar mountains on elevated heating and the pressure gradient through central Algeria. Studies of orographic influences at the scale of individual

dust sources require relatively high resolution, however, and if key processes such as moisture transport due to CPOs and monsoonal LLJs are poorly represented, dynamical downscaling will add little value. Nonetheless, high resolution satellite analyses which can distinguish dust plumes and the processes driving them could be used to study the variability of individual dust sources. This is especially true when supporting in situ observations are available. Unfortunately, the practical and political difficulty of accessing major natural dust sources in the Sahara means that such observations are likely to remain rare. Without a dense observing network in the remote Sahara, satellite methods will remain the main tool for monitoring and characterising the desert's dust sources for a long time yet.

This thesis has characterised summertime dust emission mechanisms in the Sahara using a combination of automated satellite algorithms and idealised numerical modelling. Although satellite datasets are inherently noisy, the large volume of data now available from SEVIRI means that clear signals and patterns are emerging, even from tracking relatively infrequent phenomena such as large dust-emitting cold pool outflows. Of all the pixels in the SEVIRI dataset used in this thesis, only 2% were identifiable dust plumes, and only 0.005% were dust-laden cold pool outflow boundaries. The ability to extract useful, robust information is therefore a testament to the efforts of scientists and engineers over the last 50 years who have developed and maintained stable satellite observing platforms and the instruments they carry. Numerical modelling is still the only tool available to predict the future, however, and Saharan dust emissions are sporadic, disaggregated and dependent on mesoscale phenomena. While the challenge of characterising physical dust emission processes lies primarily in working around the sparsity of in situ data, the challenge for modellers will be improving simulations of the dust cycle at the resolutions needed for climate projections of the coming century.

Appendices

A

Statement of Authorship

Paper 1: A 14-Year Climatology of Saharan Dust Emission Mechanisms Inferred From Automatically Tracked Plumes

I created and applied the algorithm, analysed the results and wrote the paper. Richard Washington and Sebastian Engelstaedter contributed to the conceptualisation and planning of the method as well as helping to interpret the results and edit the manuscript. Sebastian Engelstaedter assisted with data access and curation.

Paper 2: Satellite-Derived Characteristics of Saharan Cold Pool Outflows During Boreal Summer

I created and applied the algorithm, analysed the results and wrote the paper. Richard Washington and Sebastian Engelstaedter contributed to the conceptualisation and planning of the method as well as helping to interpret the results and edit the manuscript.

Paper 3: Influence of orography upon summertime low-level jet dust emission in the central and western Sahara

I designed and ran the model experiments, analysed the results and wrote the paper. Richard Washington and Sebastian Engelstaedter contributed to the conceptualisation and planning of the method as well as helping to interpret the results and edit the manuscript. Richard Jones facilitated access to the Met Office Unified Model and to relevant expertise within the Hadley Centre, as well as reviewing the manuscript. Nick Savage trained me in running the Unified Model and provided technical support at all stages of the model experiments, as well as helping to edit the manuscript.

References

Ackerman, Steven A (1997). "Remote sensing aerosols using satellite infrared observations". *Journal of Geophysical Research: Atmospheres* 102.D14, pp. 17069–17079.

Allen, Christopher J (2015). "Atmospheric mechanisms of central Saharan dust storm formation in boreal summer: observations from the Fennec campaign". PhD thesis. University of Oxford, p. 359.

Allen, Christopher JT, R Washington, and A Saci (2015). "Dust detection from ground-based observations in the summer global dust maximum: Results from Fennec 2011 and 2012 and implications for modeling and field observations". *Journal of Geophysical Research: Atmospheres* 120.3, pp. 897–916.

Allen, Christopher JT and Richard Washington (2014). "The low-level jet dust emission mechanism in the central Sahara: Observations from Bordj-Badji Mokhtar during the June 2011 Fennec Intensive Observation Period". *Journal of Geophysical Research: Atmospheres* 119.6, pp. 2990–3015.

Allen, Christopher JT, Richard Washington, and Sebastian Engelstaedter (2013). "Dust emission and transport mechanisms in the central Sahara: Fennec ground-based observations from Bordj-Badji Mokhtar, June 2011". *Journal of Geophysical Research: Atmospheres* 118.12, pp. 6212–6232.

Ansmann, Albert, Jens Bösenberg, Anatoli Chaikovsky, Adolfo Comerón, Sabine Eckhardt, Ronald Eixmann, Volker Freudenthaler, Paul Ginoux, Leonce Komguem, Holger Linnè, et al. (2003). "Long-range transport of Saharan dust to northern Europe: The 11–16 October 2001 outbreak observed with EARLINET". *Journal of Geophysical Research: Atmospheres* 108.D24.

Ansmann, Albert, Matthias Tesche, Peter Knippertz, Eike Bierwirth, Dietrich Althausen, Detlef Mueller, and Oliver Schulz (2009). "Vertical profiling of convective dust plumes in southern Morocco during SAMUM". *Tellus B: Chemical and Physical Meteorology* 61.1, pp. 340–353.

Ashpole, Ian and Richard Washington (2012). "An automated dust detection using SEVIRI: A multiyear climatology of summertime dustiness in the central and western Sahara". *Journal of Geophysical Research: Atmospheres* 117.D8.

— (2013a). "A new high-resolution central and western Saharan summertime dust source map from automated satellite dust plume tracking". *Journal of Geophysical Research: Atmospheres* 118.13, pp. 6981–6995.

— (2013b). "Intraseasonal variability and atmospheric controls on daily dust occurrence frequency over the central and western Sahara during the boreal summer". *Journal of Geophysical Research: Atmospheres* 118.23.

Bachl, Fabian E, Christoph S Garbe, and Paul Fieguth (2012). "A Bayesian approach to spaceborn hyperspectral optical flow estimation on dust aerosols". *Geoscience and Remote Sensing Symposium (IGARSS), 2012 IEEE International*. IEEE, pp. 256–259.

Bachl, Fabian E, Alex Lenkoski, Thordis L Thorarinsdottir, Christoph S Garbe, et al. (2015). "Bayesian motion estimation for dust aerosols". *The Annals of Applied Statistics* 9.3, pp. 1298–1327.

Bagnold, Ralph Alger (1941). *The physics of blown sand and desert dunes*. Methuen.

Bain, Caroline L, Douglas J Parker, Christopher M Taylor, Laurent Kergoat, and Françoise Guichard (2010a). "Observations of the nocturnal boundary layer associated with the West African monsoon". *Monthly Weather Review* 138.8, pp. 3142–3156.

Bain, CL, G Magnusdottir, P Smyth, and H Stern (2010b). "Diurnal cycle of the Intertropical Convergence Zone in the east Pacific". *Journal of Geophysical Research: Atmospheres* 115.D23.

Bakker, N, N Drake, and Charlie Bristow (2019). "Evaluating the relative importance of northern African mineral dust sources using remote sensing". *Atmospheric Chemistry and Physics* 19.16, pp. 10525–10535.

Balme, Matt and Ronald Greeley (2006). "Dust devils on Earth and Mars". *Reviews of Geophysics* 44.3.

Banks, Jamie R, Anja Hünerbein, Bernd Heinold, Helen E Brindley, Hartwig Deneke, and Kerstin Schepanski (2019). "The sensitivity of the colour of dust in MSG-SEVIRI Desert Dust infrared composite imagery to surface and atmospheric conditions". *Atmospheric Chemistry and Physics* 19.10, pp. 6893–6911.

Banks, Jamie R, Kerstin Schepanski, Bernd Heinold, Anja Hünerbein, and Helen E Brindley (2018). "The influence of dust optical properties on the colour of simulated MSG-SEVIRI Desert Dust infrared imagery". *Atmospheric Chemistry and Physics* 18.13, pp. 9681–9703.

Banks, JR and HE Brindley (2013). "Evaluation of MSG-SEVIRI mineral dust retrieval products over North Africa and the Middle East". *Remote Sensing of Environment* 128, pp. 58–73.

Banks, JR, HE Brindley, Cyrille Flamant, MJ Garay, NC Hsu, OV Kalashnikova, Lars Klüser, and AM Sayer (2013). "Intercomparison of satellite dust retrieval products over the west African Sahara during the Fennec campaign in June 2011". *Remote sensing of environment* 136, pp. 99–116.

Barkan, Joseph and Pinhas Alpert (2010). "Synoptic analysis of a rare event of Saharan dust reaching the Arctic region". *Weather* 65.8, pp. 208–211.

Basart, Sara, Carlos Pérez, Slodoban Nickovic, Emilio Cuevas, and JoséMARÍA Baldasano (2012). "Development and evaluation of the BSC-DREAM8b dust regional model over Northern Africa, the Mediterranean and the Middle East". *Tellus B: Chemical and Physical Meteorology* 64.1, p. 18539.

Bedka, Kristopher, Jason Brunner, Richard Dworak, Wayne Feltz, Jason Otkin, and Thomas Greenwald (2010). "Objective satellite-based detection of overshooting tops using infrared window channel brightness temperature gradients". *Journal of applied meteorology and climatology* 49.2, pp. 181–202.

Bedka, Kristopher M and Konstantin Khlopenkov (2016). "A probabilistic multispectral pattern recognition method for detection of overshooting cloud tops using passive satellite imager observations". *Journal of Applied Meteorology and Climatology* 55.9, pp. 1983–2005.

Bedka, Kristopher M and John R Mecikalski (2005). "Application of satellite-derived atmospheric motion vectors for estimating mesoscale flows". *Journal of Applied Meteorology and Climatology* 44.11, pp. 1761–1772.

Bergametti, G, B Marticorena, Jean-Louis Rajot, B Chatenet, A Féron, C Gaimoz, G Siour, M Coulibaly, I Koné, A Maman, et al. (2017). "Dust uplift potential in the Central Sahel: an analysis based on 10 years of meteorological measurements at high temporal resolution". *Journal of Geophysical Research: Atmospheres* 122.22, pp. 12–433.

Bergametti, G, Jean-Louis Rajot, C Pierre, Christel Bouet, and B Marticorena (2016). "How long does precipitation inhibit wind erosion in the Sahel?" *Geophysical Research Letters* 43.12, pp. 6643–6649.

Birch, Cathryn E, Douglas J Parker, John H Marsham, and Gerard M Devine (2012). "The effect of orography and surface albedo on stratification in the summertime Saharan boundary layer: Dynamics and implications for dust transport". *Journal of Geophysical Research: Atmospheres* 117.D5.

Birch, CE, DJ Parker, JH Marsham, D Copsey, and L Garcia-Carreras (2014). "A seamless assessment of the role of convection in the water cycle of the West African monsoon". *Journal of Geophysical Research: Atmospheres* 119.6, pp. 2890–2912.

Blackadar, A.K. (1957). "Boundary layer wind maxima and their significance for the growth of nocturnal inversions". *Bull. Amer. Meteor. Soc* 38.5, pp. 283–290.

Bormann, Niels, Sami Saarinen, Graeme Kelly, and Jean-Noël Thépaut (2003). "The spatial structure of observation errors in atmospheric motion vectors from geostationary satellite data". *Monthly Weather Review* 131.4, pp. 706–718.

Bou Karam, D, Cyrille Flamant, P Knippertz, Oliver Reitebuch, Jacques Pelon, Michel Chong, and Alain Dabas (2008). "Dust emissions over the Sahel associated with the West African monsoon intertropical discontinuity region: A representative case-study". *Quarterly Journal of the Royal Meteorological Society* 134.632, pp. 621–634.

Bou Karam, Diana, Earle Williams, Matthew Janiga, Cyrille Flamant, Michael McGraw-Herdeg, Juan Cuesta, Antoine Auby, and Chris Thorncroft (2014). "Synoptic-scale dust emissions over the Sahara Desert initiated by a moist convective cold pool in early August 2006". *Quarterly Journal of the Royal Meteorological Society* 140.685, pp. 2591–2607.

Boucher, Olivier, David Randall, Paulo Artaxo, Christopher Bretherton, Gragam Feingold, Piers Forster, V-M Kerminen, Yutaka Kondo, Hong Liao, Ulrike Lohmann, et al. (2013). "Clouds and aerosols". *Climate change 2013: the physical science basis. Contribution of Working Group I to the Fifth Assessment Report of the Intergovernmental Panel on Climate Change*. Cambridge University Press, pp. 571–657.

Bouet, Christel, Guy Cautenet, Richard Washington, Martin C Todd, Benoit Laurent, Beatrice Marticorena, and Gilles Bergametti (2007). "Mesoscale modeling of aeolian dust emission during the BoDEx 2005 experiment". *Geophysical research letters* 34.7.

Brindley, Helen, Peter Knippertz, Claire Ryder, and Ian Ashpole (2012). "A critical evaluation of the ability of the Spinning Enhanced Visible and Infrared Imager (SEVIRI) thermal infrared red-green-blue rendering to identify dust events: Theoretical analysis". *Journal of Geophysical Research: Atmospheres* 117.D7.

Brown, AR, RJ Beare, JM Edwards, AP Lock, SJ Keogh, SF Milton, and DN Walters (2008). "Upgrades to the boundary-layer scheme in the Met Office numerical weather prediction model". *Boundary-layer meteorology* 128.1, pp. 117–132.

Bryant, Robert G (2013). "Recent advances in our understanding of dust source emission processes". *Progress in Physical Geography* 37.3, pp. 397–421.

Buckle, Colin (1996). *Weather and climate in Africa*. Longman.

Bullard, Joanna E, Sandy P Harrison, Matthew C Baddock, Nick Drake, Thomas E Gill, Grant McTainsh, and Youbin Sun (2011). "Preferential dust sources: A geomorphological classification designed for use in global dust-cycle models". *Journal of Geophysical Research: Earth Surface* 116.F4.

Cakmur, Reha V, Ron L Miller, and Ina Tegen (2001). "A comparison of seasonal and interannual variability of soil dust aerosols over the Atlantic Ocean as inferred by

the TOMS AI and AVHRR AOT retrievals". *Journal of Geophysical Research: Atmospheres* 106.D16, pp. 18287–18303.

Cakmur, RV, RL Miller, and O Torres (2004). "Incorporating the effect of small-scale circulations upon dust emission in an atmospheric general circulation model". *Journal of Geophysical Research: Atmospheres* 109.D7.

Callewaert, Sieglinde, Sophie Vandenbussche, Nicolas Kumps, Arve Kylling, Xiaoxia Shang, Mika Komppula, Philippe Goloub, and Martine De Mazière (2019). "The Mineral Aerosol Profiling from Infrared Radiances (MAPIR) algorithm: version 4.1 description and evaluation". *Atmospheric Measurement Techniques* 12.7, pp. 3673–3698.

Caton Harrison, T, R Washington, and S Engelstaedter (2020). "Satellite-derived characteristics of Saharan cold pool outflows during boreal summer". *Journal of Geophysical Research: Atmospheres*.

Caton Harrison, Thomas, Richard Washington, and Sebastian Engelstaedter (2019). "A 14-Year Climatology of Saharan Dust Emission Mechanisms Inferred From Automatically Tracked Plumes". *Journal of Geophysical Research: Atmospheres* 124.16, pp. 9665–9690.

Cavazos, Carolina, Martin C Todd, and Kerstin Schepanski (2009). "Numerical model simulation of the Saharan dust event of 6–11 March 2006 using the Regional Climate Model version 3 (RegCM3)". *Journal of Geophysical Research: Atmospheres* 114.D12.

Chaboureau, Jean-Pierre, Cyrille Flamant, Thibaut Dauhut, Cécile Kocha, Jean-Philippe Lafore, Christophe Lavaysse, Fabien Marnas, Mohamed Mokhtari, Jacques Pelon, Irene Reinares Martınez, et al. (2016). "Fennec dust forecast intercomparison over the Sahara in June 2011". *Atmospheric Chemistry and Physics Discussions*, (under review).

Chaibou, Abdoul Aziz Saidou, Xiaoyan Ma, Kanike Raghavendra Kumar, Hailing Jia, Yaoguo Tang, and Tong Sha (2020). "Evaluation of dust extinction and vertical profiles simulated by WRF-Chem with CALIPSO and AERONET over North Africa". *Journal of Atmospheric and Solar-Terrestrial Physics* 199, p. 105213.

Chang, Chia-Jung and Mehrdad Jazayeri (2018). "Integration of speed and time for estimating time to contact". *Proceedings of the National Academy of Sciences* 115.12, E2879–E2887.

Chauvin, Fabrice, Romain Roehrig, and Jean-Philippe Lafore (2010). "Intraseasonal variability of the Saharan heat low and its link with midlatitudes". *Journal of Climate* 23.10, pp. 2544–2561.

Chédin, A, V Capelle, NA Scott, and MC Todd (2020). "Contribution of IASI to the observation of dust aerosol emissions (morning and nighttime) over the Sahara desert". *Journal of Geophysical Research: Atmospheres* 125.15, e2019JD032014.

Chellali, Farouk, Adballah Khellaf, Adel Belouchrani, and Abdelmadjid Recioui (2011). "A contribution in the actualization of wind map of Algeria". *Renewable and Sustainable Energy Reviews* 15.2, pp. 993–1002.

Chelton, Dudley B, Michael H Freilich, and Steven K Esbensen (2000). "Satellite observations of the wind jets off the Pacific coast of Central America. Part I: Case studies and statistical characteristics". *Monthly Weather Review* 128.7, pp. 1993–2018.

Chen, Qian, Yan Yin, Hui Jiang, Zhigang Chu, Lulin Xue, Rulin Shi, Xin Zhang, and Jinghua Chen (2019). "The roles of mineral dust as cloud condensation nuclei and

ice nuclei during the evolution of a hail storm". *Journal of Geophysical Research: Atmospheres* 124.24, pp. 14262–14284.

Choobari, O Alizadeh, P Zawar-Reza, and A Sturman (2014). "The global distribution of mineral dust and its impacts on the climate system: A review". *Atmospheric Research* 138, pp. 152–165.

Colarco, PR, OB Toon, JS Reid, JM Livingston, PB Russell, J Redemann, B Schmid, HB Maring, D Savoie, EJ Welton, et al. (2003). "Saharan dust transport to the Caribbean during PRIDE: 2. Transport, vertical profiles, and deposition in simulations of in situ and remote sensing observations". *Journal of Geophysical Research: Atmospheres* 108.D19.

Couvreux, Fleur, F Guichard, Olivier Bock, B Campistron, J-P Lafore, and J-L Redelsperger (2010). "Synoptic variability of the monsoon flux over West Africa prior to the onset". *Quarterly Journal of the Royal Meteorological Society* 136.S1, pp. 159–173.

Cowie, SM, P Knippertz, and JH Marsham (2014). "A climatology of dust emission events from northern Africa using long-term surface observations". *Atmospheric Chemistry and Physics* 14.16, pp. 8579–8597.

Cowie, Sophie M, John H Marsham, and Peter Knippertz (2015). "The importance of rare, high-wind events for dust uplift in northern Africa". *Geophysical Research Letters* 42.19, pp. 8208–8215.

Crook, Julia, Cornelia Klein, Sonja Folwell, Christopher M Taylor, Douglas J Parker, Rachel Stratton, and Thorwald Stein (2019). "Assessment of the representation of West African storm lifecycles in convection-permitting simulations". *Earth and Space Science* 6.5, pp. 818–835.

Cuesta, Juan, Dimitri Edouart, Mohamed Mimouni, Pierre H Flamant, Claude Loth, Fabien Gibert, Fabien Marnas, Abdelkrim Bouklila, Mohamed Kharef, Bouziane Ouchène, et al. (2008). "Multiplatform observations of the seasonal evolution of the Saharan atmospheric boundary layer in Tamanrasset, Algeria, in the framework of the African Monsoon Multidisciplinary Analysis field campaign conducted in 2006". *Journal of Geophysical Research: Atmospheres* 113.D23.

Cuesta, Juan, Christophe Lavaysse, Cyrille Flamant, Mohamed Mimouni, and Peter Knippertz (2010). "Northward bursts of the West African monsoon leading to rainfall over the Hoggar Massif, Algeria". *Quarterly Journal of the Royal Meteorological Society* 136.S1, pp. 174–189.

Cuesta, Juan, John H Marsham, Douglas J Parker, and Cyrille Flamant (2009). "Dynamical mechanisms controlling the vertical redistribution of dust and the thermodynamic structure of the West Saharan atmospheric boundary layer during summer". *Atmospheric Science Letters* 10.1, pp. 34–42.

Cuevas, E, AJ Gómez-Peláez, S Rodrıguez, Enric Terradellas, Sara Basart, RD Garcıa, OE Garcıa, and Silvia Alonso-Pérez (2017). "The pulsating nature of large-scale Saharan dust transport as a result of interplays between mid-latitude Rossby waves and the North African Dipole Intensity". *Atmospheric environment* 167, pp. 586–602.

De Longueville, Florence, Yvon-Carmen Hountondji, Sabine Henry, and Pierre Ozer (2010). "What do we know about effects of desert dust on air quality and human health in West Africa compared to other regions?" *Science of the Total Environment* 409.1, pp. 1–8.

Dee, DP, SM Uppala, AJ Simmons, Paul Berrisford, P Poli, S Kobayashi, U Andrae, MA Balmaseda, G Balsamo, P Bauer, et al. (2011). "The ERA-Interim reanalysis: Configuration and performance of the data assimilation system". *Quarterly Journal of the royal meteorological society* 137.656, pp. 553–597.

DeMott, Paul J, Kenneth Sassen, Michael R Poellot, Darrel Baumgardner, David C Rogers, Sarah D Brooks, Anthony J Prenni, and Sonia M Kreidenweis (2003). "African dust aerosols as atmospheric ice nuclei". *Geophysical Research Letters* 30.14.

Diallo, Ismaıla, Caroline L Bain, Amadou T Gaye, Wilfran Moufouma-Okia, Coumba Niang, Mame DB Dieng, and Richard Graham (2014). "Simulation of the West African monsoon onset using the HadGEM3-RA regional climate model". *Climate Dynamics* 43.3-4, pp. 575–594.

Dione, C, M Lothon, D Badiane, B Campistron, F Couvreux, F Guichard, and SM Sall (2014). "Phenomenology of Sahelian convection observed in Niamey during the early monsoon". *Quarterly Journal of the Royal Meteorological Society* 140.679, pp. 500–516.

Drobinski, Philippe, Benjamin Sultan, and Serge Janicot (2005). "Role of the Hoggar massif in the West African monsoon onset". *Geophysical research letters* 32.1.

Dubuisson, Philippe, Hervé Herbin, Fanny Minvielle, M Compiègne, François Thieuleux, Fédéric Parol, and Jacques Pelon (2014). "Remote sensing of volcanic ash plumes from thermal infrared: a case study analysis from SEVIRI, MODIS and IASI instruments". *Atmospheric Measurement Techniques* 7.2, pp. 359–371.

Durre, Imke, Russell S Vose, and David B Wuertz (2006). "Overview of the integrated global radiosonde archive". *Journal of Climate* 19.1, pp. 53–68.

— (2008). "Robust automated quality assurance of radiosonde temperatures". *Journal of Applied Meteorology and Climatology* 47.8, pp. 2081–2095.

Eckardt, FD, S Bekiswa, JR Von Holdt, C Jack, NJ Kuhn, F Mogane, JE Murray, N Ndara, and AR Palmer (2020). "South Africa's agricultural dust sources and events from MSG SEVIRI". *Aeolian Research* 47, p. 100637.

Eigenwillig, Norbert and Herbert Fischer (1982). "Determination of midtropospheric wind vectors by tracking pure water vapor structures in METEOSAT water vapor image sequences". *Bulletin of the American Meteorological Society*, pp. 44–58.

Eldridge, RH (1957). "A synoptic study of West African disturbance lines". *Quarterly Journal of the Royal Meteorological Society* 83.357, pp. 303–314.

Emmel, C, P Knippertz, and O Schulz (2010). "Climatology of convective density currents in the southern foothills of the Atlas Mountains". *Journal of Geophysical Research: Atmospheres* 115.D11.

Engelstaedter, Sebastian, Ina Tegen, and Richard Washington (2006). "North African dust emissions and transport". *Earth-Science Reviews* 79.1, pp. 73–100.

Engelstaedter, Sebastian and Richard Washington (2007). "Atmospheric controls on the annual cycle of North African dust". *Journal of Geophysical Research: Atmospheres* 112.D3.

Engelstaedter, Sebastien, Richard Washington, Cyrille Flamant, Doug J Parker, CJT Allen, and MC Todd (2015). "The Saharan heat low and moisture transport pathways in the central Sahara—Multiaircraft observations and Africa-LAM evaluation". *Journal of Geophysical Research: Atmospheres* 120.10, pp. 4417–4442.

Engerer, Nicholas A, David J Stensrud, and Michael C Coniglio (2008). "Surface characteristics of observed cold pools". *Monthly Weather Review* 136.12, pp. 4839–4849.

Escudero, M, A Stein, RR Draxler, X Querol, A Alastuey, S Castillo, and A Avila (2006). "Determination of the contribution of northern Africa dust source areas to PM10 concentrations over the central Iberian Peninsula using the Hybrid Single-Particle Lagrangian Integrated Trajectory model (HYSPLIT) model". *Journal of Geophysical Research: Atmospheres* 111.D6.

Evan, Amato T, Stephanie Fiedler, Chun Zhao, Laurent Menut, Kerstin Schepanski, Cyrille Flamant, and Owen Doherty (2015). "Derivation of an observation-based map of North African dust emission". *Aeolian Research* 16, pp. 153–162.

Evan, Amato T, Cyrille Flamant, Stephanie Fiedler, and Owen Doherty (2014). "An analysis of aeolian dust in climate models". *Geophysical Research Letters* 41.16, pp. 5996–6001.

Evan, Amato T, Cyrille Flamant, Marco Gaetani, and Françoise Guichard (2016). "The past, present and future of African dust". *Nature* 531.7595, pp. 493–495.

Evan, Amato T, Gregory R Foltz, Dongxiao Zhang, and Daniel J Vimont (2011). "Influence of African dust on ocean-atmosphere variability in the tropical Atlantic". *Nature Geoscience* 4.11, pp. 762–765.

Evan, Amato T, Andrew K Heidinger, and Michael J Pavolonis (2006). "Development of a new over-water Advanced Very High Resolution Radiometer dust detection algorithm". *International Journal of Remote Sensing* 27.18, pp. 3903–3924.

Evan, AT (2018). "Surface winds and dust biases in climate models". *Geophysical Research Letters* 45.2, pp. 1079–1085.

Evans, Adrian N (2006). "Cloud motion analysis using multichannel correlation-relaxation labeling". *IEEE Geoscience and Remote Sensing Letters* 3.3, pp. 392–396.

Fécan, F, B Marticorena, and G Bergametti (1998). "Parametrization of the increase of the aeolian erosion threshold wind friction velocity due to soil moisture for arid and semi-arid areas". *Annales Geophysicae*. Vol. 17. 1. Springer, pp. 149–157.

Feuerstein, Stefanie and Kerstin Schepanski (2019). "Identification of dust sources in a Saharan dust hot-spot and their implementation in a dust-emission model". *Remote Sensing* 11.1, p. 4.

Fiedler, S, K Schepanski, B Heinold, P Knippertz, and I Tegen (2013). "Climatology of nocturnal low-level jets over North Africa and implications for modeling mineral dust emission". *Journal of Geophysical Research: Atmospheres* 118.12, pp. 6100–6121.

Fiedler, S, K Schepanski, P Knippertz, B Heinold, and I Tegen (2014). "How important are atmospheric depressions and mobile cyclones for emitting mineral dust aerosol in North Africa?" *Atmospheric Chemistry and Physics* 14.17, pp. 8983–9000.

Fiedler, Stephanie, ML Kaplan, and P Knippertz (2015). "The importance of Harmattan surges for the emission of North African dust aerosol". *Geophysical Research Letters* 42.21, pp. 9495–9504.

Fiedler, Stephanie, Peter Knippertz, Stephanie Woodward, Gill M Martin, Nicolas Bellouin, Andrew N Ross, Bernd Heinold, Kerstin Schepanski, Cathryn E Birch, and Ina Tegen (2016). "A process-based evaluation of

dust-emitting winds in the CMIP5 simulation of HadGEM2-ES". *Climate Dynamics* 46.3-4, pp. 1107–1130.

Flamant, Cyrille, J-P Chaboureau, DJ Parker, CM Taylor, J-P Cammas, Olivier Bock, Franck Timouk, and Jacques Pelon (2007). "Airborne observations of the impact of a convective system on the planetary boundary layer thermodynamics and aerosol distribution in the inter-tropical discontinuity region of the West African monsoon". *Quarterly Journal of the Royal Meteorological Society* 133.626, pp. 1175–1189.

Flamant, Cyrille, Peter Knippertz, Andreas H Fink, Aristide Akpo, B Brooks, Christine J Chiu, Hugh Coe, Sylvester Danuor, M Evans, Oluwagbemiga Jegede, et al. (2018). "The dynamics–aerosol–chemistry–cloud interactions in West Africa field campaign: Overview and research highlights". *Bulletin of the American Meteorological Society* 99.1, pp. 83–104.

Flamant, Cyrille, Peter Knippertz, Douglas J Parker, J-P Chaboureau, Christophe Lavaysse, A Agusti-Panareda, and L Kergoat (2009a). "The impact of a mesoscale convective system cold pool on the northward propagation of the intertropical discontinuity over West Africa". *Quarterly Journal of the Royal Meteorological Society: A journal of the atmospheric sciences, applied meteorology and physical oceanography* 135.638, pp. 139–159.

Flamant, Cyrille, Christophe Lavaysse, Martin C Todd, J-P Chaboureau, and Jacques Pelon (2009b). "Multi-platform observations of a springtime case of Bodélé and Sudan dust emission, transport and scavenging over West Africa". *Quarterly Journal of the Royal Meteorological Society: A journal of the atmospheric sciences, applied meteorology and physical oceanography* 135.639, pp. 413–430.

Foroutan, Hosein and Jonathan E Pleim (2017). "Improving the simulation of convective dust storms in regional-to-global models". *Journal of advances in modeling earth systems* 9.5, pp. 2046–2060.

Francis, Diana, Ricardo Fonseca, Narendra Nelli, Juan Cuesta, Michael Weston, Amato Evan, and Marouane Temimi (2020). "The Atmospheric Drivers of the Major Saharan Dust Storm in June 2020". *Geophysical Research Letters* 47.24, e2020GL090102.

Gaberšek, Saša and Dale R Durran (2004). "Gap flows through idealized topography. Part I: Forcing by large-scale winds in the nonrotating limit". *Journal of the atmospheric sciences* 61.23, pp. 2846–2862.

Gamo, M (1996). "Thickness of the dry convection and large-scale subsidence above deserts". *Boundary-Layer Meteorology* 79.3, pp. 265–278.

Garcia-Carreras, L, JH Marsham, DJ Parker, CL Bain, S Milton, A Saci, M Salah-Ferroudj, B Ouchene, and R Washington (2013). "The impact of convective cold pool outflows on model biases in the Sahara". *Geophysical Research Letters* 40.8, pp. 1647–1652.

Garcia-Carreras, Luis, DJ Parker, JH Marsham, PD Rosenberg, IM Brooks, AP Lock, F Marenco, JB McQuaid, and M Hobby (2015). "The turbulent structure and diurnal growth of the Saharan atmospheric boundary layer". *Journal of the Atmospheric Sciences* 72.2, pp. 693–713.

Garreaud, RenéD and Ricardo C Muñoz (2005). "The low-level jet off the west coast of subtropical South America: Structure and variability". *Monthly Weather Review* 133.8, pp. 2246–2261.

Ge, Jin Ming, Huayue Liu, Jianping Huang, and Qiang Fu (2016). "Taklimakan Desert nocturnal low-level jet: climatology and dust activity". *Atmospheric Chemistry and Physics* 16.12, pp. 7773–7783.

Gentine, Pierre, Alix Garelli, Seung-Bu Park, Ji Nie, Giuseppe Torri, and Zhiming Kuang (2016). "Role of surface heat fluxes underneath cold pools". *Geophysical research letters* 43.2, pp. 874–883.

Gibbons, Matthew, Qilong Min, and Jiwen Fan (2018). "Investigating the impacts of Saharan dust on tropical deep convection using spectral bin microphysics". *Atmospheric Chemistry and Physics (Online)* 18.PNNL-SA-134455.

Giglio, L and DP Roy (2020). "On the outstanding need for a long-term, multi-decadal, validated and quality assessed record of global burned area: Caution in the use of Advanced Very High Resolution Radiometer data". *Science of Remote Sensing* 2, p. 100007.

Gillette, Dale A, Irving H Blifford Jr, and DW Fryrear (1974). "The influence of wind velocity on the size distributions of aerosols generated by the wind erosion of soils". *Journal of Geophysical Research* 79.27, pp. 4068–4075.

Gilmore, Matthew S and Louis J Wicker (1998). "The influence of midtropospheric dryness on supercell morphology and evolution". *Monthly Weather Review* 126.4, pp. 943–958.

Ginoux, P, M Chin, I Tegen, J Prospero, B Holben, O Dubovik, and SJ Lin (2001a). "Global simulation of dust in the troposphere: Model description and assessment". *J. Geophys. Res* 106.20, pp. 255–20.

Ginoux, Paul, Mian Chin, Ina Tegen, Joseph M Prospero, Brent Holben, Oleg Dubovik, and Shian-Jiann Lin (2001b). "Sources and distributions of dust aerosols simulated with the GOCART model". *Journal of Geophysical Research: Atmospheres* 106.D17, pp. 20255–20273.

Ginoux, Paul, Joseph M Prospero, Thomas E Gill, N Christina Hsu, and Ming Zhao (2012). "Global-scale attribution of anthropogenic and natural dust sources and their emission rates based on MODIS Deep Blue aerosol products". *Reviews of Geophysics* 50.3.

Grams, Christian M, Sarah C Jones, John H Marsham, Douglas J Parker, Jim M Haywood, and Vincent Heuveline (2010). "The Atlantic inflow to the Saharan heat low: Observations and modelling". *Quarterly Journal of the Royal Meteorological Society* 136.S1, pp. 125–140.

Grandpeix, Jean-Yves and Jean-Philippe Lafore (2010). "A density current parameterization coupled with Emanuel's convection scheme. Part I: The models". *Journal of Atmospheric Sciences* 67.4, pp. 881–897.

Gregory, D and PR Rowntree (1990). "A mass flux convection scheme with representation of cloud ensemble characteristics and stability-dependent closure". *Monthly Weather Review* 118.7, pp. 1483–1506.

Grogan, Dustin FP and Christopher D Thorncroft (2019). "The characteristics of African easterly waves coupled to Saharan mineral dust aerosols". *Quarterly Journal of the Royal Meteorological Society* 145.720, pp. 1130–1146.

Guirado, C, Emilio Cuevas, VE Cachorro, C Toledano, Silvia Alonso-Pérez, JJ Bustos, Sara Basart, PM Romero, C Camino, M Mimouni, et al. (2014). "Aerosol characterization at the Saharan AERONET site Tamanrasset". *Atmospheric Chemistry and Physics* 14.21, pp. 11753–11773.

Haustein, K, C Pérez, JM Baldasano, O Jorba, S Basart, RL Miller, Z Janjic, T Black, S Nickovic, Martin C Todd, et al. (2012). "Atmospheric dust modeling from meso to global scales with the online NMMB/BSC-Dust model–Part 2: Experimental campaigns in Northern Africa". *Atmospheric Chemistry and Physics* 12.6, pp. 2933–2958.

Heinold, B, P Knippertz, JH Marsham, S Fiedler, NS Dixon, K Schepanski, B Laurent, and I Tegen (2013). "The role of deep convection and nocturnal low-level jets for dust emission in summertime West Africa: Estimates from convection-permitting simulations". *Journal of Geophysical Research: Atmospheres* 118.10, pp. 4385–4400.

Heinold, Bernd, Peter Knippertz, and Robert J Beare (2015). "Idealized large-eddy simulations of nocturnal low-level jets over subtropical desert regions and implications for dust-generating winds". *Quarterly Journal of the Royal Meteorological Society* 141.690, pp. 1740–1752.

Heinold, Bernd, Ina Tegen, Kerstin Schepanski, and Jamie R Banks (2016). "New developments in the representation of Saharan dust sources in the aerosol–climate model ECHAM6-HAM2". *Geoscientific Model Development* 9.2, p. 765.

Herman, JR, PK Bhartia, Or Torres, C Hsu, C Seftor, and E Celarier (1997). "Global distribution of UV-absorbing aerosols from Nimbus 7/TOMS data". *Journal of Geophysical Research: Atmospheres* 102.D14, pp. 16911–16922.

Hersbach, Hans and DJEN Dee (2016). "ERA5 reanalysis is in production". *ECMWF newsletter* 147.7, pp. 5–6.

Hirose, Masafumi, Riko Oki, Shuji Shimizu, Misako Kachi, and Tomohiko Higashiuwatoko (2008). "Finescale diurnal rainfall statistics refined from eight years of TRMM PR data". *Journal of Applied Meteorology and Climatology* 47.2, pp. 544–561.

Hobby, Matthew, Matthew Gascoyne, John H Marsham, Mark Bart, Christopher Allen, Sebastian Engelstaedter, Dieh Mohamed Fadel, Abdoulaye Gandega, Richard Lane, James B McQuaid, et al. (2013). "The Fennec automatic weather station (AWS) network: Monitoring the Saharan climate system". *Journal of Atmospheric and Oceanic Technology* 30.4, pp. 709–724.

Hoffman, Matthew D and Andrew Gelman (2014). "The No-U-turn sampler: adaptively setting path lengths in Hamiltonian Monte Carlo." *Journal of Machine Learning Research* 15.1, pp. 1593–1623.

Holben, Brent N, T F Eck, Iet al Slutsker, D Tanre, JP Buis, A Setzer, E Vermote, John A Reagan, YJ Kaufman, T Nakajima, et al. (1998). "AERONET—A federated instrument network and data archive for aerosol characterization". *Remote sensing of environment* 66.1, pp. 1–16.

Holmes, John D and SE Oliver (2000). "An empirical model of a downburst". *Engineering structures* 22.9, pp. 1167–1172.

Hoose, C, U Lohmann, R Erdin, and I Tegen (2008). "The global influence of dust mineralogical composition on heterogeneous ice nucleation in mixed-phase clouds". *Environmental Research Letters* 3.2, p. 025003.

Hourdin, F, M Gueye, B Diallo, J-L Dufresne, J Escribano, L Menut, B Marticoréna, G Siour, and F Guichard (2015). "Parameterization of convective transport in the boundary layer and its impact on the representation of the diurnal cycle of wind and dust emissions". *Atmospheric Chemistry and Physics* 15.12, pp. 6775–6788.

Houze, Robert A (1977). "Structure and dynamics of a tropical squall–line system". *Monthly Weather Review* 105.12, pp. 1540–1567.

Hsu, N Christina, Si-Chee Tsay, Michael D King, and Jay R Herman (2004). "Aerosol properties over bright-reflecting source regions". *IEEE Transactions on Geoscience and Remote Sensing* 42.3, pp. 557–569.

Huang, Qian, John H Marsham, Wenshou Tian, Douglas J Parker, and Luis Garcia-Carreras (2018). "Large-eddy simulation of dust-uplift by a haboob density current". *Atmospheric Environment* 179, pp. 31–39.

Hughes, Ralph H (1992). *A directory of African wetlands*. IUCN.

Huneeus, N, M Schulz, Y Balkanski, J Griesfeller, MJ Prospero, Stefan Kinne, S Bauer, O Boucher, M Chin, F Dentener, et al. (2011). "Global dust model intercomparison in AeroCom phase I". *Atmospheric Chemistry and Physics* 11, pp. 7781–7816.

Husar, Rudolf B, Joseph M Prospero, and Larry L Stowe (1997). "Characterization of tropospheric aerosols over the oceans with the NOAA advanced very high resolution radiometer optical thickness operational product". *Journal of Geophysical Research: Atmospheres* 102.D14, pp. 16889–16909.

Jackson, Peter L, Georg Mayr, and Simon Vosper (2013). "Dynamically-driven winds". *Mountain weather research and forecasting*. Springer, pp. 121–218.

Jickells, TD, ZS An, Katrine K Andersen, AR Baker, G Bergametti, Nick Brooks, JJ Cao, PW Boyd, RA Duce, KA Hunter, et al. (2005). "Global iron connections between desert dust, ocean biogeochemistry, and climate". *science* 308.5718, pp. 67–71.

Kalu, AE (1979). "The African dust plume: its characteristics and propagation across West Africa in winter". *Saharan dust*, pp. 95–118.

Karam, Diana Bou, Earle Williams, Matthew Janiga, Cyrille Flamant, Michael McGraw-Herdeg, Juan Cuesta, Antoine Auby, and Chris Thorncroft (2014). "Synoptic-scale dust emissions over the Sahara Desert initiated by a moist convective cold pool in early August 2006". *Quarterly Journal of the Royal Meteorological Society* 140.685, pp. 2591–2607.

Karydis, VA, P Kumar, D Barahona, IN Sokolik, and Athanasios Nenes (2011). "On the effect of dust particles on global cloud condensation nuclei and cloud droplet number". *Journal of Geophysical Research: Atmospheres* 116.D23.

Kelly, James T, Catherine C Chuang, and Anthony S Wexler (2007). "Influence of dust composition on cloud droplet formation". *Atmospheric Environment* 41.14, pp. 2904–2916.

King, Michael D, Yoram J Kaufman, Didier Tanré, and Teruyuki Nakajima (1999). "Remote sensing of tropospheric aerosols from space: Past, present, and future". *Bulletin of the American Meteorological society* 80.11, pp. 2229–2260.

Klein, H, S Nickovic, W Haunold, U Bundke, B Nillius, M Ebert, S Weinbruch, L Schuetz, Z Levin, LA Barrie, et al. (2010). "Saharan dust and ice nuclei over Central Europe". *Atmospheric Chemistry and Physics* 10.21, pp. 10211–10221.

Klose, Martina and Yaping Shao (2013). "Large-eddy simulation of turbulent dust emission". *Aeolian Research* 8, pp. 49–58.

Knippertz, P, C Deutscher, K Kandler, T Müller, O Schulz, and L Schütz (2007). "Dust mobilization due to density currents in the Atlas region: Observations from the Saharan Mineral Dust Experiment 2006 field campaign". *Journal of Geophysical Research: Atmospheres* 112.D21.

Knippertz, P, J Trentmann, and A Seifert (2009). "High-resolution simulations of convective cold pools over the northwestern Sahara". *Journal of Geophysical Research: Atmospheres* 114.D8.

Knippertz, Peter (2008). "Dust emissions in the West African heat trough–the role of the diurnal cycle and of extratropical disturbances". *Meteorologische Zeitschrift* 17.5, pp. 553–563.

Knippertz, Peter and Andreas H Fink (2006). "Synoptic and dynamic aspects of an extreme springtime Saharan dust outbreak". *Quarterly Journal of the Royal Meteorological Society: A journal of the atmospheric sciences, applied meteorology and physical oceanography* 132.617, pp. 1153–1177.

Knippertz, Peter and Jan-Berend W Stuut (2014). *Mineral Dust: A Key Player in the Earth System*. Springer.

Knippertz, Peter and Martin C Todd (2010). "The central west Saharan dust hot spot and its relation to African easterly waves and extratropical disturbances". *Journal of Geophysical Research: Atmospheres* 115.D12.

— (2012). "Mineral dust aerosols over the Sahara: Meteorological controls on emission and transport and implications for modeling". *Reviews of Geophysics* 50.1.

Kocha, Cécile, Pierre Tulet, J-P Lafore, and Cyrille Flamant (2013). "The importance of the diurnal cycle of Aerosol Optical Depth in West Africa". *Geophysical Research Letters* 40.4, pp. 785–790.

Kok, Jasper F, Adeyemi A Adebiyi, Samuel Albani, Yves Balkanski, Ramiro Checa-Garcia, Mian Chin, Peter R Colarco, Douglas S Hamilton, Yue Huang, Akinori Ito, et al. (2021). "Contribution of the world's main dust source regions to the global cycle of desert dust". *Atmospheric Chemistry and Physics Discussions*, pp. 1–34.

Kok, Jasper F, Adeyemi A Adebiyi, Samuel Albani, Yves Balkanski, Ramiro Checa-Garcia, Mian Chin, Peter R Colarco, Douglas Stephen Hamilton, Yue Huang, Akinori Ito, et al. (2020). "Improved representation of the global dust cycle using observational constraints on dust properties and abundance". *UMBC Joint Center for Earth Systems Technology (JCET)*.

Kok, Jasper F, Eric JR Parteli, Timothy I Michaels, and Diana Bou Karam (2012). "The physics of wind-blown sand and dust". *Reports on progress in Physics* 75.10, p. 106901.

Kok, Jasper F, David A Ridley, Qing Zhou, Ron L Miller, Chun Zhao, Colette L Heald, Daniel S Ward, Samuel Albani, and Karsten Haustein (2017). "Smaller desert dust cooling effect estimated from analysis of dust size and abundance". *Nature Geoscience* 10.4, pp. 274–278.

Koren, Ilan and Yoram J Kaufman (2004). "Direct wind measurements of Saharan dust events from Terra and Aqua satellites". *Geophysical research letters* 31.6.

Koren, Ilan, Yoram J Kaufman, Richard Washington, Martin C Todd, Yinon Rudich, J Vanderlei Martins, and Daniel Rosenfeld (2006). "The Bodélé depression: a single spot in the Sahara that provides most of the mineral dust to the Amazon forest". *Environmental Research Letters* 1.1, p. 014005.

Kumar, P, IN Sokolik, and Athanasios Nenes (2011). "Measurements of cloud condensation nuclei activity and droplet activation kinetics of fresh unprocessed regional dust samples and minerals". *Atmospheric Chemistry and Physics* 11.7, pp. 3527–3541.

Lal, Rattan et al. (1994). *Soil erosion research methods*. CRC Press.

Lamancusa, Carmen and Kristina Wagstrom (2019). "Global transport of dust emitted from different regions of the Sahara". *Atmospheric environment* 214, p. 116734.

Largeron, Yann, Francoise Guichard, Dominique Bouniol, Fleur Couvreux, Laurent Kergoat, and Béatrice Marticorena (2015). "Can we use surface wind fields from meteorological reanalyses for Sahelian dust emission simulations?" *Geophysical Research Letters* 42.7, pp. 2490–2499.

Lavaysse, Christophe, Jean-Pierre Chaboureau, and Cyrille Flamant (2011). "Dust impact on the West African heat low in summertime". *Quarterly Journal of the Royal Meteorological Society* 137.658, pp. 1227–1240.

Lavaysse, Christophe, Cyrille Flamant, Amato Evan, Serge Janicot, and Marco Gaetani (2016). "Recent climatological trend of the Saharan heat low and its impact on the West African climate". *Climate Dynamics*, pp. 1–20.

Lavaysse, Christophe, Cyrille Flamant, Serge Janicot, DJ Parker, J-P Lafore, Benjamin Sultan, and Jacques Pelon (2009). "Seasonal evolution of the West African heat low: a climatological perspective". *Climate Dynamics* 33.2-3, pp. 313–330.

Lavi Bekin, Ofer, Onn Crouvi, and Dan G Blumberg (2020). "Areal Extent of Dust Emission Events and Source Geomorphology in Northern Africa from MSG-SEVIRI Data". *Remote Sensing* 12.17, p. 2775.

Lawson, TJ (1971). "Haboob structure at Khartoum". *Weather* 26.3, pp. 105–112.

Lensky, IM and Daniel Rosenfeld (2008). "Clouds-aerosols-precipitation satellite analysis tool (CAPSAT)". *Atmospheric Chemistry and Physics* 8.22, pp. 6739–6753.

Levelt, PF and R Noordhoek (2002). "OMI Algorithm Theoretical Basis Document Volume I: OMI Instrument, Level 0-1b Processor, Calibration & Operations". *Technology Report ATBD-OMI-01, Version* 1.

Liu, Chenyi, Paul Fieguth, and Christoph Garbe (2012). "Background subtraction and dust storm detection". *Geoscience and Remote Sensing Symposium (IGARSS), 2012 IEEE International*. IEEE, pp. 2179–2181.

Lock, AP, AR Brown, MR Bush, GM Martin, and RNB Smith (2000). "A new boundary layer mixing scheme. Part I: Scheme description and single-column model tests". *Monthly weather review* 128.9, pp. 3187–3199.

Lott, François and Martin J Miller (1997). "A new subgrid-scale orographic drag parametrization: Its formulation and testing". *Quarterly Journal of the Royal Meteorological Society* 123.537, pp. 101–127.

Lunt, DJ and PJ Valdes (2002). "The modern dust cycle: Comparison of model results with observations and study of sensitivities". *Journal of Geophysical Research: Atmospheres* 107.D23, AAC–1.

Luo, Chao, Natalie M Mahowald, and John Del Corral (2003). "Sensitivity study of meteorological parameters on mineral aerosol mobilization, transport, and distribution". *Journal of Geophysical Research: Atmospheres* 108.D15.

Mahajan, PN, VR Mupmdar, and SP Ghanekar (1989). "Excitation of low-level jet as seen by GOES (IO) satellite off the Somali coast". *Advances in Atmospheric Sciences* 6.4, pp. 475–482.

Mahowald, Natalie M, Sebastian Engelstaedter, Chao Luo, Andrea Sealy, Paulo Artaxo, Claudia Benitez-Nelson, Sophie Bonnet, Ying Chen, Patrick Y Chuang, David D Cohen, et al. (2008). "Atmospheric iron deposition: global distribution, variability, and human perturbations".

Mahowald, Natalie M, Silvia Kloster, S Engelstaedter, J Keith Moore, S Mukhopadhyay, Joseph R McConnell, S Albani, Scott C Doney, A Bhattacharya, MAJ Curran, et al. (2010). "Observed 20th century desert dust variability: impact on climate and biogeochemistry". *Atmospheric Chemistry and Physics* 10.22, pp. 10875–10893.

Marcella, MP and EAB Eltahir (2010). "Effects of mineral aerosols on the summertime climate of southwest Asia: Incorporating subgrid variability in a dust emission scheme". *Journal of Geophysical Research: Atmospheres* 115.D18.

Marsham, John H, Nick S Dixon, Luis Garcia-Carreras, Grenville MS Lister, Douglas J Parker, Peter Knippertz, and Cathryn E Birch (2013a). "The role of moist convection in the West African monsoon system: Insights from continental-scale convection-permitting simulations". *Geophysical Research Letters* 40.9, pp. 1843–1849.

Marsham, John H, Matt Hobby, CJT Allen, JR Banks, M Bart, BJ Brooks, C Cavazos-Guerra, S Engelstaedter, M Gascoyne, AR Lima, et al. (2013b). "Meteorology and dust in the central Sahara: Observations from Fennec supersite-1 during the June 2011 Intensive Observation Period". *Journal of Geophysical Research: Atmospheres* 118.10, pp. 4069–4089.

Marsham, John H, Peter Knippertz, Nick S Dixon, Douglas J Parker, and Grenville Lister (2011). "The importance of the representation of deep convection for modeled dust-generating winds over West Africa during summer". *Geophysical Research Letters* 38.16.

Marsham, John H, Douglas J Parker, Christian M Grams, Christopher M Taylor, and Jim M Haywood (2008). "Uplift of Saharan dust south of the intertropical discontinuity". *Journal of Geophysical Research: Atmospheres* 113.D21.

Marsham, John H, Douglas J Parker, Martin C Todd, Jamie R Banks, Helen E Brindley, Luis Garcia-Carreras, Alexander J Roberts, and Claire L Ryder (2016). "The contrasting roles of water and dust in controlling daily variations in radiative heating of the summertime Saharan heat low". *Atmospheric Chemistry and Physics* 16.5, pp. 3563–3575.

Marticorena, B and G Bergametti (1995). "Modeling the atmospheric dust cycle: 1. Design of a soil-derived dust emission scheme". *Journal of Geophysical Research: Atmospheres* 100.D8, pp. 16415–16430.

Martin, John H (1990). "Glacial-interglacial CO2 change: The iron hypothesis". *Paleoceanography* 5.1, pp. 1–13.

Menut, Laurent (2008). "Sensitivity of hourly Saharan dust emissions to NCEP and ECMWF modeled wind speed". *Journal of Geophysical Research: Atmospheres* 113.D16.

Menzel, W Paul (2001). "Cloud tracking with satellite imagery: From the pioneering work of Ted Fujita to the present". *Bulletin of the American Meteorological Society* 82.1, pp. 33–48.

Messaoudi, Djilali, Noureddine Settou, Belkhir Negrou, Soumia Rahmouni, Belkhir Settou, and Ishak Mayou (2019). "Site selection methodology for the wind-powered hydrogen refueling station based on AHP-GIS in Adrar, Algeria". *Energy Procedia* 162, pp. 67–76.

Middleton, NJ and AS Goudie (2001). "Saharan dust: sources and trajectories". *Transactions of the Institute of British Geographers* 26.2, pp. 165–181.

Miller, RL, RV Cakmur, Ja Perlwitz, IV Geogdzhayev, P Ginoux, D Koch, KE Kohfeld, C Prigent, R Ruedy, GA Schmidt, et al. (2006). "Mineral dust aerosols in the NASA Goddard Institute for Space Sciences ModelE atmospheric general circulation model". *Journal of Geophysical Research: Atmospheres* 111.D6.

Miller, RL, Ja Perlwitz, and I Tegen (2004). "Feedback upon dust emission by dust radiative forcing through the planetary boundary layer". *Journal of Geophysical Research: Atmospheres* 109.D24.

Miller, RL and Ina Tegen (1998). "Climate response to soil dust aerosols". *Journal of climate* 11.12, pp. 3247–3267.

Miller, Steven D, Arunas P Kuciauskas, Ming Liu, Qiang Ji, Jeffrey S Reid, Daniel W Breed, Annette L Walker, and Abdulla Al Mandoos (2008). "Haboob dust storms of the southern Arabian Peninsula". *Journal of Geophysical Research: Atmospheres* 113.D1.

Min, Q-L, R Li, B Lin, E Joseph, S Wang, Y Hu, V Morris, and F Chang (2009). "Evidence of mineral dust altering cloud microphysics and precipitation." *Atmospheric Chemistry & Physics* 9.9.

Muhs, Daniel R, Joseph M Prospero, Matthew C Baddock, and Thomas E Gill (2014). "Identifying sources of aeolian mineral dust: Present and past". *Mineral Dust*. Springer, pp. 51–74.

Murphy, JM, GR Harris, DMH Sexton, EJ Kendon, PE Bett, RT Clark, KE Eagle, G Fosser, F Fung, JA Lowe, et al. (2018). "UKCP18 land projections: Science report".

Murray, Jon E, Helen E Brindley, Robert G Bryant, Jacqui E Russell, Katherine F Jenkins, and R Washington (2016). "Enhancing weak transient signals in SEVIRI false color imagery: Application to dust source detection in southern Africa". *Journal of Geophysical Research: Atmospheres* 121.17.

Nousiainen, Timo (2009). "Optical modeling of mineral dust particles: A review". *Journal of Quantitative Spectroscopy and Radiative Transfer* 110.14-16, pp. 1261–1279.

Pantillon, Florian, Peter Knippertz, John H Marsham, and Cathryn E Birch (2015). "A parameterization of convective dust storms for models with mass-flux convection schemes". *Journal of the Atmospheric Sciences* 72.6, pp. 2545–2561.

Pantillon, Florian, Peter Knippertz, John H Marsham, Hans-Jürgen Panitz, and Ingeborg Bischoff-Gauss (2016). "Modeling haboob dust storms in large-scale weather and climate models". *Journal of Geophysical Research: Atmospheres* 121.5, pp. 2090–2109.

Parajuli, Sagar Prasad, Ted M Zobeck, Gary Kocurek, Zong-Liang Yang, and Georgiy L Stenchikov (2016). "New insights into the wind-dust relationship in sandblasting and direct aerodynamic entrainment from wind tunnel experiments". *Journal of Geophysical Research: Atmospheres* 121.4, pp. 1776–1792.

Parker, DJ, RR Burton, A Diongue-Niang, RJ Ellis, M Felton, CM Taylor, CD Thorncroft, P Bessemoulin, and AM Tompkins (2005a). "The diurnal cycle of the West African monsoon circulation". *Quarterly Journal of the Royal Meteorological Society* 131.611, pp. 2839–2860.

Parker, Douglas J (1996). "Cold pools in shear". *Quarterly Journal of the Royal Meteorological Society* 122.535, pp. 1655–1674.

Parker, Douglas J, Chris D Thorncroft, Ralph R Burton, and Aıda Diongue-Niang (2005b). "Analysis of the African easterly jet, using aircraft observations from the

JET2000 experiment". *Quarterly Journal of the Royal Meteorological Society: A journal of the atmospheric sciences, applied meteorology and physical oceanography* 131.608, pp. 1461–1482.

Pérez, Carlos, Slobodan Nickovic, Goran Pejanovic, José Marıa Baldasano, and Emin Özsoy (2006). "Interactive dust-radiation modeling: A step to improve weather forecasts". *Journal of Geophysical Research: Atmospheres* 111.D16.

Pérez Garcıa-Pando, Carlos, Michelle C Stanton, Peter J Diggle, Sylwia Trzaska, Ron L Miller, Jan P Perlwitz, José M Baldasano, Emilio Cuevas, Pietro Ceccato, Pascal Yaka, et al. (2014). "Soil dust aerosols and wind as predictors of seasonal meningitis incidence in Niger". *Environmental health perspectives* 122.7, pp. 679–686.

Pokharel, Ashok Kumar and Michael L Kaplan (2019). "Organization of dust storms and synoptic-scale transport of dust by Kelvin waves". *Earth System Dynamics* 10.4, pp. 651–666.

Pope, RJ, JH Marsham, P Knippertz, ME Brooks, and AJ Roberts (2016). "Identifying errors in dust models from data assimilation". *Geophysical research letters* 43.17, pp. 9270–9279.

Price, HC, KJ Baustian, JB McQuaid, A Blyth, KN Bower, T Choularton, RJ Cotton, Z Cui, PR Field, M Gallagher, et al. (2018). "Atmospheric ice-nucleating particles in the dusty tropical Atlantic". *Journal of Geophysical Research: Atmospheres* 123.4, pp. 2175–2193.

Prospero, Joseph M, Anne E Barkley, Cassandra J Gaston, Alexandre Gatineau, Arthur Campos y Sansano, and Kathy Panechou (2020). "Characterizing and quantifying African dust transport and deposition to South America: implications for the phosphorus budget in the Amazon Basin". *Global Biogeochemical Cycles* 34.9, e2020GB006536.

Prospero, Joseph M, Joanna E Bullard, and Richard Hodgkins (2012). "High-latitude dust over the North Atlantic: Inputs from Icelandic proglacial dust storms". *science* 335.6072, pp. 1078–1082.

Prospero, Joseph M, Paul Ginoux, Omar Torres, Sharon E Nicholson, and Thomas E Gill (2002). "Environmental characterization of global sources of atmospheric soil dust identified with the Nimbus 7 Total Ozone Mapping Spectrometer (TOMS) absorbing aerosol product". *Reviews of geophysics* 40.1.

Prospero, Joseph M and Peter J Lamb (2003). "African droughts and dust transport to the Caribbean: Climate change implications". *Science* 302.5647, pp. 1024–1027.

Provod, M, JH Marsham, DJ Parker, and CE Birch (2016). "A characterization of cold pools in the West African Sahel". *Monthly Weather Review* 144.5, pp. 1923–1934.

Querol, Xavier, Andrés Alastuey, Sergio Rodriguez, Felicià Plana, Carmen R Ruiz, Nuria Cots, Guillem Massagué, and Oriol Puig (2001). "PM10 and PM2. 5 source apportionment in the Barcelona Metropolitan area, Catalonia, Spain". *Atmospheric Environment* 35.36, pp. 6407–6419.

Rácz, Zsuzsanna and Roger K Smith (1999). "The dynamics of heat lows". *Quarterly Journal of the Royal Meteorological Society* 125.553, pp. 225–252.

Rajot, JL, SC Alfaro, L Gomes, and A Gaudichet (2003). "Soil crusting on sandy soils and its influence on wind erosion". *Catena* 53.1, pp. 1–16.

Ramon, Jaume, Llorenç Lledó, Verónica Torralba, Albert Soret, and Francisco J Doblas-Reyes (2019). "What global reanalysis best represents

near-surface winds?" *Quarterly Journal of the Royal Meteorological Society* 145.724, pp. 3236–3251.

Ranjha, Raza, Gunilla Svensson, Michael Tjernström, and Alvaro Semedo (2013). "Global distribution and seasonal variability of coastal low-level jets derived from ERA-Interim reanalysis". *Tellus A* 65.

Redelsperger, Jean-Luc, Françoise Guichard, and Sylvain Mondon (2000). "A parameterization of mesoscale enhancement of surface fluxes for large-scale models". *Journal of Climate* 13.2, pp. 402–421.

Redelsperger, Jean-Luc and Jean-Philippe Lafore (1988). "A three-dimensional simulation of a tropical squall line: Convective organization and thermodynamic vertical transport". *Journal of Atmospheric Sciences* 45.8, pp. 1334–1356.

Redl, Robert, Andreas H Fink, and Peter Knippertz (2015). "An objective detection method for convective cold pool events and its application to Northern Africa". *Monthly Weather Review* 143.12, pp. 5055–5072.

Redl, Robert, Peter Knippertz, and Andreas H Fink (2016). "Weakening and moistening of the summertime Saharan heat low through convective cold pools from the Atlas Mountains". *Journal of Geophysical Research: Atmospheres* 121.8, pp. 3907–3928.

Reinfried, F, I Tegen, B Heinold, O Hellmuth, Kerstin Schepanski, U Cubasch, H Huebener, and P Knippertz (2009). "Simulations of convectively-driven density currents in the Atlas region using a regional model: Impacts on dust emission and sensitivity to horizontal resolution and convection schemes". *Journal of Geophysical Research: Atmospheres* 114.D8.

Reynolds, Richard W, Nick A Rayner, Thomas M Smith, Diane C Stokes, and Wanqiu Wang (2002). "An improved in situ and satellite SST analysis for climate". *Journal of climate* 15.13, pp. 1609–1625.

Ridley, DA, CL Heald, and B Ford (2012). "North African dust export and deposition: A satellite and model perspective". *Journal of Geophysical Research: Atmospheres* 117.D2.

Roberts, AJ and P Knippertz (2014). "The formation of a large summertime Saharan dust plume: Convective and synoptic-scale analysis". *Journal of Geophysical Research: Atmospheres* 119.4, pp. 1766–1785.

Roberts, Alex and Peter Knippertz (2012). "Haboobs: convectively generated dust storms in West Africa". *Weather* 67.12, pp. 311–316.

Roberts, Alexander J, John H Marsham, and Peter Knippertz (2015). "Disagreements in low-level moisture between (re) analyses over summertime West Africa". *Monthly Weather Review* 143.4, pp. 1193–1211.

Roberts, Alexander J, John H Marsham, Peter Knippertz, Douglas J Parker, Mark Bart, Luis Garcia-Carreras, Matthew Hobby, James B McQuaid, Philip D Rosenberg, and Daniel Walker (2017). "New Saharan wind observations reveal substantial biases in analysed dust-generating winds". *Atmospheric Science Letters* 18.9, pp. 366–372.

Roberts, Alexander J, Margaret J Woodage, John H Marsham, Ellie J Highwood, Claire L Ryder, Willie McGinty, Simon Wilson, and Julia Crook (2018). "Can explicit convection improve modelled dust in summertime West Africa?" *Atmospheric Chemistry and Physics* 18.12, pp. 9025–9048.

Rodrıguez, S, E Cuevas, JM Prospero, A Alastuey, X Querol, J López-Solano, MI Garcıa, and Silvia Alonso-Pérez (2015). "Modulation of Saharan dust export

by the North African dipole". *Atmospheric Chemistry and Physics* 15.13, pp. 7471–7486.

Ross, AN, Adrian M Tompkins, and DJ Parker (2004). "Simple models of the role of surface fluxes in convective cold pool evolution". *Journal of the atmospheric sciences* 61.13, pp. 1582–1595.

Ryder, CL, EJ Highwood, TM Lai, Harald Sodemann, and John H Marsham (2013). "Impact of atmospheric transport on the evolution of microphysical and optical properties of Saharan dust". *Geophysical Research Letters* 40.10, pp. 2433–2438.

Ryder, CL, JB McQuaid, Cyrille Flamant, PD Rosenberg, Richard Washington, HE Brindley, EJ Highwood, JH Marsham, DJ Parker, MC Todd, et al. (2015). "Advances in understanding mineral dust and boundary layer processes over the Sahara from Fennec aircraft observations". *Atmospheric Chemistry and Physics* 15.14, pp. 8479–8520.

Ryder, Claire L, Elleanor J Highwood, Adrian Walser, Petra Seibert, Anne Philipp, and Bernadett Weinzierl (2019). "Coarse and giant particles are ubiquitous in saharan dust export regions and are radiatively significant over the sahara". *Atmospheric Chemistry and Physics* 19, pp. 15353–15376.

Sandu, Irina, Anton Beljaars, Peter Bechtold, Thorsten Mauritsen, and Gianpaolo Balsamo (2013). "Why is it so difficult to represent stably stratified conditions in numerical weather prediction (NWP) models?" *Journal of Advances in Modeling Earth Systems* 5.2, pp. 117–133.

Schepanski, K, P Knippertz, S Fiedler, Franck Timouk, and Jérome Demarty (2015). "The sensitivity of nocturnal low-level jets and near-surface winds over the Sahel to model resolution, initial conditions and boundary-layer set-up". *Quarterly Journal of the Royal Meteorological Society* 141.689, pp. 1442–1456.

Schepanski, K, I Tegen, and A Macke (2012). "Comparison of satellite based observations of Saharan dust source areas". *Remote Sensing of Environment* 123, pp. 90–97.

Schepanski, Kerstin, Cyrille Flamant, J-P Chaboureau, Cécile Kocha, JR Banks, HE Brindley, Christophe Lavaysse, Fabien Marnas, Jacques Pelon, and Pierre Tulet (2013). "Characterization of dust emission from alluvial sources using aircraft observations and high-resolution modeling". *Journal of Geophysical Research: Atmospheres* 118.13, pp. 7237–7259.

Schepanski, Kerstin, Bernd Heinold, and Ina Tegen (2017). "Harmattan, Saharan heat low, and West African monsoon circulation: modulations on the Saharan dust outflow towards the North Atlantic". *Atmospheric Chemistry and Physics* 17.17, pp. 10223–10243.

Schepanski, Kerstin, I Tegen, B Laurent, B Heinold, and Andreas Macke (2007). "A new Saharan dust source activation frequency map derived from MSG-SEVIRI IR-channels". *Geophysical Research Letters* 34.18.

Schepanski, Kerstin, Ina Tegen, MC Todd, B Heinold, Gerhard Bönisch, B Laurent, and Andreas Macke (2009). "Meteorological processes forcing Saharan dust emission inferred from MSG-SEVIRI observations of subdaily dust source activation and numerical models". *Journal of Geophysical Research: Atmospheres* 114.D10.

Schmetz, Johannes, Kenneth Holmlund, Joel Hoffman, Bernard Strauss, Brian Mason, Volker Gaertner, Arno Koch, and Leo Van De Berg (1993). "Operational

cloud-motion winds from Meteosat infrared images". *Journal of Applied Meteorology and Climatology* 32.7, pp. 1206–1225.

Schmetz, Johannes, Paolo Pili, Stephen Tjemkes, Dieter Just, Jochen Kerkmann, Sergio Rota, and Alain Ratier (2002). "An introduction to Meteosat second generation (MSG)". *Bulletin of the American Meteorological Society* 83.7, pp. 977–992.

Schulz, Michael, Joseph M Prospero, Alex R Baker, Frank Dentener, Luisa Ickes, Peter S Liss, Natalie M Mahowald, Slobodan Nickovic, Carlos Pérez Garcıa-Pando, Sergio Rodrıguez, et al. (2012). "Atmospheric transport and deposition of mineral dust to the ocean: Implications for research needs". *Environmental science & technology* 46.19, pp. 10390–10404.

Schwendike, Juliane, Sarah C Jones, Bernhard Vogel, and Heike Vogel (2016). "Mineral dust transport toward Hurricane Helene (2006)". *Journal of Geophysical Research: Atmospheres* 121.10, pp. 5538–5566.

Semazzi, Frederick HM and Liqiang Sun (1997). "The role of orography in determining the Sahelian climate". *International journal of climatology* 17.6, pp. 581–596.

Shao, Yaping, MR Raupach, and PA Findlater (1993). "Effect of saltation bombardment on the entrainment of dust by wind". *Journal of Geophysical Research: Atmospheres* 98.D7, pp. 12719–12726.

Shao, Yaping, Karl-Heinz Wyrwoll, Adrian Chappell, Jianping Huang, Zhaohui Lin, Grant H McTainsh, Masao Mikami, Taichu Y Tanaka, Xulong Wang, and Soonchang Yoon (2011). "Dust cycle: An emerging core theme in Earth system science". *Aeolian Research* 2.4, pp. 181–204.

Shenk, William E and Robert J Curran (1974). "The detection of dust storms over land and water with satellite visible and infrared measurements". *Monthly Weather Review* 102.12, pp. 830–837.

Simpson, JE (1969). "A comparison between laboratory and atmospheric density currents". *Quarterly Journal of the Royal Meteorological Society* 95.406, pp. 758–765.

Sinclair, Samantha N and Sandra L LeGrand (2019). "Reproducibility assessment and uncertainty quantification in subjective dust source mapping". *Aeolian research* 40, pp. 42–52.

Skinner, Christopher Bryan and Noah S Diffenbaugh (2014). "Projected changes in African easterly wave intensity and track in response to greenhouse forcing". *Proceedings of the National Academy of Sciences* 111.19, pp. 6882–6887.

Smith, RNB (1990). "A scheme for predicting layer clouds and their water content in a general circulation model". *Quarterly Journal of the Royal Meteorological Society* 116.492, pp. 435–460.

Soares, Pedro MM, Rita M Cardoso, Álvaro Semedo, Maria J Chinita, and Raza Ranjha (2014). "Climatology of the Iberia coastal low-level wind jet: weather research forecasting model high-resolution results". *Tellus A* 66.

Soares, Pedro MM, Daniela CA Lima, Álvaro Semedo, Rita M Cardoso, William Cabos, and Dmitry Sein (2019). "The North African coastal low level wind jet: a high resolution view". *Climate dynamics* 53.1-2, pp. 1211–1230.

Sodemann, Harald, TM Lai, Franco Marenco, Claire L Ryder, Cyrille Flamant, P Knippertz, Phil Rosenberg, Mark Bart, and Jim B Mcquaid (2015). "Lagrangian dust model simulations for a case of moist convective dust emission and transport

in the western Sahara region during Fennec/LADUNEX". *Journal of Geophysical Research: Atmospheres* 120.12, pp. 6117–6144.

Solmon, Fabien, Nellie Elguindi, and Marc Mallet (2012). "Radiative and climatic effects of dust over West Africa, as simulated by a regional climate model". *Climate Research* 52, pp. 97–113.

Spengler, Thomas, Michael John Reeder, and Roger K Smith (2005). "The dynamics of heat lows in simple background flows". *Quarterly Journal of the Royal Meteorological Society: A journal of the atmospheric sciences, applied meteorology and physical oceanography* 131.612, pp. 3147–3165.

Spengler, Thomas and Roger K Smith (2008). "The dynamics of heat lows over flat terrain". *Quarterly Journal of the Royal Meteorological Society: A journal of the atmospheric sciences, applied meteorology and physical oceanography* 134.637, pp. 2157–2172.

Stevens, Bjorn, Stephanie Fiedler, Stefan Kinne, Karsten Peters, Sebastian Rast, Jobst Müsse, Steven J Smith, and Thorsten Mauritsen (2017). "MACv2-SP: A parameterization of anthropogenic aerosol optical properties and an associated Twomey effect for use in CMIP6". *Geoscientific Model Development* 10, pp. 433–452.

Stowe, Larry L, Alexander M Ignatov, and Ramdas R Singh (1997). "Development, validation, and potential enhancements to the second-generation operational aerosol product at the National Environmental Satellite, Data, and Information Service of the National Oceanic and Atmospheric Administration". *Journal of Geophysical Research: Atmospheres* 102.D14, pp. 16923–16934.

Stull, Roland B (2012). *An introduction to boundary layer meteorology*. Vol. 13. Springer Science & Business Media.

Sultan, Benjamin and Serge Janicot (2003). "The West African monsoon dynamics. Part II: The "preonset" and "onset" of the summer monsoon". *Journal of climate* 16.21, pp. 3407–3427.

Sutton, LJ (1925). "Haboobs". *Quarterly Journal of the Royal Meteorological Society* 51.213, pp. 25–30.

Swap, Robert, Michael Garstang, S Greco, R Talbot, and P Kållberg (1992). "Saharan dust in the Amazon Basin". *Tellus B* 44.2, pp. 133–149.

Tegen, I, K Schepanski, and B Heinold (2013). "Comparing two years of Saharan dust source activation obtained by regional modelling and satellite observations". *Atmospheric Chemistry and Physics* 13.5, pp. 2381–2390.

Tegen, Ina (2003). "Modeling the mineral dust aerosol cycle in the climate system". *Quaternary Science Reviews* 22.18-19, pp. 1821–1834.

Tegen, Ina and Inez Fung (1994). "Modeling of mineral dust in the atmosphere: Sources, transport, and optical thickness". *Journal of Geophysical Research: Atmospheres* 99.D11, pp. 22897–22914.

Tegen, Ina, Sandy P Harrison, Karen Kohfeld, I Colin Prentice, Michael Coe, and Martin Heimann (2002). "Impact of vegetation and preferential source areas on global dust aerosol: Results from a model study". *Journal of Geophysical Research: Atmospheres* 107.D21, AAC–14.

Tegen, Ina and Michael Schulz (2014). "Numerical dust models". *Mineral Dust*. Springer, pp. 201–222.

Textor, C, M Schulz, S Guibert, Stefan Kinne, Y Balkanski, SE Bauer, T Berntsen, TF Berglen, Olivier Boucher, M Chin, et al. (2006). "Analysis and quantification

of the diversities of aerosol life cycles within AeroCom". *Atmospheric Chemistry and Physics* 6, pp. 1777–1813.

Thorncroft, CD and M Blackburn (1999). "Maintenance of the African easterly jet". *Quarterly Journal of the Royal Meteorological Society* 125.555, pp. 763–786.

Thorne, PW and RS Vose (2010). "Reanalyses suitable for characterizing long-term trends". *Bulletin of the American Meteorological Society* 91.3, pp. 353–362.

Todd, Martin C, D Bou Karam, C Cavazos, Christel Bouet, B Heinold, JM Baldasano, Guy Cautenet, I Koren, C Perez, Fabien Solmon, et al. (2008a). "Quantifying uncertainty in estimates of mineral dust flux: An intercomparison of model performance over the Bodélé Depression, northern Chad". *Journal of Geophysical Research: Atmospheres* 113.D24.

Todd, Martin C and Carolina Cavazos-Guerra (2016). "Dust aerosol emission over the Sahara during summertime from Cloud-Aerosol Lidar with Orthogonal Polarization (CALIOP) observations". *Atmospheric Environment* 128, pp. 147–157.

Todd, Martin C, Richard Washington, José Vanderlei Martins, Oleg Dubovik, Gil Lizcano, Samuel M'bainayel, and Sebastian Engelstaedter (2007). "Mineral dust emission from the Bodélé Depression, northern Chad, during BoDEx 2005". *Journal of Geophysical Research: Atmospheres* 112.D6.

Todd, Martin C, Richard Washington, Srivatsan Raghavan, Gil Lizcano, and Peter Knippertz (2008b). "Regional model simulations of the Bodélé low-level jet of northern Chad during the Bodélé Dust Experiment (BoDEx 2005)". *Journal of Climate* 21.5, pp. 995–1012.

Todd, MC, CJ T Allen, M Bart, M Bechir, J Bentefouet, BJ Brooks, C Cavazos-Guerra, T Clovis, S Deyane, M Dieh, et al. (2013). "Meteorological and dust aerosol conditions over the western Saharan region observed at Fennec Supersite-2 during the intensive observation period in June 2011". *Journal of Geophysical Research: Atmospheres* 118.15, pp. 8426–8447.

Tompkins, AM, C Cardinali, J-J Morcrette, and M Rodwell (2005). "Influence of aerosol climatology on forecasts of the African Easterly Jet". *Geophysical research letters* 32.10.

Trzeciak, Tomasz M, Luis Garcia-Carreras, and John H Marsham (2017). "Cross-Saharan transport of water vapor via recycled cold pool outflows from moist convection". *Geophysical research letters* 44.3, pp. 1554–1563.

Uno, I, Zifa Wang, M Chiba, YS Chun, Sun Ling Gong, Y Hara, E Jung, S-S Lee, M Liu, M Mikami, et al. (2006). "Dust model intercomparison (DMIP) study over Asia: Overview". *Journal of Geophysical Research: Atmospheres* 111.D12.

Van Der Does, Michèlle, Peter Knippertz, Philipp Zschenderlein, R Giles Harrison, and Jan-Berend W Stuut (2018). "The mysterious long-range transport of giant mineral dust particles". *Science advances* 4.12, eaau2768.

Vandenbussche, Sophie, Sieglinde Callewaert, Kerstin Schepanski, and Martine De Mazière (2020). "North African mineral dust sources: new insights from a combined analysis based on 3D dust aerosol distributions, surface winds and ancillary soil parameters". *Atmospheric Chemistry and Physics* 20.23, pp. 15127–15146.

Vanderwende, Brian J, Julie K Lundquist, Michael E Rhodes, Eugene S Takle, and Samantha L Irvin (2015). "Observing and simulating the summertime low-level jet in central Iowa". *Monthly Weather Review* 143.6, pp. 2319–2336.

Vizy, Edward K and Kerry H Cook (2009). "A mechanism for African monsoon breaks: Mediterranean cold air surges". *Journal of Geophysical Research: Atmospheres* 114.D1.

Wagner, Robert, Kerstin Schepanski, Bernd Heinold, and Ina Tegen (2016). "Interannual variability in the Saharan dust source activation—Toward understanding the differences between 2007 and 2008". *Journal of Geophysical Research: Atmospheres* 121.9, pp. 4538–4562.

Wald, AE, YJ Kaufman, D Tanré, and B-C Gao (1998). "Daytime and nighttime detection of mineral dust over desert using infrared spectral contrast". *Journal of Geophysical Research: Atmospheres* 103.D24, pp. 32307–32313.

Walters, David, Anthony J Baran, Ian Boutle, Malcolm Brooks, Paul Earnshaw, John Edwards, Kalli Furtado, Peter Hill, Adrian Lock, James Manners, et al. (2019). "The Met Office Unified Model global atmosphere 7.0/7.1 and JULES global land 7.0 configurations". *Geoscientific Model Development* 12.5, pp. 1909–1963.

Walters, David, Malcolm Brooks, Ian Boutle, Thomas Melvin, Rachel Stratton, Simon Vosper, Helen Wells, Keith Williams, Nigel Wood, Thomas Allen, et al. (2017). "The Met Office unified model global atmosphere 6.0/6.1 and JULES global land 6.0/6.1 configurations". *Geoscientific Model Development* 10.4, pp. 1487–1520.

Wang, Zhen-Ting (2016). "A theoretical interpretation of the "giant" dust particle conundrum". *Science of The Total Environment* 553, pp. 673–675.

Washington, R, C Flamant, DJ Parker, J Marsham, JB McQuaid, H Brindley, M Todd, EJ Highwood, CL Ryder, JP Chaboureau, et al. (2012). "Fennec–the Saharan climate system". *CLIVAR Exchanges* 17.3, pp. 31–33.

Washington, Richard, Christel Bouet, Guy Cautenet, Elisabeth Mackenzie, Ian Ashpole, Sebastian Engelstaedter, Gil Lizcano, Gideon M Henderson, Kerstin Schepanski, and Ina Tegen (2009). "Dust as a tipping element: the Bodélé Depression, Chad". *Proceedings of the National Academy of Sciences* 106.49, pp. 20564–20571.

Washington, Richard, Martin Todd, Nicholas J Middleton, and Andrew S Goudie (2003). "Dust-storm source areas determined by the total ozone monitoring spectrometer and surface observations". *Annals of the Association of American Geographers* 93.2, pp. 297–313.

Washington, Richard and Martin C Todd (2005). "Atmospheric controls on mineral dust emission from the Bodélé Depression, Chad: The role of the low level jet". *Geophysical Research Letters* 32.17.

Washington, Richard, Martin C Todd, Sebastian Engelstaedter, Samuel Mbainayel, and Fiona Mitchell (2006). "Dust and the low-level circulation over the Bodélé Depression, Chad: Observations from BoDEx 2005". *Journal of Geophysical Research: Atmospheres* 111.D3.

Williams, ER (2008). "Comment on "Atmospheric controls on the annual cycle of North African dust" by S. Engelstaedter and R. Washington". *Journal of Geophysical Research: Atmospheres* 113.D23.

Wolyn, Paul G and Thomas B Mckee (1994). "The mountain-plains circulation east of a 2-km-high north–south barrier". *Monthly weather review* 122.7, pp. 1490–1508.

Woodward, S (2011). "Mineral dust in HadGEM2". *Hadley Centre Technical Note* 87.

Wu, Chenglai, Zhaohui Lin, and Xiaohong Liu (2020). "The global dust cycle and uncertainty in CMIP5 (Coupled Model Intercomparison Project phase 5) models". *Atmospheric Chemistry and Physics* 20.17, pp. 10401–10425.

Wu, Qing X (1995). "A correlation-relaxation-labeling framework for computing optical flow-template matching from a new perspective". *IEEE Transactions on Pattern Analysis & Machine Intelligence* 9, pp. 843–853.

Xian, Peng, Philip J Klotzbach, Jason P Dunion, Matthew A Janiga, Jeffrey S Reid, Peter R Colarco, and Zak Kipling (2020). "Revisiting the relationship between Atlantic dust and tropical cyclone activity using aerosol optical depth reanalyses: 2003–2018". *Atmospheric Chemistry and Physics* 20.23, pp. 15357–15378.

Xu, Yiwen (2018). "Evaluation of mineral dust aerosol optical depth and related components from the CHIMERE-DUST model using satellite remote sensing and ground-based observations". *Atmospheric Environment* 191, pp. 395–413.

Yu, Hongbin, Mian Chin, Tianle Yuan, Huisheng Bian, Lorraine A Remer, Joseph M Prospero, Ali H Omar, David M Winker, Yuekui Yang, Yan Zhang, et al. (2015). "Saharan Dust Fertilizing Atlantic Ocean and Amazon Rainforest via Long-range Transport and Deposition: A Perspective from Multiyear Satellite Measurements". *AGU Fall Meeting Abstracts*. Vol. 2015, EP42A–05.

Yu, Hongbin, Qian Tan, Lillian Zhou, Yaping Zhou, Huisheng Bian, Mian Chin, Claire L Ryder, Robert C Levy, Yaswant Pradhan, Yingxi Shi, Qianqian Song, Zhibo Zhang, Peter R Colarco, Dongchu Kim, Lorraine A Remer, Tianle Yuan, Olga Mayol-Bracero, and Brent N Holben (2021). "Observation and modeling of a historic African dust intrusion into the Caribbean Basin and the southern U.S. in June 2020". *Atmospheric Chemistry and Physics Discussions*.

Yu, Yan, Olga V Kalashnikova, Michael J Garay, Huikyo Lee, and Michael Notaro (2018). "Identification and characterization of dust source regions across North Africa and the Middle East using MISR satellite observations". *Geophysical Research Letters* 45.13, pp. 6690–6701.

Yu, Yan, Olga V Kalashnikova, Michael J Garay, Huikyo Lee, Michael Notaro, James R Campbell, Jared Marquis, Paul Ginoux, and Gregory S Okin (2020). "Disproving the Bodélé depression as the primary source of dust fertilizing the Amazon Rainforest". *Geophysical Research Letters* 47.13, e2020GL088020.

Zängl, Günther and Silvia Gonzalez Chico (2006). "The thermal circulation of a grand plateau: Sensitivity to the height, width, and shape of the plateau". *Monthly weather review* 134.9, pp. 2581–2600.

Zender, Charles S, RLRL Miller, and Ina Tegen (2004). "Quantifying mineral dust mass budgets: Terminology, constraints, and current estimates". *Eos, Transactions American Geophysical Union* 85.48, pp. 509–512.

Zhang, Kai, Chun Zhao, Hui Wan, Yun Qian, Richard C Easter, Steven J Ghan, Koichi Sakaguchi, and Xiaohong Liu (2016). "Quantifying the impact of sub-grid surface wind variability on sea salt and dust emissions in CAM5". *Geoscientific Model Development* 9.2, pp. 607–632.